MAVERICK

Design of a Multi-fuel Aircraft for Viable Emission-Reduction with Integrated Combustion of Hydrogen and Kerosene

DSE Group 21

MAVERICK

by

DSE Group 21

Student Name	Student Number
Amaya Arena Lázaro	5989167
Dominik Cienkowski	5971683
Manuel de Gouvêa Pinto e Cruz	5920027
Simonas Koncevičius	5966124
Tim Nootenboom	5778948
Marcin Nowacki	5998085
Mara Orzu	5931711
Luca Rinalducci	5950317
Luuk Valkering	5962889
Yaan Wang	5941555

Course:	Design Synthesis Exercise
Tutor:	Dr Francesca De Domenico
External Tutor:	Daniel Diaz
Coaches:	Fynn Oppermann, Antonia Rahn
Project Duration:	April–June 2026
Faculty:	Faculty of Aerospace Engineering

This report was written within the AE3200 Design Synthesis Exercise course as part of the BSc Aerospace Engineering degree.

Preface

This report presents the work of ten Aerospace Engineering students at Delft University of Technology, completed as the capstone Design Synthesis Exercise of the Bachelor's programme. Over the course of the project, we developed MAVERICK: a 180-passenger dual-fuel aircraft concept that integrates hydrogen and kerosene/SAF combustion in a single propulsion system. Our aim was to design a viable transition between today's conventional narrow-body aircraft and future hydrogen-powered concepts, reducing emissions without requiring hydrogen infrastructure to be available in every route from entry into service.

The project required us to develop and integrate the aircraft as a complete system, from aircraft sizing, aerodynamics, structures, stability and control, and mission performance to the dual-fuel engine, liquid hydrogen tank, cryogenic feed system, operations, sustainability assessment, and market-entry strategy. 5–7 describe the core hydrogen and propulsion innovations, while Chapter 8 evaluates their environmental implications and the resulting life cycle emission reduction.

We would like to sincerely thank our tutor, Dr. Francesca De Domenico, for her continuous guidance that kept us on the right track for the length of the project, and for her invaluable advice in her speciality of combustion and propulsion, and beyond. We would also like to thank our coaches Antonia Rahn and Fynn Oppermann for their indispensable help, thorough feedback, routine visits to the Fellowship, and for tirelessly answering all our questions. Equally, we would like to extend our gratitude to our external tutor Daniel Diaz for his advice on the project from an industrial point of view. Special thanks to Dr. Arvind Gangoli Rao and Dr. Rishikesh Sampat for their valuable guidance in addressing the complex propulsion challenges encountered throughout this project.

Delft, 23 June 2026

Team MAVERICK

Executive Overview

The Multi-fuel Aircraft for Viable Emission Reduction with Integrated Combustion of Hydrogen and Kerosene (MAVERICK) is a 180-passenger dual-fuel narrow-body aircraft designed for a 2040 entry into service. It uses hydrogen where infrastructure is available while retaining kerosene/SAF flexibility for longer routes or airports where hydrogen refuelling is not available. Its market analysis showed a clear business opportunity due to increasing carbon costs, regulations, and pressure to decarbonise aviation, creating demand for aircraft that reduce lifecycle emissions. MAVERICK bridges the gap between current technologies and future hydrogen aviation, with an easier market entry and lower risk. Its expected early market is European network airlines operating from major hydrogen-ready or hydrogen-developing hubs, especially on 1000–2000 km routes. Overall, MAVERICK is feasible as a transitional aircraft towards hydrogen aviation because it combines emissions reduction, operational flexibility, narrow-body capacity, and a phased market-entry strategy aligned with the expected development of future aviation infrastructure.

The aircraft is designed as a transitional solution between conventional kerosene aviation and future fully hydrogen-powered aviation. It implements a dual-fuel propulsion system capable of combusting both hydrogen and kerosene/SAF in the same engine. As a result, the fuel mixture can be adapted to mission, airport infrastructure, emission targets, and operational constraints. The product's target lifetime emissions of CO_2 and NO_x are 50% compared to the reference aircraft, the A320neo. The aircraft is designed as a 180-passenger single-aisle aircraft intended to enter service by 2040. Its operating mission range is 2000 km, based on the operating missions of its competitors, while maintaining a maximum range capability of 3000 km to provide airlines with sufficient route flexibility.

Aircraft Design

MAVERICK aircraft was designed using a multidisciplinary iteration loop that connects aerodynamic-performance evaluation, mission-fuel sizing, component-wise weight estimation, Centre of Gravity (CG) analysis, and stability and control driven wing positioning, all closed within a higher-level propulsion-integration loop. The converged design point for 180 passenger dual fuel aircraft provides aircraft with a Maximum Take-Off Mass (MTOM) of 95 533 kg at an Operating Empty Mass (OEM) of 63 433 kg, with external dimensions of 50.56 × 35.90 × 13.31 m. The aircraft was sized for two out-and-back mission profiles; the nominal 2000 km and maximum 3000 km range; which yield fuel masses of 3435 kg of liquid hydrogen (LH_2), 5845 kg of kerosene (including contingency) and an additional 4700.6 kg of kerosene for the maximum mission range. This results in total tank volumes of 51.9 m^3 for hydrogen and 13.6 m^3 for kerosene.

The internal layout places the liquid-hydrogen tank aft of the rear cargo hold, while kerosene is stored in a forward trim tank and wing tanks. This arrangement preserves passenger and cargo capacity while enabling hydrogen feed to both engines and active fuel transfer for centre of gravity control, as shown in Figure 1.

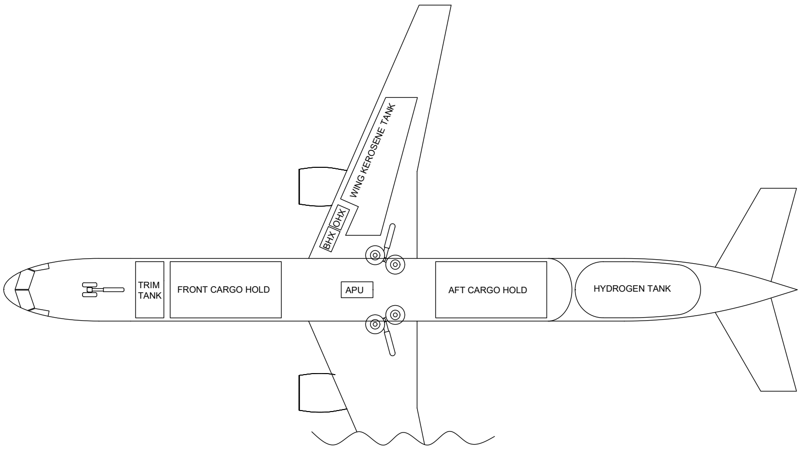

Figure 1: MAVERICK internal layout, showing the forward trim tank, cargo holds, and aft LH2 tank. Both the bleed-air heat exchanger (BHX) and oil heat exchanger (OHX) are shown.

Aerodynamic sizing was based on the CS-25 regulations through the matching diagram, leading to a wing surface area equal to 147.5 m^2, with an aspect ratio of 8.74. To match the controllability and stability requirement, the tail surface was set to 40.6 m^2 with the wing positioned toward optimised balance at 21.6 m from the nose. The final external layout is shown in Figure 2.

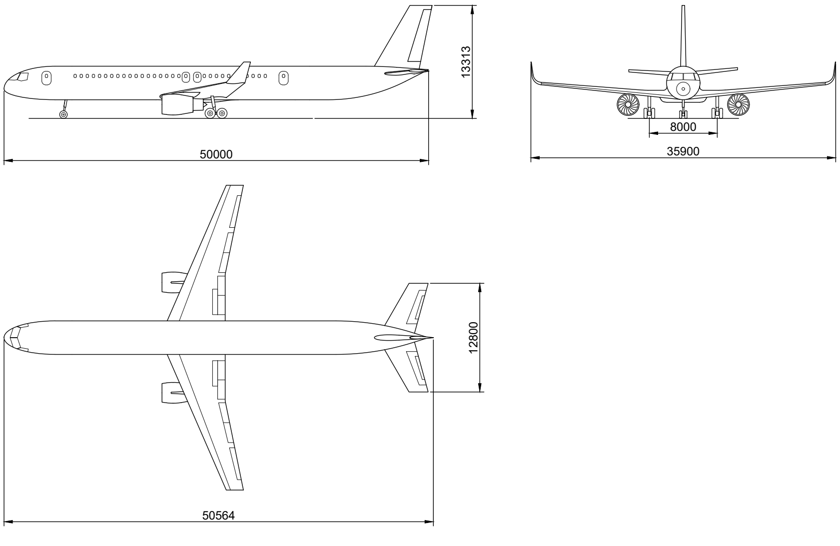

Figure 2: External Layout Drawing. Units in millimetres.

Aircraft Characteristics

The aircraft flies at a cruise altitude of 34 000 ft with a cruise Mach number of 0.74. Using the NASA SC(2)-0712 airfoil, it cruises at a design lift coefficient of 0.61, with a lift-to-drag ratio of 15.6. By using High-Lift Devices, the maximum lift coefficient of the aircraft increases to 2.8 to comply with the landing requirements.

To reduce the aircraft's weight and improve sustainability, the design uses a combination of lightweight aluminium alloys and thermoplastic composites. Additionally, single-panel wing and fuselage elements, as well as thermoplastic welding, are used to further reduce the structural weight of the aircraft.

The hydrogen is stored in liquid form at 2 bar in a double-walled cryogenic tank. The inner pressure shell is AA2219 aluminium-copper, selected for its toughness at liquid-hydrogen temperature and its conventional weldability. The outer shell is carbon fibre reinforced polymer, sized against buckling under external pressure. Insulation is provided by a vacuum-shelled multi-layer-insulation (MLI) system, the lowest-conductivity established approach for sustained, low-boil-off LH_2 storage. Vacuum integrity is identified as the governing reliability concern. Each wall thickness was sized from first principles against its specific failure mode, yielding an empty tank mass of 1636 kg.

The aft placement of the hydrogen tank makes extensive CG excursion during cruise a concern, as the large fuel mass behind the centre of gravity causes the longitudinal CG to migrate continuously as fuel is burnt, which would otherwise increase trim drag and fuel burn. To counter this, the forward kerosene tank doubles as a trim tank: a closed-loop controller actively transfers fuel between the trim tank and the wing tanks (at up to 1.5 kg/s) to hold the CG on the station that minimises trim drag throughout the mission. The control law and the coupled dual-fuel burn were modelled in Simulink to confirm the CG can be held within limits across all flight phases.

Engine Design

The innovative engine reduces emissions through the combustion of hydrogen and kerosene. Its design entails two core components: the injector and the combustion chamber. This is due to the fact that emissions stem from chemical reactions taking place in the combustor and are influenced by how the fuel is injected and mixed.

Combustion strategies are also examined and discussed in detail, since the choice of fuel mixture ratio governs emissions, thrust throughout the mission, and the amount of fuel used. For the nominal mission, the optimal hydrogen ratios were found to be 0.24 by mass (0.47 by energy) at take-off and 0.43 by mass (0.68 by energy) at cruise, leading to a maximum provided thrust at take-off conditions of 160 kN per engine.

For the combustion chamber, among mature combustion methods such as a rich-quench-lean (RQL), twin annular premixing swirler (TAPS), and lean direct injection (LDI), a TAPS-like approach has been chosen, as used on the reference CFM LEAP-1A engine. It offers lower NO_x than RQL through partially premixed, swirl-stabilised lean combustion, and can incorporate the flashback-prevention benefits of LDI through a tailored injector. Preliminary modelling confirmed turbine inlet temperatures remain below the baseline engine's estimated 1970 K limit.

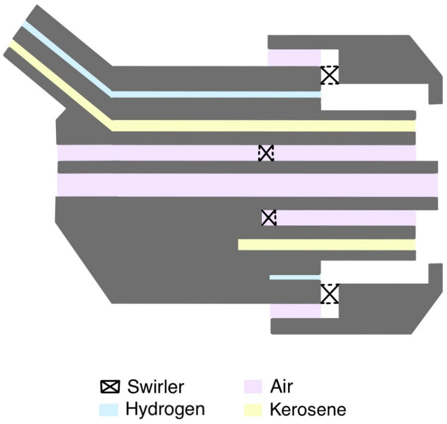

Figure 3: Schematic of dual-fuel injector.

The injector (Figure 3) features separated hydrogen and kerosene paths, with gaseous hydrogen injected through multiple small orifices, partial hydrogen-air premixing, liquid kerosene atomisation, two air swirlers for mixing and flame stabilisation, and a central axial air stream to prevent flashback. A schematic of the injector is shown in Figure 3. A staged pilot-and-main architecture distributes the full blend of fuel and air (30% pilot, 70% main) to enable lean operation.

Hydrogen Feed System

A hydrogen feed system is developed to transport LH_2 from the aft tank to the engines. The feed system consists of a series of pipes, pumps, and heat exchangers, designed to deliver the hydrogen directly to the injectors at the required conditions. Since hydrogen is injected gaseous (or supercritical) and at high pressures of up to 55.94 bar at take-off conditions, the feed system is designed to provide this pressure while vaporising the hydrogen.

The hydrogen is drawn from the tank by a cryogenic turbopump, which provides an initial 6.0 bar pressure increase. Two pumps are used per branch of the feed system for redundancy. The hydrogen is then delivered to a pair of heat exchangers via a series of pipes. The liquid hydrogen (LH_2) feed lines are sized as vacuum-jacketed cryogenic pipes to negligible temperature rise and pressure drop, in addition to avoiding two-phase flow. The selected pipe design has a mass of 16.83 kg per branch. The heat exchangers, arranged in series, will vaporise the hydrogen, and a gas compressor will provide the final pressure and temperature increase required at the injector.

The first heat exchanger uses bleed air from the Low-Pressure Compressor (LPC) to heat up the hydrogen. This bleed air is, in turn, cooled and can then be used to more effectively cool the High-Pressure Turbine (HPT) blades. The cooling is necessary to maintain the blades within their maximum operating temperature, which for turbine blades made from nickel-based superalloys is around 1320 K [1]. A turbine blade film cooling model (Horlock [2]) yields an estimated cooling air mass flow decrease of around 4.6% relative to using bleed air that was not cooled in the heat exchanger, providing a potential increase in engine efficiency. The second heat exchanger uses hot engine oil to heat up the hydrogen, allowing the engine oil to also be cooled.

The total weight of the feed system is therefore the combined weight of the pipes, pumps, and heat exchangers. A preliminary estimate yields a total weight of 662.1 kg.

Electrical System

The aircraft's electrical system is based on that of the Airbus A320, due to the similarities between the two aircraft and a similar expected power demand of the aircraft's conventional electric systems. However, a significant difference is caused by the large power requirements of the pumps in the feed system. It is estimated that the engines' electric generators would need to draw approximately 45.1% more power from the engines compared to those of the A320 to meet the power requirements during cruise. Take-off is more demanding, and with the Auxiliary Power Unit (APU) running and providing electrical power, two battery packs of 19.2 kW h in total would be required, weighing an estimated 276.6 kg.

Verification & Validation

To ensure that the aircraft is designed according to its specifications and can perform as it is designed, thorough Verification & Validation processes are performed. The models used in the design process are verified and validated by a variety of tests, with the type of test depending on the criticality and complexity of the model. The product verification is performed using a compliance matrix, and the product validation procedure is described as well.

Sustainability

MAVERICK provides an emission reduction pathway for short and medium haul aviation before hydrogen infrastructure is widely available. By replacing part of the kerosene energy demand with hydrogen, the aircraft meets the 50% CO_2 and NO_x reduction target relative to the A320neo while maintaining the ability to operate conventional routes and airports. The sustainability assessment shows that MAVERICK reduces life cycle environmental impact by 13.96% compared with the reference aircraft, while also reducing soot emissions and lowering noise levels.

The environmental benefit is primarily achieved during flight, where fuel substitution has greatest influence. MAVERICK demonstrates that meaningful emissions reductions can be achieved without requiring an immediate hydrogen infrastructure rollout, making it a credible bridging step towards future hydrogen aviation.

Operating the Aircraft

All differences in the operations of the MAVERICK aircraft come from its hydrogen systems. The hydrogen for refuelling is brought by a special bowser, and the end of the hose is a quick disconnect that keeps it clean from any external impurities. It is pressurised with the help of an additional gaseous hydrogen (GH_2) tank which can be collected from the boil-off. For longer stays on the ground, the aircraft has multiple pressure-relieving valves that can release boil-off hydrogen even if it is not collected in a pressurised GH_2 tank. During the airborne phase, the fuel fractions are managed automatically. Apart from those novelties, the operations aim to stay as similar to conventional airliners to ensure maximum reliability and safety.

Maintenance

The additional maintenance tasks come from the aircraft's hydrogen systems. A frequency and duration are assessed for each of those systems, and the maintenance task is then added to usual scheduled maintenance checks.

Market Entry

MAVERICK delivers the operational flexibility that a fully hydrogen aircraft cannot. As shown in Figure 4, it can maximise hydrogen use on routes served by airports that support hydrogen while retaining kerosene capability for return flights, longer missions, diversions, and destinations without LH_2. This allows airlines to decarbonise their network progressively rather than waiting for every airport to have hydrogen available, reducing entry-into-service and risk.

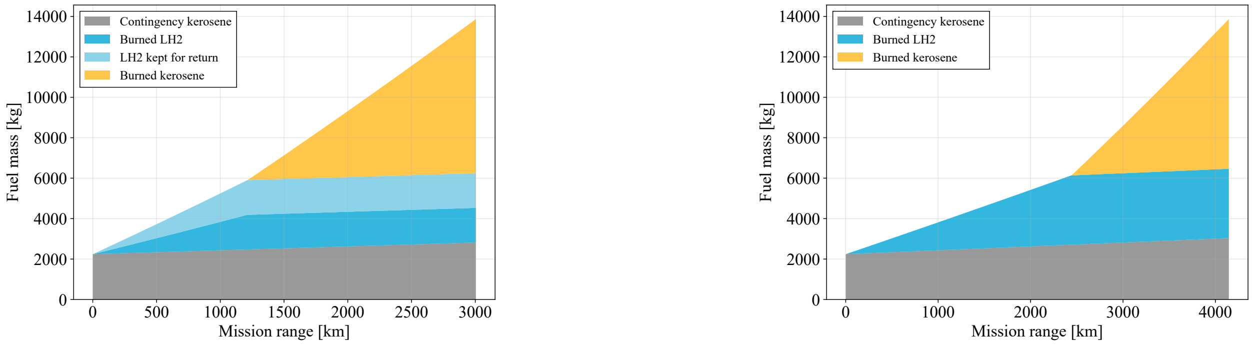

(a) Out-and-back mission without hydrogen refuelling.

(b) Mission with full refuelling at the destination.

Figure 4: Beach diagrams representing fuel required as a function of range.

The cost estimation indicates that MAVERICK remains competitive if the assumed production volume is achieved. For a baseline production run of 300 aircraft, the total programme cost is estimated at €24.3 billion, corresponding to a production cost of €81.1 million per aircraft including amortised Research, Development, Test, and Evaluation (RDTE). This is lower than the selling price of €150 million, suggesting that the production case can have a margin. However, supplier margins, airline discounts, programme risk, and hydrogen uncertainty are not fully captured at this stage.

The financial analysis presents the principal constraint on the concept, which is evaluated using Available Seat Kilometres (ASK). MAVERICK carries the highest net present cost at €418.1 M, against €396.1 M for a kerosene aircraft and €387.1 M for a full-hydrogen aircraft. MAVERICK falls marginally short of break-even, with a net present value of €-32.5 M and a break-even revenue of 8.59 c/ASK against the 8.19 c/ASK earned by a representative full-service operator today. The shortfall is attributable to the additional cost of the hydrogen technology, acquisition, and maintenance. The programme becomes profitable once unit revenue clears break-even, a margin reachable at the stronger end of current full-service yields.

Table of Contents

List of Acronyms

AC	Alternating Current
AFP	Automated Fibre Placement
APU	Auxiliary Power Unit
ASK	Available Seat Kilometres
BOG	Boil-Off Gas
CC	Combustion Chamber
CFRP	Carbon Fibre Reinforced Plastic
CG	Centre of Gravity
CPR	Core Pressure Ratio
CRZ	Central Recirculation Zone
CS	Certification Specification
DC	Direct Current
DOT	Design Option Tree
DSE	Design Synthesis Exercise
EASA	European Union Aviation Safety Agency
ECAM	Electronic Centralised Aircraft Monitoring
EI	Environmental Impact
EI$_{xx}$	Emission Index
EPNdB	Effective Perceived Noise in Decibels
ETW	European Transonic Windtunnel
FADEC	Full Authority Digital Engine Control
FAL	Final Assembly Line
FC	Flight Cycle
FH	Flight Hour
FHV	Fuel Heating Value
GH$_2$	Gaseous Hydrogen
HFCC	Hydrogen Feed Control Computer
HLD	High-Lift Device
HPT	High-Pressure Turbine
IFR	Instruments Flight Rules
JICF	Jet in Cross-Flow
LBO	Lean Blowout
LBPF	Laser Powder Bed Fusion
LDI	Lean Direct Injection
LEDs	Leading Edge Devices
LH$_2$	Liquid Hydrogen
LHS	Latin Hypercube Sampling
LHV	Lower Heating Value
LPC	Low-Pressure Compressor
LTO	Landing to Take-Off
MAC	Mean Aerodynamic Chord
MAVERICK	Multi-fuel Aircraft for Viable Emission Reduction with Integrated Combustion of Hydrogen and Kerosene
MLI	Multi-Layer Insulation
MMH	Maintenance Man Hours
MML	Modular Mounting System on Linear Axes
MOS	Metal-Oxide Semiconductor
MTOM	Maximum Take-Off Mass
NPSH	Net Positive Suction Head
NTP	Normal Temperature and Pressure
NTU	Number of Transfer Units
OEI	One-Engine Inoperative
OEM	Operating Empty Mass
OPR	Overall Pressure Ratio
PD&D	Project Design and Development Logic
PNL	Perceived Noise Level
PNLT	Tone-Corrected Perceived Noise Level
RDTE	Research, Development, Test, and Evaluation
RQL	Rich-Burn Quick-quench Lean-burn
SAF	Sustainable Aviation Fuel
SLCA	Steamlined Life Cycle Assessment
SMD	Sauter Mean Diameter
SPL	Sound Pressure Level
TAPS	Twin Annular Premixing Swirler
TEDs	Trailing Edge Devices
TIT	Turbine Inlet Temperature
TRL	Technology Readiness Level
TSFC	Thrust Specific Fuel Consumption
UHC	Unburnt Hydrocarbons
V&V	Verification & Validation
VJP	Vacuum-Jacketed Piping
ZFM	Zero Fuel Mass

List of Symbols

$(c'/c)_{TED}$	Chord extension ratio of the Trailing Edge Devices
A	Area
AR	Aspect Ratio
C	Overall Technology Factor for Horlock Model
C_D	Drag coefficient of the aircraft
C_L	Lift coefficient
C_R	Ratio of Fluids' Specific Heat Capacity Rates
C_{D_0}	Zero-lift drag coefficient of the aircraft
C_{D_c}	Drag coefficient of an aircraft component
C_{L_α}	Lift curve slope
C_{L_α}	Lift curve slope
$C_{L_{des}}$	Design lift coefficient of the wing
$C_{L_{max}}$	Maximum lift coefficient of the wing
$C_{l_{des}}$	Design lift coefficient of the airfoil
$C_{l_{max}}$	Maximum lift coefficient of the airfoil
C_{lam}	Turbine Blade Geometry Constant for Horlock Model
D	Diameter
E	Young's Modulus
H_{bar}	Barometric Head
H_{dyn}	Dynamic Pressure Head
H_{vap}	Vapour Pressure Head
L/D	Lift-to-drag ratio
M_{app}	Approach Mach number
M_{cr}	Cruise Mach number
M_{dd}	Mach Drag Divergence
Nu	Nusselt Number
P	Power
P_3	Pressure at the compressor exit
Pr	Prandtl Number
R_{th}	Material Thermal Resistance
Re	Reynolds Number
S	Wing surface area
S_{wet_c}	Wetted area of an aircraft component
Sn	Swirl number
St_g	Stanton Number
T	Temperature
U	Heat Transfer Coefficient
$\Delta\alpha_{C_{L,max}}$	Change in angle of attack of the maximum lift coefficient
$\dot{Q}$	Heat Flow Rate
$\dot{m}$	Mass Flow Rate
$\Lambda_{c/2}$	Half-chord sweep angle
α_{0L}	Zero-lift angle of attack
α_{stall}	Stall angle of attack
β	Prandtl-Glauert correction factor
ϵ_0	Overall Cooling Effectiveness for Horlock Model
ϵ_R	Absolute Surface Roughness
ϵ_{HX}	Heat Exchanger Effectiveness
η_c	Turbine Blade Cooling Efficiency for Horlock Model
η_f	Film Cooling Efficiency for Horlock Model
η_{AF}	Airfoil efficiency
η_{isen}	Isentropic Efficiency
$\frac{S_{wf,LED}}{S_{wf,TED}}$	Ratio of the flapped area of the LEDs to the TEDs
ν	Kinematic Viscosity
ϕ	Energy Flow Rate
ϕ	Equivalence Ratio
ρ	Density
σ_y	Yield strength
σ_{UTS}	Ultimate tensile strength
ζ	Cooling Air Mass Flow Ratio for Horlock Model
c_p	Specific Heat Capacity at Constant Pressure
e	Oswald efficiency factor
f	Darcy Friction Factor
$f_{D_{misc}}$	Factor to account for the miscellaneous drag
h	Specific Enthalpy
k_{th}	Thermal Conductivity
p	Pressure
u	Specific Internal Energy
v	Specific Volume

1 Introduction

Despite global pressure to decarbonise, aviation remains a significant contributor to climate change. In 2024, the airline sector emitted approximately 942 Mt of gross CO_2, exceeding its 2019 pre-pandemic level [1]. Although aviation accounts for only around 2.5% of global CO_2 emissions, its environmental impact extends beyond carbon dioxide and includes non-CO_2 effects, including NO_x and soot emissions and contrail formation[2]. Furthermore, decarbonising the aviation sector is a complex challenge. At the same time, tighter emissions regulation, increasing Sustainable Aviation Fuel (SAF) mandates [3], and the expansion of carbon emissions prices are increasing pressure on kerosene operators. Fully hydrogen-powered aircraft offer a potential long-term decarbonisation pathway, but their deployment is constrained by limited Liquid Hydrogen (LH_2) airport infrastructure, challenging cryogenic onboard storage, evolving safety and certification requirements, and the need for an affordable, scalable supply of low-carbon hydrogen. [4], as well as the low volumetric energy density of hydrogen, requiring more space for storage and less for payload. This creates a need for a transitional aircraft concept that bridges current kerosene aircraft and future hydrogen aviation, balancing emission reduction, route flexibility, and aircraft size.

The objective of this report is to present the preliminary design of Multi-fuel Aircraft for Viable Emission Reduction with Integrated Combustion of Hydrogen and Kerosene (MAVERICK), a 180-passenger short-to-medium range aircraft planned for entry into service in 2040. The aircraft uses a dual-fuel combustion architecture, combining hydrogen with SAF, to bridge the gap between conventional kerosene aircraft and future fully hydrogen-powered aircraft. In line with the project objective, MAVERICK aims to reduce CO_2 and NO_x emissions by at least 50% relative to the A320neo aircraft, while maintaining the operational flexibility required for conventional European short and medium range routes.

The report is structured as follows. Chapter 2 introduces the project context, mission, market opportunity, and main requirements. The aircraft sizing process and resulting configuration are presented in Chapter 3, while Chapter 4 describes the main aerodynamic, structural, and performance characteristics. The novel hydrogen subsystems are then detailed: Chapter 5 presents the dual-fuel engine design, Chapter 6 develops the hydrogen storage system, and Chapter 7 describes the feed system delivering hydrogen to the engines. The environmental impact is assessed in Chapter 8. Verification, validation, and design sensitivity analysis are presented in Chapter 9, followed by the operational considerations for multi-fuel aircraft in Chapter 10. Finally, Chapter 11 discusses the market entry strategy, production planning, maintenance, cost estimation, and financial feasibility of the project.

2 Project Overview

In this chapter, a high-level overview of the MAVERICK project is presented. The project mission and objective are described in Section 2.1, then a market analysis is presented in Section 2.2. The design missions are described in Section 2.3 and the technical risk assessment is shown in Section 2.4. Lastly, an overview of the trade-off performed in the Midterm Report [5] is presented in Section 2.5.

2.1. Project Mission and Objective

Transitioning the aviation sector to net-zero is of paramount importance to reduce global warming. However, this transition is obstructed by operational, regulatory, and certification issues. This means that, despite tremendous efforts, no viable option exists to leap towards a world where aircraft are carbon-neutral. Transitional aircraft designs, combining both novel and conventional

---

[1] `https://www.iea.org/reports/global-energy-review-2026/oil` (Accessed: 23/06/2026)

[2] `https://www.iata.org/en/programs/sustainability/non-co2-emissions-contrails/` (Accessed: 16/06/2026)

technologies, can help bridge this gap. As of 2026, no transitional technology towards a decarbonised aviation sector exists yet. Project MAVERICK will fill exactly this gap. Its mission is to reduce air transport emissions by providing a pathway towards net-zero aviation, doing this by achieving the MAVERICK project objective: to design a dual-fuel, short-medium range passenger airliner that uses both hydrogen and kerosene/SAF to reduce emissions compared to state-of-the-art aircraft.

The functions that the MAVERICK aircraft must fulfil are summarised in a functional flow diagram and functional breakdown structure at the end of the report in Appendix A.

2.2. Market Analysis

The market analysis evaluates the commercial feasibility of MAVERICK in the future aviation market, since the aircraft is intended to enter service in 2040. Hence, the analysis considers changes in emissions regulations, SAF mandates, hydrogen infrastructure and accessibility, and competing decarbonisation concepts. The section aims to identify where MAVERICK can provide the strongest value, reducing lifecycle emissions and carbon-cost exposure while maintaining the operational flexibility required by airlines during the transition toward hydrogen aviation.

2.2.1. Product Definition

MAVERICK is a short-to-medium range passenger aircraft designed as a transitional solution between conventional kerosene aviation and future fully hydrogen-powered aviation. It implements a dual-fuel propulsion system capable of combusting both hydrogen and kerosene/SAF in the same engine. As a result, the fuel mixture can be adapted to mission, airport infrastructure, emission targets, and operational constraints.

The product's target lifetime emissions of CO_2 and NO_x are 50% compared to the reference aircraft, the A320neo. The aircraft is designed as a 180-passenger single-aisle aircraft intended to enter service by 2040. Its operating mission range is 2000 km, based on the operating missions of its competitors, while maintaining a maximum range capability of 3000 km to provide airlines with sufficient route flexibility. The operating mission and maximum range will be further discussed in Section 2.3. The key characteristics of the product are summarised in Table 2.1.

Table 2.1: Key MAVERICK market-positioning characteristics.

Characteristic	MAVERICK positioning
Aircraft class	Single-aisle passenger aircraft
Passenger capacity	180 passengers
Target entry into service	2040
Operating mission range	2000 km
Maximum range capability	3000 km
Lifecycle emissions reduction target	50%

Finally, MAVERICK's value proposition is to offer airlines a transitional aircraft that reduces emissions and exposure to carbon-based fuel costs while maintaining the operational flexibility needed during the gradual development of hydrogen airport infrastructure.

2.2.2. Business Opportunity

The MAVERICK aircraft is positioned in the short-to-medium range single-aisle market, which is one of the largest and most active segments of commercial aviation. This market is valued at approximately $116 billion in 2025, growing to $193 billion by 2034. The top 10 busiest routes worldwide fall within a 3,000 km range, and a steady 3.6% air traffic growth was estimated through 2044. These values show that the market segment targeted by MAVERICK is large, growing, and strongly aligned with the aircraft's intended mission. Moreover, this segment is currently dominated by aircraft such as the Airbus A320neo and Boeing 737 MAX families, used extensively on European and global short-to-medium haul routes.

Capturing a share in this large and growing market requires a competitive edge, achieved by the advantage of the dual-fuel aircraft, reducing emissions relative to state-of-the-art aircraft, making it well positioned as emissions regulations tighten. The main business opportunity for MAVERICK hence arises from the increasing economic pressure on conventional kerosene-powered aircraft. The Emissions Trading System is used as a representative carbon-pricing mechanism. Under this system, the price of carbon allowances was projected to reach up to €218 per tonne of CO_2-equivalent by 2035. This presents a business opportunity that the MAVERICK aircraft can exploit due to the targeted 50% emissions reduction. This opportunity is further quantified in Section 11.4.

Additionally, MAVERICK's 50% reduction target is more ambitious than previous hydrogen integration studies. It is 20 percentage points more than Airbus's integration exercise, which indicated ~30% reduction in CO_2 [6]. The primary driver of this reduction is hydrogen, whose combustion produces no CO_2; hence, an airline operating MAVERICK on a short-to-medium range route could reduce its exposure to emission costs in direct proportion to the hydrogen blending ratio achieved per flight hour. With approximately 6,000 narrow-body aircraft projected to enter service across Europe between 2027 and 2043,[1] a 5% market share of 300 aircraft would translate to €45 billion in revenue at the target unit cost. At the aircraft level, the €38 million reduction in projected carbon liability positions MAVERICK as competitive within a €150 million unit cost budget, benchmarked against the A320neo list price of €110 million [7], with the emissions cost advantage partially offsetting the price premium for airlines.

Beyond carbon pricing, SAF mandate compliance constitutes a parallel and growing structural cost driver for airlines. The EU ReFuelEU Aviation regulation mandates progressive SAF blending ratios of 2% from 2025, rising to 20% by 2035 and 34% by 2040 [3]. At current SAF production costs of approximately 3 times that of kerosene [8], sustained compliance with these blending obligations translates directly into elevated block fuel costs for kerosene-only operators, with no architectural pathway to reduce that exposure. MAVERICK's dual-fuel design provides a structural advantage in this regulatory environment. By substituting a portion of kerosene energy output with hydrogen combustion, operators can reduce the volume of SAF-blended kerosene required per flight hour, thereby limiting direct exposure to SAF supply constraints and price volatility. This fuel-source flexibility affords MAVERICK-operating airlines a degree of commercial manoeuvrability on a per-route basis that is structurally unavailable to conventional narrow-body competitors.

2.2.3. Market segmentation

Market segmentation identifies where the aircraft has the strongest commercial case and its relevance and attractiveness depending on the market segment, in order to develop an appropriate market strategy. The MAVERICK market is segmented according to route length, customer type, and airport-hydrogen infrastructure readiness. These factors determine where the aircraft can add the greatest commercial and environmental value and are explained below. The most attractive market segments are those where a significant share of kerosene or SAF can be replaced by hydrogen while still preserving the operational flexibility expected from a narrow-body aircraft.

Route-length segmentation

The aircraft is now positioned around a 2000 km operating mission, while retaining a 3000 km maximum range. Therefore, the main commercial segment is the 1000-2000 km range, while the 2000-3000 km range is treated as an extended flexibility segment. Short hydrogen-priority routes fall within 0-100 km. These allow the highest hydrogen share and the strongest on-flight CO_2 reduction. They are suitable for early hydrogen use and introduction in the industry; however, these routes face competition from high-speed rail or small regional aircraft.

Routes ranging 1000-2000 km are core operating routes, representing the main target segment for MAVERICK. These align with the 2000 km operating mission while offering a balance between high narrow-body demand and significant hydrogen use. Therefore, this allows for a significant emission reduction when applied across a large number of operations. Additionally, 2000-3000 km routes

---

[1] `https://www.aircraft.airbus.com/en/newsroom/press-releases/2024-10-european-aircraft-services-market-to-grow-in-maintenance-and` (Accessed: 28/04/2026)

are within the maximum range capability and improve the airline's flexibility, allowing them to compete in the short-medium range aircraft market. However, they may require a higher share of kerosene or SAF and should not be used as the primary emissions-performance case. Routes exceeding 3000 km are outside the intended MAVERICK market.

Customer Segmentation

The second segmentation criterion is customer type. For MAVERICK, the most relevant distinction is between traditional flag carriers or network airlines and low-cost carriers. Flag carriers are considered the primary early customers because they typically operate from large hub airports and use hub-and-spoke networks. This makes them more compatible with early hydrogen infrastructure deployment, since hydrogen refuelling can initially be concentrated at a limited number of major airports rather than being required across an entire route network[2].

Suitable early customers include airlines such as KLM, Lufthansa, Air France, and British Airways. Their main hubs include Amsterdam Schiphol[3], Frankfurt[4], Munich[5], Paris Charles de Gaulle[3], and London Heathrow[6]. These airports are attractive initial operating bases because they are large, strategically important, and more likely to justify investment in hydrogen infrastructure. In addition, these airlines operate several routes within MAVERICK's 3000 km maximum range, such as Amsterdam-Frankfurt, Amsterdam-Madrid, and Amsterdam-Istanbul.

Low-cost carriers, such as Ryanair, Wizz Air, and easyJet, are less suitable as first customers. Although many of their routes also fall within MAVERICK's range, their operating model depends strongly on low cost, high aircraft utilisation, fleet commonality, short turnaround times, and operations from secondary or regional airports. These airports are less likely to develop hydrogen infrastructure in the near term. In addition, introducing a dual-fuel aircraft would increase maintenance, crew training, and operational complexity, which conflicts with the simplified fleet strategy typically used by low-cost carriers. For this reason, low-cost carriers are treated as secondary customers that may become relevant only after hydrogen infrastructure and dual-fuel operations become more mature.

Additionally, customer segments include regional airlines and non-European airlines. All customer segments are shown and briefly evaluated in Table 2.2.

Table 2.2: Customer segmentation for MAVERICK.

Customer segment	Examples	Suitability	Motive
Flag carriers/network airlines	KLM, Lufthansa, Air France, British Airways	High	Operate from major hubs, have many routes within 3000 km, and are more likely to use airports where hydrogen infrastructure can be developed.
Large low-cost carriers	Ryanair, Wizz Air, easyJet	Medium to low for early entry	Routes are relevant, but reliance on secondary airports, fleet commonality, and fast turnaround times makes early adoption less likely.
Regional airlines	Smaller operators below narrow-body capacity	Low	MAVERICK's 180-passenger capacity may be too large, while smaller hydrogen-electric aircraft may be more suitable for this segment.
Non-European airlines	Future international customers	Medium in later phases	Relevant if hydrogen infrastructure and emissions regulation develop outside Europe.

---

[2] `https://www.research.airbus.com/en/products-systems/goliat` (Accessed: 15/06/2026)

[3] `https://www.klm.com/information/corporate/network-alliances` (Accessed: 15/06/2026)

[4] `https://www.lufthansa.com/xx/en/lufthansa-am-flughafen-frankfurt` (Accessed: 15/06/2026)

[5] `https://www.lufthansa.com/xx/en/lufthansa-terminal-muenchen` (Accessed: 15/06/2026)

[6] `https://www.britishairways.com/content/information/airport-information/london-heathrow-airport` (Accessed: 15/06/2026)

Airport Infrastructure Segmentation

The last segmentation criterion is airport hydrogen-infrastructure readiness. MAVERICK's emissions advantage can only be implemented if hydrogen is available at the operating airport, and fully exploited if appropriate hydrogen infrastructure exists at both the operating and destination airports. On the other hand, the dual-fuel aircraft's architecture reduces the need for hydrogen infrastructure at every airport, highlighting one of the main advantages of the MAVERICK aircraft.

Currently, there are no airports fully operating with hydrogen; however, current ongoing initiatives, such as the EU-funded GOLIAT project, prove the future accessibility of hydrogen infrastructure at European international airports [7]. GOLIAT aims to provide ground-based refuelling and supply systems for liquid hydrogen at air transport ground infrastructures, and upscaling at system level by 2027[2]. It also expects to produce validated liquid hydrogen demand and supply-matching models at air transport infrastructures globally, with a service entry by 2035. Both dates show the feasibility of the MAVERICK aircraft operating by 2040.

The aircraft must depart from a hydrogen-ready hub and be able to operate in destinations that do not yet have hydrogen infrastructure. For shorter routes, the aircraft may carry enough energy to complete the return mission on hydrogen without refuelling at the destination. For longer routes up to 3000 km, conventional kerosene or SAF refuelling can be used when hydrogen is unavailable at the outstation. This makes MAVERICK more flexible than a hydrogen-only aircraft during the transition period.

Based on this, the most suitable early operating bases are major European airports involved in liquid hydrogen infrastructure development, such as Schiphol, Rotterdam, Stuttgart, Budapest, and Lyon. Larger hub airports such as Frankfurt, Munich, Paris Charles de Gaulle, and London Heathrow would also be attractive early candidates if hydrogen refuelling capability is developed, since they combine high traffic demand, network-carrier operations, and stronger justification for infrastructure investment[8]. This results in the following airport readiness segmentation, shown in Table 2.3.

Table 2.3: Airport hydrogen-infrastructure segmentation for MAVERICK.

Airport segment	Hydrogen-readiness level	Relevance for MAVERICK
Hydrogen-ready or developing major hubs	LH_2 refuelling, ground-handling procedures, safety zones, and certification framework available, or ground operations and refuelling concepts under development.	Primary operating bases and strong candidates for early adoption. They allow regular hydrogen refuelling and maximise the emissions-reduction benefit of MAVERICK.
Major hubs without hydrogen infrastructure	No current LH_2 refuelling capability, but high traffic demand and investment potential	Potential second-stage market once hydrogen infrastructure becomes commercially justified.
Secondary and regional airports	Limited likelihood of early LH_2 infrastructure deployment if it has not started already.	Suitable mainly as destinations with kerosene or SAF used when hydrogen refuelling is unavailable. These airports are easier to adapt to novel operations, but as new operations are not being developed yet, capability by 2040 cannot be justified.

For a further analysis on potential hubs for the MAVERICK aircraft, the readiness levels of several relevant hubs, based on the market segmentation, have been evaluated and are shown in Table 2.4. A score of 4 indicates an existing liquid-hydrogen aviation demonstration facility, 3 indicates participation in a liquid-hydrogen aircraft ground-operation demonstration or hydrogen-airport network, 2 indicates a feasibility study or hydrogen-infrastructure programme, and 1 indicates a strategically relevant hub with no specific public liquid-hydrogen aviation project identified.

---

[7] `https://cordis.europa.eu/project/id/101138379` (Accessed 16/06/2026)

[8] `https://mediaassets.airbus.com/pm_38_747_747228-ni0nsggi79.pdf` (Accessed: 17/06/2026)

Table 2.4: Indicative hydrogen-readiness of selected European airports.

Airport	Level	Hydrogen-readiness evidence	Relevant airlines
Rotterdam The Hague (RTM)	4	Liquid-hydrogen refuelling facility opened for aviation R&D and demonstration, not yet commercial narrow-body service[9].	Transavia, TUI fly, British Airways, Pegasus
Stuttgart (STR)	3	GOLIAT airport site for liquid-hydrogen aircraft ground-operation demonstrations[10].	Eurowings, Lufthansa Group, Turkish Airlines
Lyon Saint-Exupéry (LYS)	3	Included in GOLIAT liquid-hydrogen aircraft ground-operation demonstrations[10].	Air France, easyJet, Transavia, Volotea
Amsterdam Schiphol (AMS)	3	Royal Schiphol Group is part of the GOLIAT consortium[10]. Schiphol is also KLM's main hub[11].	KLM, Transavia, easyJet, Delta
Budapest (BUD)	2-3	Budapest Airport is part of the GOLIAT consortium, although it is not one of the main demonstration airports[10].	Wizz Air, Ryanair, Lufthansa, KLM
London Gatwick (LGW)	3	Airbus, Gatwick, easyJet and Air Products are studying hydrogen supply, storage, refuelling and ground handling[12].	easyJet, British Airways, TUI Airways, Wizz Air
Hamburg (HAM)	3	First German airport to join Airbus' Hydrogen Hub at Airports network[13].	Eurowings, Lufthansa, Condor, easyJet
Stockholm Arlanda (ARN)	2	Airbus, Avinor, SAS, Swedavia and Vattenfall are studying hydrogen infrastructure in Sweden and Norway[14].	SAS, Norwegian, Ryanair, Lufthansa
Oslo Gardermoen (OSL)	2	Included in the Airbus–Avinor–SAS–Swedavia–Vattenfall hydrogen infrastructure collaboration[14].	SAS, Norwegian, Wideroe, Lufthansa
Madrid Barajas (MAD)	2	Airbus, Aena, Air Nostrum, Iberia, Exolum and Repsol are studying an aviation hydrogen hub in Spain[15].	Iberia, Air Europa, Ryanair, Iberia Express
Frankfurt (FRA)	1-2	No public LH2 aviation demonstration identified, but it is Lufthansa's largest hub[16].	Lufthansa, Condor, Discover Airlines
Paris Charles de Gaulle (CDG)	1-2	No public LH2 aviation demonstration identified, but it is Air France's central hub[11].	Air France, easyJet, Delta
London Heathrow (LHR)	1-2	No public LH2 aviation demonstration identified, but it is British Airways' main hub[17].	British Airways, Virgin Atlantic
Munich (MUC)	1-2	No public LH2 aviation demonstration identified, but it is a major Lufthansa Group hub[18].	Lufthansa, Discover Airlines, Eurowings

Overall, the airport segmentation shows that MAVERICK's early market entry should be concentrated around major European hubs and airports already involved in hydrogen-infrastructure initiatives. However, the analysis also shows that commercial hydrogen readiness is still at an early stage, with most airports currently involved in demonstration projects and feasibility studies. For this reason, MAVERICK's dual-fuel architecture is a key advantage, allowing operation from hydrogen-ready hubs while still serving destinations without hydrogen refuelling capability.

Product Strategy Derived from Market Segmentation

In conclusion, the market segmentation indicates that MAVERICK should be introduced as a hub-based transitional aircraft rather than as a direct replacement for all narrow-body operations. The most attractive initial market consists of European flag carriers and network airlines operating from major hubs, where hydrogen infrastructure is more likely to be developed and where route density is high enough to justify investment in new fuel systems and operational procedures.

The primary operating segment should be routes between 1000 and 200 km aligning with MAVERICK's nominal operating mission and providing a strong balance between emissions reduction and commercial usability. On these routes, hydrogen can replace a significant share of kerosene or SAF, while performing missions long enough to be relevant for narrow-body fleet utilisation. Routes below 1000 km can also be used for early hydrogen-intensive operations, but face stronger competition from other alternatives, such as rail and smaller regional aircraft. Routes between 2000 and 3000 km should be treated as a flexibility segment, allowing airlines to remain competitive by performing long popular routes, but implementing a smaller hydrogen share.

The product is hence positioned as a flexible decarbonisation tool for airlines during the transition toward hydrogen aviation. Its dual-fuel architecture allows operators to reduce lifecycle emissions on suitable routes while retaining the ability to operate at airports without hydrogen refuelling capability, reducing the impact of hydrogen accessibility issues.

Based on the market segmentation, the adopted market-entry strategy consists of starting with a limited number of hydrogen-ready or hydrogen-developing hubs, such as Rotterdam The Hague, and Stuttgart airports. As hydrogen airport infrastructure expands, the aircraft can then be introduced to additional hubs and, finally, to selected low-cost or non-European operators.

In conclusion, the product strategy is not to maximise immediate market coverage, but to capture a focused serviceable market where the aircraft's dual-fuel capability provides a clear advantage. MAVERICK should be marketed as a 2040 transitional narrow-body aircraft that combines emissions reduction, regulatory resilience, and operational flexibility.

2.2.4. Competitor Analysis

The competitor analysis evaluates MAVERICK within the expected 2040 aviation market, rather than only against current aircraft. This allows the aircraft's competitive position to be assessed in terms of emissions reduction, infrastructure dependency, certification risk, and operational flexibility.

Future Aviation Scenario

By 2040, the European aviation market is expected to be shaped by stronger emissions regulation, increasing SAF mandates, higher exposure to carbon pricing, and gradual development of hydrogen airport infrastructure. The competitive landscape is therefore expected to feature alternative fuels, new propulsion systems, and clean-sheet aircraft concepts besides conventional narrow-body aircraft.

As mentioned, in Europe ReFuelEU Aviation requires the minimum SAF share in aviation fuel to increase progressively from 2% in 2025 to 6% in 2030, 20% in 2035, 34% in 2040, and 70% in 2050[19].

---

[9] `https://hydrogeneurope.eu/rotterdam-the-hague-airport-opens-liquid-hydrogen-refuelling-station-for-aviation/` (Accessed 16/06/2026)

[10] `https://www.research.airbus.com/en/products-systems/goliat` (Accessed: 15/06/2026)

[11] `https://www.klm.com/information/corporate/network-alliances` (Accessed: 15/06/2026)

[12] `https://www.airbus.com/en/newsroom/press-releases/2024-07-airbus-welcomes-london-gatwick-to-global-hydrogen-hub-network` (Accessed 16/06/2026)

[13] `https://www.airbus.com/en/newsroom/press-releases/2023-12-hamburg-airport-joins-international-hydrogen-hub-at-airport-network` (Accessed 16/06/2026)

[14] `https://www.airbus.com/en/newsroom/press-releases/2024-01-airbus-avinor-sas-swedavia-and-vattenfall-pave-the-way-for-hydrogen` (Accessed 16/06/2026)

[15] `https://www.airbus.com/en/newsroom/press-releases/2024-07-airbus-aena-air-nostrum-iberia-exolum-and-repsol-join-forces-to` (Accessed 16/06/2026)

[16] `https://www.lufthansa.com/xx/en/lufthansa-am-flughafen-frankfurt` (Accessed: 15/06/2026)

[17] `https://www.britishairways.com/content/information/airport-information/london-heathrow-airport` (Accessed: 15/06/2026)

[18] `https://www.lufthansa.com/xx/en/lufthansa-terminal-muenchen` (Accessed: 15/06/2026)

[19] `https://transport.ec.europa.eu/transport-modes/air/environment/refueleu-aviation_en` (Accessed: 16/06/2026)

This pushes the need for SAF implementation in SAF-compatible aircraft, but also increases airline exposure to the cost and availability of SAF. SAF can be used in current and future aircraft with limited infrastructure disruption due to being a drop-in fuel. Current certified SAF blends are compatible with existing aircraft technology up to 50%, while research and certification work is being directed towards 100% SAF capability[19]. On the other hand, SAF production remains limited and scaling it to the required volumes is one of the major uncertainties in aviation decarbonisation.

At the same time, hydrogen aircraft require new storage, refuelling, safety, and certification. For this reason, EASA has launched a hydrogen certification roadmap to define the scope and timelines of hydrogen certification, identify gaps in existing certification specifications, and create a consolidated action plan for hydrogen technology in aviation[20]. Therefore, the 2040 aviation market is likely to contain several competing decarbonisation alternatives rather than a single dominant solution.

For this reason, MAVERICK's competitors can be divided into three main categories: novel fuels, novel propulsion systems, and novel aircraft concepts. Novel fuels include SAF, synthetic fuels, and hydrogen. Novel propulsion systems consist of hydrogen combustion, hydrogen fuel-cell propulsion, open-fan engines, hybrid-electric systems, and improved geared turbofans. Novel aircraft concepts include next-generation single-aisle aircraft from Airbus and Boeing, currently dominating the market, hydrogen concepts such as Airbus ZEROe and Fokker Next Gen, and smaller hydrogen-electric aircraft from manufacturers such as Embraer. These three categories are further explained below. Additionally, there are also alternatives to the MAVERICK aircraft present, which fulfil the same customer need but follow a different goal. These are, for example, high-speed trains or electric cars; however, these will not be evaluated since the analysis at this stage of the project will focus mainly on direct competitors.

Novel Fuel Competitors

The first competitor group consists of novel fuels, such as SAF and liquid hydrogen. SAF is the strongest near-term competitor due to its current implementation in aviation, making it attractive for airlines to reduce lifecycle emissions without changing aircraft architecture, airport operations, or maintenance procedures. Current narrow-body aircraft such as the Airbus A320neo and Boeing 737 MAX can already operate using approved SAF blends. Airbus states that all Airbus aircraft are currently capable of flying with up to 50% SAF blend, with a target of up to 100% SAF capability by 2030[21]. Boeing has also committed to making its commercial aircraft capable and certified to fly on 100% SAF by 2030 [22].

However, even if SAF reduces lifecycle emissions, it does not remove airline exposure to fuel price, fuel availability, and carbon regulation. As previously mentioned in Subsection 2.2.2, current SAF production costs are approximately 3 times that of kerosene [8]. Hence, compliance with ReFuelEU Aviation obligations leads to elevated block fuel costs.

LH_2 is the main fuel competitor, offering high emissions reduction if produced from low-carbon or renewable energy sources. However, it requires a new airport fuel infrastructure, including cryogenic storage, refuelling equipment, safety zones, trained ground crews, and certification standards. Also, due to the low volumetric energy density of LH_2, large cryogenic tanks are required, which can potentially reduce the available payload volume in full LH_2 powered aircraft. Since MAVERICK is positioned between these two fuel concepts, it offers the airline the possibility to use hydrogen where infrastructure is available, while retaining kerosene or SAF as a fallback when hydrogen is inaccessible.

---

[20] `https://www.easa.europa.eu/en/newsroom-and-events/events/easa-certification-roadmap-h2-international-workshop-2024` (Accessed: 16/06/2026)

[21] `https://www.airbus.com/en/innovation/energy-transition/our-commitment-to-saf` (Accessed 16/06/2026)

[22] `https://www.boeing.com/company/about-bca/washington/boeing-will-deliver-commercial-airplanes-ready-to-fly-on-100-sus` (Accessed 16/06/2026)

Novel Propulsion System Competitors

The second competitor group is formed of new propulsion systems. The most relevant example is the CFM RISE open-fan programme, developed by CFM International [23]. It targets a novel engine architecture that could be available around 2030, aiming to improve fuel efficiency by more than 20% compared with today's engines. When integrated into current narrow-body aircraft, such as Airbus and Boeing, it could become a strong competitor due to its fuel burn reduction, without the need for additional infrastructure.

At the same time, Pratt & Whitney is developing the GTF Advantage engine, building on the geared turbofan architecture and aiming to improve fuel efficiency, durability, and compatibility with future SAF specifications. It is expected that the engine will be compatible with future specifications for 100% SAF [24]. This concept could make conventional aircraft more competitive by reducing fuel burn and operating cost while preserving the current airline operating model. Pratt & Whitney is also developing the Hydrogen Steam Injected, Inter-Cooled Turbine Engine, or HySIITE, a LH_2 propulsion concept using intercooling, water recovery, and steam injection to improve efficiency and reduce NOx emissions, representing a more direct hydrogen propulsion competitor to MAVERICK, although still face similar challenges related to LH_2 storage, aircraft integration, airport infrastructure, and certification [25].

Finally, Rolls-Royce is also actively developing future propulsion. Rolls-Royce and easyJet demonstrated the first successful testing of a modern aero engine on hydrogen in a ground test [26]. However, several challenges are still present regarding hydrogen implementation in propulsion, including certification, aircraft integration, airport infrastructure, and operational safety. The development of infrastructure and integration of hydrogen propulsion in aviation present both a threat and an opportunity to MAVERICK, since hydrogen propulsion competitors could become stronger by 2040, but their development also supports the wider hydrogen aviation ecosystem needed for MAVERICK.

Novel Aircraft Competitors

The third competitor group is novel aircraft concepts. The single-aisle market remains dominated by Airbus and Boeing, being the most important airframe manufacturers. Airbus is preparing technologies for a next-generation single-aisle aircraft that could enter service in the second half of the 2030s, with an expected 20-30% increase in fuel efficiency compared with the current generation and capability to fly with up to 100% SAF [27]. Boeing is also committed to 100% SAF-capable commercial aircraft by 2030[28], making future aircraft highly efficient and SAF-compatible. This makes both manufacturers direct competitors to MAVERICK in 2040.

Additionally, fully-hydrogen projects are also ongoing and will be in the market around 2040, making them direct MAVERICK competitors. Airbus ZEROe is the most visible hydrogen aircraft programme and is currently focused on hydrogen fuel-cell propulsion [29]. In this configuration, liquid hydrogen is converted into electricity through fuel cells, which then power electric propellers. Fully hydrogen fuel-cell aircraft could eventually offer larger operational emissions reductions than MAVERICK; however, they have a stronger dependency on hydrogen availability at both departure and destination airports and require novel aircraft integration due to the volume and cryogenic storage requirements of LH2. MAVERICK's dual-fuel architecture reduces the risk of the entry market infrastructure barrier because of its ability to operate in conventional airports.

---

[23] `https://www.cfmaeroengines.com/rise` (Accessed 16/06/2026)

[24] `https://www.rtx.com/en/prattwhitney/products/commercial-engines/gtf/advantage` (Accessed 16/06/2026)

[25] `https://www.rtx.com/en/prattwhitney/future-of-flight/alternative-fuel` (Accessed 16/06/2026)

[26] `https://www.rolls-royce.com/media/press-releases/2022/28-11-2022-rr-and-easyjet-set-new-aviation-world-first-with-successful-hydrogen-engine-run` (Accessed 16/06/2026)

[27] `https://www.airbus.com/en/newsroom/press-releases/2025-03-airbus-advances-key-technologies-for-next-generation-single-aisle` (Accessed 16/06/2026)

[28] `https://www.boeing.com/company/about-bca/washington/boeing-will-deliver-commercial-airplanes-ready-to-fly-on-100-sus` (Accessed 16/06/2026)

[29] `https://www.airbus.com/en/innovation/energy-transition/hydrogen` (Accessed 16/06/2026)

Fokker Next Gen is also a relevant competitor, with an aircraft concept close to MAVERICK's positioning[30]. It is designed to operate on liquid hydrogen, SAF, and kerosene, developed for 120-150 passengers and with a range of around 2500 km[31], making it a direct competitor in terms of fuel flexibility and European route applicability. However, MAVERICK is positioned at a higher capacity of 180 passengers and a maximum range of 3000 km, making it more directly aligned with the main narrow-body replacement market and dense European hub routes.

Finally, Embraer is also developing future sustainable aircraft concepts through its Energia programme, which investigates hybrid-electric and hydrogen fuel-cell propulsion for 19, 30, and 50 passenger aircraft, and ranges of up to 600 nautical miles[32]. Its concept is expected to be ready by 2030 and is therefore important in the future aviation landscape, but they mainly target regional and lower-capacity routes. Hence, they are not direct replacements for 180-passenger narrow-body aircraft nor direct competitors of the MAVERICK aircraft.

Future Competitor Landscape
The discussed competitor groups then come together to generate the future competitor landscape for MAVERICK. This consists mainly of novel fuels, SAF-compatible aircraft, new propulsion systems, fully and dual-fuel hydrogen aircraft, hydrogen-electric aircraft, and the next generation of airframes. The competitors are analysed in Table 2.5.

Table 2.5: Future competitor landscape for MAVERICK.

Competitor category	Examples	Main advantage	MAVERICK positioning
Novel fuels	SAF, synthetic fuels, liquid hydrogen	SAF can use existing infrastructure; hydrogen enables deeper emissions reduction.	MAVERICK combines hydrogen use with kerosene/SAF fallback, reducing dependence on either pathway alone.
SAF-compatible conventional aircraft	Airbus A320neo, Boeing 737 MAX, future SAF-compatible narrowbodies	Mature operations, lower infrastructure disruption, strong airline familiarity.	MAVERICK has a higher acquisition cost but lower lifecycle emissions and lower long-term carbon-cost exposure.
New propulsion systems	CFM RISE open fan, Pratt & Whitney GTF Advantage, Rolls-Royce hydrogen combustion	Can reduce fuel burn or enable new fuels without necessarily changing the whole aircraft market.	MAVERICK can benefit from future propulsion developments while differentiating itself through dual-fuel aircraft-level integration.
Fully hydrogen aircraft	Airbus ZEROe	Potential for very low operational CO_2 emissions when using green hydrogen.	MAVERICK has lower infrastructure dependency as it can operate from hydrogen-ready hubs and serve non-hydrogen destinations.
Dual-fuel hydrogen aircraft	Fokker Next Gen	Similar flexibility due to operation on hydrogen, SAF, or kerosene.	MAVERICK targets a larger 180-passenger narrow-body segment and a maximum range of 3000 km.
Hydrogen-electric regional aircraft	Embraer Energia concepts	Attractive for short regional routes with lower passenger demand.	MAVERICK serves denser 1000–2000 km narrow-body routes where regional aircraft are not direct substitutes.

Continued on next page

---

[30] `https://www.fokkernextgen.com/the-aircraft` (Accessed 16/06/2026)

[31] `https://www.greenairnews.com/?p=5680` (Accessed 16/06/2026)

[32] `https://embraercommercialaviationsustainability.com/concepts/` (Accessed 16/06/2026)

Competitor category	Examples	Main advantage	MAVERICK positioning
Next-generation efficient airframes	Future Airbus/Boeing single-aisle aircraft, truss-braced wings, advanced composite aircraft	Lower fuel burn with less operational disruption than hydrogen aircraft.	MAVERICK offers deeper decarbonisation potential if hydrogen infrastructure is available at major hubs.

The competitor analysis shows that MAVERICK's success will depend not only on the design of the aircraft but also on the overall environment required to support a dual-fuel aircraft. To complete the analysis of the MAVERICK environment, a stakeholder identification has also been developed, and is discussed in the next subsection.

2.2.5. Stakeholder Identification

This subsection identifies stakeholders that can either enable or constrain MAVERICK's entry into service, influencing the development, certification, market entry, and operation. In addition to airline demand, MAVERICK depends on hydrogen infrastructure, fuel availability, certification, propulsion-system development, and operational acceptance.

The main stakeholders are network airlines, airport operators, fuel suppliers, investors, and shareholders, due to their high influence and interest in the project. As primary customers, airlines are key stakeholders, especially European flag carriers operating from major hubs. Airports are also key stakeholders due to the provision of LH_2 storage, refuelling equipment, safety procedures, and trained ground crews. Fuel suppliers are more relevant than in a conventional-fuel project as the economic and environmental performance of the aircraft strongly depends on LH_2 availability.

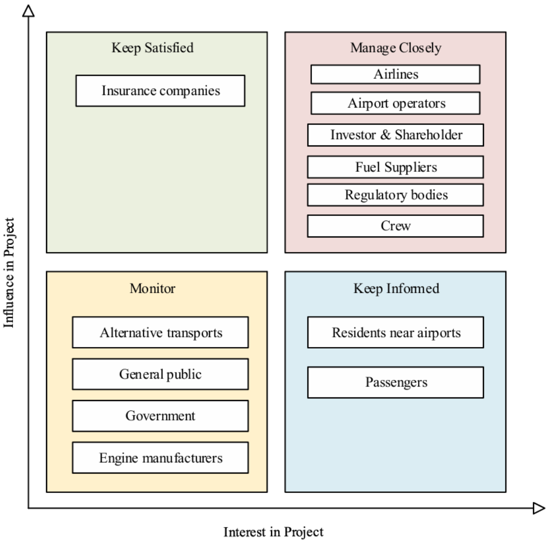

Figure 2.1: Stakeholder map.

Regulatory bodies and insurance companies, certification authorities such as European Union Aviation Safety Agency (EASA), FAA, ICAO, and national aviation authorities are also relevant, as they will determine whether the hydrogen storage system, dual-fuel propulsion architecture, refuelling procedures, and safety systems can be certified. Since aviation LH_2 standards are still under development, MAVERICK may need to contribute to defining future certification frameworks.

Engine manufacturers, fuel-system suppliers, ground-handling companies, and maintenance providers are also important enabling stakeholders. The success of MAVERICK depends on the availability of reliable dual-fuel propulsion, cryogenic fuel systems, hydrogen leak detection, maintenance procedures, and safe ground operations. Lastly, aircraft crew, passengers, and residents near airports are important groups to keep informed regarding safety, reliability, crew training, cost, noise, and environmental impact, although their direct influence on the project remains low. Concerns may arise regarding hydrogen flammability, cryogenic storage, refuelling safety, airport safety zones, and the reliability of a dual-fuel aircraft; hence, although these groups may have lower direct influence on the technical development of MAVERICK, their acceptance is important for operational deployment and passenger confidence. The map of stakeholders is presented in Figure 2.1.

Furthermore, the expectations of each stakeholder group must also be taken into account. Airlines expect competitive lifecycle cost, reduced exposure to carbon pricing, operational reliability, and compatibility with existing aircraft operations. Investors and shareholders expect a successful return on investment and a clear market-entry strategy. Airports expect hydrogen infrastructure to be demanded enough to make the investment profitable. Also, fuel suppliers require predictable long-term demand for hydrogen and SAF, while regulatory bodies might seek cooperation in the certification process. In conclusion, MAVERICK's market entry depends mainly on coordinated action between airlines, airports, fuel suppliers, regulators, propulsion-system manufacturers, and investors.

2.2.6. SWOT Analysis

Finally, the performed market analysis concludes in a SWOT analysis, indicating the Strengths, Weaknesses, Opportunities, and Threats MAVERICK faces. This is shown in Table 2.6 below.

Table 2.6: SWOT analysis of the product

Strengths (Internal)	**Weaknesses (Internal)**
• Phased decarbonisation pathway – Kerosene covers long-haul or LH_2 supply gaps; H_2 burns for shorter segments. Decarbonization is a long-term process; airlines can more gradually introduce aircraft that meet environmental regulations. • No direct CO_2 emissions from hydrogen combustion – The only product of combusting H_2 is water, so no CO, CO_2, soot or SO_x. • Route and fuel flexibility – 2000 km operating mission and 3000 km maximum range allow serving short- and medium-haul routes while adapting the hydrogen accessibility. • Range / energy-density flexibility – Combustion of hydrogen generates around 3 times more energy per unit mass than kerosene. • Compatible with existing airspace rules – Kerosene fallback eases EASA/FAA certification compared to pure hydrogen.	• Increase in mass and complexity due to dual-fuel system – Two full fuel circuits, cryogenic LH_2 tanks add significantly more structural weight. • LH_2 volumetric challenge – H_2 requires larger tank volume than jet-A fuel for an equivalent energy. • High development & certification cost – Novel engine modifications, materials, and safety envelopes require extensive testing and certification. • NO_x emissions, as well as contrails remain during H_2 mode – The high temperature of H_2 combustion still produces thermal NO_x and water vapour. • Complex maintenance and operations workflow – Maintenance staff must be qualified on cryogenic handling, leak detection, H_2 refuelling and dual-fuel engine logic.
Opportunities (External)	**Threats (External)**
• EU & ICAO carbon regulation pressure – CORSIA requires airlines to offset or reduce emissions on international routes. • Green hydrogen cost trajectory – The cost of green hydrogen, produced by electrolysing water using renewable electricity, may significantly drop[9]. • Airport infrastructure co-investment – Major European airports are already investing in hydrogen infrastructure, targeting H_2 fuelling capability for regional aircraft. • Regional aviation first-mover window – Introduction on short-haul routes can support industry adoption of state-of-the-art hydrogen technology.	• Lack of hydrogen infrastructure at airports for refuelling and general maintenance. • Insurance risk – High H_2 flammability and cryogenic hazard may complicate aircraft insurance. • Regulatory timeline uncertainty – Absence of harmonised standards between EASA, FAA, and ICAO for LH_2 in commercial aviation. • SAF as competing compliance route – Airframe does not change for SAFs; airlines may prefer SAF in the short term. • Competition from hydrogen-electric aircraft – A fully hydrogen-electric aircraft eliminates combustion emissions entirely, making it more attractive for short-haul routes.

2.3. Mission Description

The maximum range of 3000km of the MAVERICK aircraft respects REQ-MIS-PERF-01 (see Appendix A), using hydrogen and kerosene. However, around 90% of all Instruments Flight Rules (IFR) flights departing and landing from the area managed by the organisation are less than 1000 NM (1852 km) long[33]. It was thus decided to have a nominal range of 2000 km, for which the aircraft design is optimised. The kerosene tank is designed to be able to contain enough fuel for the 3000 km range to cover the required range, even if the hydrogen tank is empty and cannot be refuelled. Additionally, kerosene must be refuelled at the destination airport in accordance with [3]. The hydrogen tank is sized to decrease CO_2 emission by 50% during its nominal range and accounting for the eventual lack of LH_2 refuelling facilities at the destination airport. Additionally, since most missions will be under 2000 km, the net reduction of emissions during flight will be over 50%.

A range of requirements pertaining to the function of the aircraft is summarised in the mission profile, shown in Figure 2.2. The profile includes an intermediate descent, landing, taxi, take-off, and climb at the turnaround point, as well as a 45-minute loiter. The loiter is composed of a 15-minute contingency hold and a 30-minute final reserve, in compliance with CAT.OP.MPA.181 [10]. This profile represents the most limiting sizing case, as it assumes operation on pure LH_2 with no refuelling available at the destination airport, thereby satisfying REQ-MIS-OPER-01 (see Appendix A).

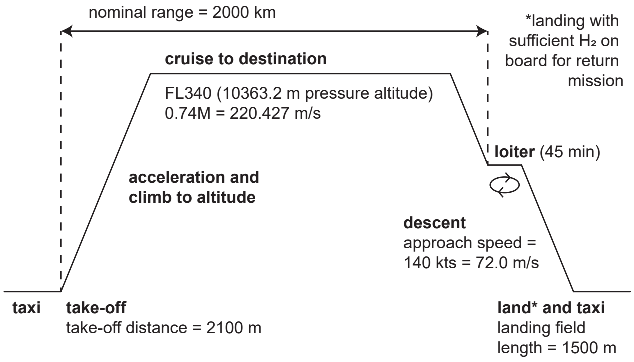

Figure 2.2: Mission profile definition.

For further calculations, assumptions are made regarding the duration of each flight phase. For the phases up to 3000 ft of altitude, the ICAO LTO cycle applies [11], which states that taxiing (out and in) lasts 26 min, the take-off phase 0.7 min, climb-out 2.2 min and the approach and landing phase 4 min. Since the remaining phases are not covered by the LTO cycle and strongly depend on the type of aircraft and mission, further assumptions are necessary. Both climb and descent are assumed to last 20 min each, which is reasonable for A320neo-type aircraft. Finally, the cruise duration is assumed to be 84.5 and 159.5 min for 2000 and 3000 km, respectively. The former was obtained by subtracting all other phases from an assumed block time of 2.6 hours. For the latter, an additional 75 min was added to the former, corresponding to 1000 km divided by the cruise speed. All durations are presented in Table 2.7.

Table 2.7: Flight-phase durations for two mission profiles (in min).

Flight phase	2000 km range	3000 km range
Taxi out and in	26.0	26.0
Take-off	0.70	0.70
Initial climb	2.20	2.20
Climb	20.0	20.0
Cruise	84.5	159.5
Descent	20.0	20.0
Approach + land	4.00	4.00
Total	**157.4**	**232.4**

The mission involves transporting a pre-defined payload. Per mission requirement REQ-MIS-OPER-03, the aircraft shall provide a nominal capacity of 180 passengers. An average mass of $m_{\text{pax}} = 84$ kg per passenger and $m_{\text{bag}} = 13$ kg per baggage is assumed per the acceptable means of compliance with EU Air Operations regulation CAT.POL.MAB.100 (Annex IV) [10]. Based on this, the mass of payload m_{pl} is $m_{pl} = (m_{\text{pax}} + m_{\text{bag}})n_{\text{pax}} = 17460$ [kg]. Additionally, per the same document, there are two flight crew members whose mass is assumed to be 85 kg for each one and one cabin crew member weighs 75 kg [10], and there is 4 of them, where each crew member also carries 13 kg of luggage.

---

[33] `https://ansperformance.eu/economics/cba/standard-inputs/latest/chapters/ifr_average_flight_distance_and_flight_duration.html` (Accessed: 14/06/2026)

2.4. Technical Risk Assessment

To deal with uncertainties in the design process, a rigorous risk assessment should be performed to improve the safety of the design. In this section, each technical risk is given a unique ID of the form TR-XXX-## where TR stands for Technical Risk, XXX are letters specific to a risk category, which are: budget (BDG), unconventional concept (UCC), operations (OPR), and design (DES). ## is the index of the categorised risk. Additionally, scores are given per risk to evaluate their severity. Their explanation is presented in Table 2.8. These scores are given twice: once before and once after the mitigation strategy has been implemented.

Table 2.8: Explanation of scores of criteria assigned to risks. They are likelihood (L), and severity of consequence (C). The score, risk (R), is the product of both criteria (R = L × C) to evaluate how critical its occurrence is on the project.

L	Description	C	Description
0	Never occurs	0	None
1	Very unlikely	1	Negligible
2	Unlikely	2	Low
3	Might happen	3	Moderate
4	Likely	4	High
5	Will certainly occur	5	Catastrophic failure

As the design of the MAVERICK aircraft has evolved since the start of the DSE, some risks that were previously defined are no longer considered as such, and some new risks have been identified. An overview of risks that are no longer relevant is shown in Table 2.9, and new risks are presented in Table 2.10.

Table 2.9: Risks previously defined during the DSE that are no longer relevant thanks to the increased design maturity and reduced number of uncertainties regarding the MAVERICK aircraft.

ID	Risk Description	Justification for Risk Removal
TR-BDG-01	Limited storage space due to multi-fuel system.	After design of the internal fuselage layout, it was seen that the hydrogen tank does not remove cargo space and that the forward kerosene trim tank does not reduce this space drastically.
TR-BDG-03	Increased mass due to the dual fuel system, leading to unfeasible design space.	The aircraft design reached a convergence after multiple iterations.
TR-UCC-01	Converging to a design taking longer than the project duration due to an unconventional propulsion system	The convergence to a design is reached and explained in Chapter 3.
TR-UCC-02	Stakeholder requirements leading to an unfeasible design space.	A design is reached while respecting the stakeholder requirements.
TR-UCC-09	Cryogenic insulation degradation over service life affecting fuel performance.	The cryogenic insulated systems are checked regularly to avoid the effects of such degradation.
TR-OPR-02	Hydrogen boil-off during extended ground holding, causing pressure build-up.	Resealable valves are present on the tank to release the pressure build-up, thus removing the consequence of this risk.
TR-OPR-04	Unscheduled diversion to an airport without hydrogen refuelling capability.	The aircraft is designed for this possibility, thus removing the severity of the risk.

Table 2.9 – continued from previous page

Risk ID	Risk Description	Justification for Risk Removal
TR-OPR-05	Icing on the external hydrogen tank affecting aerodynamics and structural integrity.	The aircraft does not have any external tanks.
TR-DES-02	Cryogenic insulation failure leading to catastrophic pressure build-up.	Three types of pressure-releasing mechanisms are implemented on the MAVERICK aircraft.

Table 2.10: Risk management table. The format in the **L**, **C**, and **R** columns is *Pre-mitigation score → Post-mitigation score*. Finally, the responsible person (**Resp.**) for each risk is denoted by their initials (AAL=Amaya, MGPC=Manuel, DC=Dominik, MO=Mara, LR=Luca, LV=Luuk, MN=Marcin, SK=Simonas, YW=Yaan, TN=Tim).

ID	Risk description	L	C	R	Mitigation strategy	Contingency plan	Resp.
TR-UCC-10	Aircraft not being competitive	4 → 2	5 → 5	20 → 10	Make the aircraft cheaper or more efficient.	Shut down the program to avoid losing more money, and use the knowledge acquired during the development in other companies or industries.	YW
TR-OPR-10	Fuel leak	4 → 2	4 → 4	16 → 8	Include sensors and maintenance intervals close enough to prevent leaks	Shut down one of the fuel intakes and run the aircraft on the remaining fuel. If hydrogen is leaking, apply the procedure outlined in Subsection 10.1.4	MO
TR-OPR-11	Fuel type running out faster than the other due to mismanagement	3 → 1	3 → 2	9 → 2	Place mass flow sensors in both fuel pipes. Sound the alarm in case the difference from the planned case goes over a threshold.	Close valve of the feed system of the fuel type that is running out, and flight continues with other fuel type.	DC
TR-OPR-12	Emergency landing, potentially destroying the tail tank	2 → 1	5 → 5	10 → 5	Have a structurally strong tank on supports that absorb the impact.	Use emergency venting system explained in Subsection 10.1.4.	MC

Table 2.10 – continued from previous page

ID	Risk description	L	C	R	Mitigation strategy	Contingency plan	Resp.
TR-OPR-13	Sensors giving false readings	4 → 1	3 → 2	12 → 2	Have 3 different sensors to have an 'odd one out' system managed by the flight computer	If sensor reading is impossible, continue flying without relying on that data. If the reading is likely valid, follow normal procedures.	LR

The newly identified risks are then shown on a risk map in Figure 2.3 to give an overview of the efficiency of the mitigation strategies. It is seen that the risks TR-OPR-10 and TR-UCC-10 that were previously rated as high risks were brought to acceptable levels thanks to the mitigation strategy. All risks are reduced by the mitigation strategy.

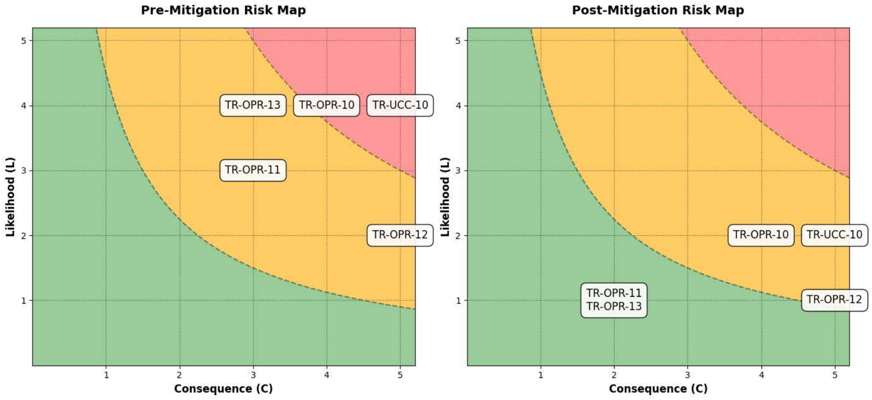

Figure 2.3: Technical risk maps before and after the mitigation strategies have been applied for the newly defined risks. The red area shows high risks that are unacceptable for this project, the risks in the yellow area are medium risks, and the green area is the low-risk zone.

2.5. Trade-off Overview

A Design Option Tree (DOT) was used to structure the initial design space. The DOT identified the viable configuration choices for the aircraft, including airframe layout, wing position, tail arrangement, propulsion location, and fuel storage integration. From this broader design space, five feasible aircraft concepts were selected for further evaluation, while options with insufficient technological readiness, excessive certification risk, or poor integration feasibility were discarded. These concepts were used as input for the configuration trade-off, ensuring that the selected configuration was not biased towards conventional aircraft layouts and instead resulted from a fair comparison of both conventional and less conventional design options.

A trade-off analysis was conducted during the previous design phase to select the most suitable aircraft configuration and propulsion system. Five aircraft layouts were evaluated: a conventional low-wing tube-and-wing, a three-engine low-wing, a high-wing open-fan, a high-wing turboprop, and a blended wing-body configuration. Their configurations were compared against criteria covering aerodynamic and fuel-integration efficiency, technology and certification risks, circularity, structural efficiency, cost, and stability & control. The resulting trade-off selected the conventional low-wing tube-and-wing layout as the preferred design.

A separate trade-off was performed for the propulsion system, since the engine is the most important and novel system of the MAVERICK concept. High-bypass turbofan, low-bypass turbofan, turboprop, and open-fan engines were compared using criteria related to environmental impact, performance, cost, complexity, and safety. The high-bypass turbofan was selected as the best option due to its strong performance, proven technology, and compatibility with the mission. Both trade-offs were supported by sensitivity analyses on criteria weights and scoring uncertainty, confirming that the selected aircraft configuration and propulsion system remained robust under variation.

3

Aircraft Design

This chapter presents the sizing and integration of the MAVERICK aircraft. The design process combines aerodynamic and performance evaluation, mission fuel sizing, Class II weight estimation, Centre of Gravity (CG) analysis, stability and controllability assessment, and wing position optimisation in an iterative framework. Fuel capacity is determined from both the nominal mission, for which a 50% reduction in CO_2 emissions is required, and the maximum range mission. After convergence of the sizing loop, the resulting aircraft mass breakdown, balance characteristics, internal arrangement, and external dimensions are described.

3.1. Aircraft sizing

The final MAVERICK design point is obtained through the iteration process shown in Figure 3.1. The procedure consists of an aircraft sizing loop and a higher-level propulsion integration loop. The Class I results provide the initial aircraft mass and performance estimates that were used as an input for the Class II iteration loop.

Within the aircraft sizing loop, the aerodynamic performance is evaluated first and used to estimate the mission fuel mass, as described in Section 3.2. First, the LH_2 tank is sized to achieve a 50% CO_2 reduction, and then the kerosene tank is sized for maximum mission range with a fixed amount of hydrogen.

The tank mass and geometry are then included in the Operating Empty Mass (OEM) calculation described in Section 3.3. The updated mass distribution is passed to the CG analysis of Section 3.4, after which stability and controllability are evaluated. The wing position is adjusted until the required CG envelope can be accommodated with the smallest feasible tail. Any change in wing position modifies the component locations, requiring the CG and stability analyses to be repeated.

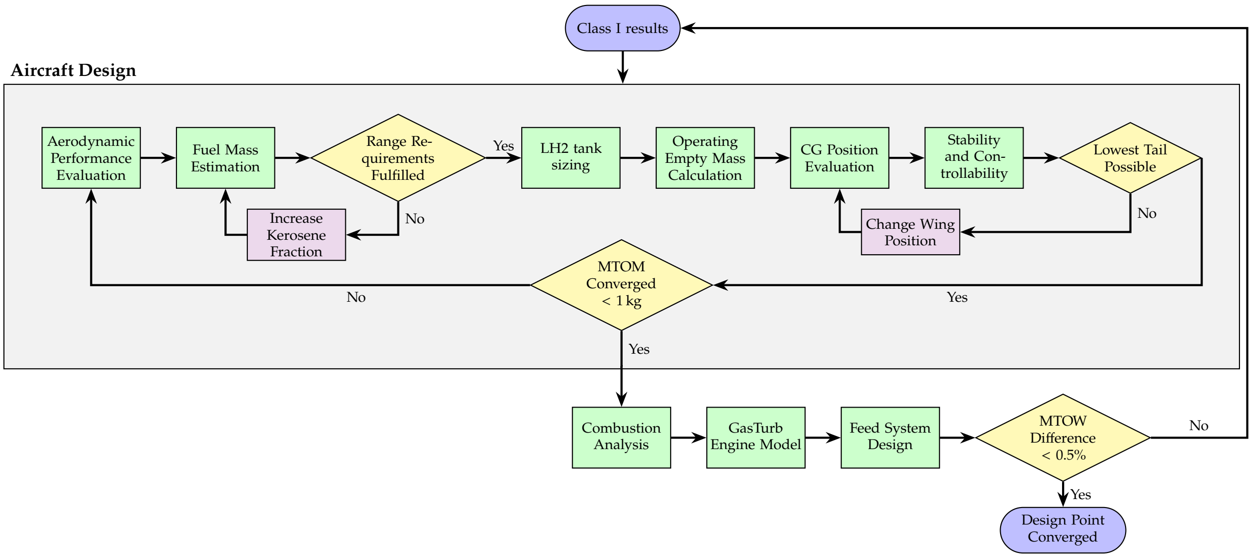

Figure 3.1: Multidisciplinary iteration process used to obtain the converged MAVERICK design point.

Once the aircraft-sizing loop has converged, the resulting design is passed sequentially to the combustion analysis, GasTurb engine model, and the hydrogen feed-system design. The combustion analysis determines the fuel split and mass flow required throughout the mission. These results are used by the gas-turbine model to update the engine performance, including the Thrust Specific Fuel Consumption (TSFC), while the feed-system model determines the mass of the hydrogen delivery system. The refined propulsion and feed-system inputs are then returned to the aircraft-sizing model. The converged design point is summarised in Table 3.1. The aircraft has an MTOM of 95.5 t, an OEM of 63.4 t, and a total fuel load of 14.0 t. This fuel load is split between 3.4 t of LH_2 and 10.5 t of kerosene.

The newly obtained MTOM is compared with the value from the previous multidisciplinary iteration. If the relative difference is greater than 0.5%, the complete aircraft-sizing process is repeated using the updated propulsion and feed-system data. The design point is considered converged when the MTOM difference between two successive multidisciplinary iterations is below 0.5%.

The final configuration is therefore sized around a medium-range, 180-passenger mission while retaining a dual-fuel architecture. The methods and assumptions used to obtain these values are presented in the following sections.

Table 3.1: Converged MAVERICK design point.

Quantity	Value
Masses	
MTOM	95,533 kg
OEM	63,433 kg
ZFM	81,552 kg
Payload	18,120 kg
LH_2	3,435 kg
Kerosene	10,546 kg
Total fuel	13,981 kg
Wing	
Reference area, S_w	147.5 m^2
Span, b	35.9 m
Aspect ratio, A	8.74
Design wing loading, W/S	6349 N/m^2
Propulsion	
Number of engines	2
Design thrust-to-weight ratio, T/W	0.321
Required sea-level thrust per engine	150.3 kN

3.2. Fuel mass sizing

Sizing the fuel mass relies on a Breguet-based model adjusted to multi-fuel aircraft. The assumptions used are collected in Table 3.2. These are stated here so that their influence on the resulting fuel loads is clear, while the sizing procedure itself is described in the remainder of this section.

Table 3.2: Assumptions used in the fuel mass sizing methodology

ID	Assumption	Justification / source
A-FU-01	Each leg is sized with the Breguet range equation at constant cruise speed, lift-to-drag ratio and TSFC, and the full range is flown as a single cruise segment with a 5% margin.	Cruise-dominated mission; preliminary range sizing.
A-FU-02	The engine burns a hydrogen-kerosene blend whose TSFC scales inversely with the mass-weighted specific energy of the two fuels.	Energy-equivalent TSFC; preliminary engine-performance simplification.
A-FU-03	Both legs of the out-and-back mission require the same amount of fuel.	Low fuel mass fraction, Conservative for return.
A-FU-04	Kerosene is refuelled at the outbound airport, so only the per-leg kerosene is carried.	Kerosene infrastructure is assumed to be available at both airports.
A-FU-05	CO_2 is produced only by the kerosene.	Hydrogen combustion produces no CO_2; REQ-MIS-SUS-02.
A-FU-06	Reserve fuel (mission margin and 45-minute loiter) and Auxiliary Power Unit (APU) fuel are kerosene, with the loiter flown at cruise speed and lift-to-drag.	Section 2.3, Section 10.3

ID	Assumption	Justification / source
A-FU-07	LH_2 boil-off is a constant hourly fraction of the initial nominal hydrogen mass, accumulated over the flight and turnaround time and added to the loaded hydrogen.	Linear boil-off model; basing it on the initial mass is conservative.

The fuel mass of the MAVERICK aircraft is sized by two requirements, REQ-MIS-PERF-01 and REQ-MIS-SUS-02, together with the market analysis of reference routes Section 2.3. Accordingly, two sizing points are defined. The hydrogen load is sized to meet the 50% CO_2 reduction target over the 2000 km out-and-back nominal mission, while the kerosene load is sized for the 3000 km maximum-range mission plus reserves. Both missions assume kerosene refuelling at the outbound airport. Each leg is sized with the Breguet range equation [12]:

$$R = \frac{L/D}{\mathrm{SFC}\, g_0} V \ln\left(\frac{m_i}{m_f}\right), \tag{3.1}$$

where m_i and m_f are the leg start and end masses, V the cruise speed, and L/D the cruise lift-to-drag ratio. As the engine burns a hydrogen–kerosene blend, the kerosene TSFC returned by the engine model is converted into an energy-equivalent blend TSFC:

$$\mathrm{SFC}_{\text{blend}} = \mathrm{SFC}_{\text{kero}} \frac{e_{\text{kero}}}{\chi\, e_{\text{kero}} + (1-\chi)\, e_{\text{LH2}}}, \qquad \chi = \frac{m_{\text{kero}}}{m_{\text{kero}} + \frac{1}{2} m_{\text{LH2}}}, \tag{3.2}$$

where e_{kero} and e_{LH2} are the specific energies of the two fuels and χ is the kerosene mass fraction of the fuel burnt on a single leg. This assumes equal thermal efficiency for both fuels, so that the TSFC scales inversely with the specific energy of the blend; as hydrogen has higher specific energy [13] than kerosene, blending lowers the effective TSFC. The factor of one half on m_{LH2} reflects the out-and-back nature of the nominal mission: hydrogen is loaded for both legs on a single fill, so only half is consumed per leg, whereas kerosene is refuelled at the outbound airport and is fully consumed each leg.

For the nominal mission, emissions drive LH_2 tank sizing. Because CO_2 is produced only by the carbon in the kerosene Section 8.1, the 50% reduction target fixes the nominal kerosene burn at half that of the A320neo reference on the same mission. With the kerosene burn fixed, the hydrogen load is the only free variable: the routine increases the LH_2 mass until the Breguet range of the blended leg (Equation 3.1, evaluated with Equation 3.2) reaches the nominal range, and retains the smallest mass that satisfies it. The nominal mission assumes a single hydrogen fill with no LH_2 refuelling at the destination, per REQ-MIS-OPER-01, so the full out-and-back hydrogen is carried while only the per-leg kerosene is on board.

Table 3.3: Fuel sizing results.

Quantity	Value
Nominal mission	
Nominal range	2,000 km
LH_2 mass per leg	1,714 kg
Kerosene mass per leg	2,913 kg
Maximum-range mission	
Maximum range	3,000 km
LH_2 mass per leg	1,714 kg
Kerosene mass	7,628 kg
MTOM fuel loading	
Total kerosene mass	10,562 kg
Total LH_2 mass	3,435 kg
Contingency kerosene	2,815 kg
APU fuel allowance	120 kg
LH_2 boil-off allowance	7 kg

The kerosene tank capacity is then sized for maximum range. Holding the hydrogen mass at its nominal value, the onboard kerosene is increased until the Breguet range meets the 3000 km maximum-range requirement of REQ-MIS-PERF-01. This case sizes the kerosene tank and the kerosene mass carried at MTOM, as it requires more fuel with a limited amount of hydrogen. Reserve fuel, comprising the mission margin and the 45-minute loiter, together with the APU fuel burnt during turnaround, are both taken as kerosene and added to the onboard load. Finally, the LH_2 boil-off accumulated over the flight and turnaround is added to the hydrogen load.

The resulting fuel loads are summarised in Table 3.3. At MTOM the aircraft carries 13.98 t of fuel, comprising 3.44 t of LH_2 loaded for the full out-and-back nominal mission and 10.55 t of kerosene sized for the maximum-range mission and reserves. The kerosene total is dominated by the 7.61 t maximum-range cruise burn, which corresponds to 22 % CO_2, with 2.81 t of reserves and 0.12 t of APU fuel. The maximum-range requirement is met at 3000 km, and the kerosene and LH_2 tanks size to 13.6 and 51.9 m^3 respectively.

3.3. Weight estimation

The OEM of the MAVERICK aircraft is estimated using the Class II component weight method presented by Roskam [14]. The method divides the aircraft empty mass into three principal groups: structures, powerplant, and fixed equipment and systems. Roskam provides several alternative statistical relations for each component, including the General Dynamics (GD) and Torenbeek methods. The relations selected for the present aircraft are listed in Table 3.5 and assumptions used throughout the calculations are depicted in Table 3.4.

Table 3.4: Assumptions used in the weight estimation methodology

ID	Assumption	Justification / source
A-WE-01	The conventional airframe (structures, powerplant, and fixed equipment) is sized with the Roskam [14] Class II statistical relations for transport aircraft.	The layout, except for the hydrogen system, is conventional, so transport-category relations apply.
A-WE-02	The engine dry mass is the LEAP-1A reference value multiplied by the engine count with a weight penalty for increased external dimensions.	The engine design is based on LEAP-1A architecture. Therefore, the LEAP-1A mass is a sufficient preliminary estimate.
A-WE-03	The powered-flight-control relation already includes the hydraulic and pneumatic equipment, so no separate hydraulic-system mass is added.	General Dynamics method, Roskam Sec. 7.2; avoids double counting.
A-WE-04	The conventional fuel-system mass is evaluated on the kerosene load only.	Applying it to total fuel would mistreat cryogenic hydrogen storage as conventional tankage.
A-WE-05	The cryogenic-tank empty mass and the hydrogen feed-system mass are supplied by their dedicated structural/thermal and feed-system models, not by statistical relations.	No statistical mass data exist for cryogenic hydrogen systems.

The statistical relations are evaluated using the imperial units prescribed by Roskam, after which the resulting component masses are converted to SI units. The conventional structural group consists of the wing, fuselage, horizontal and vertical tail, landing gear, and nacelles. The powerplant group comprises the engines, conventional fuel system, engine controls, and engine starting system. The fixed-equipment group contains the flight controls, electrical system, avionics, environmental-control system, oxygen system, APU, and furnishings. The engine dry mass is not obtained from a Roskam statistical sizing relation. Instead, the mass of each engine is taken from the selected LEAP-1A reference engine and multiplied by an upsizing factor, which is the inlet area increase fraction and the number of installed engines.

Table 3.5: Component masses, estimation methods and CG positions used in the loading diagram. Masses are from the converged design point. $\bar{c}$ is the mean aerodynamic chord length, x_{LEMAC} is the longitudinal coordinate of its leading edge, L_f is the fuselage length

Component	CG location	Method [14]	Mass [kg]	Comments
Structures				
Wing	$x_{\mathrm{LEMAC}} + 0.50\bar{c}$	Torenbeek Eq. (5.7)	23 657	

Component	**CG location**	**Method**	**Mass [kg]**	**Comments**
Fuselage	$0.50\,L_f$	Torenbeek Eq. (5.27), $K_f=1.08$	11 696	Pressurised; LH_2 penalty factor set to 1
Horizontal tail	$x_{\mathrm{LEMAC,h}} + 0.42\,c_h$	Torenbeek Eq. (5.19), $K_h=1.1$	708	Variable incidence
Vertical tail	$x_{\mathrm{LE,v}} + 0.42\,c_v$	Torenbeek Eq. (5.20), $K_v=1.0$	736	Fuselage-mounted
Landing gear	$0.40\,L_f$	Torenbeek Eq. (5.42), Table 5.1	3 747	Retractable, civil
Nacelle	$x_{\mathrm{LEMAC}} - 3 + 0.40 L_{\mathrm{nac}}$	GD Eq. (5.35)	2 954	Podded; incl. air induction
Powerplant group				
Engines	nacelle CG	LEAP-1A ref. $\times\, n_{eng}$	6 946	No statistical relation
Kerosene fuel system	nacelle CG	Torenbeek Eq. (6.24)	324	Kerosene load only
Engine controls	nacelle CG	GD Eq. (6.24), 6.5.2.1	67	Wing-mounted jets
Engine starting	nacelle CG	GD Eq. (6.27)	80	Pneumatic
Hydrogen feed system	$0.2\,(x_{\mathrm{H2,cg}} + x_{\mathrm{nac,cg}})$	Project-specific	500	From feed-system model (Chapter 7)
Fixed equipment and systems (at $0.40\,L_f$)				
Flight controls	$0.40\,L_f$	GD Eq. (7.5)	1 134	Incl. hydraulics
Electrical	$0.40\,L_f$	GD Eq. (7.15)	994	
Avionics	$0.40\,L_f$	Torenbeek Eq. (7.25)	1 262	Glass cockpit
Air conditioning & pressurisation	$0.40\,L_f$	GD Eq. (7.29)	1 947	Incl. anti-icing
Oxygen	$0.40\,L_f$	GD Eq. (7.35)	124	
APU	$0.40\,L_f$	Eq. (7.40), 0.85% MTOM	812	Section 10.3
Furnishings	$0.40\,L_f$	GD Eq. (7.44)	3 660	Seats, galleys, lavatories
Hydrogen system and crew				
Cryogenic LH_2 tank (empty)	$x_{\mathrm{H2,cg}}$	First-principles model Chapter 6	1 636	Structural/thermal model
Crew	$0.40\,L_f$	Assumed crew mass	450	Carried in OEM
Payload and fuel (loading-diagram items, not part of OEM)				
Passengers	rows 8.0–31.0 m	Payload	15 120	180 passengers
Forward cargo	$0.32\,L_f$	Payload	1 500	
Aft cargo	$0.70\,L_f$	Payload	1 500	
Wing kerosene tank	$x_{\mathrm{LEMAC}} + 0.50\bar{c}$	Fuel sizing (Section 3.2)	7 111	
Forward kerosene tank	$0.184\,L_f$	Fuel sizing	3 435	Balances aft LH_2
LH_2 fuel	$x_{\mathrm{H2,cg}}$	Fuel sizing	3 435	

The conventional kerosene fuel-system mass is calculated using the integral-tank relation from Roskam and is evaluated using the kerosene load only. The empty cryogenic tank mass and the hydrogen feed-system mass are therefore introduced as separate project-specific contributions. The resulting OEM is calculated as follows, where m_{struct}, m_{pwr}, and m_{sys} denote the structural, powerplant, and fixed-equipment mass groups, respectively:

$$\begin{aligned} m_{\text{OEM}} &= m_{\text{struct}} + m_{\text{pwr}} + m_{\text{sys}} \\ &\quad + m_{\text{tank},\text{H}_2} + m_{\text{feed},\text{H}_2} + m_{\text{crew}} \end{aligned} \tag{3.3}$$

Since several component masses depend on MTOM, the Class II estimate is closed iteratively. At each iteration, the updated OEM, payload mass, and mission fuel mass from Section 3.2 are summed to obtain a new MTOM. This value is subsequently fed back into the weight, fuel, propulsion-installation, and wing-sizing models. The process is repeated until the relative change in MTOM drops below 1 kg. The converged results are presented in Table 3.6.

Table 3.6: Converged mass breakdown by group.

Group	**Mass [kg]**	**% MTOM**
Structures	43 497	45.5
Powerplant group	7 917	8.3
Fixed equipment	9 933	10.4
Cryogenic LH_2 tank (empty)	1 636	1.7
Crew	450	0.5
OEM	**63 433**	**66.4**
Payload	18 120	19.0
ZFM	**81 553**	**85.4**
Fuel (LH_2 + kerosene)	13 981	14.6
MTOM	**95 533**	**100.0**

3.4. Centre of gravity variations

With the component masses of Section 3.3 established, the longitudinal centre of gravity can be estimated and its travel during loading assessed. The CG is evaluated at three reference states, OEM, ZFM and MTOM, and a loading diagram is constructed to determine the full forward and aft CG travel that the subsequent stability, control and wing-positioning analysis must accommodate. The assumptions underlying the analysis are listed in Table 3.7.

Table 3.7: Assumptions used in the centre-of-gravity analysis

ID	**Assumption**	**Justification / source**
A-CG-01	Component CG positions are taken as typical fractional locations from Roskam rather than from a detailed internal layout.	Internal arrangement is not yet fixed at the conceptual stage.
A-CG-02	Hydrogen cannot be loaded with passengers on board, so the loading sequence is fixed as cargo, then fuel, then passengers.	Safety constraint on cryogenic refuelling with occupants present Section 10.1.
A-CG-03	Passenger CG excursions are bounded by considering both front-to-aft and aft-to-front boarding under a window–middle–aisle rule.	Captures the extreme forward and aft CG positions during boarding.
A-CG-04	Each fuel quantity acts at the centroid of its tank (forward and wing kerosene tanks, LH_2 tank).	Tank-level resolution; intra-tank fuel migration is not modelled.
A-CG-05	A 2% Mean Aerodynamic Chord (MAC) margin is added to the forward and aft CG limits taken from the loading diagram.	Allowance for the uncertainty of a Class II estimate [15].

Each mass group from the weight estimation is assigned a longitudinal station. The structural and systems groups are placed at typical fractional locations: the wing group and wing kerosene tank at the wing MAC, the fuselage, landing gear, fixed equipment and crew at fractions of the fuselage length, and the powerplant at the nacelle centroid. Two features dominate the CG behaviour. The first is the cryogenic LH_2 tank, whose centroid lies far aft, taken from the sized tank layout. The second is a dedicated forward kerosene tank, placed well ahead of the wing specifically to counterbalance the aft hydrogen tank. The complete set of component positions is given in Table 3.5.

The loading diagram traces the CG as the aircraft is filled from its empty state. The final loading diagram achieved after the last iteration is presented in Figure 3.2. The order in which mass is added is set by an operational constraint unique to the hydrogen architecture: the LH_2 tank cannot be refuelled while passengers are on board (see Chapter 10). Fuelling must therefore be completed before boarding, which fixes the loading order as cargo, then fuel, then passengers.

Cargo is loaded first, with the forward hold ($0.32\,L_f$) filled before the aft hold ($0.70\,L_f$). Filling the forward hold first moves the CG forward, and the aft hold then draws it back.

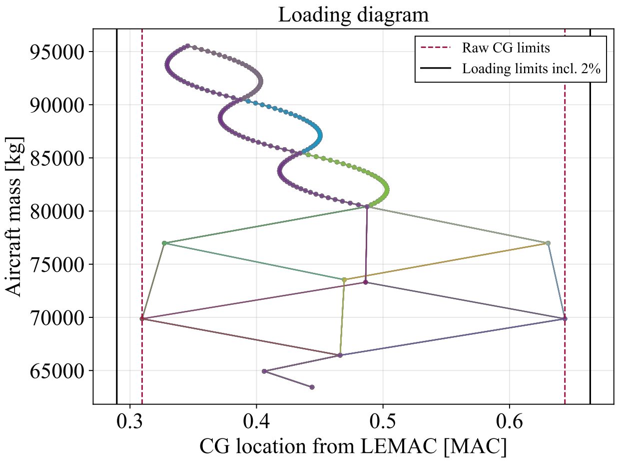

Figure 3.2: Loading diagram of MAVERICK, with cargo, then fuel, then passengers loaded.

The fuelling stage causes the highest CG variation. Because the LH_2 fuel sits well aft, filling the hydrogen tank drives the CG aft. The forward kerosene tank is filled to offset this, while the wing kerosene tank, positioned at the wing, barely moves the CG. The possible filling sequences of the forward kerosene, wing kerosene and aft LH_2 tanks are therefore all traced, so that the most forward and most aft intermediate positions reached during refuelling are captured.

Passengers board last. To bound their contribution, both front-to-aft and aft-to-front boarding orders are considered, each following a window-middle-aisle rule, with the passenger rows distributed between 8.0 and 31.0 m from the nose. The forward and aft CG limits are taken from the extreme excursions across all of these loading paths.

The final CG positions are summarised in Table 3.8. The high CG variation it presents is mainly caused by the hydrogen tank placed in the rear of the fuselage. Operation over this range is still possible, but is not optimal for performance. The front kerosene tank is positioned just after the nose landing gear to counteract that mass as described in Section 6.4. The aircraft is therefore not expected to operate in aft CG limits, but it is still designed to stay stable in that regime.

Table 3.8: Summary of the converged longitudinal centre-of-gravity results.

Condition	Mass [kg]	CG position [m]	CG position [% MAC]
Forward-most loading position	–	22.973	30.8
Aft-most loading position	–	24.466	64.3
OEM	63362	23.600	44.9
ZFM	81482	22.910	29.4
MTOM	95479	23.083	33.3

3.5. Stability and Control

The longitudinal stability and control of MAVERICK are assessed with the scissor-plot (X-plot) method, which sizes the horizontal tail and sets the longitudinal wing position through iteration. The tail must satisfy two requirements: keep the aircraft both statically stable and controllable. Each requirement defines a line of required tail-area ratio S_h/S against CG position, and the tail is sized by the lowest S_h/S fulfilling both requirements. The assumptions behind the analysis are listed in Table 3.9.

Table 3.9: Assumptions used in the stability and control analysis

ID	Assumption	Justification / source
A-ST-01	The wing is positioned to balance the scissor plot (equal stability- and control-driven tail area), giving the smallest horizontal tail, rather than to minimise the CG range.	The trim tank lets the aircraft fly at its optimal CG regardless, so CG range is not the sizing objective, as the aircraft utilises trim tank Section 6.4; so minimum tail area is preferred.
A-ST-02	A static margin of 5% MAC is applied at both stability and controllability curves.	Standard safety margin [16]
A-ST-04	The aerodynamic coefficients are taken from aerodynamic design and airfoil selection.	Subsection 4.1.3.
A-ST-05	A tail dynamic-pressure ratio $(V_h/V)^2 = 0.95$ is assumed.	Conventional value for a fuselage-mounted tail [17].

The stability line places the aft CG a stability margin ahead of the neutral point

$$\frac{S_h}{S} = \frac{\bar{x}_{cg} - \bar{x}_{ac} + \mathrm{SM}}{\frac{C_{L_{\alpha_h}}}{C_{L_{\alpha_{A\text{-}h}}}}\left(1 - \frac{d\varepsilon}{d\alpha}\right)\frac{l_h}{\bar{c}}\left(\frac{V_h}{V}\right)^2}, \tag{3.4}$$

and the controllability line places the forward CG where the tail can still trim the aircraft:

$$\frac{S_h}{S} = \frac{\bar{x}_{cg} - \bar{x}_{ac} + \frac{C_{m_{ac}}}{C_{L_{A\text{-}h}}}}{\frac{C_{L_h}}{C_{L_{A\text{-}h}}}\frac{l_h}{\bar{c}}\left(\frac{V_h}{V}\right)^2}, \tag{3.5}$$

where $\bar{x}_{cg}$ and $\bar{x}_{ac}$ are the CG and wing-body aerodynamic-centre positions as fractions of the MAC from the leading edge of the MAC, l_h is the tail arm, $\bar{c}$ the MAC, SM the stability margin, $C_{L_{\alpha_h}}$ and $C_{L_{\alpha_{A\text{-}h}}}$ the tail and aircraft-less-tail lift-curve slopes, $d\varepsilon/d\alpha$ the downwash gradient, and C_{L_h}, $C_{L_{A\text{-}h}}$ and $C_{m_{ac}}$ the tail-lift, aircraft-less-tail lift and aerodynamic-centre moment coefficients [16].

The longitudinal wing position x_{LEMAC} sets where these two lines fall relative to the CG range. Because the MAC moves with the wing, the physical CG limits map to different fractions of MAC as the wing is shifted, so moving the wing trades stability margin against control authority. The wing is therefore placed at the position where the smallest possible tail size places CG limits at the stability and controllability margins at the same time, leading to optimised scissor plot and minimised mass of the horizontal tail.

The CG range is not optimised, as the MAVERICK aircraft is equipped with automated trim control Section 6.4 managing CG during flight. The resulting CG travel with wing position, and the sized scissor plot are shown in Figure 3.3.

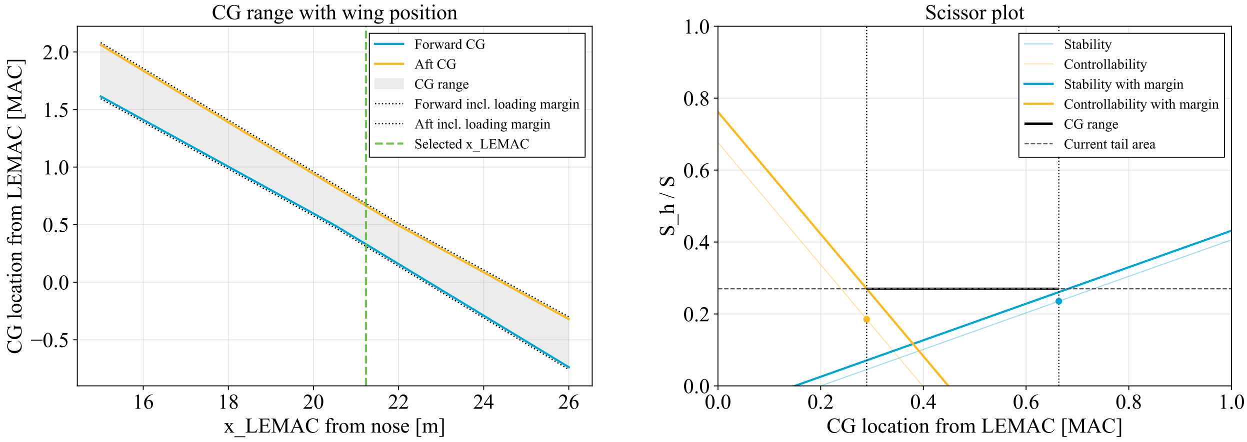

(a) Centre-of-gravity travel against wing position, with the selected x_{LEMAC}.

(b) Scissor plot: stability and controllability lines with the sized tail area and CG range.

Figure 3.3: CG and horizontal-tail sizing results.

At the converged design point, the balanced-scissor plot gives a wing position with the MAC leading edge at 0.432 L_f, corresponding to 21.6 m from the nose. The resulting tail and CG properties are summarised in Table 3.10. The stick-fixed neutral point is located at 0.79 MAC, aft of the aft CG limit with a 5% static-margin requirement. The final horizontal-tail size is therefore $S_h/S = 0.276$, corresponding to a tail area of 40.6 m^2.

Table 3.10: Converged stability and control results.

Quantity	**Value**
Horizontal-tail area, S_h	40.6 m^2
Tail-area ratio, S_h/S	0.276
Tail arm, l_h	23.1 m
Wing position, x_{LEMAC}	0.432 L_f
Wing position from nose	21.6 m
Stick-fixed neutral point	0.79 MAC
CG range, incl. 2% margin	0.29–0.68 MAC

3.6. Wing and propulsion system sizing

The matching diagram allows for sizing the wing (wing area) and propulsion system (thrust) such that the aircraft design is feasible. It considers requirements on take-off and landing distances, climb rate and climb gradient, and cruise and approach speeds.

Its relevant requirements are expressed in terms of wing loading (W/S) and thrust-to-weight ratio (T/W), and yield the design space of thrust and wing area values. Results for converged design point are presented in Table 3.1. The weight considered in every case is the maximum take-off weight $W_{\text{TO}} = m_{\text{TO}}g$, and the take-off thrust T_{TO}. The highest wing loading leads to the smallest wing surface, which is the optimal wing sizing. The method follows the algorithm presented by Vos [12].

3.7. Internal Aircraft Layout

The fuselage is divided longitudinally into a flight deck, a forward service area, the passenger cabin, a rear service section, and the unpressurised hydrogen-tank bay. The flight deck occupies the first 4 m, followed by 4 m of forward galleys and lavatories, so the cabin begins 8 m from the nose. The cabin extends to 31.3 m and seats 180 passengers in 30 rows at a 0.75 m pitch, six-abreast in a 3 - 3 layout. The two rows aligned with the emergency exits are given an additional 0.40 m of legroom, which accounts for the cabin length exceeding the nominal 30 × 0.75 m. This pitch sits at the middle of current narrow-body economy practice, between the 0.71 m to 0.74 m (28–29 in) used by low-cost carriers and the 0.76 m to 0.79 m (30–31 in) typical of mainline carriers [12]. A 4.7 m rear section houses the aft galley and lavatory group and closes at the pressure bulkhead, 36 m from the nose. The tank is placed in the rear part of the fuselage, it starts 36 m from the nose, behind the pressure bulkhead. The fuselage region where the tank is located will thus not be pressurised. This is done to allow for the presence of multiple panels on the fuselage that can be unmounted, thus enabling the removal of the hydrogen tank for inspection and maintenance. These steps are discussed later in

Section 11.2. Having multiple panels cannot carry the pressure load efficiently. The tail cone starts at 38 metre, shrinking the fuselage over the hydrogen tank.

3.8. Aircraft External Dimensions

With the converged design parameters fixed, the technical drawings were produced to support the subsequent design steps. The main landing gear was positioned from the wing and CG locations, and the nose gear from the internal tank layout. The main-gear height was driven by the tail-strike and engine-clearance requirements. Because the fuselage is long for a narrow-body aircraft, a levered shrink mechanism at the main landing gear that extends during rotation [18], with a pivotal cart [19] was selected. With these technologies, a tail-strike angle of 10.8 ° was achieved, with one additional degree of clearance at take off due to the semi-levered system. A ground clearance of 0.59 m was achieved during phases with fully extended gear.

The nose and tailcone lengths follow the fineness-ratio guidelines described by Vos [12], $l = k\, d_f$, with $k_n = 1.5$ for the nose and $k_t = 3.0$ for the tailcone, giving 6.0 m and 12.0 m. Final dimensions of the aircraft are summarised in Figure 3.4 and Table 3.11.

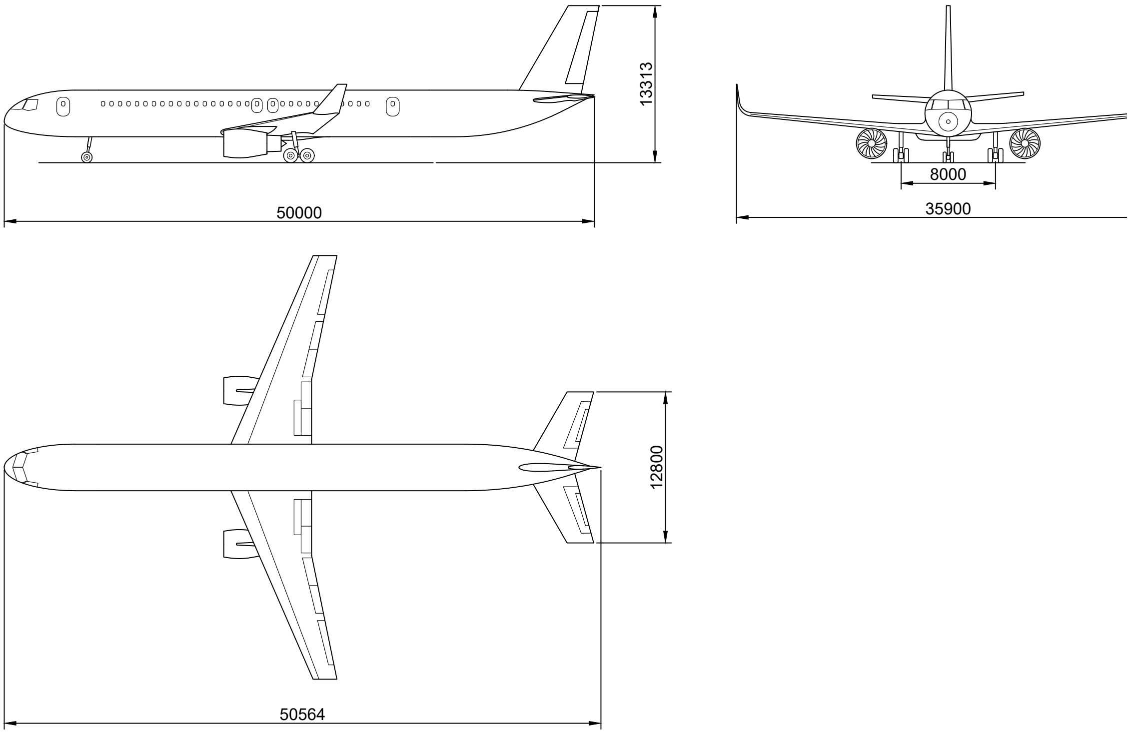

Figure 3.4: External Layout Drawing. Units in millimetres.

Table 3.11: Summary of external dimensions.

Parameter	Value	Parameter	Value
Overall		*Landing gear*	
Length overall, l_{oa}	50.56 m	Main gear length, l_{mg}	2.0–2.25 m
Wing span, b	35.9 m	Lowered gear length, $l_{\text{mg,lo}}$	1.75 m
Height overall, h_{oa}	13.31 m	Wheel track, T	8.0 m
Fuselage		*Clearances*	
Fuselage length, l_f	50.0 m	Tail-strike angle, θ_{ts}	10.8°
Diameter, d_f	3.95 m	Engine clearance, extended	0.59 m
Nose length, l_n	6.0 m	Engine clearance, lowered	0.35 m
Tailcone length, l_t	12.0 m	Belly clearance, c_{belly}	1.9 m

4 Aircraft Characteristics

In this chapter, key characteristics related to the aircraft design can be found. In Section 4.1, the aerodynamic design of the aircraft is presented. In Section 4.2, the structural design of the aircraft and material choices are described, and in Section 4.3, the range of the aircraft is evaluated for a variety of missions.

4.1. Aerodynamics

The aerodynamic characteristics of MAVERICK affect the weight and drag of the aircraft, and must thus be designed carefully. The aerodynamic design process is described in the rest of this section.

4.1.1. Assumptions

The assumptions used during the aerodynamic design are shown in Table 4.1.

Table 4.1: Assumptions used in the aerodynamic design process

ID	Assumption	Justification
A-AD-01	The symmetrical drag polar equation can be used to approximate the relationship between C_L and C_D.	The airfoil has moderate camber, thus $C_{L,min\,drag}$ is approximately zero [20].
A-AD-02	Drag components other than profile drag and induced drag (e.g. interference drag, wave drag) are accounted for by a constant factor of 1.1.	Recommended method by Vos [12]. Accurate estimation of these components is not possible in this design stage as the aircraft design is not detailed enough yet. This assumption limits the accuracy of the drag prediction at transonic Mach.
A-AD-03	The inclusion of a winglet does not affect the wingspan.	The width of the winglet is negligible with respect to the span (3%).
A-AD-04	The non-linear part of the lift curve can be approximated by a parabolic function.	The stalling behaviour does not require accurate modelling in this design stage.
A-AD-05	The effects of the Leading Edge Devices (LEDs) and Trailing Edge Devices (TEDs) can be superimposed.	The LEDs actually improves the flow characteristics downstream; this is likely a conservative assumption [21].

4.1.2. Method

The aerodynamic design of the MAVERICK aircraft is performed in four steps. First, the airfoil is selected, then the lift-to-drag ratio of the aircraft is estimated, after which the High-Lift Device (HLD)s are designed. Lastly, lift curves and a drag polar of the aircraft are created.

The airfoil is selected based on the required design lift coefficient ($C_{L_{des}}$) and limits on thickness-to-chord ratio (t/c). The $C_{L_{des}}$ is calculated at cruise conditions, with the design wing loading taken as the average of the wing loadings at take-off and landing. The limits on t/c are set by the form drag and shock wave formation at high subsonic Mach. They are calculated using methods proposed by Vos [12]. These calculations are performed using an estimated cruise Mach number (M_{cr}) based on reference aircraft. After the selection, the estimated M_{cr} is adjusted to be compatible with the chosen airfoil. The quarter-chord sweep angle and taper ratio are determined, again using relations by Vos [12]. Additionally, using the design wing loading, design lift coefficient, and the cruise Mach number, the cruise altitude is determined to ensure the aircraft flies at a C_L as close to $C_{L_{des}}$ as possible.

Secondly, the lift-to-drag ratio (L/D) is estimated. To do this, the zero-lift drag coefficient (C_{D_0}) is estimated using Equation 4.1 [20]:

$$C_{D_0} = \frac{f_{D_{misc}}}{S} \sum_c C_{D_c} S_{wet_c}, \tag{4.1}$$

where S is the wing surface area, C_{D_c} a drag coefficient specific for each component, S_{wet_c} the wetted area of each component, and $f_{D_{misc}}$ a factor to account for drag forms that are not included in the profile drag or induced drag. The total C_D is calculated using the simplified drag polar equation:

$$C_D = C_{D_0} + \frac{{C_L}^2}{\pi A R e}, \tag{4.2}$$

where C_{D_0} is the zero-lift drag, C_L is the lift coefficient, $AR$is the effective aspect ratio, and e is the Oswald efficiency factor. The effective aspect ratio is calculated by adding the contribution of the winglet ($\Delta AR = 1.9 \frac{h_{winglet}}{b} AR$) to the aspect ratio [20]. $(L/D)_{cruise}$ is found by dividing $C_{L_{des}}$ by the C_D calculated for the design lift coefficient.

Thirdly, the HLDs are designed. The types and combinations of LEDs and TEDs are chosen by studying the HLDs of similar aircraft. Then, the required flapped surface area for the TEDs is calculated using Equation 4.3 [21]:

$$\frac{S_{wf,TED}}{S} = \frac{\Delta C_{L_{max}}}{0.9\,(\Delta C_{l_{max,LED}} \cos \Lambda_{hinge,TED} + \frac{S_{wf,LED}}{S_{wf,TED}} \Delta C_{l_{max,LED}} \cos \Lambda_{hinge,LED})}, \tag{4.3}$$

where $\Delta C_{L_{max}}$ is the change of maximum lift coefficient between the clean wing and maximum HLD deployment, $\Delta C_{l_{max,LED/TED}}$ is the change in maximum lift coefficient for the airfoil caused by the LED or TED, $\Lambda_{hinge,LED/TED}$ is the sweep angle of hinge line of the LED or TED (approximated by the sweep angle of the front and rear spar, respectively), and $\frac{S_{wf,LED}}{S_{wf,TED}}$ is the ratio of the flapped area of the LEDs to the TEDs. The required flapped surface area for the LEDs is found by multiplying $S_{wf,TED}$ with $\frac{S_{wf,LED}}{S_{wf,TED}}$, which is an estimated ratio based on similar aircraft.

Lastly, the aircraft polars are created for approach conditions using the simplified drag polar equation (Equation 4.2). The characteristics for the polars are determined through a combination of simulation data and semi-empirical relationships, as the software used (XFLR5) cannot accurately simulate flow near stall conditions. C_{L_α} is estimated using Equation 4.4 [21]:

$$C_{L_\alpha} = \frac{2\pi AR}{2 + \sqrt{4 + (\frac{AR\beta}{\eta})^2 (1 + \frac{\tan^2 \Lambda_{c/2}}{\beta^2})}}, \tag{4.4}$$

where AR is the aspect ratio, β the Prandtl-Glauert correction factor, η_{AF} the airfoil efficiency, and $\Lambda_{c/2}$ the half chord sweep angle. For the landing configuration, the increase of surface area due to the HLDs is accounted for by multiplying C_{L_α} with $\frac{S'}{S}$, the wing area with deployed HLDs divided by the wing area of the clean wing. To create the complete lift curve, $C_{L_{max}}$ and α_{0L} are found by simulating the airfoil in XFLR5. α_{stall} is determined from Equation 4.5:

$$\alpha_{stall} = \frac{C_{L_{max}}}{C_{L_\alpha}} + \alpha_{0L} + \Delta\alpha_{C_{L,max}}, \tag{4.5}$$

where $C_{L_{max}}$ is the maximum lift coefficient of the wing, α_{0L} is the zero-lift angle of attack of the wing, and $\Delta\alpha_{C_{L,max}}$ the offset of the stall angle with respect to the linear part of the lift curve [20]. The lift curve is finally created using the slope and fitting a parabolic function through a chosen end of the linear zone and the stall point.

4.1.3. Results

The chosen airfoil is the NASA SC(2)-0712. It is a supercritical airfoil, which means that it reduces the shockwave strength in the transonic regime. Its most important characteristics are shown in Table 4.2.

Table 4.2: Key characteristics of the SC(2)-0712 airfoil. $C_{l_{max}}$ and α_{0L} are presented for approach conditions.

Parameter	**Value**
Thickness-to-chord ratio t/c	0.12 [-]
Maximum camber	0.022 [-]
Maximum camber location	0.81 [-]
Design lift coefficient $C_{l_{des}}$	0.7 [-]
Maximum lift coefficient $C_{l_{max}}$	1.96 [-]
Mach Drag Divergence M_{dd}	0.76 [-]
Zero-lift angle α_{0L}	-4.6°

This airfoil $C_{l_{des}}$ of 0.7 is slightly higher than that of airfoils used on most passenger aircraft. This is due to the expected higher weight of the aircraft caused by the hydrogen system. M_{cr} is determined to be 0.74. This value is about 0.02 less than the M_{dd} of the SC(2)-0712 airfoil, avoiding high drag at cruise [22]. Although M_{cr} could be increased further when taking into account the sweep of the wing (increasing M_{dd} further), this would mean a slimmer airfoil would need to be used to comply with the t/c limits. However, this would increase the structural weight [12].

The lift-to-drag ratio of the aircraft in cruise is 15.6. This is based on a design $C_{L_{des}}$ of 0.61, which gives a C_D of 0.039. The lift curves and drag polar at approach conditions are presented in Figure 4.1 and Figure 4.2. It can be seen that L/D_{cruise} is quite close to the maximum possible L/D.

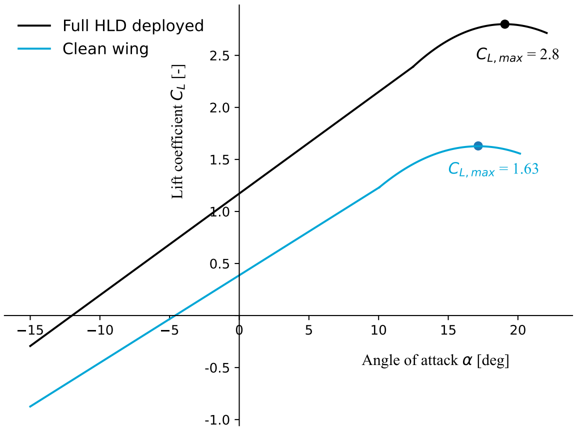

Figure 4.1: Lift curves of the clean wing and the wing in landing configuration at M_{app}.

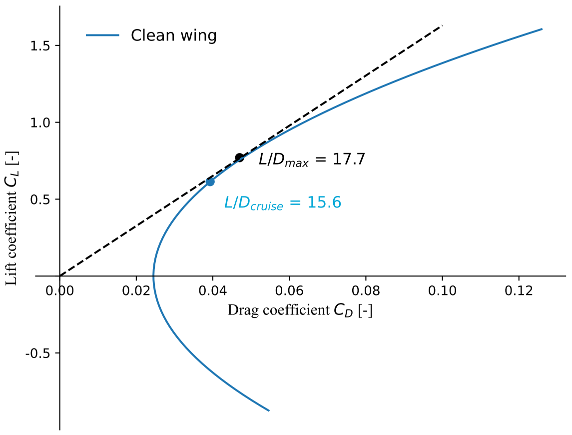

Figure 4.2: Drag polar at M_{app} of the clean wing.

The required $C_{L_{max}}$ in landing configuration is 2.8. As this requires a large $\Delta C_{L_{max}}$, a combination of slats and double-slotted Fowler flaps has been selected. To achieve the required $C_{L_{max}}$, the slats have a flapped area of 103.2 m^2 and the flaps 79.4 m^2. For the slats, this means they will range from 5% to 95% of the exposed wing span. This includes a margin of 4.18 m^2 to take care of unusable space due to the engine pylons. The flaps will range from 5% to 65% of the exposed wing span, which also includes a margin of 2.78 m^2. These values are comparable to those of similar aircraft and allow for sufficient space for the ailerons. An overview of the aerodynamic properties of MAVERICK is shown in Table 4.3.

Table 4.3: Aerodynamic parameters overview of the MAVERICK aircraft.

Flight phase parameters		**Clean wing parameters**	
Cruise altitude h_{cr}	FL340 [-]	Zero-lift drag coefficent C_{D_0}	0.024 [-]
Approach altitude h_{app}	0 [ft]	Oswald efficiency factor e	0.82 [-]
Cruise speed M_{cr}	0.74 [-]	Lift curve slope C_{L_α}	4.82 rad^{-1}
Approach speed M_{app}	0.20 [-]	Design lift coefficent $C_{L_{des}}$	0.61 [-
Geometric parameters		Maximum lift coefficient $C_{L_{max}}$	1.63 [-]
Surface area S	147.5 m	Cruise lift-to-drag ratio $(L/D)_{cruise}$	15.6 [-]
Span b	35.9 m	Trim angle of attack α_{trim}	1.1°
MAC	4.46 m	**HLD parameters**	
Aspect Ratio AR	8.74 [-]	LED flapped area $S_{wf,LED}$	103.2 m^2
Quarter-chord sweep $\Lambda_{c/4}$	20.7°	TED flapped area $S_{wf,TED}$	79.4 m^2
Taper ratio λ	0.33 [-]	HLD total wing surface area increase	19.7%
Root chord length c_r	6.19 m	Lift curve slope C_{L_α}	5.60 rad^{-1}
Tip chord length c_t	2.03 m	Maximum lift coefficient $C_{L_{max}}$	2.8 [-]
Winglet height $h_{winglet}$	2.43 m	HLD change in zero-lift angle of attack $\Delta\alpha_{0L}$	-7.4°

4.2. Structures and Materials

The structural design of MAVERICK is approached qualitatively due to the large similarity with the reference aircraft. Structural elements are discussed first, followed by the selected materials.

The main structural components of the aircraft will be very similar to those of the A320neo. The wing will contain a front and rear spar, which form a wing box together with the skins. This carries the bending and torsion. The ribs are perpendicular to the spars to maintain the wing shape and transfer loads between the spars and the skin. The fuselage will feature stringers and longerons to carry the bending loads, while the frames are present in the hoop direction to carry pressurisation loads, together with the bulkheads. The skin mainly carries shear loads, but also helps to carry pressurisation loads. Single-panel structures will be used on the fuselage and/or wings. These reduce the structural weight of the aircraft by removing the need for overlapping sheets and fasteners [23].

Regarding the materials, the aircraft will feature conventional aluminium alloys and composites. The conventional aluminium alloys are favoured over novel aluminium-lithium alloys because they are more recyclable [24], reducing the end-of-life Environmental Impact (EI). To reduce weight, composites will be used in the aircraft too. Thermoplastic resins will be used as much as possible as they are more recyclable and thus have a lower EI than thermosets. An overview of material properties is presented in Table 4.4.

Table 4.4: Overview of the main materials used and their properties. For CFRP, the values are given in the fibre direction.

Material	ρ [kg/m^3]	E [GPa]	σ_y [MPa]	σ_{UTS} [MPa]
Al2024T3[1]	2780	73.1	345	483
Al7075T6[1]	2810	71.7	503	572
CFRP (T800H) [25]	1810	170	N/A	2650

4.3. Range

The range performance was evaluated for two mission strategies. One includes refuelling only kerosene at the outbound airport, while the other is a one-way flight that can be fully refuelled before the next take-off. Range envelopes were calculated using the methods described in Section 3.2. Since these follow from preliminary tank sizing, based on flight profile simplification (AS-FU-01),

---

[1] `https://www.aerospacemetals.com/aluminum-distributor/` (Accessed: 16-06-2026)

the results overestimate fuel consumption by around 3 %. Resulting relations between range and fuel mass are visualised in Figure 4.3.

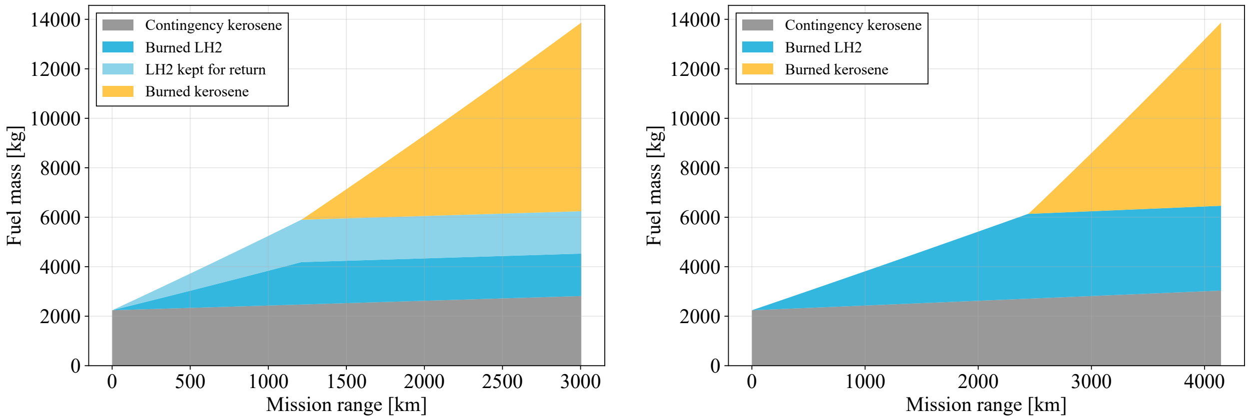

(a) Out-and-back mission without hydrogen refuelling.

(b) Mission with full refuelling at the destination.

Figure 4.3: Beach Diagrams representing fuel mass required as a function of mission range.

A parameter of sustainable operation is the range achievable on hydrogen alone. For the first strategy (Figure 4.3a), this limit is 1200 km; for the mission permitting hydrogen refuelling, it extends to 2440 km. Using the full tank capacity for the mission gives a range of 3000 km for the first mission profile, and 4150 km for operation between two hydrogen hubs. The ferry range, the one-way range at full fuel capacity and zero payload, is 5365 km, allowing for easy, versatile export of the aircraft.

5

Engine Design

The design of the engine is the core innovation of MAVERICK. It aims to allow simultaneous combustion with two fuels, hydrogen and kerosene, while maintaining performance relative to the state-of-the-art technology. To achieve this, a base engine is first chosen and modelled in Section 5.1. This engine must accept the hydrogen-kerosene fuel ratios as devised in Section 5.2. Then the combustion chamber for dual-fuel combustion is considered in Section 5.3. Finally, in Section 5.4 the fuel injector design is explained.

5.1. Base Engine Choice and Model

The engine innovation aimed for in this report regards the reduction of emissions through a combination of fuels. To limit the scope of engine design in this context, a base engine is therefore chosen and modified to allow dual-fuel combustion. Choosing a base engine involves balancing the core propulsion system requirements of creating a competitive value proposition (stakeholder requirement REQ-STK-COST-01), and reducing CO_2 and NO_x emissions by 50% (REQ-MIS-SUS-01,02), while requiring no additional maintenance relative to its number of parts (REQ-SYS-PRO-12).

To achieve this, a strategy is chosen to use the architecture of an efficient state-of-the-art engine as used on modern, comparable aircraft. Hence, a range of reference engines selected in a previous report [5] are considered. These represent the state of the art of comparable safe, reliable and deployed technologies (REQ-STK-SAFE-01). Besides, the environmental impact of the aircraft is compared against the reference aircraft (REQ-STK-SUS-01), which in this case is the Airbus A320neo.

To ease the creation of a less polluting engine design, a representative engine architecture is hence chosen as one of its engine options, the CFM LEAP-1A. Its other engine option is a geared turbofan, which has been excluded due to its additional complexity and lower reliability, leading to the grounding of numerous aircraft and extended inspection times, as identified in a previous report [5]. This engine must first be modelled to determine the flow conditions at its different stages. The modelling is done through the use of the gas turbine performance software GasTurb 11, which simulates a zero-dimensional thermodynamic cycle. Modelling an engine in this software therefore requires a series of assumptions, summarised in Table 5.1.

Table 5.1: Assumptions made in modelling the base engine.

ID	Assumption	Justification / source
A-EN-01	The engine design, focusing on emissions, entails the reconsideration of only two core components: the injector and the Combustion Chamber (CC).	Engine emissions arise from chemical reactions in the CC, influenced by fuel injection, mixing and burning. Blade geometry design is outside the scope of this report; thus, for this design stage, the rest of the engine architecture remains unchanged when ensuring the redesigned components increase the thermal energy of the incoming gas to achieve the values of the base engine.
A-EN-02	The pressure ratios of the fan, turbine interduct, bypass duct, compressor, turbine exit duct, and burner for the base engine are approximated to match high-level properties in GasTurb and are kept for the modified engine.	The rest of the engine is beyond the scope of this stage of design; to get an idea of what is possible, these unpublished pressure ratios must be approximated from known high-level properties such as cruise TSFC, Overall Pressure Ratio (OPR) and Core Pressure Ratio (CPR).
A-EN-03	The only parameter assumed to change in the non-redesigned parts of the engine is the mass flow rate.	The mass flow rate will change as the thrust requirement is higher than the reference, but will be lower with a higher hydrogen proportion due to its higher Lower Heating Value (LHV). For this design stage, this difference is assumed small and must be verified in further stages.

5.2. Fuel Mixtures and Masses

This section covers the process by which fuel mixture ratios were chosen, as well as the total fuel needed to fly a mission. Since there are multiple factors that influenced the final decision, all of them are discussed in separate subsections.

5.2.1. Combustion Strategy for Design Mission

A combustion strategy is developed to balance emissions production, thrust requirements, and fuel mass consumption. It determines the selection of fuel mixture ratios across all flight phases, prioritising the reduction of CO_2 and NO_x emissions while still delivering the thrust necessary for each phase and minimising the amount of fuel. The proposition of the strategy is presented below.

Starting with the taxi and take-off phases, both affect the environment at airports as well as in their vicinity. However, each phase has different characteristics. Taxiing requires far less power than take-off and lasts longer, so combustion at higher hydrogen ratios should be considered in order to minimise the production of emissions. For the take-off phase, the case is the opposite: it is very short and requires the most thrust. This means that the aircraft needs a large amount of energy in a short period of time, as well as a high volumetric energy density of fuel. For this phase, as well as the climb phases, the strategy is to use higher kerosene concentrations. For the cruise phase, which again requires less thrust and has a longer duration, the fuel mixture ratios at which the aircraft flies should favour hydrogen over kerosene. This can be justified by the fact that hydrogen has a higher specific energy, so less fuel in terms of mass would be used. With combustion at higher hydrogen concentrations, the risk of higher NO_x emissions arises; this issue is addressed in Section 5.3. For the descent phase, as well as the approach and landing, the hydrogen concentrations are gradually lowered. During the descent, the aircraft flies with idle power, requiring less thrust.During landing, it needs more power to manage the rate of descent, as well as decelerate in a short period of time.

The blend ratios are adjusted by a Full Authority Digital Engine Control (FADEC) module with a prepared fuel schedule for all the stages of a given mission. The emissions per flight phase for the nominal mission are quantified and discussed in Section 8.1, where the approach and results are described in detail.

5.2.2. Combustion Strategy for Special Cases

The logic described above applies to the case when the aircraft flies the design mission and carries the maximum amount of kerosene for meeting the CO_2 mission requirement (REQ-MIS-SUS-02). However, there are multiple special cases when different combustion strategies should be taken into account. These mainly concern emergency cases.

The first case is when the aircraft flies shorter distances. This means the hydrogen ratios should be increased. If the range can be covered only on hydrogen fuel, the pure hydrogen mode should be considered, minimising the weight of the aircraft and using the more efficient fuel, as well as reducing CO and CO_2 emission up to 100% in comparison with the reference aircraft.

On the other hand, when routes are longer than the design mission range, the hydrogen ratios might be decreased. This is due to the fact that the hydrogen tank is designed for the design mission and has a limited volume. More kerosene is therefore taken for additional range above 2000 km, up to the maximum range of 3000 km.

Other special cases are the go-around phase or touch-and-go landings. For both of these, the full-kerosene mode is used. Switching the modes is changed automatically by FADEC when the full throttle is suddenly applied. In case of a leak in any of the feed systems, the faulty system is shut down, and the fuel mode is automatically switched to the fuel which does not have a leak.

Overall, the design assumes suitability of the aircraft to operate in both fully kerosene and fully hydrogen modes. As mentioned before, the adjustment operations will be managed through the FADEC module, which receives data from sensors or can be managed by the pilot in case of an emergency.

5.2.3. Fuel Mass Flows

Another crucial aspect that drives the selection of fuel mixture ratios was the required fuel mass flows per flight phase. The formula of a required fuel mass flow per phase is given by $\dot{m}_f = \text{TSFC} \cdot T_{\text{req}}$ where TSFC is the thrust-specific fuel consumption of the hydrogen-kerosene blend and T_{req} is the thrust required in each flight phase. Since currently there is no aircraft on the market that uses hydrogen and kerosene for dual-fuel combustion, the specific fuel consumption levels for 2000 km and 3000 km mission profiles are unknown. However, using an iterative process (illustrated in Figure 3.1), they were estimated by starting with GasTurb 11 data for CFM LEAP 1-A at take-off and cruise TSFC levels and assigning initial fuel mixture ratios. After multiple iterations (using both Class II estimation for thrust and GasTurb 11 for TSFC), the final values of TSFC for both take-off and cruise were obtained, and those for other phases were approximated by interpolation and extrapolation. The take-off thrusts for both missions were taken from the class-II estimation using matching diagrams. It is important to note that the thrusts used for both missions are the thrusts scaled for the take-off masses for each mission, not the maximum thrusts the engine can produce.

For taxi, initial climb and approach & landing, the ICAO LTO cycle [11] applies, while for the cruise phase the values were calculated by assuming the aircraft is in static equilibrium: $T = D = W \cdot \frac{D}{L}$. Here, W is the weight of the aircraft in cruise, and $\frac{D}{L}$ is the drag-to-lift ratio for cruise conditions. Finally, the thrust levels for climb and descent were chosen and assumed to be 60% of take-off thrust and 20% of cruise thrust, respectively. That is because, for climb, the ICAO LTO cycle was expanded by another 15% reduction in take-off thrust. On the other hand, during descent, the thrust setting is close to idle in order to slow down and descend without using any additional power. The summarised values for thrust and TSFC levels are given in Table 5.2. It is important to note that the values apply only to one engine.

Table 5.2: Thrust, TSFC and total fuel mass flow per flight phase for 2000 km and 3000 km range (for one engine).

	2000 km			**3000 km**		
Phase	**T [kN]**	**TSFC**	$\dot{m}_f$ **[kg/s]**	**T [kN]**	**TSFC**	$\dot{m}_f$ **[kg/s]**
Taxiing	8.3	8.91	0.074	8.8	8.91	0.078
Take-off	119.1	5.94	0.708	125.3	5.94	0.744
Initial climb	101.2	7.20	0.729	106.5	7.20	0.767
Climb	71.5	7.20	0.515	75.2	7.20	0.541
Cruise	27.1	9.07	0.248	28.5	9.13	0.261
Descent	5.4	11.47	0.062	5.7	11.47	0.065
App.+Land.	35.7	11.47	0.410	37.6	11.47	0.431

During the iteration process, a number of assumptions were made due to limited data, as well as for the simplicity of the models. The list of all assumptions is presented in Table 5.3.

Table 5.3: Assumptions used in the fuel mixtures and masses computations

ID	**Assumption**	**Justification / source**
A-FM-01	The TSFC for taxi, climb, descent and approach & landing are interpolated or extrapolated from the values from take-off and cruise	Rough estimates for simplicity due to lack of data for better estimation
A-FM-02	The thrust-specific consumption levels are assumed to be the same for both mission profiles	Simplification for rough estimates due to data and time constraints
A-FM-03	The aircraft weight during cruise for which the required thrust is calculated is equal to 95% of take-off weight	Class II estimations
A-FM-04	The thrust levels for taxiing, initial climb and approach & landing are assumed to be the same as the ICAO LTO cycle states	ICAO LTO cycle [11]
A-FM-05	The thrust level for climb is assumed to be 60% of take-off thrust	Extension of the ICAO LTO cycle, further 15% reduction in thrust level as from take-off to climb out
A-FM-06	The thrust level for descent is assumed to be 20% of cruise thrust	Near-idle thrust conditions, slowing down is efficient at minimum power setting

5.2.4. Final Values

The results of the iteration process are presented in Table 5.4 and Table 5.5 for 2000 km and 3000 km missions, respectively. It is important to note that the results are for one engine. The hydrogen mass ratios (H2_mf) have their corresponding hydrogen energy ratio (H2_ef), i.e. what fraction of energy is extracted from hydrogen fuel (Figure 5.1a and Figure 5.1b). The tables also present calculated mass flow rates, namely total fuel mass flow ($\dot{m}_f$), hydrogen mass flow ($\dot{m}_{H2}$) and kerosene mass flow ($\dot{m}_{H2}$). Finally, for each phase, the total fuel consumed is calculated with distinction for hydrogen and kerosene.

Table 5.4: Results for the iteration process for hydrogen mass and energy fractions, mass flows, and fuel combusted (one engine, 2000 km mission).

Phase	H2_mf [%]	H2_ef [%]	$\dot{m}_f$ [kg/s]	$\dot{m}_{H2}$ [kg/s]	$\dot{m}_K$ [kg/s]	Fuel burnt [kg]	H2 mass [kg]	Kero mass [kg]
Taxiing	50	74	0.074	0.037	0.037	115.9	58.0	58.0
Take-off	24	47	0.708	0.170	0.538	29.7	7.1	22.6
Initial climb	24	47	0.729	0.175	0.554	96.2	23.1	73.1
Climb	25	48	0.515	0.129	0.386	617.5	154.4	463.1
Cruise	43	68	0.248	0.107	0.141	1255.5	539.9	715.6
Descent	33	58	0.062	0.021	0.042	74.6	24.6	50.0
App.+Land.	31	56	0.410	0.127	0.283	98.4	30.5	67.9
Total						2287.8	837.5	1450.3

Table 5.5: Results for the iteration process for hydrogen mass and energy fractions, mass flows, and fuel combusted (one engine, 3000 km mission).

Phase	H2_mf [%]	H2_ef [%]	$\dot{m}_f$ [kg/s]	$\dot{m}_{H2}$ [kg/s]	$\dot{m}_K$ [kg/s]	Fuel burnt [kg]	H2 mass [kg]	Kero mass [kg]
Taxiing	50	74	0.078	0.039	0.039	121.9	61.0	61.0
Take-off	14	31	0.744	0.104	0.640	31.3	4.4	26.9
Initial climb	17	36	0.767	0.130	0.637	101.2	17.2	84.0
Climb	18	38	0.541	0.097	0.444	649.6	116.9	532.7
Cruise	24	47	0.261	0.063	0.198	2493.0	598.3	1894.7
Descent	21	43	0.065	0.014	0.052	78.5	16.5	62.0
App.+Land.	19	40	0.431	0.082	0.349	103.5	19.7	83.8
Total						3579.0	833.9	2745.0

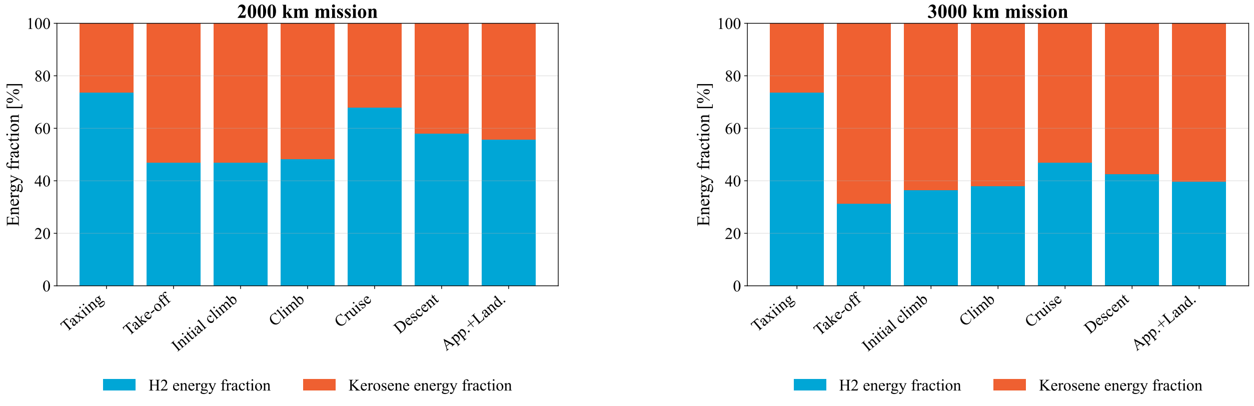

(a) Energy fractions for 2000 km mission.

(b) Energy fractions for 3000 km mission.

Figure 5.1: Energy fractions for both the 2000 km and 3000 km missions.

For the 2000 km mission profile, the more power-demanding flight phases have lower hydrogen energy fractions, hence more power comes from kerosene. Contrastingly, phases such as taxi (lower thrust level, high duration) or cruise (stable conditions, relatively low thrust, long duration) have larger hydrogen energy fractions, confirming consistency with the combustion strategy mentioned earlier. The further adjustment of hydrogen ratios between iterations, besides emissions, was driven by the amount of required kerosene. This is because, for the design mission profile (2000 km), a reduction of CO_2 is the mission requirement. CO_2 emissions depend only on the amount of kerosene burnt, which means a certain amount of kerosene is the maximum. In this case, to achieve exactly a 50% reduction, this is 2912.6 kg of kerosene per mission, so to 1456.3 kg per engine.

However, for the 3000km mission, the adjustment of fuel mixture ratios was mainly driven by the amount of hydrogen calculated for the 2000km mission, since that is the design mission profile and the hydrogen tank is sized for it. The adjustment process for this mission is then opposite to the 2000km mission. The constraint is the hydrogen mass, and the rest of the fuel necessary for this mission profile is taken as kerosene fuel.

Based on the final hydrogen mass ratios, the Fuel Heating Value (FHV) is derived for both take-off and cruise conditions. These values are then used in GasTurb, with the LEAP-1A taken as the reference engine. To limit redesign complexity and ease the certification process, the bypass ratio, component efficiencies, and rotational speeds are kept equal to the reference engine values. The main engine model inputs are summarised in Figure 5.6. The stations of the engine, together with an overview of the bleeding system, are indicated in Figure 5.2, obtained from GasTurb software.

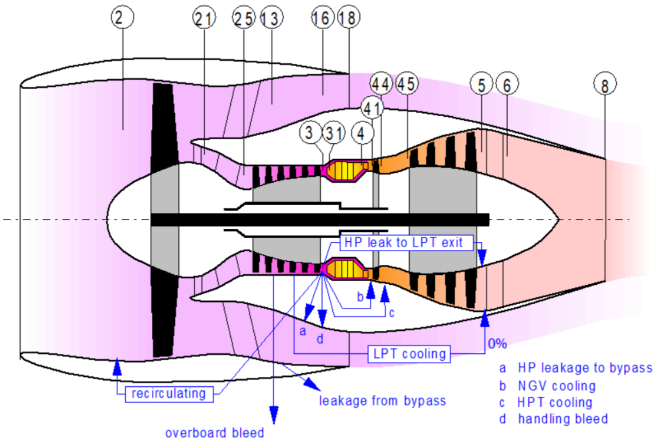

Figure 5.2: Engine stations and bleeding layout overview.

Table 5.6: Engine model input parameters.

Input parameter	**Value**
Intake pressure ratio	0.99
Core pressure loss option	0
Inner fan pressure ratio	2.2
Outer fan pressure ratio	1.6
Compressor interduct pressure ratio	0.99
HP compressor pressure ratio	19.5
Bypass duct pressure ratio	0.98
Turbine interduct pressure ratio	0.98
Design bypass ratio	11
Burner design efficiency	0.9995
Burner part-load constant	1.6
Overboard bleed	0 kg/s
Power offtake	50 kW
HP spool mechanical efficiency	0.99
LP spool mechanical efficiency	1.00
Burner pressure ratio	0.95
Turbine exit duct pressure ratio	0.98

The FHV inputs are 61.5 for take-off and 76.1 for cruise. The corresponding burner exit temperatures are 1885 K and 1864 K, respectively. The resulting engine performance and pressure values are presented in Table 5.7

Table 5.7: Engine performance and station conditions at cruise and take-off.

Parameter	**Station**	**Cruise**			**Take-off**		
		W **[kg/s]**	T **[K]**	P **[kPa]**	W **[kg/s]**	T **[K]**	P **[kPa]**
Net thrust, F_N	–	34.25 kN			159.14 kN		
TSFC	–	9.0733 g/(kN s)			5.9470 g/(kN s)		
Inlet	2	221.089	245.02	35.616	574.200	288.15	100.312
Compressor entry	25	18.424	314.62	78.356	47.850	369.72	220.686
Compressor exit	3	18.424	762.15	1527.943	47.850	883.71	4303.374
Turbine entry	4	17.445	1864.00	1451.546	45.447	1885.00	4088.205
Turbine exit	5	17.814	1028.33	78.988	46.404	914.65	115.394
Core nozzle	8	17.814	1028.33	77.408	46.404	914.65	113.086
Bypass nozzle	18	202.665	284.21	55.795	526.350	334.06	157.144

5.3. Combustion Chamber Design

The purpose of the CC is to accommodate the chemical reactions that increase the thermal energy of the gas flowing through it [26]. This section aims to propose a combustion chamber that effectively extracts thermal energy from both fuels (hydrogen and kerosene), providing the required thrust in each flight phase while minimising the resulting emissions. This is done in conjunction with the injector, which sets up the flow field at the combustor's inlet.

5.3.1. Design Driver: Emissions

The CC must achieve near-complete combustion while minimising emissions. Hence, the design of the dual-fuel combustion chamber aims to strike this balance. The most important CC emissions to consider are nitrogen oxides NO_x (i.e. NO and NO_2), carbon dioxide CO_2 , carbon monoxide CO, Unburnt Hydrocarbons (UHC), soot, and sulphur oxides. NO_x is the single most important emission arising from hydrogen combustion, and is highly notable for kerosene combustion [27]. NO_x mostly formed through a thermal mechanism in the post-flame region at >1800 K, where atmospheric nitrogen and oxygen react to form NO exponentially with increasing temperature [28]. In both hydrogen and kerosene combustion in gas turbine conditions, the NNH mechanism is also highly relevant. It takes place at the beginning of the flame zone, in regions where hydrogen radical concentration is high, in the fuel-rich zone [29]. Another mechanism of NO formation, much less prevalent in gas turbines, is through reaction of dinitrogen with hydrocarbon radicals [28].

The rest of the notable emissions are formed by the combustion of hydrocarbons, i.e. kerosene. Carbon dioxide is formed from the complete combustion of carbon, while CO is formed through incomplete combustion. This takes place either when operating fuel-rich or at low power when the temperature and pressure at the inlet are low during lean combustion. Incomplete combustion, poor atomisation, and low reaction rates give rise to UHCs. Soot is produced in regions where fuel is rich or mixing is poor [28]. As a result, by extracting higher fractions of energy from hydrogen, it is expected that all but the nitrogen oxide emissions will decrease. Additional methods must be devised to manage the latter.

5.3.2. Design Driver: Hydrogen Concerns

Introducing hydrogen into fuel raises additional concerns apart from increased NO_x emissions. This can be seen from the differences in properties of hydrogen and kerosene (Jet-A) contrasted in Table 5.8. Firstly, a core difference is in the injection states of kerosene and hydrogen. Hydrogen is injected in a gaseous/supercritical state (elaborated upon in Subsection 5.4.2), while kerosene is atomised as a liquid. Hydrogen's higher LHV reflects its viable potential as a combustion fuel, and its low boiling point its particular conditions for storage. Hydrogen has a high diffusion velocity, which has a strong impact on the mixing process [30], encouraging more complete combustion [31]: the stark ten-fold difference in diffusion velocity may provide significant advantages.

Table 5.8: Fuel properties of hydrogen and kerosene (Jet-A) at Normal Temperature and Pressure (NTP) [13].

Property	H_2	Jet-A
LHV ($kJ\,g^{-1}$)	119.96	42.8
Boiling point at 1 atm (K)	20.27	440–539
Diffusion velocity in air ($m\,s^{-1}$)	2.00	<0.17
Flammability limits in air (% vol)	4.0–75.0	0.6–4.7
Autoignition temperature (K)	858	>500
Burning velocity in air ($cm\,s^{-1}$)	265–325	18–38
Adiabatic flame temp. at ϕ=1 (K)	2318	2200

Hydrogen is also significantly more flammable. It burns at a wide range of volume fractions in air, which allows leaner burning without blowing out; its Lean Blowout (LBO) limit is lower. This means its equivalence ratio ϕ, defined as $\phi = f/f_{st}$, with $f = \dot{m}_f/\dot{m}_a$ [32], is low, as the ratio f of its fuel to air mass flow is higher than the stoichiometric. As discussed in Subsection 5.3.1, this provides opportunities for reducing NO_x, CO, UHC and soot emissions. The wider flammability limits also make relight at altitude more achievable. However, this also means that flames in accidental hydrogen-air mixtures could be sustained in a wide range of fuel-to-air mixtures, requiring significantly higher dilution than standard hydrocarbon fuels to no longer be able to sustain flaming.

Its autoignition temperature is also significantly higher than that of kerosene, hence raising concerns of flashback, where burning would happen outside the combustion chamber for which it was designed. This is further emphasised by its significantly higher burning velocity, meaning the flame propagates faster. This is an explicit concern that must be addressed when introducing hydrogen. Finally, its adiabatic flame temperature, or the maximum temperature achieved from its combustion, is 118K higher. It indicates that the combustion chamber must be cooled effectively, or materials withstanding higher temperatures must be used.

5.3.3. Combustion Method

A range of combustion chamber architectures are available which efficiently provide the required thermal energy while minimising emissions. An important initial design choice is the arrangement of the liner (that holds the flame) and casing (that keeps the pressure). The "annular" combustor is standard in jet engines and chosen for the design. It wraps its liner and casing concentrically with the shaft axis, minimising pressure loss and needing less cooling air, thus allowing higher-temperature combustion than its alternatives [33]. This choice is especially valid with the inclusion of hydrogen, a fuel with a higher flame temperature at any equivalence ratio [34].

More crucially, a wide variety of combustion strategies exists. Given the requirement for simultaneous kerosene-hydrogen combustion and the intended introduction around 2040, only combustion strategies with sufficient technological maturity are considered. They must either be fully proven in kerosene-fuelled engines, i.e. have a Technology Readiness Level (TRL) of 9, or be under active development with strong potential benefits for kerosene-hydrogen operation with at least TRL 7. To limit the scope, combustion strategies which significantly increase size, weight or complexity, such as axially-staged or variable-geometry combustion, are excluded. Three viable combustion methods are then considered: Rich-Burn Quick-quench Lean-burn (RQL), Twin Annular Premixing Swirler (TAPS), and Lean Direct Injection (LDI). All three are combustion strategies that aim to produce a stable flame while minimising NO_x emissions.

RQL begins with a fuel-rich mixture in its primary region. This stabilises the flame and minimises NO_x due to low temperatures and oxygen concentrations. Yet the incomplete combustion has high CO, UHCs and soot. This is mitigated by a quench section, which adds and quickly mixes sufficient airflow such that there is no flame or combustion at a low equivalence ratio. Since NO_x formation peaks near $\phi = 1$, a quick transition from high to low equivalence ratio significantly limits NO_x formation. Further dilution creates a lean zone, ensuring more complete combustion, reducing CO, UHC and soot [28]. This strategy has been experimentally studied for hydrogen combustion, which found reductions in NO at increased dilution air velocity [35].

TAPS involves partially premixed combustion, staged in concentric pilot and main stages. Only the pilot stage operates at low power settings, which atomises liquid fuels and mixes these with swirling air to ensure a stable flame is created through a recirculation zone. At high power settings, the main stage is additionally activated, which features a premixing stage where liquid fuel jets mix with swirling air. As the pilot and main stages mix, the flame stabilises as a recirculation zone is created. This allows for lean combustion in the primary zone and beyond, limiting temperatures for NO_x prevention and favouring complete combustion while preventing blowout through the injector architecture [28, 36]. A similar partially premixed swirl-stabilised combustor has been studied for dual-fuel hydrogen-kerosene combustion, which was sustained and its emissions studied for the full range of hydrogen-kerosene fuel mixtures [34].

LDI has a similar strategy to TAPS since it features concentric pilot and main stages, with strong axial swirlers on the latter. However, instead of premixing the fuel, it is directly injected into the combustion zone, preventing auto-ignition and flashback. This technology has been demonstrated in its relevant environment but not fully proven in its operational environment [28, 37]. The approach has been tested with hydrogen fuel, where stable operation was achieved with no flashback or autoignition encountered [38].

The **TAPS combustion strategy has been chosen**; a TAPS-like combustor (as is used on the base LEAP-1A engine) must hence be modified for injection and burning of a hydrogen-kerosene blend and addressing the concerns raised in Subsection 5.3.2. The chosen combustion strategy a mature technology that has been proven in its operational environment for kerosene (with TRL 9). It involves enhanced premixing of the fuel, hence reducing local hot spots, effectively stabilising the flame with a recirculation zone while limiting burning temperatures, helping reduce NO_x emissions. This is critical, as hydrogen burns hotter and can hence promote the thermal NO_x formation pathway more than kerosene. The benefits of LDI can still be achieved with a TAPS strategy through a specialised injector design that prevents flashback and autoignition. Additionally, TAPS' strategy of partially premixing fuel improves stabilisation and favours more complete combustion.

To assess the dual-fuel burning properties of the TAPS-like combustor at the mixture ratios defined in Section 5.2, a simplified model is simulated in Subsection 8.1.1. This model yields estimates of the Turbine Inlet Temperature (TIT). This temperature must not exceed that of the base engine, the LEAP-1A, due to material and cooling limitations. The cruise TIT for the base engine is estimated to be 1970 K [39], while that estimated by the model for this flight phase is 1864K for a 2000 km mission (Table 8.2) and 1734 K for a 3000 km mission (Table 8.3). These are lower than the presumed allowable TIT and hence require no additional considerations at this design stage. It is, however, advised that this is revisited with a more accurate model of the combustion characteristics and hence a clearer view of the combustion chamber and the required cooling and dimensions. The temperature profile within the combustion chamber should also be verified. Considerations with respect to other areas critical to the performance of the CC, especially with areas critical to hydrogen, are addressed through the design of the injector.

5.4. Injector Design

To ensure a hydrogen and kerosene fuel blend at the operating conditions of the engine is feasible, more attention is given to the design of the fuel injector. The injector design must address four key hydrogen challenges identified previously: flashback, premature autoignition, increased NO_x formation, and the distinct mixing behaviour resulting from hydrogen's high diffusivity and flame speed. A preliminary quantification of NO_x emissions is also provided, as these are closely related to the type and quality of injection. This section deals with the full injector design process, while the emission assessment is performed in Chapter 8.

5.4.1. Assumptions

In this subsection, the main assumptions used to develop the preliminary injector design model are presented. The injector is evaluated using simplified analytical and empirical correlations, hence these assumptions define the scope of the model and clarify which effects are included in the preliminary design stage.

Table 5.9: Assumptions used in the injector design methodology

ID	Assumption	Justification / source
A-IN-01	Sn is based on injector geometry, not CFD results or measured velocity profiles.	[40].
A-IN-02	Both air and kerosene Sn are estimated using a geometric Sn formula.	[40].
A-IN-03	Increasing the axial air fraction reduces the effective air Sn.	Axial air is assumed not to contribute to tangential momentum.
A-IN-04	A factor of 0.7 is applied to the effective flow area as an empirical correction for blockage and discharge effects.	[41].
A-IN-05	The effective total Sn is assumed to be the simple average of the air and kerosene Sn.	Preliminary model simplification; a higher-fidelity model would use momentum or angular-momentum weighting.

ID	Assumption	Justification / source
A-IN-06	The spray cone angle is estimated using a linear relation with the effective Sn.	Empirical simplification [40].
A-IN-07	Central recirculation is assumed to be established when the effective $Sn > 0.6$.	Swirl-stabilised flames rely on recirculation zones for flame stabilisation [40].
A-IN-08	The droplet-size distribution is assumed to follow a Rosin-Rammler distribution.	[41].
A-IN-09	Jet penetration is estimated using a simplified jet-in-crossflow relation based on the momentum flux ratio.	Jet penetration is governed primarily by momentum flux ratio in preliminary combustor jet models [41].
A-IN-10	Hydrogen and kerosene momentum flux ratios are combined additively.	Preliminary dual-fuel modelling simplification; needs validation with higher-fidelity mixing analysis.
A-IN-11	Kerosene atomisation is modelled using empirical SMD correlations.	[41]
A-IN-12	Combustion stability is only checked against the weak/lean blowout boundary.	Lefebvre-Ballal lean blowout correlation provides the weak boundary; rich boundary needs experimental data [41].
A-IN-13	The injector uses a staged TAPS-like architecture with a pilot zone and an outer main stage.	Improves operability and emissions over the operating range [36].

5.4.2. Selected Design

The design was selected based on a dual-fuel concept able to operate with both hydrogen and kerosene/SAF as main fuels, as well as a mixture of both. This subsection discusses the selected design, shown in Figure 5.3.

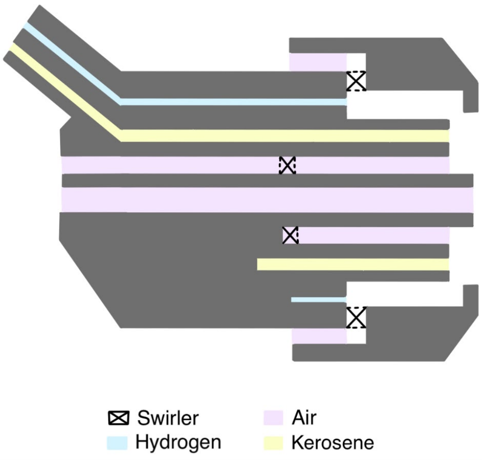

Figure 5.3: Sketch of the selected injector design.

The hydrogen is already vaporised before reaching the injector, because, in the selected fuel system, liquid hydrogen is stored cryogenically in the aircraft tanks but is converted into a gaseous/supercritical state. Hydrogen must be injected within a particular temperature range as it is partially premixed with air, as is done per Figure 5.3. Injector temperature T_{inj} must be higher than 150 K due to the risk of icing of the water in the air and flame stability limits. It must also be lower than 673 K due to the hydrogen auto-ignition temperature (approx. 823 K) and stability limits of the flame due to hydrogen-air interactions [42, 43]. At these temperatures, hydrogen can only exist in gaseous or supercritical form and must be preconditioned. Since the kerosene is injected as an atomised liquid, hydrogen and kerosene paths are kept separate to allow each fuel to be treated according to its state and behaviour [41, 44].

The design includes two air swirlers to generate recirculation of the air, mixing, and flame stabilisation in the primary zone of the combustion chamber [40, 41]. The swirling brings hot combustion products back towards the incoming reactants to support stable combustion [41]. At the same time, hydrogen is partially premixed with air before entering the combustor and injected through small orifices to improve the distribution of hydrogen and reduce the formation of highly fuel-rich regions [44–46].

A fully premixed hydrogen-air system was discarded due to the high flame velocity of hydrogen, making hydrogen flames more prone to **flashback**. For this reason, the design also includes an axial stream of air through the centre of the injector, with the intention to avoid any flashback risk

[41, 44, 47]. The kerosene atomiser is placed around the axial air stream, where it injects kerosene through small, partly tangential passages to generate a swirling hollow-cone spray. The surrounding high-speed air then assists the breakup of the liquid sheet into small droplets, improving evaporation and mixing before combustion.

An additional feature of the selected design is the use of a main hydrogen injection stage around the pilot injector. The pilot injector provides the initial **flame stabilisation**, while additional gaseous hydrogen is injected through outer orifices with an additional air swirler [45, 46]. The outer hydrogen stream is the main combustion stage, allowing the combustor to operate under leaner conditions. By distributing the hydrogen over a larger annular region and mixing it with swirling air before combustion, the local fuel concentration is reduced, and the flame can burn with a lower overall equivalence ratio [44]. Lean combustion helps limit the **flame temperature**, reducing NO_x formation [47]. The pilot stage maintains flame stability, while the outer main stage provides most of the heat release during normal operation.

Overall, the selected design combines separated hydrogen and kerosene injection paths with swirl-stabilised combustion. The key qualitative features are Gaseous Hydrogen (GH_2) injection through multiple small orifices, partial hydrogen-air premixing, liquid kerosene atomisation, two air swirlers for mixing and flame stabilisation, and a central axial air stream to reduce flashback risk.

Compared to a conventional kerosene injector, the MAVERICK design accommodates both liquid fuel atomisation and GH_2 injection. This means two separate design paths are needed, one for each fuel, leading to a more complex architecture [44]. Also, it adds additional hydrogen during the main combustion stage, which is done using generic fuel in conventional injectors. Finally, the main difference is the additional axial airstream at the centre of the injector to prevent flashback, while atomising kerosene around this centre point.

5.4.3. Method

To determine the geometry of the selected design, the injector was evaluated using a simplified correlation-based model. This model includes geometric swirl calculations, air and fuel velocity estimates, atomisation correlations, and momentum penetration estimates. The model aims to size and evaluate the injector geometry by estimating air-flow distribution, pressure drop, swirl strength, hydrogen penetration, kerosene droplet size, and off-design behaviour. The flow of this model is shown in Figure 5.4.

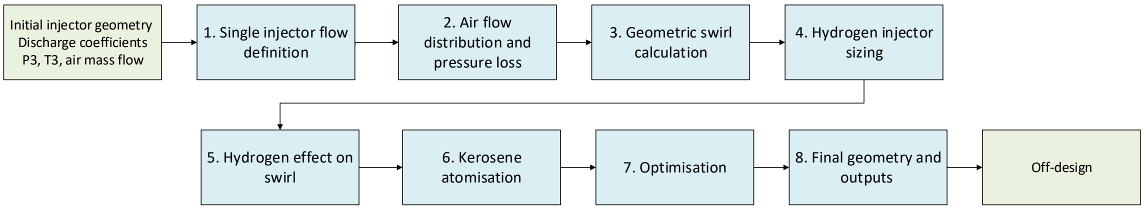

Figure 5.4: Injector evaluation model workflow, from initial geometry and flow properties to off-design evaluation.

First, input values are extracted from Cantera and GasTurb and input into the injector model. In block 1, the flow is divided into several burners to evaluate the geometry for a single injector. Then, in block 2, the geometric areas of the different air passages are multiplied by their discharge coefficients to obtain the effective areas, and the air mass flow is distributed between the passages [41]. The total effective area is also used to estimate the pressure loss across the injector [48].

In block 3, Sn is then calculated for each swirler, using an annular geometric swirl relation for the pilot axial swirler and simplified radial swirler relations for the pilot and main radial swirlers [40, 41]. These Sn are combined using a mass-flow-weighted average to obtain the overall Sn. Then, in block 4, the hydrogen flow is split 30% and 70% between the pilot and main stages, respectively [45, 46]. The hydrogen feed pressure is set to 1.3 times the combustor inlet pressure to provide an injection margin, and the model then calculates hydrogen density, orifice area, jet velocity, and jet penetration [43]. Different combinations of orifice number, orifice diameter, and mixing height are swept until the target penetration is achieved while satisfying the residence-time constraint of 0.028 ms, explained in Subsection 5.4.4.

The hydrogen jets partially block the local air-flow area and add momentum to the flow. These effects are calculated in block 5 through blockage and momentum penalties, which reduce the radial swirl contribution and give the corrected effective Sn. The kerosene atomisation performance is then evaluated in block 6, using Lefebvre-type airblast atomisation correlations [41, 47]. The Sauter Mean Diameter is calculated separately for the pilot and main stages, and the final kerosene droplet size is represented using a mass-flow-weighted harmonic average. Finally, the optimisation in block 7 combines these previous calculations, adjusting the hydrogen hardware to meet the target penetration and varying the swirler vane angles to obtain an acceptable effective Sn while minimising Sauter Mean Diameter (SMD). Once a suitable geometry is selected, the injector is checked at off-design operating points to verify the quality remains acceptable outside the design point.

5.4.4. Results

To get a better understanding of the geometric properties of the injector, a visualisation has been created to see the effects of changing geometry on the Sn and SMD. A number of these visualisation plots are shown in Figure 5.5 and Figure 5.6.

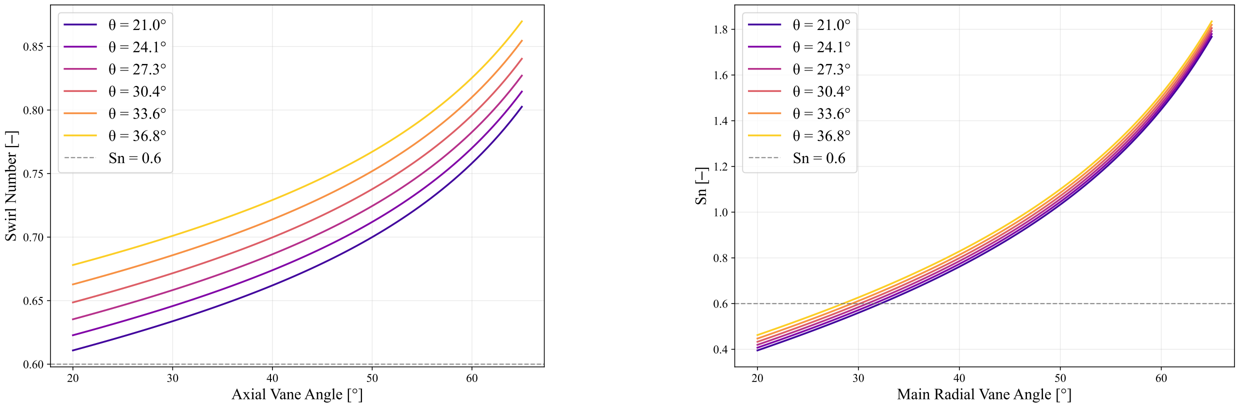

(a) Sn for varying axial and pilot radial vane angle.

(b) Sn for varying pilot and main radial vane angle/

Figure 5.5: Effect of changing geometric parameters on Sn

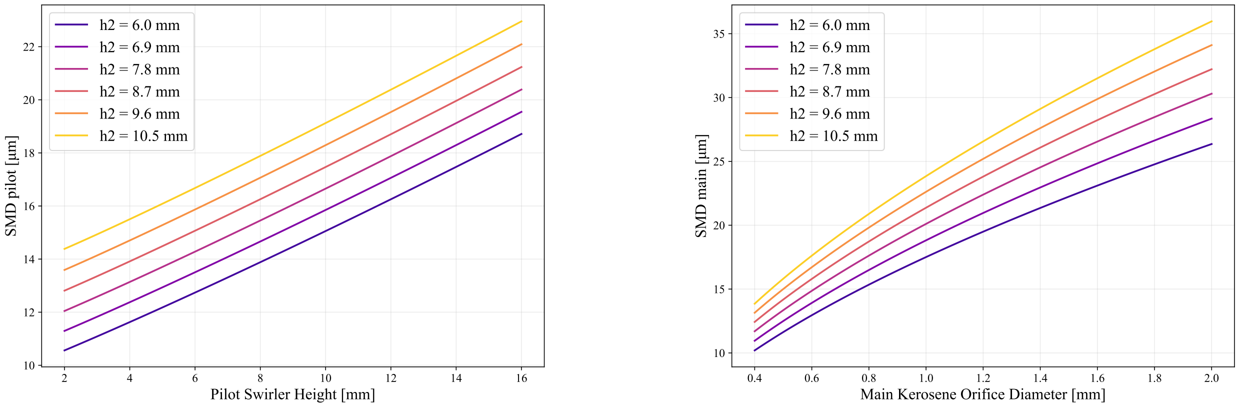

(a) SMD for varying pilot and main swirler heights.

(b) SMD for varying main swirler height and orifice diameter

Figure 5.6: Effect of changing geometric parameters on SMD

The distribution of air through the main and pilot mixers is taken to be 70% and 30%, respectively, similar to the split in the GEnx TAPS engine [28]. The hydrogen passages are designed to achieve sufficient jet penetration for mixing, while preventing the risk of auto-ignition. This risk occurs if the residence time of a premixed fuel is too high. For a kerosene TAPS injector, the residence time that can pose a risk for auto-ignition can be as low as 1 ms [28]. However, due to the introduction of hydrogen in the combustion chamber, the laminar flame speed increases and the residence time decreases even more. At an equivalence ratio of 0.6 and a pressure of 20 atmospheres, the propagation flame speed can be increased by a factor of approximately 25 when transitioning to pure hydrogen fuel [49]. As our richest equivalence ratio is 0.5 and P_3 40 atmospheres, as calculated in Subsection 5.2.4, this factor is doubled, which is a worst-case scenario. As can be seen in Figure 5.7, increasing the pressure by a factor of 5 doubles the flame speed factor. As the pressure for the MAVERICK combustion chamber is increased by a factor of 2 from the 20 atmospheres shown in Figure 5.7, the flame speed factor is increased by a factor of 1.4 from 25, resulting in a final flame speed that is 35 times higher than pure kerosene. This means the residence time has to be decreased from 1 ms down to 0.028 ms. Including a safety factor as this result is obtained using data on methane fuels, the residence time limit is set to 0.02 ms.

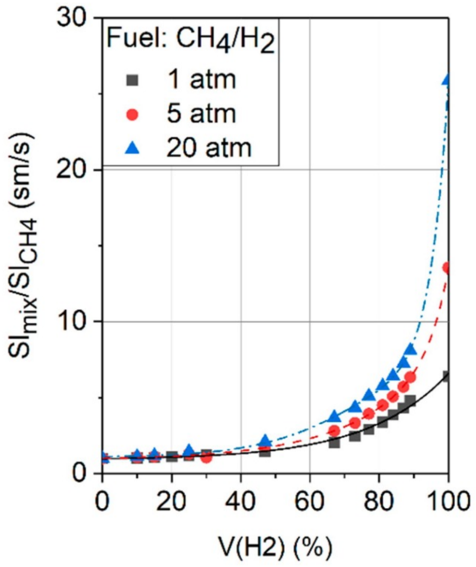

Figure 5.7: Relationship between the propagation laminar flame speed of methane and hydrogen mixture and the volume concentration of hydrogen. As this is not a one-to-one match with kerosene, these findings should be used with caution and a safety factor. ϕ = 0.6, close to the MAVERICK design point [49].

To ensure prevention of auto-ignition, this residence time is calculated using $\tau_{res} = \frac{l}{v}$, where l is the length of the premixing chamber and v is the hydrogen jet velocity. By adjusting the premixing chamber lengths and orifice diameters, both l and v can be controlled to prevent the auto-ignition risk threshold of 0.02 ms. The injector is designed using cruise and climb conditions, as these are the main contributors to the Landing to Take-Off (LTO) cycle and overall NO_x emissions. The design is optimised to minimise these emissions by reducing the SMD as much as possible and decreasing the Central Recirculation Zone (CRZ). The actual effects of these metrics are discussed along with the in-flight emissions in Chapter 8. Additionally, the swirl number is bounded to make sure recirculation is achieved and flashback is prevented. The hydrogen pressure is selected such that it is 30% more than P_3, and the minimum temperature is selected to be 150 K [43].

The hydrogen injection reduces the Sn of both the pilot and the main swirlers, as it is injected perpendicular to the swirling air and thus reduces the swirl. This thus requires tuning of the swirler vanes. Increasing the angle creates a larger Sn, as can be seen in Figure 5.5, which increases the recirculation zone and provides a more stable flame, but also increases the risk of flashback. Following the method described in Subsection 5.4.3, applying these constraints results in the injector geometry shown in Figure 5.8 and Table 5.10.

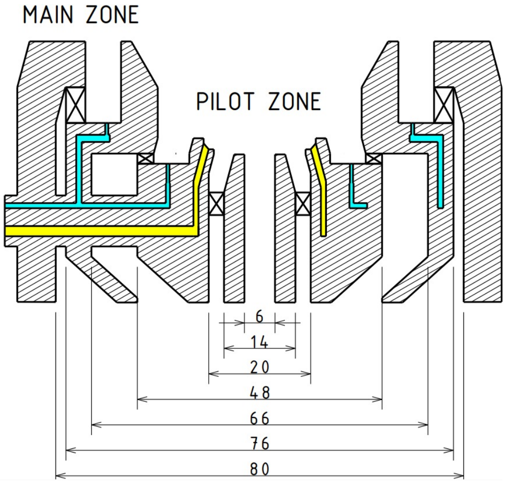

Figure 5.8: Fuel injector cross-section, with swirlers indicated by X, kerosene with yellow, and hydrogen with blue. All dimensions are in mm. The air enters from the underside and is then split into the pilot and main zones. Both fuel types are fed through the fuel feed system and enter from the left of the cross-section.

Table 5.10: Injector geometric properties.

Dimension	Pilot radial	Main swirler
Swirler height [mm]	2	7
Premixing height [mm]	5	16
N H_2 orifices [-]	6	4
H_2 orifice diameter [mm]	0.6	0.6
Vane angle [deg]	20	28
Pilot axial vane angle [deg]	60	

This injector provides a stable flame with low NO_x emissions, which will be quantified in Section 8.1. The stability is governed by the Sn, which is 0.612 at cruise, but varies throughout the flight. This analysis is discussed in Subsection 5.4.5, which also deals with the varying SMD.

5.4.5. Off-Design

As the injector is a fixed component, varying the environmental parameters will affect its performance. To ensure the injector maintains a stable flame and good atomisation throughout the entire flight envelope, an off-design analysis is performed. The injector is evaluated at all different flight phases, using input data from Subsection 5.2.4, while varying the air and fuel mass flow at every flight phase to create a clear envelope. For take-off and cruise, this results in the design space shown in Figure 5.9a and Figure 5.9b. These phases are selected as they are designed in more detail using the GasTurb software in Table 5.7.

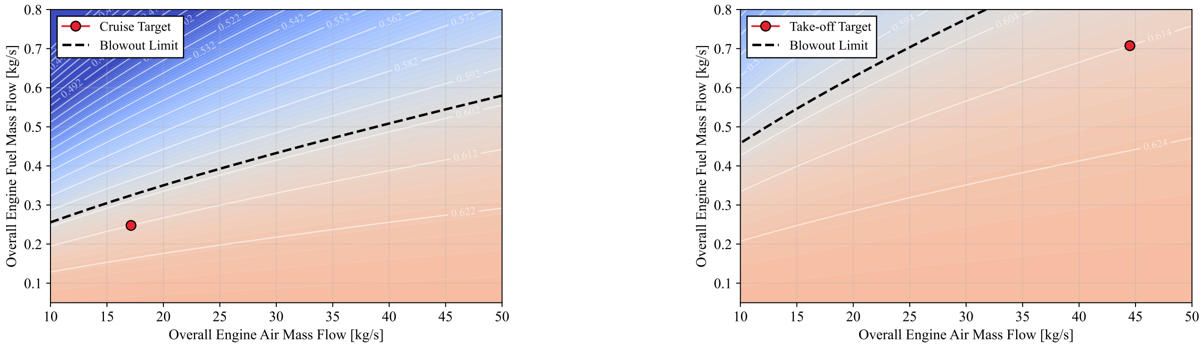

(a) Sn for varying air and fuel mass flows at a hydrogen mass fraction of 43%. The cruise design point is indicated with a Sn of 0.612

(b) Sn for varying air and fuel mass flows at a hydrogen mass fraction of 24%. The take-off design point is indicated with a Sn of 0.614

Figure 5.9: Operating envelope for cruise and take-off.

From these figures, it is clear that for both cruise and take-off, the operating envelope is quite large. The operating envelope is the space where a Sn is kept above 0.6. Flying below this Sn will create an unstable flame and could cause engine shutdown. For cruise, the blowout limit is more present due to the larger fraction of hydrogen in this scenario, which, as discussed in Subsection 5.4.4, reduces the Sn and thus the CRZ. This reduces the flame stability. However, the blowout limit would also change as this is currently determined for a kerosene fuel blend. Additional research is required to determine the flame stability of the injector for full hydrogen operation. For both the case where only kerosene will be used as fuel and only hydrogen as fuel, these envelopes are also evaluated, and the full hydrogen envelope is visualised in Figure 5.10. The full kerosene envelope is not shown, as only the hydrogen mass flow has an effect on the Sn, rendering the full kerosene envelope almost stationary at Sn around 0.631.

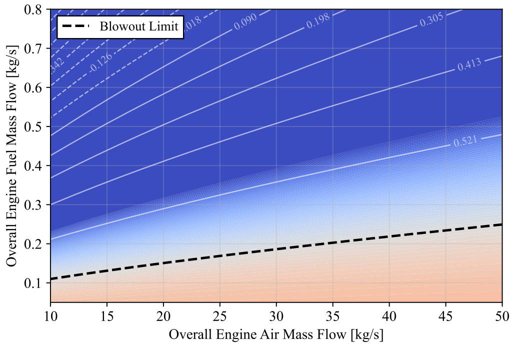

Figure 5.10: Operating envelope for full hydrogen fuel mixture.

Table 5.11: Sn for each flight phase. A Sn larger than 0.6 indicates stable combustion.

Phase	Sn
Taxiing	0.626
Take-off	0.614
Initial climb	0.613
Climb	0.617
Cruise	0.612
Descent	0.629
App.+Land.	0.614

From Table 5.11 it is clear that the Sn stays just above the stability limit for all flight phases, minimising the flashback risk while maintaining a stable CRZ and thus flame. As for the full hydrogen operation, the operating envelope is much smaller. A design point for this phase is not specified as this was not evaluated in detail, but careful consideration would have to be taken with respect to the blowout limit.

6

Tank Design

This chapter develops the design of the dual-fuel tank system. Section 6.1 selects the placement of the hydrogen and kerosene tanks within the airframe. Section 6.2 sets the insulation approach for the cryogenic hydrogen tank. Section 6.3 selects the shell materials and sizes the tank walls from first principles to find the empty tank mass. Section 6.4 models the in-flight centre-of-gravity migration and the fuel-transfer controller that holds the centre of gravity on station.

6.1. Tank Layout

The tank layout was chosen from different options and has an aft hydrogen tank behind the pressure bulkhead, a forward kerosene tank to control the CG shift across the mission, and kerosene tanks in the wings. This option provides the large aft volume the cryogenic tank needs without splitting the hydrogen storage (one of the studied options had both a forward and an aft LH_2 tank) and keeps the tank clear of the main heat sources while remaining behind protective structures.

Another option was to have two external hydrogen tanks on top of each wing, but this would introduce weight and drag penalties, increasing energy use by 32% per passenger-kilometre [50].

The tank is placed behind the cabin, behind the pressure bulk, in the tail cone. As such, the fuselage section where the LH_2 tank is placed is not pressurised, and thus the skin does not need to be made out of a single part in order to sustain hoop stress. There is a top panel that can be removed, allowing the hydrogen tank to be removed for maintenance as further explained in Subsection 11.2.1. Smaller access doors allow for easy external tank inspection.

6.2. Tank Insulation

MAVERICK uses vacuum-shelled Multi-Layer Insulation (MLI) for the LH_2 tank. MLI under vacuum has the lowest density and thermal conductivity among common cryogenic insulation materials such as perlite and aerogels [51]. The NASA Glenn state-of-the-art review of LH_2 tank structures for aircraft identifies a high vacuum with polished wall surfaces, with or without MLI, as the approach capable of meeting the insulation needs of lightweight long-term cryogenic applications, with MLI adding further reduction of radiation heat transfer beyond a bare vacuum shell. The same review positions foam-based insulation as possibly suited only to short-duration use, or as a supplementary system for longer durations [52]. A vacuum-shelled construction with MLI therefore follows from the established approach for sustained low boil-off LH_2 storage, and is adopted without a separate weighted trade-off.

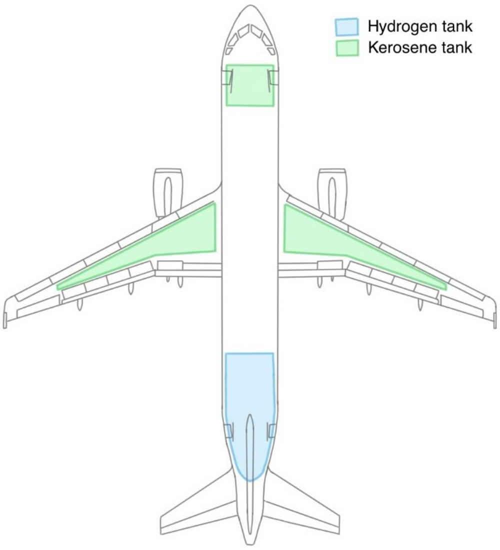

Figure 6.1: Selected dual-fuel tank layout.

The governing limitation is vacuum integrity. A vacuum shell with polished surfaces and a vacuum with MLI system have similar insulating properties and both are critically sensitive to the vacuum level. Any degradation significantly reduces the insulating performance, so the dominant reliability concern is the outer shell and the maintenance of vacuum rather than the insulation material [52]. For the design of the tank a thermal conductivity of $10^{-4}\,\mathrm{W\,m^{-1}\,K^{-1}}$ and density of $40\,\mathrm{kg\,m^{-3}}$[52, 53].

6.3. Tank Materials and Structures

In this section, material will first be selected for both the inner and outer shell, then the structure will be constructed to calculate the final mass to validate the gravimetric efficiency assumption made.

6.3.1. Tank Materials

The cryogenic tank consists of two main structural elements. An outer shell that resists the external pressure, and an inner shell that resists internal pressure. There are different material constraints for these two components. The outer shell will not operate at cryogenic temperatures, while the inner shell shall be able to do so. From analysis, the primary failure modes are also different for these two structures. For the outer shell, the primary failure mode is buckling due to the external pressure. For the inner shell, the primary failure mode is material yielding due to excessive hoop stress from internal pressure.

For the inner shell, three materials are considered: 316L stainless steel, 2195 aluminium-lithium, and 2219 aluminium-copper. They were chosen due to their industry precedent in cryogenics[54].

316L stainless steel is the established default for cryogenic and hydrogen service, valued for its toughness at low temperature and its resistance to hydrogen embrittlement, and it is in routine use in liquid-hydrogen ground systems, feed lines, and pressure vessels[54–56]. It is excluded due to its mass penalty. Its density is roughly 2.8 times higher than that of Aluminium-2219 [56][1], which drives the design into an unfeasible design space. The alloy is well matched to the service environment but far too heavy for a flight structure.

2195 aluminium-lithium is roughly 30 % stronger and has about 5 % lower density than Al-2219, which is why it replaced 2219 on the Space Shuttle Super Lightweight Tank[55]. Among 2195,

---

[1] `https://www.thyssenkrupp-materials.co.uk/stainless-steel-316l-14404.html` (Accessed 09-06-2026)

2219, and 2014, 2195 shows the highest solidification cracking susceptibility and 2219 the lowest across all the weldability tests applied [57]. It is therefore usually joined by friction stir welding rather than by fusion welding, but the large process forces involved require heavy, purpose-built tooling and fixturing to weld full-scale tank barrels[58]. The dedicated friction stir welding facility needed for tanks of this diameter is expensive to procure and operate, and that cost is not justified at this production scale. 2195 is therefore ruled out on manufacturing cost rather than on material performance.

2219 aluminium-copper is the selected inner-shell material, as it is not susceptible to hydrogen embrittlement [59]. It retains good fracture toughness and strength at liquid-hydrogen temperatures [56], and it can be fusion welded with established procedures and standard arc-welding equipment [60], so it avoids the dedicated friction stir welding line that 2195 requires. It is denser and lower in strength than 2195, but it avoids the tooling and facility cost that disqualifies the lithium alloy while still meeting the cryogenic requirements. 2219 is selected for its performance in cryogenic temperatures and conventional manufacturability, with the accepted penalty of a higher shell mass than 2195 would give.

For the outer shell, buckling is the primary failure mode. Carbon fibre reinforced polymer (CFRP) is the natural candidate, owing to its high specific stiffness, which directly raises the critical buckling load per unit mass[61][2]. CFRP is also an established material in the aviation industry. Table 6.1 shows the material properties chosen for the tank.

Table 6.1: Material properties at operating temperature for the inner and outer shell[25, 56, 62].

Shell	**Material**	**Poisson ratio (ν)**	E **(GPa)**	σ_y **(MPa)**	**Density (kg/m^3)**
Inner shell	AA2219	0.318	85	480	2820
Outer shell	CFRP	0.316	170	2 650	1810

6.3.2. Tank Structures

The vacuum-shelled tank is sized from first principles rather than from statistical mass fractions, so that every wall thickness traces back to a specific governing failure mode. Because the tank is double-walled, the two shells carry opposite loads and are therefore sized against different criteria: the inner pressure vessel is loaded from within and limited by membrane yield, whereas the outer vacuum shell is loaded from outside by the surrounding atmosphere and fails by elastic buckling well before yield. Both shells share the same geometry (a cylindrical barrel closed by two hemispherical caps), so each criterion is applied once to the cylinder and once to the dome.

Assumptions

Table 6.2: Assumptions used in the tank wall sizing methodology

ID	**Assumption**	**Justification / source**
A-TK-01	Both shells are thin-walled ($t \ll r$), so stress is uniform through the thickness and bending is ignored. Cap-to-cylinder junction stresses are not resolved, and caps and barrels are sized independently.	Thin-shell membrane theory.
A-TK-02	The buckling and ring-inertia relations are isotropic, each using a single E and ν.	The CFRP outer shell is a quasi-isotropic laminate; a directional layup is left to a detailed laminate analysis.

---

[2] `https://www.samaterials.com/content/specific-modulus-of-engineering-materials.html` (Accessed 22/06/2026)

ID	Assumption	Justification / source
A-TK-03	The domes and stiffeners act as perfect, equally spaced supports, and each ring buckles as a free circular ring in its $n = 2$ mode. The shell strip b_{eff} is fully effective and shares the ring's curvature.	Preliminary sizing simplification.
A-TK-04	Only pressure loads are carried: internal gauge pressure on the inner shell, atmospheric collapse pressure on the outer shell. Airframe and slosh loads are reacted elsewhere.	Preliminary load-path simplification.
A-TK-05	Differential thermal contraction is managed by variable supports and not added to the membrane stress. Properties are constant at each shell's working temperature.	Preliminary model simplification.
A-TK-06	The shells are axisymmetric and welds, joints and penetrations are not modelled, so the wall is continuous; a 1.03 factor accounts for their added weight.	Preliminary geometry idealisation.

6.3.3. Method

Inner Shell: Hoop Stress

The wall thickness, $t_{\text{cyl/sph}}$ (with the subscript indicating whether it is a cylinder or sphere) required to hold the tank with pressure p_{int} can be expressed as:

$$t_{\text{cyl}} = \frac{\text{SF} \cdot p_{\text{int}} \cdot r}{\sigma_y}, \qquad t_{\text{sph}} = \frac{\text{SF} \cdot p_{\text{int}} \cdot r}{2 \cdot \sigma_y}, \tag{6.1}$$

where r is the radius, and σ_y is the yield stress, with a safety factor, SF = 1.5. The factor of two means the caps need only half the cylinder's thickness.

Outer shell: Buckling

The outer shell is under net external pressure p_{ext} due to the vacuum layer between the inner and outer shell. For the cylinder, the governing equation is the Windenburg-Trilling inter-frame collapse pressure of a ring-stiffened shell [61]:

$$p_{\text{cr}} = \frac{2.42\, E\, (t/D)^{2.5}}{\left(1 - \nu^2\right)^{0.75} \left(L/D - 0.45\sqrt{t/D}\right)}, \tag{6.2}$$

where E is the Young's modulus, t is the thickness of the cylinder, ν is the Poisson ratio, D is the outer diameter, and L is the length between ring stiffeners [63], with the two end domes acting as the outermost supports. The design requirement $p_{\text{cr}} \geq \text{SF}_b\, p_{\text{ext}}$ cannot be inverted in closed form, so Equation 6.2 is solved for t by bisection. Taking $\nu = 0.3$, the hemispherical caps' buckling pressure is [64]:

$$p_{\text{cr}} = 1.21\, E \left(\frac{t}{R}\right)^2 \quad \Longrightarrow \quad t_{\text{sph}} = R\sqrt{\frac{\text{SF}_b\, p_{\text{ext}}}{1.21\, E}}. \tag{6.3}$$

A single buckling factor $\text{SF}_b = 3.0$ is carried on the external pressure. This factor absorbs both imperfections from manufacturing and design margin. Since A-TK-04 assumes that the shell carries no load from the aircraft, and the supports are beyond the scope of this estimation, the shell is sized purely on buckling, the resulting wall is cross-checked against compressive yield, $\sigma = p_{\text{ext}} r/t \leq \sigma_y/\text{SF}$, to confirm the buckling criterion is indeed the driving failure mode.

Ring stiffeners

Equation 6.2 assumes the barrel is divided into bays by stiffening rings, and those rings must be stiff enough to act as genuine lines of support. Each ring arrests the shell over its tributary bay and so carries a radial line load $q = p_{\text{ext}}\, L$. A free circular ring buckles at $q_{\text{cr}} = 3EI/R^3$ [65], which with the same buckling factor sets the required second moment of area

$$I_{\text{req}} = \frac{\text{SF}_b\, q\, R^3}{3E}. \tag{6.4}$$

Each ring is modelled as an I-section acting together with an effective strip of shell plating $b_{\mathrm{eff}} = 1.10\sqrt{D\, t_{\mathrm{skin}}}$ [63], the combined inertia assembled by the parallel-axis theorem. The web height is increased until I_{req} is met, but capped so its radial tip stays clear of the insulation gap; if that cap is reached, the flange is widened instead.

Stiffener Spacing Optimisation

The bay length L is the single free structural variable, and it drives three coupled quantities. A longer L makes the barrel buckle more easily, so Equation 6.2 demands a thicker skin. At the same time it reduces the ring count, while increasing the load each remaining ring must carry. Short bays therefore give a thin skin but many heavy rings, and long bays a thick skin but few light rings, so there exists an outer-shell mass optimum.

The optimiser minimises the empty tank mass over L. Because the objective function is non-smooth, jumping each time n_{rings} changes by a discrete step, a dense grid search is first used to identify the region containing the global minimum, then the optimum is located within the best grid cell. Figure 6.2 shows the resulting trade-off. Skin mass increases and ring mass decreases with L, and their sum passes through a shallow minimum that determines the chosen spacing. The optimisation process is presented in Figure 6.2.

This resulted in a tank as presented in Figure 6.3, and key values presented in Table 6.3. The result is further discussed in Subsection 9.1.6.

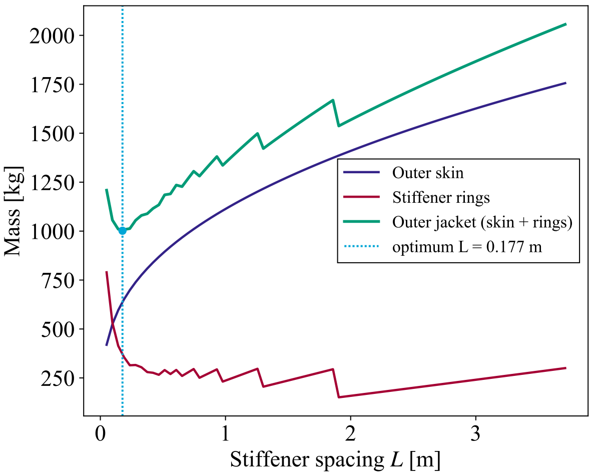

Figure 6.2: Stiffener spacing optimisation, outer-shell mass split into skin and rings.

Table 6.3: Final LH2 tank inputs and sizing outputs.

Quantity	**Value**	**Quantity**	**Value**
Inputs / operating conditions			
Internal design pressure	2.0 bar	External pressure	1.013 bar
Insulation thickness	0.10 m	Safety factor (pressure)	2.25
Buckling safety factor	3.0	Stiffener spacing	0.18 m
Mass margin fraction	0.03		
Geometry / outputs			
Volume (req./achieved)	51.94 m^3	Total tank length	7.051 m
Cylindrical length	3.714 m	Inner radius	1.669 m
Outer shell radius	1.775 m	Fineness ratio	2.113
Inner wall thk. (cyl/sph)	1.566/1.000 mm	Outer wall thk. (cyl/sph)	4.927/3.797 mm
Stiffener rings	20	Heat leak	20.70 W
Boil-off	4.01 kg/day	Boil-off fraction	0.117 %/day
Mass breakdown			
Inner shell (wall)	270.55 kg	Outer shell (wall)	1 008.33 kg
Insulation	309.31 kg	Stiffener rings	366.93 kg
Subtotal (unmargined)	1 588.19 kg	Mass margin (3%)	47.65 kg
Tank empty mass (total)			**1 635.83 kg**

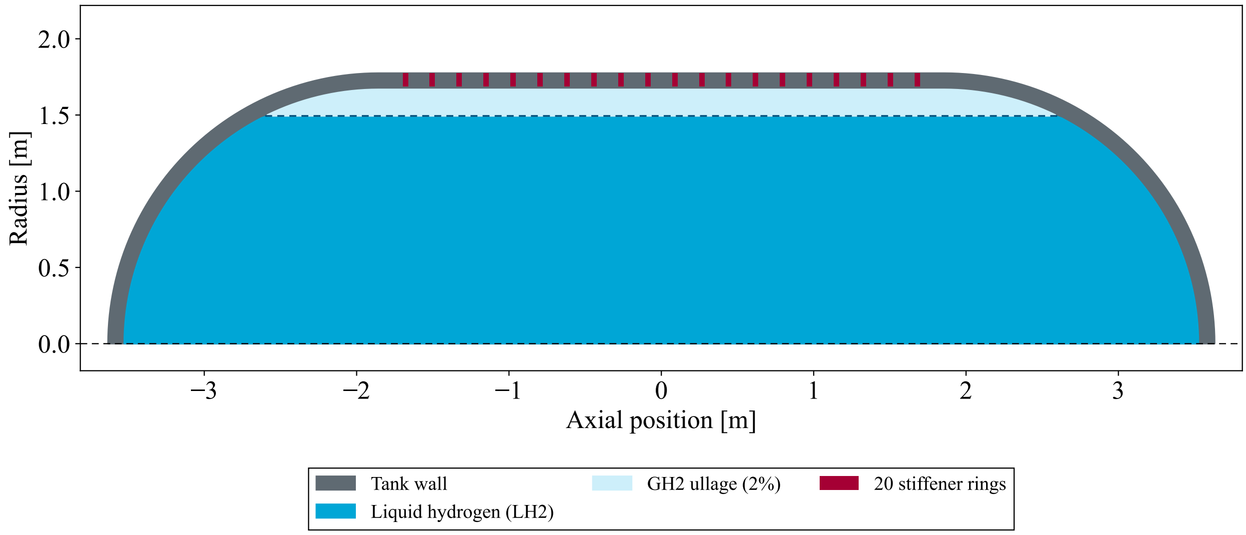

Figure 6.3: Radial build of the vacuum-shelled tank, ullage not to scale.

6.4. Trim Tank Control

The longitudinal CG of the aircraft migrates continuously in flight as fuel is drawn from the tanks. An uncontrolled CG excursion forces the horizontal tail to carry a larger balancing load for much of the mission, penalising the lift-to-drag ratio and hence the fuel burn. The goal of the work described here is to actively hold it at the station that minimises trim drag, so that the aircraft can fly with the smallest possible trim drag penalty throughout the cruise.

To achieve this, a mass-and-moment model of the aircraft is built in Simulink, and a feedback loop is closed around the CG location by transferring fuel between a forward trim tank and the main wing tank. The model captures (i) the simultaneous dual-fuel burn of liquid hydrogen and Jet A-1, (ii) the resulting depletion of each tank, (iii) the instantaneous CG computed from the live tank masses, and (iv) a capped, bidirectional controller that commands the trim transfer required to drive the CG onto its target station.

The model is deliberately reduced to the mass-and-moment level needed to study CG migration and its control, and the simplifications this entails are collected in Table 6.4.

Table 6.4: Assumptions used in the CG control and trim model (`cg_control.slx`).

ID	**Assumption**	**Justification / source**
A-CG-01	The aircraft is modelled as four point masses and only the longitudinal CG is modelled. Distributed mass, structural flexibility, and lateral and vertical CG are ignored.	Sufficient for a pitch-trim study.
A-CG-02	Tank centroids and the nose datum are fixed, fuel does not migrate within a tank as it drains and slosh is neglected.	Sufficient for this model's fidelity.
A-CG-03	Each tank is an ideal saturating integrator clamped between [0, Capacity], with mass conserved exactly and no line losses, leaks, or unusable fuel.	Sufficient for this model's fidelity.
A-CG-04	The transfer pump responds instantaneously, with no ramp or lag.	Pump timescale $\ll$ Mission timescale.
A-CG-05	Fuel is transferred only between the trim and wing tanks, and the LH_2 tank only drains.	Fixed by the feed architecture.
A-CG-06	Fuel burn is prescribed as a mass flow per phase. Thrust and engine performance are not modelled.	Sufficient for this fidelity.
A-CG-07	The CG is known perfectly and instantaneously, and is held to a single fixed target station.	Sufficient for this fidelity.

ID	Assumption	Justification / source
A-CG-08	No aerodynamic model is computed: trim drag, tail load, and the fuel-burn benefit are inferred from CG position.	CG station used as a proxy.

Detailed Tank Layout

The front trim tank is connected to both the port and starboard side wing tank using a pump [3] with a mass flow rate of $0.75\,\mathrm{kg\,s^{-1}}$ on each side, leading to a maximum transfer rate of $1.5\,\mathrm{kg\,s^{-1}}$. The two wing tanks are also connected to each other with the same pump as redundancy.

6.4.1. Mass and moment model

The aircraft mass is lumped into a zero fuel mass (which includes the 180-passenger payload) and three fuel masses at fixed longitudinal stations: a forward trim tank, the wing tank carrying the Jet A-1 kerosene, and an aft tank carrying the liquid hydrogen. The reference data are listed in Table 6.5.

Table 6.5: Lumped masses and longitudinal stations used in the CG model. Stations are measured from the nose datum.

Component	Location x_i [m]	Initial mass [kg]
Zero fuel weight	22.91	81482
Trim tank	9.20	3435
Wing tank	23.83	7127
LH_2 tank	39.53	3435

Each tank is modelled as a saturating integrator. The mass is initialised at the tank's mission fuel load and then evolves as the time integral of the net mass flow rate, which accounts for the fuel usage rate. The integrator output is clamped between zero and the tank capacity, so the stored mass can never go negative or exceed the physical limit. Fuel is transferred between the trim and wing tanks under the action of the controller, while the LH_2 tank mass is drained directly according to the fuel schedule.

The instantaneous CG station follows directly from the mass-weighted first moment, evaluated continuously by the CG calculator function block from the integrator outputs. In flight, the CG cannot be measured directly, so it must be inferred. The present model evaluates it from the live tank masses, which mirrors the practical approach of computing the CG from measured fuel quantities together with the known fixed masses and stations. An alternative is to estimate the CG from accelerometer measurements of the aircraft's attitude, which removes the reliance on fuel quantity sensing but brings its own noise and calibration demands.[4] Either way the controller acts on a computed or estimated CG rather than a directly measured one, consistent with AS-CG-07. The model can be seen in Figure 6.4.

---

[3] `https://shop.boeing.com/cpd/bdi_110000-100%3D2i` (Accessed:12-06-2026)

[4] Personal communication with Dr.ir. E. van Kampen, Associate Professor in Advanced Flight Control at Delft University of Technology on 11/06/2026.

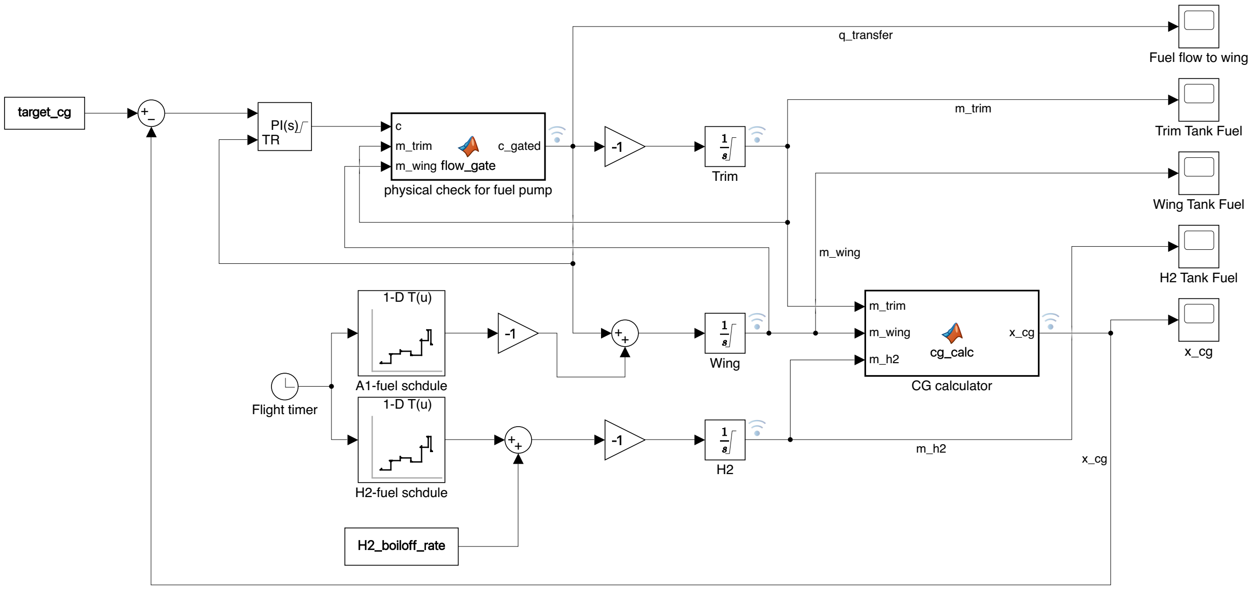

Figure 6.4: Simulink block diagram

6.4.2. Dual-fuel burn schedule

The burn is specified directly as a mass flow per flight phase per fuel, with seven phases (taxi, take-off, initial climb, climb, cruise, descent, and approach) whose boundaries are listed in Table 5.5. A clock feeds two one-dimensional lookup tables, one per fuel, keyed on the phase-boundary breakpoints, which collapse the fourteen per-phase rates into the two live burn signals $\dot{m}_{\mathrm{H2}}(t)$ and $\dot{m}_{\mathrm{A1}}(t)$ used above. Both fuels are active throughout, and the hydrogen path additionally carries the constant boil-off term to model the heat influx during flight.

6.4.3. Closed-loop trim control

The CG is held on station by a closed-loop, bidirectional fuel-transfer controller. The CG error $e(t) = x^*_{\mathrm{cg}} - x_{\mathrm{cg}}(t)$ between the target station, $x^*_{\mathrm{cg}} = 23.083\,\mathrm{m}$ and the live CG drives a PID controller whose output is the commanded transfer rate q_{tr}. The command is capped to the pump limit, $q_{\mathrm{tr}} = \mathrm{sat}_{\pm q_{\max}}$, with $\big(\mathrm{PID}\big(e(t)\big)\big)$, $q_{\max} = 1.5\,\mathrm{kg\,s^{-1}}$, such that the actuator never demands more flow than the transfer pumps can deliver. The sign of the command sets the direction: a positive command moves fuel from the forward trim tank to the wing tank, shifting the CG aft, while a negative command pulls fuel the other way to move the CG forward. This bidirectional authority lets the loop reject CG drift in either direction.

A pair of full-tank gates protects the transfer against overfilling. When the receiving tank reaches its capacity, the corresponding valve latches shut and transfer in that direction stops. It is the gate, not the controller, that arrests the flow. The empty tank lower clamp on each integrator restricts the tank from transferring fuel after it is depleted. Together, these guarantee that the model conserves mass and that the CG command stays well behaved when a tank limit, rather than the controller, sets the binding constraint.

The system is linearised, and the controller is tuned from the resulting linear transfer function. Priority is given to closed-loop stability with a deliberately slow response, because the fuel transfer system is intended only to track the large, slow CG migration produced by fuel burn over the mission. Faster, smaller disturbances such as passenger movement or short-term load shifts are left to the aerodynamic control surfaces, which can react far quicker than fuel can be pumped between tanks. Sizing the loop this way keeps the trim transfer gentle and avoids chasing high-frequency excursions that the pump could not usefully follow.

Finally, a flight with different fuel burn phases: take-off, climb, cruise, descent, and landing is simulated and shown in Figure 6.5.

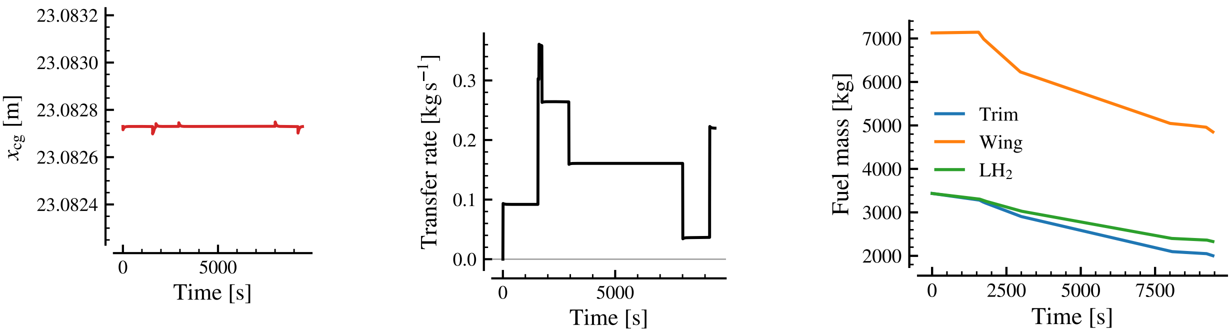

(a) CG station held at the 23.08 m target.

(b) Trim-wing transfer rate.

(c) Tank fuel levels.

Figure 6.5: MAVERICK CG-control results over the mission.

Figure 6.5 shows that the active fuel transfer controller is able to offset the centre-of-gravity excursion caused by hydrogen consumption and keep the CG close to its 23.08 m target throughout the flight. As fuel is drawn from the tanks, the CG would drift, but Figure 6.5a shows the controller holding the station near the set point, with small overshoots appearing only at the phase transitions where the burn rates step to new values. The transfer rate in Figure 6.5b stays below 0.4 kg s^{-1} for the entire mission, under the 1.5 kg s^{-1} pump limit, so the system corrects the imbalance with a large actuation margin and never saturates. Figure 6.5c shows the trim, wing, and liquid-hydrogen tanks draining smoothly as fuel is consumed, with the forward trim tank feeding the wing tank to compensate for the shifting fuel distribution, and all three tanks retain positive reserves at landing. Together, these results demonstrate that the trim tank can absorb the centre-of-gravity migration.

7

Hydrogen Feed System Design

The fuel feed system is designed to ensure that hydrogen is safely transported from the tank to the engines. The hydrogen is liquid in the tank, and then vaporised and delivered to the engine gaseous. An overview of this system is provided in Section 7.1. As explained in Chapter 6, the hydrogen will be stored in liquid form at 2 bar. It is transported through a series of pipes, which are sized in Section 7.2. To achieve the required mass flow rate, pressure and temperature, pumps and heat exchangers are required. Their design is presented in Section 7.3 and Section 7.4, respectively. The usage of bleed air, cooled with the heat exchangers, for turbine cooling is discussed in Section 7.5. Lastly, the required valves and sensors are presented in Section 7.6 and Section 7.7.

7.1. System Architecture & Model Overview

First, the overall layout of the feed system is determined. This is driven mainly by the mass flow, temperature, and pressure requirements, as set in Section 5.4. The system is sized for the most demanding flight phase (take-off). In take-off conditions, a mass flow rate of 0.17kg s^{-1} is required, and the hydrogen should be delivered to the injector at 55.94 bar. The minimum required injector inlet temperature has also been constrained to a minimum of 150K, as explained in Section 5.4. An off-design analysis is also performed for cruise conditions to ensure that the demands of this flight phase are also met.

LH$_2$ feed systems for aircraft have been studied several times in the past, and they usually follow a similar structure, with multiple pumps and heat exchangers at various stages of the feed system. The concept was proven in the 1980s on the USSR's experimental Tupolev Tu-155 [66]. The Tu-155 uses multiple pumps to provide the required pressure increase and mass flow rate. This was also used in another concept for a hydrogen-fuelled, turbofan-powered aircraft developed by NASA and Lockheed in the 1970s [67], illustrated in Figure 7.1.

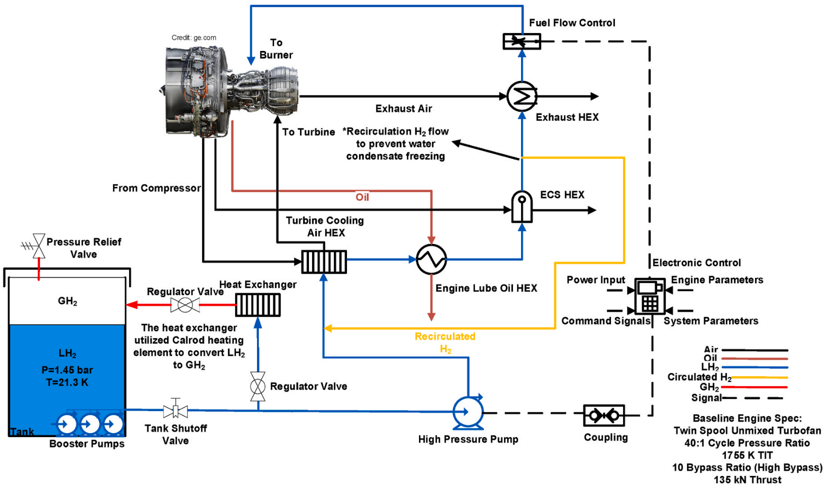

Figure 7.1: Layout of the NASA-Lockheed LH_2 feed system. Diagram by Ebrahimi et al. [43].

This brings multiple advantages, such as splitting the work between multiple smaller, lighter pumps. Furthermore, a single pump would need to require the entire pressure increase in one go, increasing the risk of cavitation. It would also need to be located near the tank to allow it to draw the hydrogen out of the tank with the correct mass flow rate. In addition, an immediate pressure rise to the 55.94 bar would require stronger and heavier pipes throughout the entire system, increasing the weight. With these considerations, the chosen layout consists of a cryogenic turbopump (boost pump) located at the exit of the tank, and a gas compressor located just before the engine, to provide the final pressure increase at the end of the feed system. Each branch will have two boost pumps laid out in parallel for redundancy, and the usage of the two will be alternated to ensure both are consistently used.

The temperature increase is also split between multiple heat exchangers. This allows the individual heat exchangers to be smaller and more compact. A big advantage, also leveraged by the NASA-Lockheed concept, is that the hydrogen can be used for the cooling of other components. Two heat exchangers are therefore chosen: one that uses engine bleed air, and one that uses engine oil. The bleed air heat exchanger will heat up the hydrogen while cooling the engine bleed air. A portion of this air will then be used for cabin pressurisation and air-conditioning, while another will be used for cooling the High-Pressure Turbine (HPT). This can increase the efficiency, as is further discussed in Section 7.5. Additionally, the engine oil heat exchanger will cool the engine oil, reducing the required size of a dedicated oil-cooling heat exchanger, as discussed in Section 7.4.

Also illustrated in Figure 7.2 is a small electric heat exchanger located in a return line from after the boost pump to the tank. This will vaporise a small quantity of hydrogen and feed it back into the tank to regulate the tank pressure. This is similar to NASA and Lockheed's concept. This heat exchanger is not sized in this chapter, and is assumed to be small enough not to play a major role in the dynamics of the rest of the system. It is not simulated, and only included in Figure 7.2 for visualisation. In further detailed design stages, it shall be sized based on estimated tank pressure drops over time to determine its required duty.

The designed feed system is modelled in Matlab's Simulink, using the Simscape Fluids library, enabling the properties and behaviour of the entire fluid network to be analysed. The layout of the feed system is presented below in Figure 7.2. Note that the model includes only one branch of the system; the actual system will have two identical branches, one feeding each engine.

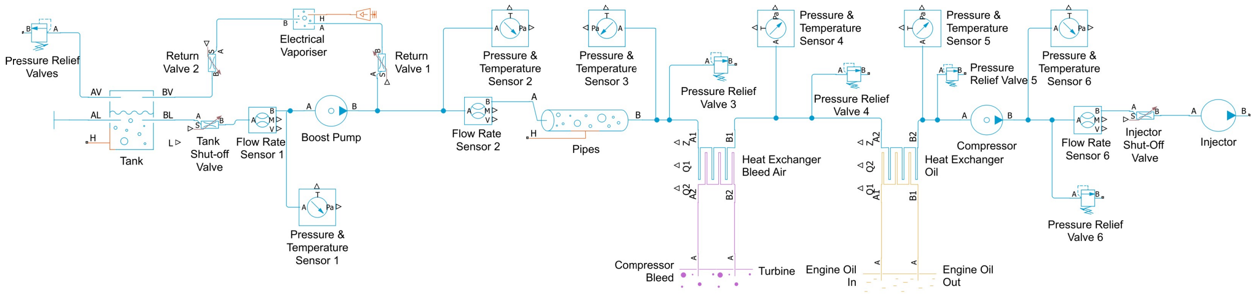

Figure 7.2: Layout of MAVERICK's LH_2 feed system, modelled as a two-phase fluid network with Simscape Fluids. This diagram is for visualisation. The full model includes a few more blocks necessary for the simulation, such as fluid properties and scopes.

In order to model the system in Simulink, the thermodynamic properties of hydrogen for a wide range of pressures and internal energies must be known, for both LH_2 and GH_2. The properties are computed using the CoolProp library[1]. For the model, the selected pressure range is 0.05-8.00 MPa, and the specific internal energy ranges from -50 to 2500 kJ kg^{-1}. These ranges ensure that properties for all operational pressures and temperatures of the system are tabulated, with a reasonable margin.

The properties required to accurately model the fluid dynamics in the system are the temperature T, specific volume v, specific enthalpy h, kinematic viscosity ν, thermal conductivity k_{th}, and Prandtl number Pr. Example contour plots for temperature and specific volume are shown in Figure 7.3.

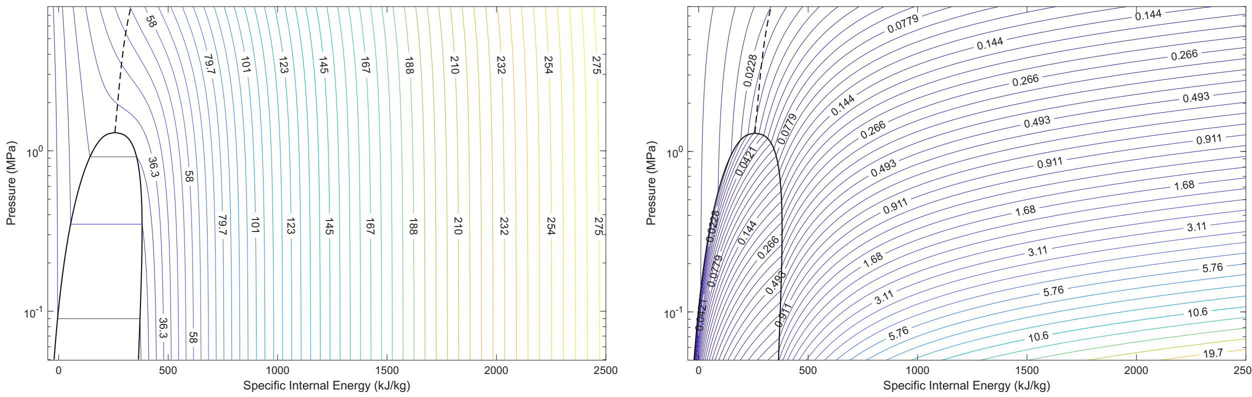

(a) Contour plot of hydrogen temperature profile with varying pressure and specific internal energy.

(b) Contour plot of hydrogen specific volume profile with varying pressure and specific internal energy.

Figure 7.3: Example contour plots for temperature and specific volume of hydrogen in the pressure range 0.05-8.00MPa and the specific internal energy range of -50-2500kJ kg^{-1}, constructed with CoolProp.

7.2. Pipes

The cryogenic piping system is sized using an in-house physics-based model.

7.2.1. Assumptions

Several assumptions are used in the model to simplify the sizing software. Only the assumptions with higher impact are shown in Table 7.1. The sizing model is preliminary and thus high-fidelity physics are generally not captured.

Table 7.1: Assumptions made for the LH_2 feed-line sizing model

ID	Assumption	Justification / source
A-PP-01	The hydrogen is modelled as single-phase LH_2 throughout the feed line.	Acceptable for preliminary sizing if the pressure remains above saturation.
A-PP-02	The flow is assumed to be steady, one-dimensional and incompressible.	Acceptable for undisturbed and slow flows.

---

[1] `https://coolprop.org/` (Accessed 14/06/2026)

ID	Assumption	Justification / source
A-PP-03	The pressure losses are only due to friction and 90° bend.	These are expected to be the major loss sources [68].
A-PP-04	The design velocity is taken as 80% of the limiting velocity.	A safety factor is applied so the selected pipe operates below the limit.
A-PP-05	The liner wall thickness is sized using the thin-wall hoop stress equation.	Neglects detailed pressure requirements, fatigue, thermal stress, buckling, and certification margins. Removes complexity.
A-PP-06	The insulation is modelled as a vacuum-jacket and MLI annulus using an equivalent thermal conductivity.	The effective conductivity represents radiation, residual gas conduction, spacer conduction and MLI performance in an integrated manner.
A-PP-07	The outer vacuum jacket is sized without buckling considerations.	Buckling is not expected to be driving [69]. Neglecting it simplifies the model.
A-PP-08	Insulation-related items (sensors, vacuum pumps, etc.) are neglected in the mass estimate.	Mass only includes the inner liner and outer jacket. The final installed system mass is expected to be higher.

7.2.2. Method

The method to size the cryogenic pipe system follows a design algorithm in which the design variables are the inner liner diameter and thickness, and insulation thickness. Design is driven by tank exit conditions, necessary cryogenic conditions in the pipes, maximum required mass flow at the injector, and length requirements, according to aircraft dimensions. Vacuum insulation was used instead of foam due to its additional insulation and smaller volume. It is also considered the state-of-the-art in aviation [52]. CoolProp was used as an open-source database for thermofluid properties. The algorithm is implemented as follows:

1. The feed-line velocity limits are calculated. These include erosional, cavitation, and Waterhammer velocities. The lowest is selected as governing.

$$v_{\text{erosional}} = \frac{C_{\text{e}}}{\sqrt{\rho}} \tag{7.1}$$

$$v_{\text{cavitation}} = \sqrt{\frac{2\left(p_{\text{line}} - p_{\text{vap}}\right)}{\rho}} \tag{7.2}$$

$$v_{\text{waterhammer}} = \frac{\Delta p_{\text{allow}}}{\rho a} \tag{7.3}$$

   Where $C_{\text{e}} = 100$ is the erosional-velocity constant; ρ the hydrogen density; p_{line} and p_{vap} are the feed line and vapour pressures, respectively; $\Delta p_{\text{allow}} = 5.0 \cdot 10^5$ Pa the allowable pressure rise; a the wave speed in the pipe.

2. A safety factor of 0.8 is applied to define the design velocity.
3. The minimum inner diameter is calculated from the design velocity, mass flow rate and LH_2 density, using the continuity equation: $\dot{m} = \rho V A$.
4. A loop is run through predefined standard outer diameters and wall thicknesses [70], selecting the lowest mass pipe that satisfies velocity and pressure constraints.
5. The pipe system is modelled as two straight pipes of 20.0 m (from LH2 tank to wing position) and 3.8 m (from wing position to engine) and a 90° bend (see Figure 11.4).
6. The pressure drop is calculated from the sum of straight pipe friction losses and bend losses. The straight pipe losses are calculated using the Darcy-Weisbach equation [71]:

$$\Delta P_{\text{pipe}} = f \frac{L}{D_{\text{in}}} \frac{1}{2} \rho V^2, \tag{7.4}$$

and the bend and other minor losses are calculated as [71]:

$$\Delta P_{\text{bend}} = K_{bend} \frac{1}{2} \rho V^2. \tag{7.5}$$

Here, f is the Darcy friction factor, L is the pipe length, D_{in} is the pipe inner diameter, ρ is the LH_2 density, V is the flow velocity, and $K_{\text{bend}} = 0.9$ is the bend loss coefficient.

7. Candidate pipe configurations are stored if they satisfy all constraints and the pressure remains above the saturation pressure plus margin.
8. The mass of all candidates is calculated using AA-2219 as a material (see Subsection 6.3.1). The lowest mass design is selected.
9. Define a maximum allowable linear heat flux, q'. This is set to be $q' = 0.5$ W/m [72].
10. The maximum allowable LH_2 temperature rise is defined to preserve the sub-cooling margin and avoid multi-phase flow.
11. r_{out}/r_{in} is calculated using the equivalent cylindrical conduction model, derived from Fourier's Law of Heat Conduction:

$$q' = \frac{2\pi k_{\text{eff}}(T_{\text{amb}} - T_{\text{LH2}})}{\ln(r_{\text{out}}/r_{\text{in}})}, \tag{7.6}$$

where k_{eff} is the equivalent vacuum/MLI conductivity. $k_{\text{eff}} = 2 \cdot 10^{-4} \text{W m}^{-2} \text{K}^{-1}$ [73].

12. The required insulation thickness that would exactly satisfy the allowed temperature rise limit is calculated.
13. The jacket mass is estimated by modelling it as a cylindrical aluminium shell.
14. The jacket mass is added to the pipe liner mass to obtain the total mass.

7.2.3. Results

The results of the feed-line sizing model are presented in terms of the selected pipe geometry, mass, hydraulic performance, and thermal behaviour. The key outputs include pressure losses, Reynolds number, allowable and design velocities, and the predicted LH_2 temperature rise along the line. The cross-section of the cryogenic pipe can be seen in Figure 7.4. Table 7.2 presents the most important flow parameters and system masses.

Table 7.2: Cryogenic feed line design and flow properties.

Parameter	Value	Unit
Maximum mass flow rate	0.17	kg/s
LH_2 temperature	20.0	K
Feed-line inlet pressure	8.0	bar
Governing velocity constraint	Waterhammer	–
Limiting velocity	6.17	m/s
Design velocity	4.94	m/s
Actual flow velocity	4.28	m/s
Reynolds number	$5.88 \cdot 10^5$	–
Total pressure drop	0.08	bar
Final feed-line pressure	7.92	bar
Total bulk temperature rise	0.006	K
Liner mass	2.90	kg
Jacket mass	13.93	kg
Total mass	16.83	kg

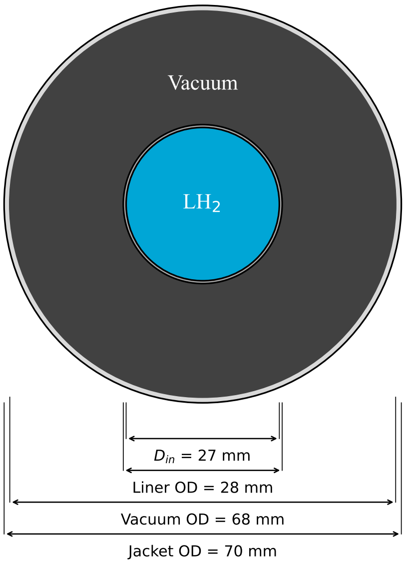

Figure 7.4: Cryogenic pipe cross-section.

Figure 7.4 shows that the feed-line diameter is dominated by the vacuum insulation layer, with the LH_2 flow pipe representing only a small fraction of the total diameter. The actual flow velocity is lower than the design velocity due to the use of standardised pipe dimensions. Matching the design velocity exactly would require a non-standard diameter and wall thickness combination, so the selected valid pipe is slightly larger than physically necessary. The resulting Reynolds number indicates turbulent flow. This is considered acceptable for preliminary feed-line sizing, since high-Reynolds-number LH_2 line operation has been experimentally investigated by NASA, with reported tests at $Re \sim \mathcal{O}(10^5)$ [74]. The LH_2 temperature rise is negligible, as the short time in the feed line, approximately 6 s, has little heat absorption and the vacuum/MLI insulation strongly reduces the heat leak into the flow.

7.3. Pumps

The pumps will provide the required pressure increase to the hydrogen to achieve the required injection pressure and mass flow rate. As specified in Section 7.1, the pumps are sized for take-off conditions, where the required injector pressure and mass flow rate are greatest: 55.94 bar and 0.17 $\mathrm{kg\,s^{-1}}$. The pressure increase is distributed between two pumps: a cryogenic turbopump and a gas compressor. The turbopump, or boost pump, will provide an initial small pressure increase to the liquid hydrogen, drawing it out of the tank. Once the hydrogen is vaporised in the heat exchangers, the final pressure increase is provided by the gas compressor. The design and sizing of these pumps is presented in this section.

7.3.1. Assumptions

Several assumptions and simplifications are made in order to model the feed system in Simulink. The system is modelled as a two-phase fluid network, which allows phase changes between liquid and gas to be simulated. The assumptions made regarding the pumps are listed in Table 7.3.

Table 7.3: Assumptions made for the pump design

ID	Assumption	Justification / source
A-PM-01	The pumps are modelled to do isentropic work on the fluid.	Done to facilitate modelling in Simulink. The pumps are modelled using the Pressure Source block[2], which adds power to the flow isentropically. The actual required pump power is approximated using an isentropic efficiency η_{isen}.
A-PM-02	There is no heat exchange with the environment in the pumps.	The pump model does not account for heat losses to the environment. This is a reasonable assumption for preliminary analysis because the mass flow rate through the pumps, on the order of 0.1 $\mathrm{kg\,s^{-1}}$, is large enough for the hydrogen to pass through the pumps in a short enough time for heat loss to be negligible. Besides, the cryogenic pumps will be well insulated to ensure this is true.
A-PM-03	The isentropic efficiency of the cryogenic pump is assumed to be 80%.	In 1977, NASA developed a small, three-stage, high-pressure LH_2 turbopump for use in rockets, achieving an isentropic efficiency of 58% [75]. More recent studies estimate that centrifugal pumps for cryogenic hydrogen refuelling stations could achieve isentropic efficiencies of around 80% [76]. A 2024 study on LH_2 centrifugal pumps for use in aircraft reports an estimated efficiency of 82.4% [77]. It is therefore estimated that with modern technological advancements, a small, high-pressure turbopump could likely achieve an isentropic efficiency of at least 80%.
A-PM-04	The isentropic efficiency of the gas compressor is assumed to be 80%.	A 1977 study on oil-flooded screw compressors for cryogenic helium claims isentropic efficiencies of ~50% [78]. The isentropic efficiency of modern industrial cryogenic gas compressors can range from 75% to 85%[3]. A value of 80% is therefore estimated, accounting for improved compressor technology, as in A-PM-03.

7.3.2. Method

The layout of MAVERICK's feed system, described in Section 7.1, includes a cryogenic turbopump at the exit of the tank to draw the LH_2 out, provide an initial pressure increase, and provide the required mass flow rate through the pipes. The magnitude of this pressure increase and the required work done is determined using the model constructed in Simulink. To ensure that the required hydrogen mass flow rate is achieved, this is set as a constraint in the system through the use of a Mass Flow Source block[4]. This block is located at the end of the network and is set such that it does not do any work on the fluid. This way, it is only acting as a constraint for the mass flow rate, and the required work is achieved by the cryogenic pump and the gas compressor.

The Pressure Source block used for the turbopump and compressor models the work done by the pump by imposing the constraints of conservation of mass $\dot{m}$ and energy ϕ flow rates between the inlet A and the outlet B[2]:

$$\begin{cases} \dot{m}_A + \dot{m}_B = 0 \\ \phi_A + \phi_B + \phi_{work} = 0 \end{cases} \tag{7.7}$$

The work rate ϕ_{work} added by the pump, or the pump's power, is determined using the specific total enthalpy h of the fluid at the inlet and outlet:

$$\phi_{work} = \dot{m}_A(h_B - h_A) \tag{7.8}$$

The specific total enthalpy is defined in terms of the fluid's specific internal energy u, pressure p, specific volume v, mass flow rate $\dot{m}$ and flow area A:

$$h = u + pv + \frac{1}{2}\left(\frac{\dot{m}v}{A}\right)^2 \tag{7.9}$$

Equation 7.9 is evaluated both at the inlet and the outlet of the pump, with the specific internal energy taken from the tabulated thermodynamic data. This enables solving for the required pump power to achieve the specified pressure increase, given that the mass flow rate is constrained by the required mass flow at the injector.

Finally, it is checked whether there is a risk of cavitation in the boost pump. Cavitation occurs when the pressure at the suction side of a pump drops below the fluid's vapour pressure, leading to the vaporisation of the fluid and the formation of bubbles. This should hence be avoided. The metric of Net Positive Suction Head (NPSH) is used to verify whether there is a cavitation risk for a given pump. It is a measure of the available pressure above the vapour pressure at the pump inlet[5]. In this case, because there is a negligible height difference between the fluid surface and the pump inlet, the main contributions to the NPSH are the barometric head H_{bar}, the dynamic pressure head H_{dyn}, and the fluid vapour pressure head H_{vap}. The total available NPSH is therefore:

$$NPSH_a = H_{bar} + H_{dyn} - H_{vap} = \frac{p_{inlet}}{\rho_{inlet} g} + \frac{v_{inlet}^2}{2g} - \frac{p_{vap}}{\rho_{inlet} g} \tag{7.10}$$

To verify that there is no risk of cavitation, the available NPSH$_a$, calculated with Equation 7.10, must be greater than the pump's required NPSH$_r$. This is, however, a pump-specific value and can hence not be evaluated for this specific pump. Nevertheless, a positive NPSH$_a$ provides an NPSH margin for the pump.

---

[2] `https://nl.mathworks.com/help/releases/R2026a/simscape/ref/pressuresource2p.html` (Accessed 03/06/2026)

[3] `https://www.shengerhk.com/en/power-consumption-in-cryogenic-air-separation/` (Accessed 11/06/2026)

[4] `https://www.mathworks.com/help/releases/R2026a/simscape/ref/flowratesource2p.html` (Accessed: 03/06/2026)

[5] `https://enghandbook.com/thermodynamics/net-positive-suction-head-npsh/` (Accessed: 14/06/2026)

7.3.3. Results

The feed system is simulated for take-off conditions, with the boost pump set to provide a pressure increase of 6.0 bar, drawing the LH_2 out of the tank. This is deemed a sufficiently large pressure increase to draw the hydrogen out of the tank, but still relatively small to avoid needing too large pipes. The LH_2 therefore enters the pipes at 8.0 bar. The gas compressor then performs the remaining pressure increase of 48.03 bar.

The on-design simulation for take-off conditions yields a required pump work rate ϕ_{work} on the fluid of 1.74kW to maintain the required mass flow and pressure increase. Factoring in the assumed isentropic efficiency η_{isen} of 80% for a small, cryogenic, reciprocating pump (A-PM-03), the required pump power output P is ϕ_{work}/η_{isen} = 2.18kW.

For the gas compressor, the required work rate ϕ_{work} is a larger 174kW. Accounting for the assumed isentropic efficiency η_{isen} of 80% (A-PM-04) yields a required pump power output P of ϕ_{work}/η_{isen} = 218kW. Estimating the weight of these components is difficult because the weights of cryogenic pumps vary greatly based on power and volumetric flow rate requirements, as well as pump type. Not much data is commercially available, specifically for the operating points required for the feed system. For the pump, an estimate is made based on a pump of similar size used on a hydrogen-powered aircraft, with a similar fuel system [71]. The authors estimate a weight of around 4kg for their booster pumps, which achieve a similar performance to the one required. This thus serves as a preliminary estimate for the weight of the boost pump. As an additional measure of redundancy, each branch of the feed system will have two boost pumps, in case one fails.

For the compressor, a patented design for a compact centrifugal gas compressor used to provide on-board inert gas and on-board oxygen generation for aircraft is used as a reference [79]. The patent claims performance numbers that translate to a specific power of approximately 2.8kW kg^{-1}. The quoted uses of such a compressor would require much lower pressure rises than that required in this case, so several similar compressor stages could be used. This would, however, likely reduce efficiency and overall specific power. Hence, taking a reasonably conservative estimate of 2kW kg^{-1}, yields a required mass of 109kg. This can serve as a reasonable first estimate.

It is important to note that, at this stage, this weight estimation does not achieve a great level of accuracy and must be refined through more detailed analysis of the geometries and performance parameters of the pump and compressor. For this, more detailed models need to be developed. On top of this, due to the limited amount of data available specific to pumps and compressors of these sizes and performance requirements, it would be necessary to either design them in detail, or request components of these specifications directly from specialised companies. Nonetheless, these estimates are used for the preliminary system sizing. An overview of the results, as well as the results for the cruise off-design iteration, is presented in Table 7.4.

The $NPSH_a$ at take-off conditions is quite small, which indicates that there is a low margin to avoid cavitation at the pump inlet. This would require information about the specific pump that will be used, specifically its required NPSH. If this is smaller than the $NPSH_a$, cavitation is avoided. Cavitation at the pump inlet is instead likely at cruise conditions, since the $NPSH_a$ is negative. This is a result of hydrogen's low vapour pressure and the relatively low flow rate through the pipes.

Table 7.4: Final pump parameters.

Parameter	**Take-off**	**Cruise**
$\dot{m}$ [$kg\,s^{-1}$]	0.17	0.1065
p_{injector} [bar]	55.94	19.86
$\Delta p_{\text{boost pump}}$ [bar]	6.0	6.0
Δp_{pipes} [bar]	-0.10	-0.05
$\Delta p_{\text{compressor}}$ [bar]	48.03	11.94
$\phi_{\text{boost pump}}$ [kW]	1.74	1.74
$\phi_{\text{compressor}}$ [kW]	174	52.3
$P_{\text{boost pump}}$ [kW]	2.18	2.18
$P_{\text{compressor}}$ [kW]	249	74.7
$NPSH_a$ [m]	0.61	-0.57

To improve the NPSH margin, as per Equation 7.10, the pressure of the LH_2 in the tank could be somewhat increased. This would increase the barometric head, and hence the $NPSH_a$, reducing the cavitation risk. However, this would come with the drawback of increasing the weight of the tank. To avoid having to do this, a pump with a very small $NPSH_r$ should be used, which may be, for example, achieved with multiple smaller pump stages or an impeller, to give a stepped pressure increase and reduce the suction load. Lastly, the inlet temperature of the hydrogen could be reduced by maintaining the tank at the same pressure, but decreasing its volume. All of these measures should be considered and carefully evaluated in subsequent design stages in order to reduce the risk of cavitation. This cavitation risk would persist even with different pump types, as it is a phenomenon associated with the flow conditions and the hydrogen properties.

7.4. Heat Exchangers

The heat exchangers will provide the required temperature increase to the hydrogen to achieve the target temperature of at least 150K at the injector. The heat exchangers, like the pumps, are sized for take-off conditions where the heat transfer demand is greatest. As described in Section 7.1, a layout with two heat exchangers per branch will be used. The first heat exchanger will use bleed air from the engine's compressor, while the second one will use engine oil. The heat exchangers are laid out in series, with the bleed air heat exchanger first. The design and sizing of the heat exchangers is presented in this section.

7.4.1. Assumptions

The heat exchangers are also simulated in Simulink in the two-phase fluid network. The bleed air heat exchanger is modelled with the Condenser Evaporator block (2P-G) block[6], and the oil heat exchanger with the Condenser Evaporator (TL-2P) block[7]. The bleed air heat exchanger block models heat transfer between the two-phase hydrogen and a gas network for the bleed air. Similarly, the engine oil heat exchanger block models heat transfer between the two-phase hydrogen and a thermal liquid network for the oil. Several assumptions are made to simplify the analysis of the heat transfer dynamics in the heat exchangers. Some simplifications are also required to ensure that the model can be simulated without issues. These assumptions and simplifications are listed in Table 7.5.

Table 7.5: Assumptions made for the heat exchanger design

ID	Assumption	Justification / source
A-HX-01	Both heat exchangers are modelled to only exchange heat between the two fluids, with no heat loss to the environment.	Similar to A-PM-02. In practice, the heat exchanger will be insulated to minimise the heat exchange with the environment, and to avoid condensation and frost on the external surfaces.
A-HX-02	Both heat exchangers are modelled with a counter-flow arrangement.	The counter-flow arrangement is the most efficient heat-exchanger layout, and outperforms parallel and cross-flow arrangements for a given heat-exchange area, reducing weight [80].
A-HX-03	The hydrogen side of both heat exchangers is modelled using a three-zone boundary-following representation, with subcooled liquid, two-phase liquid-vapour mixture, and superheated vapour zones.	This is the model used by both the heat exchanger blocks[6] [7], ensuring that the hydrogen side is modelled consistently between the two heat exchangers. The zone boundaries evolve dynamically based on local fluid enthalpy relative to the saturated liquid and saturated vapour enthalpies tabulated with CoolProp.
A-HX-04	The inner diameter of the tubes of the heat exchangers is the same as that of the pipes.	This avoids velocity and pressure changes into and out of the heat exchangers due to the Venturi effect at the interfaces.

---

[6] `https://nl.mathworks.com/help/releases/R2026a/hydro/ref/condenserevaporator2pg.html` (Accessed 03/06/2026)

[7] `https://www.mathworks.com/help/releases/R2026a/hydro/ref/condenserevaporatortl2p.html` (Accessed 03/06/2026)

ID	Assumption	Justification / source
A-HX-05	For the oil heat exchanger, the heat transfer coefficient model is set to the *Correlation for flow inside tubes* option, which uses the Gnielinski correlation for the subcooled liquid and superheated vapour zones, and the Cavallini-Zecchin correlation for the two-phase mixture zone[2]. For the bleed air heat exchanger, the *Colburn equation* is used instead, with default coefficients $[a, b, c] = [0.023, 0.8, 0.4]$ for the subcooled liquid and two-phase mixture zones, and a reduced coefficient $a = 0.002$ for the superheated vapour zone[8].	The *Correlation for flow inside tubes* option is the default option for both blocks[8] [9], but it produced non-physical, numerical instabilities in the simulation in the bleed air heat exchanger around hydrogen's phase transition. Using the Colburn equation with a reduced heat transfer coefficient in the superheated vapour zone ($a = 0.002$) was found to sufficiently stabilise the simulation. This artificially lowers the computed heat transfer rate in the superheated vapour zone, damping the rate at which the vapour zone boundary evolves and preventing the oscillations. The effect on the accuracy of the steady-state results is expected to be small and mainly affect the transient phase of the simulation where the boundaries of the zones in the heat exchangers are still evolving.
A-HX-06	The heat transfer is assumed to be isobaric, and the only pressure losses considered are those due to viscous friction of the fluids in the pipes.	This simplifies the model, as the pressure losses due to height changes and bends in the pipes are negligible in these compact heat exchangers.
A-HX-07	The model is initialised with liquid hydrogen at 23K and at 8.0 bar in the pipes and heat exchangers. These are the conditions of hydrogen in the tank, plus the pressure increase provided by the boost pump (6.0 bar).	This allows the transient response of the system to be modelled, simulating the state of the system until it achieves a steady-state output of hydrogen at the required conditions. This approach is chosen over the option of allowing Simulink to solve for a steady-state solution and start the simulation from it, because it is observed that this sometimes provides non-physical solutions, such as reversed flows and vaporisation in the pipes.
A-HX-08	The conductive heat transfer between the fluids and the pipe walls is quantified by a thermal resistance R_{th} of the walls. This is specific to the material and wall geometry chosen for the heat exchanger pipes.	This allows the effect of the pipe material to be accounted for, while still maintaining the conductive heat transfer simple enough for this stage of the design.
A-HX-09	The fouling factor for all tubes is assumed to be 0. The fouling factor accounts for additional thermal resistance caused by fouling (impurity) layers on the surface of the tubes.	This is neglected, as it is difficult to quantify and would build up over time. In practice, the fouling build-up would be significantly slow because only pure hydrogen will flow through the pipes. Nevertheless, as discussed in Subsection 11.2.1, the inside of the pipes will be inspected every 10 years, and the buildup of fouling will be quantified and the pipes cleaned if necessary.
A-HX-10	The internal absolute surface roughness ϵ_R of the pipes in the heat exchanger is assumed to be $1.5 \cdot 10^{-6}$m.	Assumed based on common values for tubing. This value can be achieved in practice by ensuring that the inside of the pipes is sanded and smoothed sufficiently[10].

ID	Assumption	Justification / source
A-HX-11	The bleed air is assumed to be an ideal gas.	Eases computation, and is sufficient to capture the heat transfer dynamics to a good degree of accuracy. Air properties are computed by the Gas Properties block[11].

7.4.2. Method

First, the heat exchanger layout and material were selected. An efficient counter-flow arrangement was chosen as per assumption A-HX-02. The pipes are chosen to be "staggered", where rows of tubes are offset relative to each other. This allows for a more efficient usage of space compared to them being aligned, as the tubes of the two fluids must be placed in contact with each other, so the two sets of pipes must interlock. This configuration allows that more easily, as there are larger gaps between tubes with the neighbouring rows. This configuration is shown in Figure 7.5.

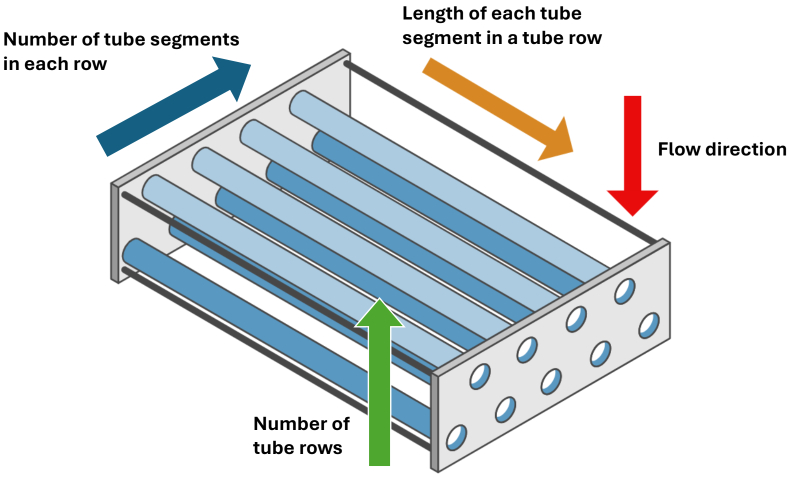

Figure 7.5: Counter-flow heat exchanger layout. Only tubes of fluid shown; the tube bank carrying the second fluid is interlocked with the the first, with flow in the opposite direction. Adapted from Condenser-Evaporator block (2P-G) documentation.[12]

For the material, a few candidates were considered: Inconel 625, stainless steel, and copper. These materials all have a large range of operating temperatures, down to cryogenic temperatures. This is a necessary property to be able to handle the large temperature difference. Approximate relevant properties of the three materials are presented below in Table 7.6.

Table 7.6: Approximate material properties of the three candidate materials

Material	Density [kg m^{-3}]	Melting Point [K]	Thermal Conductivity [W m^{-1} K^{-1}]	Yield Strength [MPa]
Inconel 625[13]	8440	1500	10	500
Stainless Steel[14]	8000	1650	15	200
Copper[15]	8890	1350	400	55-200

---

[8] `https://nl.mathworks.com/help/releases/R2026a/hydro/ref/condenserevaporator2pg.html` (Accessed: 03/06/2026)

[9] `https://nl.mathworks.com/help/releases/R2026a/hydro/ref/condenserevaporatortl2p.html` (Acccessed: 03/06/2026)

[10] `https://www.pipeflow.com/pipe-pressure-drop-calculations/pipe-roughness` (Accessed: 15/06/2026)

[11] `https://nl.mathworks.com/help/releases/R2026a/simscape/ref/gaspropertiesg.html` (Accessed: 03/06/2026)

[12] `https://nl.mathworks.com/help/releases/R2026a/hydro/ref/condenserevaporator2pg.html` (Accessed: 03/06/2026)

All three of these materials can function at cryogenic temperatures, close to 20K. They all have high melting points, although because copper can lose around 30% of its mechanical strength at temperatures of 600K[16], its use would limit the bleed air to that tapped from the Low-Pressure Compressor (LPC). Nevertheless, it more than makes up for this lower operating temperature with a much greater thermal conductivity than the other two materials. Due to the materials' similar densities, copper would be the most efficient for use in the heat exchanger pipes, provided that the hot side temperatures do not get too high. Copper pipes with a thickness of 0.5mm are therefore used, as they can withstand the internal pressure of 8.0bar of the hydrogen in the heat exchanger, with a corresponding hoop stress for a pipe with radius 18.5mm: $pr/t = (8{\cdot}10^5{\cdot}0.0185)/0.0005 = 29.6{\cdot}10^6$Pa

This is below the yield strength range reported in Table 7.6. Nevertheless, in a more detailed structural analysis of the heat exchanger pipes, the thermal stresses exhibited on the pipes should be further assessed. These are heavily dependent on complex flow and heat transfer dynamics between the two fluids and the pipe, as well as the constraints on the expansion of the pipes.

Both heat exchangers model the hydrogen side using the three-zone boundary-following approach as per A-HX-03. At each time step, the local fluid enthalpy is compared to the saturated liquid and saturated vapour enthalpies in the property tables. This allows the length of the subcooled liquid, two-phase mixture, and superheated vapour zones in the exchanger to be determined. The heat transfer is then computed for each zone, and summed to yield the total heat flow rate $\dot{Q}$ in the heat exchangers.[17] [18] The three zones are illustrated in Figure 7.6.

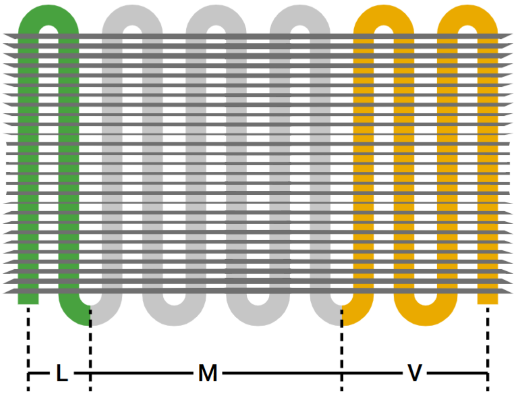

Figure 7.6: Heat exchanger zones: subcooled liquid (L), two-phase mixture (M), and superheated vapour(V). Image from the Condenser-Evaporator block (2P-G) documentation.[18]

In each zone, the heat transfer coefficient U for both fluid streams is calculated as per A-HX-04. First, the Nusselt number Nu is calculated for the subcooled liquid and superheated vapour zones, using the Gnielinski correlation for turbulent flow tubes:

$$Nu = \frac{(f/8)(Re - 1000)Pr}{1 + 12.7\sqrt{f/8}\left(Pr^{2/3} - 1\right)} \tag{7.11}$$

Here, the Reynolds number Re and Prandtl number Pr are determined from the local fluid properties in each zone. Meanwhile, the Darcy friction factor f is computed with the Haaland correlation:

$$f = \left(-1.8\log_{10}\left[\frac{6.9}{Re} + \left(\frac{\epsilon_R}{3.7D}\right)^{1.11}\right]\right)^{-2} \tag{7.12}$$

The Darcy friction factor f is a function of Reynolds number Re, the pipe diameter D, and the pipe's internal surface absolute roughness ϵ_R, assumed to be $1.5 \cdot 10^{-6}$m as per A-HX-10.

---

[13] `https://www.specialmetals.com/documents/technical-bulletins/inconel/inconel-alloy-625.pdf` (Accessed: 10/06/2026)

[14] `https://www.theworldmaterial.com/aisi-316l-stainless-steel/` (Accessed: 10/06/2026)

[15] `https://www.copper.org/publications/newsletters/innovations/2001/08/intro_fac.html` (Accessed: 10/06/2026)

[16] `https://www.engineeringtoolbox.com/metal-temperature-strength-d_1353.html` (Accessed 10/06/2026)

[17] `https://nl.mathworks.com/help/releases/R2026a/hydro/ref/condenserevaporator2pg.html` (Accessed 03/06/2026)

[18] `https://www.mathworks.com/help/releases/R2026a/hydro/ref/condenserevaporatortl2p.html` (Accessed 03/06/2026)

For hydrogen's two-phase liquid-vapour mixture zone, the Nusselt number Nu_M is instead calculated using the Cavallini-Zecchin correlation, which expresses it as a function of the saturated liquid Reynolds and Prandtl numbers, and other fluid properties and empirical constants[19]. In each case, the heat transfer coefficient U is determined from the Nusselt number in terms of the fluid's thermal conductivity k_{th} (taken in the property tables for the given hydrogen conditions), and the pipe inner diameter D (0.27mm):

$$U = \frac{Nu\, k_{th}}{D} \tag{7.13}$$

The combined effect of the heat transfer coefficients of the hydrogen U_{H2}, of the bleed or oil U_{hot}, and the conductive thermal resistance of the tube wall, $R_{th,wall}$ (A-HX-08), is used to determine the total thermal resistance for each zone:

$$R_{zone} = \frac{1}{U_{H2}A_{H2}} + R_{th,wall} + \frac{1}{U_{hot}A_{hot}} \tag{7.14}$$

Here, A_{H2} and A_{hot} are the wetted heat transfer areas of the hydrogen-side and hot-side tube banks within that zone, consisting of the total area of the tubes and fins in the computed respective zones at a given time. $R_{th,wall}$ depends on the thermal conductivity and wall and the thickness of the tubes. To reduce the total thermal resistance and increase the heat transfer rate, fins can be added to the heat exchanger. The fins will also be made of copper and will be placed at regular intervals along the tube length. This way, the total heat transfer area increases, and the total thermal resistance is reduced.

The convective heat flow rate in each zone $\dot{Q}_{zone}$ is then obtained from the local temperature difference between the two fluids ΔT_{zone}:

$$\dot{Q}_{zone} = \epsilon C_{min} \Delta T_{zone} \tag{7.15}$$

C_{min} is the smaller of the heat capacity rates of the two fluids, and is the product of the fluid specific heat capacity c_p and mass flow rate $\dot{m}$. The heat exchanger effectiveness ϵ_{HX} depends on the ratio of heat capacity rates of the fluids C_R, and for a counter-flow configuration is:

$$\epsilon = \frac{1 - \exp[-\mathrm{NTU}(1 - C_R)]}{1 - C_R \cdot \exp[-\mathrm{NTU}(1 - C_R)]} \tag{7.16}$$

The Number of Transfer Units (NTU) depends on the total zone thermal resistance R_{zone}, C_{min}, and the length fraction z of the zone:

$$\mathrm{NTU} = \frac{z}{C_{min} R_{zone}} \tag{7.17}$$

With these parameters computed, Equation 7.15 can be used to compute the zone heat flow rate in each zone. The total convective heat flow rate $\dot{Q}$ for each heat exchanger is the sum of the heat flow rates in the subcooled liquid, two-phase mixture, and superheated vapour zones. Conductive heat transfer also occurs, and is computed similarly, except with conduction-related coefficients. Nevertheless, with fluid flowing quickly in the tubes, it has a very small contribution relative to convection.

With the tube diameter fixed to that of the pipes (A-HX-05), and the material chosen to be copper, the free design variables are the tube length, the number of tubes in each heat exchanger, and the number of fins. The number of tubes is distributed among a certain number of rows, with a specified pitch. These are iterated systematically until a configuration is achieved where the hydrogen reaches the target outlet temperature of at least 150K at take-off conditions. The resulting heat exchanger dimensions, heat duties, and pressure drops are presented in Subsection 7.4.3.

---

[19] `https://nl.mathworks.com/help/releases/R2026a/hydro/ref/condenserevaporator2pg.html#mw_58148bce-ac69-4adf-91ac-c504bc576c6a` (Accessed: 03/06/2026)

7.4.3. Results

For the final design of the two heat exchangers, the dimensions are chosen to be the same. This works well, however, the relative dimensions could be fine-tuned to improve the total weight and packaging. The final arrangement of the two exchangers is with 8 rows of 15 tubes, each 1.4m in length. The spacing between the rows is 5cm, and is the same as the spacing between tubes in each row. Including 6 copper fins, equally distributed over the 1.4m length, equates to a total heat transfer area of 18.2m^2. The total mass of the heat exchangers is estimated using these dimensions and the density of copper (8890kg m^{-3}, see Table 7.6), resulting in a mass of 98.6kg each. With these dimensions, the heat exchangers provide the performance presented in Table 7.7. These results are for the steady-state response, achieved when the system stabilises, after 120s. Both the performance at the take-off (TO) conditions and at cruise (CR) conditions are presented.

Table 7.7: Heat Exchanger Sizing Results for Take-Off (TO) and Cruise (CR) Conditions

	Bleed Air HX - TO	Oil HX - TO	Bleed Air HX - CR	Oil HX - CR
$\dot{m}_{\mathrm{H2}}$ [kg s^{-1}]	0.17	0.17	0.11	0.11
$T_{\mathrm{H2},in}$ [K]	23.3	46.1	65.9	65.2
$T_{\mathrm{H2},out}$ [K]	46.1	73.9	23.4	113.8
$p_{\mathrm{H2},in}$ [bar]	7.806	7.805	8.044	8.044
Δp_{H2} [bar]	-0.001	-0.004	-0.000	-0.002
$\dot{m}_{hot}$ [kg s^{-1}]	4.79	0.33	1.84	0.33
$T_{hot,in}$ [K]	573.9	453.2	579.9	453.2
$T_{hot,out}$ [K]	548.1	423.6	545.3	430.0
$\dot{Q}$ [kW]	128.6	63.1	83.2	56.3

It is important to note that the heat exchangers alone cannot bring the hydrogen to the required 150K. This final temperature increase is achieved by the gas compressor, which, by doing work on the GH$_2$, provides final temperatures at the injector of 151.0K and 152.6K at cruise.

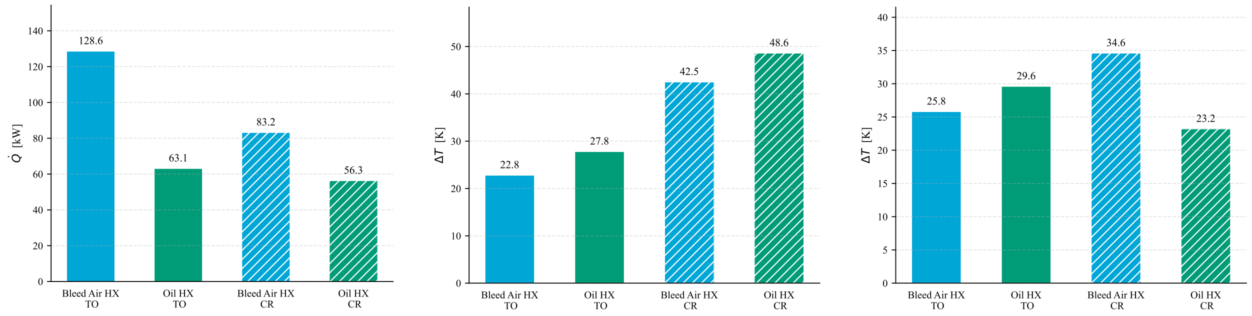

(a) Heat duty $\dot{Q}$ **(b)** H$_2$ temperature rise ΔT_{H_2} **(c)** Hot-side temperature drop ΔT_{hot}

Figure 7.7: Heat exchanger sizing results for the bleed air and oil heat exchangers at take-off (TO) and cruise (CR) conditions.

The conditions of the bleed air at the inlet of the heat exchanger are taken to be 580K and 850kPa. The bleed air will be extracted from the LPC, as the temperature is limited by the operating range of copper, as discussed previously. Since a precise map of the pressure and temperature profile in the LPC has not yet been developed, the pressure corresponding to this temperature is interpolated based on the pressure increase provided by the LPC as reported in Table 5.7. The same values are assumed for both take-off and cruise conditions for the preliminary sizing, assuming that the bleed air will be able to be extracted at multiple locations in the LPC based on the demand for the specific flight phase. The mass flow is instead taken to be 10% of the total core mass flow rate. This is a conservative estimate, as modern jet engines can sometimes bleed over 20% of the core mass flow [81]. It is hence possible to bleed more air, which could either be used for purposes such as cabin pressurisation and air conditioning directly, or could also be passed through the heat exchanger and improve its performance.

The engine oil is modelled using Simscape Fluid's built-in model for the SAE 5W-30 oil, with the Thermal Liquid Properties block[20]. This is done because the properties of aircraft engine oil are not readily available, and while aircraft engine oil generally has slightly higher operating temperatures and tends to be less viscous[21] [22], the properties are considered similar enough for this preliminary analysis. The oil is assumed to be circulated at a rate of $25\,\mathrm{L\,min^{-1}}$, and to exit the engine at a temperature of 180°C (453.2K)[20]. It is estimated that, for the Airbus A320, and hence also similar aircraft in its class, a normal oil operating temperature in the reservoir would be around 120°C (393.2K), as an oil temperature warning is displayed when the oil in the reservoir rises above 140°C[23]. Based on this estimate, the oil-cooling potential of the heat exchanger layout is highlighted. For take-off and cruise conditions, the oil is cooled from 453.2K to 423.6K and 430.0K respectively. Out of the required cooling ΔT of 60K, the oil heat exchanger provides 29.6K at take-off, and 23.2K at cruise conditions. The oil heat exchanger can therefore provide 49.3% of the oil cooling duty at take-off and 38.7% in cruise. This could lead to a significant reduction in the size of the conventional heat exchanger that would be used to cool the oil, somewhat compensating for the weight of the hydrogen-oil heat exchanger.

7.5. Turbine Cooling

As mentioned in Section 7.1, a portion of the bleed air that gets cooled down in the first heat exchanger is then used to cool the turbine blades of the HPT. This will be done in the form of film cooling, where cooling airflow is directed over the surface of the turbine blades to provide a layer of thermal insulation against the hotter core mass flow [48]. In this section, a preliminary analysis is performed to demonstrate the potential turbine blade cooling performance improvements that the cooling of the bleed air in the heat exchanger can provide. The analysis is performed at take-off conditions, for the single rotor-stator stage of the HPT.

7.5.1. Assumptions

Turbine cooling is still a heavily researched topic, and performing a detailed analysis is beyond the scope of this early design phase of project MAVERICK. In order to at least demonstrate the potential benefit of using cooled bleed air from the hydrogen heat exchanger, rather than the hotter bleed air directly from the LPC, a simplified, semi-empirical model for turbine film cooling effectiveness is used, proposed by Horlock [2]. The assumptions that this model makes are listed in Table 7.8.

Table 7.8: Assumptions made for the turbine cooling model

ID	Assumption	Justification / source
A-TC-01	The turbine blades are approximated by simple plate heat exchangers.	This keeps the heat transfer dynamics simple and can provide a reasonable first estimate for the heat transfer. [81]
A-TC-02	The constant C_{lam}, which accounts for the blade geometry and the heat capacity ratio of the hot and cooling gases, is set to 20.	During the early stages of design, the exact blade geometry and layout are unknown, so an accurate estimate for this value is difficult to obtain. Horlock recommends this value for state-of-the-art gas turbines [2].

---

[20] `https://nl.mathworks.com/help/releases/R2026a/hydro/ref/thermalliquidpropertiestl.html` (Accessed: 03/06/2026)

[21] `https://www.exxonmobildistributor.com/media/files/pdsMobil-Jet-Oil-II_3.pdf` (Accessed: 10/03/2026)

[22] `https://wiki.anton-paar.com/en/sae-viscosity-grades/` (Accessed:10/03/2026)

[23] `https://www.blackbox711.com/docs/site/Doc-A320/technical/oil-system-schematic/` (Accessed: 10/03/2026)

ID	Assumption	Justification / source
A-TC-03	The Stanton Number St_g of the hot gas is assumed constant at $1.5 \cdot 10^{-3}$.	Accurately determining the heat transfer properties, among which the Stanton Number, would require detailed knowledge of the blade geometry and the fluid dynamics in the turbine section. Horlock therefore recommends this value for state-of-the-art gas turbines [2].
A-TC-04	The overall technology factor C for the Horlock model is assumed to be 0.045. This is the product of C_{lam} and St_g, with an additional safety factor of 1.5.	The safety factor is assumed to correct the equation so as to better match real-world data. [81]
A-TC-05	Changes in fluid properties have a negligible effect on the overall technology factor C	Horlock notes that within the range of 1500K to 2200K and with conventional fluid cycles, C can be assumed constant without losing significant accuracy, as the changes in fluid properties have a negligible effect on it. [2]
A-TC-06	The cooling efficiency η_c is assumed to be 0.7.	Fixing a constant cooling efficiency simplifies the model by removing the need to accurately simulate the heat transfer dynamics. This value is recommended to better match real-world data [81].
A-TC-07	The film cooling efficiency η_f is assumed to be 0.4.	Fixing a constant film cooling efficiency simplifies the model by removing the need to accurately simulate the heat transfer dynamics. This value is recommended to better match real-world data [81].
A-TC-08	The stagnation temperature of the hot gas T_g for a stator row matches the temperature of the free stream. However, for a rotor, it is reduced by 100K.	This is done to account for the rotating frame of reference of the rotor blades. [81]
A-TC-09	The turbine blades will be made out of a nickel-based superalloy, with a maximum operating temperature T_b of 1320K.	Nickel-based superalloys are widely used for aircraft turbine blades due to their strength, toughness, and resistance to fatigue at high temperatures. Such a material will hence be used for the HPT blades, and can tolerate average temperatures of around 1320K. [1]

7.5.2. Method

Having determined the temperature of the bleed air when it exits the heat exchanger, the Horlock model allows the required cooling mass flow rate $\dot{m}_{fc}$ to achieve the maximum operating temperature of the HPT blades, 1320K (A-TC-08), through turbine film cooling. The algorithm described below follows the methodology used by Schneider [81].

For a rotor or stator stage, the thermal shielding of the turbine blade by the layer of cooling air is computed. This is quantified by the overall cooling effectiveness ϵ_0, which depends on the gas stagnation temperature T_g, the temperature of the cooling airflow T_c, and the blade's maximum operating temperature T_b (1320K as per A-TC-09):

$$\epsilon_0 = \frac{T_g - T_b}{T_g - T_c} \tag{7.18}$$

The cooling air mass flow ratio ζ is then computed using Horlock's equation for film cooling, using the computed ϵ_0, and the assumed values for C, η_c, and η_f listed in Table 7.8:

$$\zeta = \frac{\dot{m}_c}{\dot{m}_g} = C\frac{\epsilon_0 - (1-\eta_c)\epsilon_f - \epsilon_0\epsilon_f\eta_c}{\eta_c(1-\epsilon_0)} \tag{7.19}$$

If this ratio comes out less than or equal to zero, it indicates that cooling is not necessary, as the hot gas is already at or below the maximum blade operating temperature. The required cooling mass flow rate $\dot{m}_c$ can then be computed from ζ, given a certain hot gas flow rate $\dot{m}_g$ through the turbine.

To evaluate the total required cooling mass flow across each stage of the HPT, ζ is computed for both the rotor and stator, and the contributions are summed.

7.5.3. Results

The results of this analysis yield a required cooling mass flow rate $\dot{m}_c$ of $1.69\,\mathrm{kg\,s^{-1}}$ for the first stage of the HPT. This is required for a turbine inlet temperature of 1875K and a bleed air temperature of 548.1K out of the heat exchanger at take-off conditions. In contrast, if this air was not cooled in the heat exchanger, but was used for cooling directly when bled, an $\dot{m}_c$ of $1.77\,\mathrm{kg\,s^{-1}}$ would be required for this stage. These two points are highlighted in Figure 7.8.

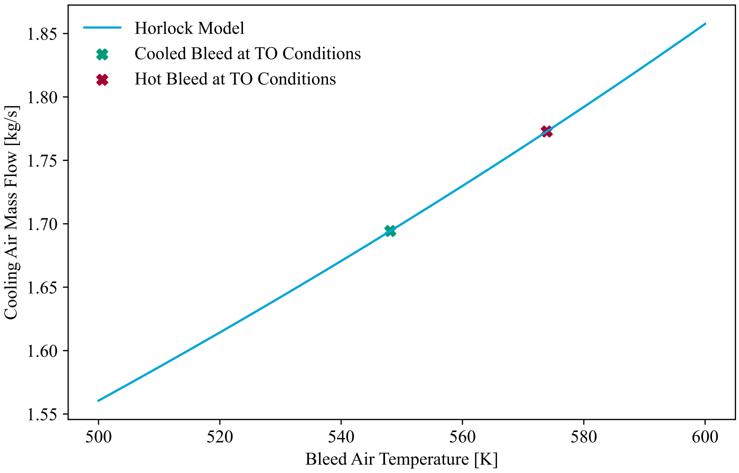

Figure 7.8: Required cooling mass flow rate predicted by the Horlock model for a single rotor-stator stage at take-off condition.

This analysis is only performed for the first stage of the turbine because it is quite complex to compute the temperature at each stage of the turbine, including the effect of the cooling of each stage before it. This would require an accurate model of the flow through the turbine and is a recommended next step to quantify the total gain that using the cooled air from the heat exchanger can provide. It is however demonstrated that using the cooled bleed air provides a reduction in required cooling mass flow of around 4.6%. A reduction in the total amount of required bleed air for turbine cooling would allow for a reduction in overall bleed mass flow, increasing the efficiency of the engine. A more detailed analysis of the turbine cooling could produce a more accurate result for this, and would allow the total engine efficiency gain over a mission to be determined.

7.6. Valves

Valves situated throughout the feed system regulate the flow of hydrogen, both liquid and gaseous. They are placed throughout the feed system diagram in Figure 7.2. They have different purposes, with five types present: shut-off (isolate flow in case of a leak), control (adjust mass flow rate per the thrust setting), pressure-regulating (open once a set pressure is exceeded), check (only allow one-way flow) and purge (for maintenance).

7.6.1. Tank control

The LH_2 tank features a specialised shut-off valve on the underside of the aircraft to enable refuelling. As explained in Section 6.3, the tank is sized for a design pressure of 2.0 bar, with a safety factor of 2.25. In situations where overpressure is encountered, a rupture disc situated on the upper side of the tank releases.

Since hydrogen contained in the tank constantly boils off, it also includes two pressure-regulating valves that maintain set tank pressures. They are set up on the upper side of the tank with significant separation between them for redundancy. One is a main pressure-regulating valve, and another is activated at higher pressures to mitigate spikes in pressure. This excess GH_2 is released through a vent stack, i.e. a pipe with an outlet at the top of the vertical stabiliser. As boil-off happens whenever there is LH_2 in the tank, including during ground operations, releasing the gas at the highest point of the aircraft when necessary to prevent overpressure in the tank is optimal for the safety of passengers and ground. This release is rare per the low hydrogen boil-off fraction of 0.117 %/day (see Table 6.3). Hence, in outpost airports during turnaround, the occurrence of gas release is rare and minimal. As hydrogen is much less dense than air with a high diffusivity [82], it floats up and gets quickly dispersed. Additionally, the tank features a purge valve for the purging of the tank during maintenance on its upper side.

Pressure in the tank must also not drop below a certain level [83] to ensure proper functioning of the pump, prevent two-phase flow and maintain flow rate controllability. This is partially mitigated by self-pressurisation of the tank, where some LH_2 vaporises at lower pressure. However, this is insufficient and is best mitigated through a classical pressurisation technique [83]. This entails extracting some LH_2 from the tank (through a control and check valve combination), heating it in a heat exchanger and returning the now-warm GH_2 to the tank ullage. This is especially relevant in periods of intense fuel use [84]. A control valve is also featured near the interface between the tank and the LH_2 pipe, which adjusts the flow from the tank. This valve can also serve to shut off the tank for its isolation. In case hydrogen fuel dumping is required, a shut-off valve opens to a dump mast and pump leading from the bottom of the tank to an outlet at the aftmost point of the aircraft.

7.6.2. Flow control

Since LH_2 is heated using a heat exchanger from bleed air, the engine is started up using kerosene. A bypass pipe is hence situated around the pump and heat exchanger, which allows recirculation of LH_2 flow and heats it quicker. To allow flow in this pipe exclusively, check valves are installed on both sides, along with shut-off valves to ensure the bypass pipe is only activated at the very beginning of operation.

Past the heat exchanger, the flow branches off into a pipe for blow-off controlled through a shut-off valve, and another into the injector. Flow into the injector is managed with a control valve, mass flow rate sensor and check valve combination, ensuring the correct non-reversed flow enters the combustion chamber.

7.7. Sensors

A range of sensors is required to ensure that the hydrogen feed system is controllable, with data coming from multiple sources for redundancy, as well as for detecting (hydrogen) leaks. Sensors are required both for controllability and leak detection. These sensors are the most important additional electronic hardware that will be required, along with a dedicated data-handling and processing module of the flight computer, which will log and process the sensor data.

7.7.1. Sensors for Controllability

As discussed in Chapter 6, the contents of the tank must be kept at highly specific conditions. Two pressure and two temperature probes are situated on the top and bottom of the tank, spaced apart longitudinally. This ensures different sources of measurements, providing redundancy. The pressure inside the tank is monitored using cryogenic pressure sensors such as HT-CPT-20SD1 from Hydrotechnik, operable from 21K for a pressure range of 0–10 bar[24]. The temperature is measured through cryogenic resistance thermometers such as the Wika Pt1000 class are appropriate with accuracy up to 3K[25]. The fuel level in the tank must also be precisely known, which is done through

---

[24] `https://www.hydrotechnik.co.uk/ht-cpt-20sd1-cryogenic-liquid-hydrogen-pressure-sensor` (Accessed 14/06/2026)

[25] `https://www.wika.com/en-gb/lp_cryogenic_thermometer.WIKA` (Accessed 14/06/2026)

capacitance level measurements[26]. This fuel level is verified through the following relation for fuel height h in the tank:

$$h = \frac{p_{\text{bottom}} - p_{\text{ullage}}}{\rho a_{\text{eff}}} \tag{7.20}$$

with ρ the density of the LH_2 and a_{eff} the effective vertical acceleration of the aircraft. The equation is obtained by considering $\Delta p = \rho g h$, where the difference in pressure between gaseous and liquid hydrogen is modelled as the hydrostatic pressure in the tank. This allows an independent fuel level calculation method, with which the other reading must match (keeping in mind that several effects such as slosh are unaccounted for by this equation).

Pressure and temperature sensors are featured at the ends of pipes around the pump and compressor to adjust the power supplied and achieve the required pressure change. These are also featured in LH_2 pipe annuli to ensure proper vacuum has been achieved. Mass flow rate sensors (placed as explained in Section 7.6), especially in the outlet of the tank and near the injector, adjust the proper setting of valves to meet the fuel flow indicated by the pilot. They also serve as an additional method to verify the tank contents, depending on the measured mass flowing out. By tuning the mass flow rate to the thrust setting and the pumps/compressors to the relevant requirements, sensors allow proper control of the fuel feed system.

7.7.2. Sensors for Leak Detection

The tank has been designed to prevent hydrogen leaks. However, in the event that leaks occur, these must be properly identified and acted upon. A robust method of monitoring the structural health of the LH_2 tank involves weaving optical fibre into the composite material. Through detecting changes in the wavelength of reflected light, the strain of optical fibres can be deduced. Structural damage can hence be detected and located as it occurs [85]. This, however, does not detect whether the change in fibre strain led to any leaks. To monitor this, three pressure and three temperature probes are built into the vacuum to detect the presence of a leak due to quick variations in these parameters. Temperature readings are especially important, as Distributed Temperature Sensors (DTS) have been found to be a reliable and sensitive manner of detecting hydrogen leaks [86]. This is especially crucial in cryogenic temperatures, where different types of hydrogen concentration sensors are not operational [87]. To verify whether it was hydrogen that leaked, Metal-Oxide Semiconductor (MOS) tin dioxide (SnO_2) sensors are integrated around the LH_2 pipes, which have been applied for precise hydrogen detection around cryogenic motors [88].

For monitoring of flow in the LH_2 pipes, five MOS sensors are integrated into the vacuum annulus, spaced equidistantly. Since there are also temperature and pressure sensors in the annulus, leaks in the pipes can also be detected from quick property (especially temperature) variations.

Leaks must also be detected in the wing where heat exchangers are situated, and in the engine bay. This is done by closely monitoring and comparing the mass flow rate entering the fuel system at the tank and that leaving at the injector, accounting for compressibility effects. Additionally, pressure and temperature are closely monitored through the sensors already in place that enable controllability. These are already located near valves, where leaks are likely to occur [89]. Additional MOS hydrogen concentration sensors are placed near the heat exchangers due to their high temperature gradients and long contained pipe length, and in the engine nacelles near the critical location of injection.

It must always be able to release hydrogen from the system, especially from the tank. As explained previously, this is done through the use of a vent stack. To verify that the vent stack is not blocked, an infrared sensor positioned at the exit pointing down the pipe verifies that the infrared light reflects and returns uninterrupted [90] and the vent stack is not blocked.

This setup of sensors provides a considerable amount of data to ensure the possibility of reliably controlling and monitoring the hydrogen feed system. This data must be processed and its result

---

[26] `https://www.endress.com/en/field-instruments-overview/level-measurement/Capacitance-level-Liquicap-FMI51` (Accessed 14/06/2026)

communicated to the pilot. The algorithm for this is explained in Section 10.2.

While each branch has two boost pumps for redundancy, only one gas compressor is present. This is because the gas compressors are much heavier, and having additional ones for redundancy would significantly add weight to the aircraft. It is therefore chosen to make use of pressure and temperature sensors located before, after, and inside the compressor to closely monitor its performance. The readings will be compared to their expected performance and power output throughout all flight phases, as well as to past performance, to detect degradation in efficiency. Any anomalous readings are flagged to the airline immediately to schedule additional inspections during maintenance. This will allow any issues to be detected early, before the performance of the compressor degrades too much and it fails. These methods of predictive maintenance are starting to become more widespread in a variety of fields, and various studies are evaluating the implementation of machine learning for these tasks [91]. Since the aircraft can still fly on kerosene alone, even if a compressor breaks, the aircraft is still able to land safely.

8

Sustainability Analysis

An important aspect of the MAVERICK design is the sustainability impact on the environment and climate in particular. The analysis starts with Section 8.1 where CO, CO_2 and NO_x emissions are quantified for the nominal mission and the trends are described, considering the feasibility of the design. In Section 8.2, the life cycle assessment of the aircraft is conducted. Furthermore, the noise emissions are discussed in Section 8.3. The chapter is finalised with additional sustainability considerations in Section 8.4.

8.1. In-flight Emissions

To quantify emissions and better visualise their trends, a Python model was developed. For the model, the Cantera library was used, allowing simulation of chemical reactions in the combustion chamber. However, before the detailed explanation of the used mechanism, it is important to mention the assumptions that were made. All of them are presented in Table 8.1.

Table 8.1: Assumptions used in the Cantera model.

ID	Assumption	Justification / source
A-CA-01	The model is zero-dimensional.	Unknown dimensions, complexity, and time constraints.
A-CA-02	The combustor has two zones - primary and dilution - where the fraction of air entering the primary zone is 0.7 of the total core air flow, and the rest goes to the dilution zone.	The combustor shall imitate the GEnx TAPS, which has a split of 70-30% for combustion and cooling, respectively [28].
A-CA-03	The fuel blend is injected fully premixed, meaning both kerosene and hydrogen are uniformly mixed.	Combustion mechanism of 0D reactor.
A-CA-04	The model does not simulate ignition mechanism and residence time.	Complexity of ignition mechanism and adjusting residence time for two zones.
A-CA-05	N-dodecane is considered a kerosene surrogate.	Good approximation for chemical properties, for simplicity, since kerosene usually is not a single compound.
A-CA-06	It is assumed that air consists only of oxygen (21%) and nitrogen (79%) particles.	Other gases in air account only for $sim1\%$ of total composition.

ID	Assumption	Justification / source
A-CA-07	Input temperatures and pressures for the primary zone are assumed to be the same as at the exit of the compressor and are taken from GasTurb 11 software for each phase.	The changes in these parameters between a compressor and a combustor are low.
A-CA-08	Air mass flows are scaled using the same approach as for thrust in Subsection 5.2.3, keeping values of 47.85 kg/s and 18.42 kg/s for take-off and cruise, respectively.	The air mass flow level depends on thrust level, so for simplicity in modelling, they are assumed to be proportional to thrust changes.

8.1.1. Cantera Method

The model aims to imitate a combustor with two zones, namely, primary and dilution. For that, two separate reactors are used and treated as ideal reactors where chemical reactions are solved based on thermodynamic and kinetic data files. For each box there are inputs and outputs. The fuel and 70% of incoming air are the inputs for the primary zone. For the dilution zone, the output from the first zone is taken as an input, and the remaining air is added. The output from the dilution zone is treated as the exit of the combustor, containing all emissions produced. Moreover, for each reactor, initial temperature and pressure are required. The input temperature and pressure for the dilution zone are those after the combustion in the primary zone. The block diagram showing the whole process is presented in Figure 8.1.

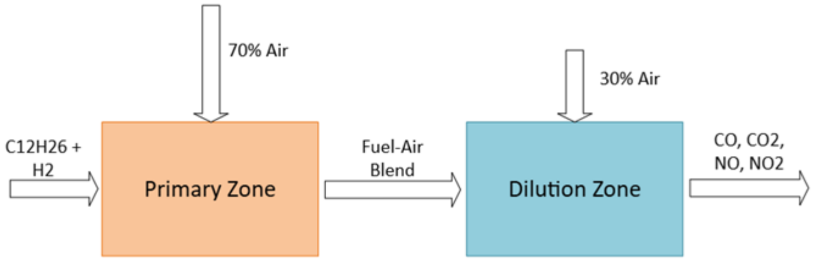

Figure 8.1: Block diagram of the combustion process in the model.

8.1.2. Results and Analysis

The emissions are simulated for one engine for a one-way mission to obtain the total emissions. For the out-and-back profile the results must be quadrupled. For the 2000 km mission profile, a summary of the results is presented in Table 8.2. For each flight phase, the following are given: hydrogen mass and energy fractions (H_{2mf} and H_{2ef}), total fuel burnt, the TIT, global and primary zone equivalence ratios (ϕ and ϕ_{pz}) and the Emission Index (EI_{xx}) for each type of emissions.

Table 8.2: Results per flight phase for one engine for the 2000 km mission (one way).

Phase	H_{2mf} [%]	H_{2ef} [%]	Fuel burnt [kg]	TIT [K]	ϕ [–]	ϕ_{pz} [–]	EI_{CO} [g/kg]	EI_{CO2} [g/kg]	EI_{NOx} [g/kg]
Taxiing	50	74	115.9	1815	0.25	0.36	0.098	1550	384.6
Take-off	24	47	29.7	1885	0.29	0.41	0.302	2356	327.3
Initial climb	24	47	96.2	2053	0.35	0.50	1.364	2356	411.7
Climb	25	48	617.5	1991	0.33	0.47	0.794	2325	386.0
Cruise	43	68	1255.5	1864	0.31	0.45	0.304	1767	330.0
Descent	33	58	74.6	1893	0.29	0.41	0.289	2077	368.4
App.+Land.	31	56	98.4	1922	0.30	0.43	0.390	2139	376.0

The adjustment of hydrogen ratios (mentioned in Section 5.2) also considered the TIT and modes of combustion. Since the design aims to imitate the TAPS, the combustion should be kept in the lean regime for each flight phase, meaning the equivalence ratios must be lower than 1 ($\phi < 1$). Furthermore, the combustor exit temperature must be kept below a limit (in this case the limit was chosen to be 2100 K), as higher temperatures could exceed the melting point of the turbine blade material.

The same format of results was obtained for a one-way, 3000 km mission. The hydrogen mass and energy ratios, the total fuel burnt, the TIT, equivalence ratios, modes and the emission indices are shown in Table 8.3. The major change in comparison to the 2000 km range mission (as already discussed in Section 5.2) is lower hydrogen ratios since for this mission profile the aircraft has more kerosene than for the nominal mission.

Table 8.3: Results per flight phase for one engine for the 3000 km mission (one way).

Phase	$H_{2\text{mf}}$ [%]	$H_{2\text{ef}}$ [%]	Fuel burnt [kg]	TIT [K]	ϕ [–]	ϕ_{pz} [–]	EI_{CO} [g/kg]	EI_{CO2} [g/kg]	EI_{NOx} [g/kg]
Taxiing	50	74	121.9	1855	0.27	0.38	0.147	1550	411.3
Take-off	14	31	31.3	1824	0.27	0.39	0.186	2666	259.7
Initial climb	17	36	101.2	2021	0.34	0.49	1.139	2573	362.1
Climb	18	38	649.6	1961	0.32	0.46	0.664	2542	339.2
Cruise	24	47	2493.0	1734	0.28	0.39	0.102	2356	208.4
Descent	21	43	78.5	1823	0.27	0.38	0.169	2449	284.9
App.+Land.	19	40	103.5	1848	0.28	0.40	0.223	2511	289.4

The comparison of total emission masses for each flight phase between 2000 km and 3000 km missions is presented in Table 8.4 (accounting for two engines). The table includes the total fuel burnt by two engines for a one-way mission, CO, CO_2 and total NO_x emissions. The values were calculated by multiplying the total fuel burnt (this includes both hydrogen and kerosene) by the emission indices (which are also scaled for total fuel burnt). The total grams per seat-kilometre were computed assuming 180 seats and the range of 2000 km and 3000 km, respectively, for each mission.

While the results for CO and CO_2 are of the correct order of magnitude, the value of NO_x emission is considerably larger. This is due to limitations of the model and complexity of modelling NO_x emissions, which will be further discussed in detail in Subsection 8.1.2 and Subsection 8.1.4.

Table 8.4: In-flight emission masses for two engines per phase, with totals. Columns compare the 2000 km and 3000 km ranges.

Phase	Fuel burnt [kg]		CO [kg]		CO_2 [kg]		NO_x [kg]	
	2000	3000	2000	3000	2000	3000	2000	3000
Taxiing	231.8	243.8	0.022	0.036	359.4	378.0	89.2	100.2
Take-off	59.4	62.6	0.018	0.012	140.0	166.8	19.4	16.2
Initial climb	192.4	202.4	0.262	0.230	453.4	520.8	79.2	73.2
Climb	1235.0	1299.2	0.980	0.862	2871.4	3302.6	476.8	440.6
Cruise	2511.0	4986.0	0.764	0.508	4437.0	11 747.0	828.6	1039.0
Descent	149.2	157.0	0.044	0.026	309.8	384.4	55.0	44.8
App.+Land.	196.8	207.0	0.076	0.046	421.0	519.8	74.0	60.0
Total [kg]	4575.6	7158.0	2.166	1.720	8992.0	17 019.4	1622.2	1774.0
Total [g/seat/km]	–	–	0.006	0.004	24.98	31.52	4.50	3.28

Furthermore, for better visualisation, emission trend graphs were created, showing the exit temperature (same as turbine inlet temperature) and emissions indices as functions of global equivalence ratios. The graphs aim to show the trends of emission production under given conditions and are presented in Figure 8.2. The values on these graphs may not reflect the results values since they were created using a constant fuel mass flow of 0.5 kg/s and varying air flows. Furthermore, on each graph, multiple lines are plotted, representing different hydrogen concentrations in the fuel blend.

Starting with the exit temperature graphs, a rapid increase in temperature is visible when increasing the equivalence ratio. That is due to less air available, acting as a heat sink. Moreover, there is no significant difference in temperature in terms of different hydrogen ratios in the lean combustion zone ($\phi < 1$).

For CO emissions, there is a visible increase in the emissions with increasing equivalence ratio due to the fact that the kerosene particles in richer combustion ($\phi > 1$) are not fully burnt and produce CO and soot. The graph shows correct behaviour, although the pure-hydrogen fuel line shows some CO emissions, which is not the case. For pure-hydrogen mode, the CO emissions must be 0 since there is no carbon in the fuel nor in air (AS-CA-06).

The CO_2 depends only on the concentration of kerosene in the fuel. For the higher hydrogen fractions, the CO_2 emissions are lower, which is clearly shown in the top right graph. The level of emissions does not change in terms of equivalence ratio for the lean combustion in the primary zone. In the rich combustion zone, it begins to decrease. However, for the global equivalence ratio, it is shifted, and values around 0.5-0.6 correspond to the higher equivalence ratios in the primary zone (about 0.85-0.95).

NO_x emissions refer primarily to NO and NO_2 compounds. Looking at the bottom-row graphs, it can be observed that most of the NO_x emissions come from NO, which is dominant. Moreover, the graphs show a peak of the emissions around the global equivalence ratio of 0.5 - 0.6 (normally it is around 0.85-0.95. However, due to the secondary zones, the values for the global equivalence ratio are shifted). This is due to a combination of higher temperature and higher air concentration, which allows production of so-called thermal NOx. Furthermore, the concentration of hydrogen significantly impacts the production of the emissions; the higher the hydrogen concentration, the higher the NO_x emissions are.

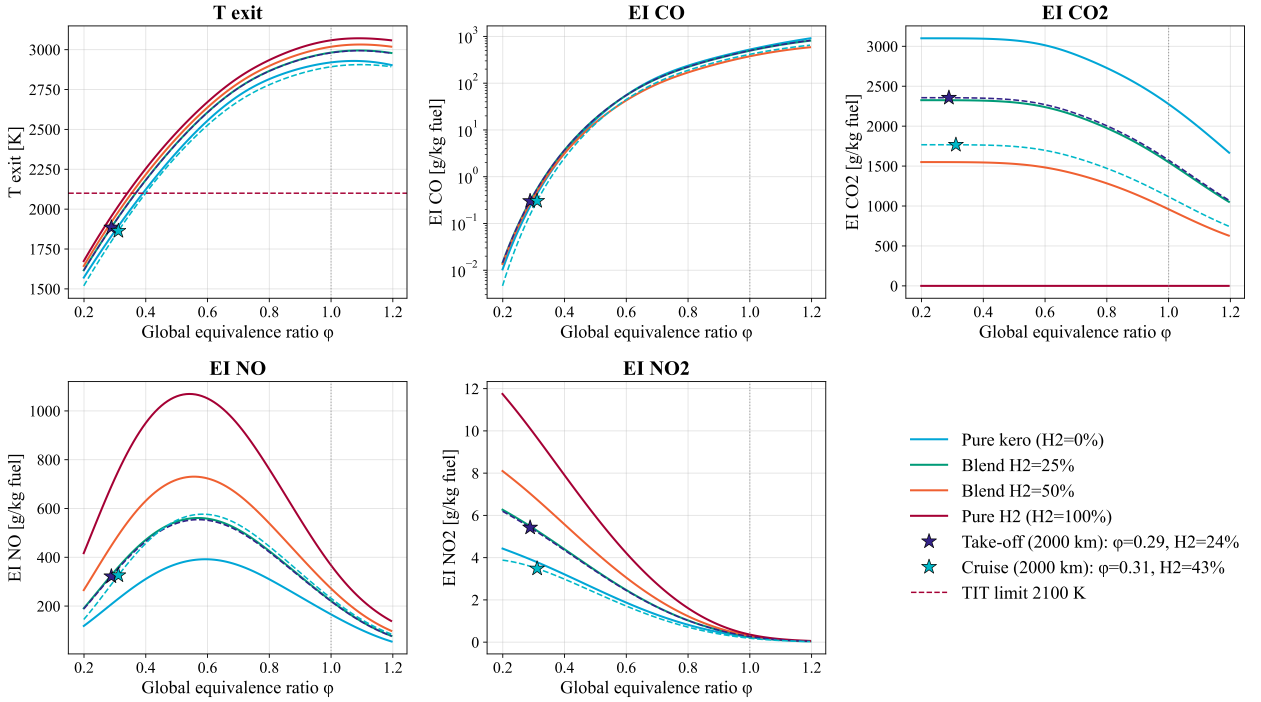

Figure 8.2: Emissions production trends for different blend and equivalence ratios with marked the design points for take-off and cruise for 2000 km mission.

8.1.3. Comparison with Pure-kerosene Mode and Reference Data

To verify the model's consistency, a comparison is conducted between the hydrogen-kerosene and pure-kerosene modes. Moreover, to confirm compliance of the design with requirements, the results are checked against reference data.

CO_2 Emission Indices

Starting with CO_2 emissions, Table 8.5 presents a comparison of CO_2 emission indices per flight phase with the indices of the pure-kerosene mode, as well as the difference in percentages.

Across all flight phases, the hydrogen-kerosene mode achieves a significant decrease in CO_2 emission indices compared to the pure-kerosene mode.

Furthermore, to verify compliance with the mission requirement REQ-MIS-SUS-02, which states a 50% reduction of CO_2 emissions per passenger-kilometre relative to the reference aircraft, as well as REQ-SUB- PRO-EMI-01, a comparison with A320neo CO_2 emission levels is conducted. For MAVERICK, the cumulative emission level is **24.98 g/seat/km**(Table 8.4) while for A320neo it is **56 g/seat/km**[92]. The resulting reduction of **55.4%** confirms compliance with both requirements REQ-MIS-SUS-02 and REQ-SUB-PRO-EMI-01, fulfilling the mission objective for CO_2 emission reduction on the nominal mission.

Table 8.5: Comparison of EI_{CO_2} between hydrogen-kerosene and pure-kerosene modes per flight phase (2000 km range).

Phase	EI_{CO_2} dual-fuel [g/kg]	EI_{CO_2} kerosene [g/kg]	Difference [%]
Taxiing	1550	3101	−50.0
Take-off	2356	3101	−24.0
Initial climb	2356	3101	−24.0
Climb	2325	3101	−25.0
Cruise	1767	3101	−43.0
Descent	2077	3101	−33.0
App.+Land.	2139	3101	−31.0

CO Emission Indices

For the CO emissions, Table 8.6 presents a comparison of CO emission indices per flight phase with the indices of the pure-kerosene mode, as well as the difference in percentages.

Across all flight phases, the hydrogen-kerosene mode achieves significantly lower CO emission indices than the pure-kerosene mode. The highest reduction occurs during taxiing, where the index falls from 0.262 g/kg to 0.098 g/kg (a reduction of 62.6%). This is a direct consequence of the combustion strategy: taxiing operates at high hydrogen ratios, and since hydrogen contains no carbon, CO formation is almost entirely suppressed. The low-power, fuel-rich conditions that normally cause poorer combustion efficiency and higher CO output in conventional engines are therefore mostly avoided.

The take-off phase shows the smallest improvement at 37.5%, with the index dropping from 0.483 g/kg to 0.302 g/kg. This is consistent with the strategy of using higher kerosene concentrations during take-off, where volumetric energy density and peak thrust take priority over emissions. With more carbon entering the combustor, the CO reduction is limited compared to the phases with hydrogen-rich blends.

Table 8.6: Comparison of EI_{CO} between hydrogen-kerosene and pure-kerosene modes per flight phase (2000 km range).

Phase	EI_{CO} dual-fuel [g/kg]	EI_{CO} kerosene [g/kg]	Difference [%]
Taxiing	0.098	0.262	−62.6
Take-off	0.302	0.483	−37.5
Initial climb	1.364	2.246	−39.3
Climb	0.794	1.319	−39.8
Cruise	0.304	0.758	−59.9
Descent	0.289	0.550	−47.5
App.+Land.	0.390	0.718	−45.7

During cruise, the index is reduced by 59.9% (from 0.758 g/kg to 0.304 g/kg), reflecting the hydrogen-favoured mixture used in this long-duration phase. The approach and landing phase shows a 45.7% reduction (from 0.718 g/kg to 0.390 g/kg), consistent with the gradual lowering of hydrogen concentration during descent while still retaining a higher hydrogen fraction.

Overall, the results confirm that the phase-dependent combustion strategy delivers a reduction in CO emissions for all of the phases in comparison to the pure-kerosene mode using the same model.

The requirement REQ-SUB-PRO-EMI-04 states that in any fuel mode, the CO characteristic emission level of 14.79 g/kN in the LTO cycle cannot be exceeded to meet 50% reduction relative to the reference engine. To confirm compliance with this requirement, Table 8.7 shows values for CO emissions in both hydrogen-kerosene and pure-kerosene modes. The thrust levels are taken from Table 5.2 and the CO masses from Table 8.4. The values for thrust are doubled, accounting for two engines for the nominal mission, while the CO masses are already given for both engines.

The table proves the reduction of CO emissions in the LTO cycle for any fuel mode, achieving a maximum value of 7.12 g/kg for the pure-kerosene mode, which confirms that the reduction is achieved for any other fuel mode as well.

Table 8.7: CO emissions per flight phase in LTO cycle for the hydrogen-kerosene and pure-kerosene modes (range 2000 km).

	T	H_2-kerosene		Pure kerosene	
Phase	[kN]	m_{CO} [g]	[g/kN]	m_{CO} [g]	[g/kN]
Taxiing	16.3	22	1.350	116	7.120
Take-off	238.2	18	0.076	41	0.172
Initial climb	202.4	262	1.294	618	3.053
App.+Land.	71.4	76	1.064	220	3.081
Total			3.784		13.426

NO_x Emissions

Since the results of NO_x emission indices are extremely high, as observed in Subsection 8.1.2, a direct comparison with the reference data is meaningless; nevertheless, the results can still be used for trend analysis. To confirm the behaviour of reducing NO_x emissions by using hydrogen-kerosene blends, a comparison with the pure-kerosene mode was conducted using the same model. This means NO_x emissions are treated separately from the CO and CO_2 emissions and can be considered for all flight phases. The results of this comparison are presented in Table 8.8.

Table 8.8: Comparison of EI NO_x, fuel masses and total NO_x emissions for hydrogen-kerosene and pure-kerosene modes for the nominal mission (one engine, range 2000 km).

Phase	Hydrogen-kerosene		Pure-kerosene	
	EI NO_x [g/kg]	Fuel mass [kg]	EI NO_x [g/kg]	Fuel mass [kg]
Taxiing	384.59	115.9	215.50	219.7
Take-off	327.34	29.7	238.12	42.5
Initial climb	411.65	96.2	299.76	137.6
Climb	385.96	617.5	277.88	893.9
Cruise	329.65	1255.5	200.46	2222.3
Descent	368.37	74.6	243.10	118.7
App.+Land.	376.03	98.4	253.49	153.0
Total NO_x [kg]	**810.6**		**860.2**	

The results show a correct behaviour of emission indices. The higher the hydrogen concentration, the higher the values for the NO_x emission index are, showing consistency with the emission trends graphs (Figure 8.2). Furthermore, using the hydrogen-kerosene mode favours a reduction of the NO_x emissions. In the case of the nominal mission, there are 49.6 kg less NO_x emissions in comparison to the pure-kerosene mode, which corresponds to a 5.8% reduction.

This confirms that the model correctly captures NO_x emission behaviour with increasing hydrogen concentrations, proving that the emissions can be reduced using hydrogen-kerosene blends.

However, to obtain correct values (and order of magnitude), the limitations of the model (described in Subsection 8.1.4) must be overcome. Furthermore, in Subsection 8.1.7 another approach for NO_x emission quantification is presented.

8.1.4. Limitations

Since the model uses multiple assumptions, it is natural that limitations may appear, affecting the results. In this case, the limitations affect primarily the NO_x emissions, where the model captures the correct trends but not the correct order of magnitude of values. The main sources of these limitations are listed below:

- The mechanism of combustion does not account for the residence time due to the complexity of ignition simulation, which is the primary cause for higher values of the NO_x emissions.
- The model assumes no dimensions (0D), so fluid dynamics are not captured, meaning the mechanism of NO_x emission production behaviour cannot be fully represented (this includes generation of hot spots, auto-ignition mechanism and possible flashbacks).
- The model injects the fuel blend as it is premixed, which is not the case in the design since only hydrogen is partially premixed and kerosene is injected as a liquid, in tiny droplets.
- The injection of the fuel blend itself is not modelled, which is crucial when modelling NO_x emissions, since it may greatly impact the generation of emissions (as discussed in Section 5.4).

8.1.5. Recommendations

To improve NO_x emission results for the 0D Cantera model, it is advised to consider the residence time and ignition mechanism. However, the main recommendation to overcome the problem with high NO_x emissions is to create a 2D (or 3D) model to better simulate fluid dynamics and capture hot spots, auto-ignition and (possible) flashback mechanisms. Moreover, it is also advised to simulate the injection of fuel since it plays a crucial role in NO_x emissions reduction. With the refined injection model, it is important to make sure the kerosene fuel is not injected premixed and pre-vaporised, since it is not the case in this design.

8.1.6. Injector Contribution

One of the most distinctive features of the injector is the TAPS-like design, using a small premixing chamber in the main mixer. Optimisation of this premixing chamber greatly reduces local hot spots, reducing NO_x production and improving the liner life [28]. Additionally, in the pilot mixer, an axial swirler is added next to the radial swirler to improve mixing of the fuel without increasing residence time, reducing both NO_x production and the risk of autoignition. This reduction in NO_x is quantified using an empirical model based on statistical relations. The assumptions used for this model are presented in Table 8.9.

Table 8.9: Assumptions used in the injector NOx model

ID	Assumption	Justification / source
A-NO-01	The baseline EI_{NOx} is calculated using an empirical correlation.	Established semi-empirical correlation for gas turbine combustors [41].
A-NO-02	The primary zone volume is modelled as a cylinder with diameter D_{sw} and axial length $1.5 \cdot D_{sw} \cdot S_n$.	Approximation where the CRZ is proportional to the swirler diameter and Sn.
A-NO-03	The richer pilot zone is the main contributor to NO_x formation.	The pilot flame is much richer and thus contributes significantly more to NO_x formation.
A-NO-04	EI_{NOx} from droplet diffusion flames scales linearly with SMD.	Mösl Eq. 5.11 [93], validated by Rink & Lefebvre observations [41].

ID	Assumption	Justification / source
A-NO-05	For a blended fuel, the overall $\mathrm{NO_x}$ is a mass-fraction weighted average of the individual fuel contributions.	Linear blending is assumed, neglecting interaction effects between hydrogen and kerosene.

These assumptions create a basis to estimate LTO $\mathrm{NO_x}$ emissions, and the overall emissions for a specified mission profile.

8.1.7. Method

Standard empirical correlations often fail to capture the severe emission penalties associated with poor atomization in lean-burn setups. Therefore, a hybrid analytical model was developed, anchoring legacy gas-phase correlations to modern droplet diffusion physics, and integrated into a multi-point optimisation framework.

The foundational $\mathrm{NO_x}$ estimation relies on a semi-empirical correlation by Lefebvre, which models thermal $\mathrm{NO_x}$ formation as a function of primary zone temperature (T_{pz}), combustor pressure (P_3), and aerodynamic residence time [41]. The baseline Emission Index (EI_{NOx}) is calculated using Equation 8.1.

$$EI_{\mathrm{NOx,\,baseline}} = \frac{9 \times 10^{-8} \cdot P_3^{1.25} \cdot V_c \cdot \exp(0.01 \cdot T_{st})}{\dot{m}_A \cdot T_{pz}} \tag{8.1}$$

where V_c is the primary zone volume dictated by the effective Sn, T_{st} is the stoichiometric flame temperature, and $\dot{m}_A$ is the primary zone air mass flow.

In a lean-burn architecture, the assumption of instantaneous vaporisation breaks down if the Sauter Mean Diameter (SMD) of the injected liquid fuel is too large. Unevaporated fuel droplets survive into the primary zone and burn as localised diffusion flames. As noted by Rink and Lefebvre [41], under high-pressure conditions where evaporation time is not negligibly small, a reduction in mean drop size actively decreases NO_x emissions by suppressing these localised high-temperature zones.

To quantify this phenomenon, the model integrates analytical droplet flame derivations by Mösl, who states that the $\mathrm{EI_{NOx}}$ scales linearly with its initial droplet diameter (D_0), $EI_{NOx} \propto D_0$ [93]. To implement this mathematically, the baseline Lefebvre equation is anchored to a reference SMD (40 μm)[94]. A continuous linear atomization multiplier is applied to the kerosene fuel fraction based on the evaluated SMD of the injector design as defined in Equation 8.2[93].

$$K_{ker} = \frac{SMD_{\mathrm{eval}}}{SMD_{\mathrm{ref}}} \tag{8.2}$$

Where K_{ker} is the constant by which the calculated SMD is multiplied, SMD_{eval} is a result of the empirical relation by Lefebvre and SMD_{ref} is 40 µm [41].

8.1.8. Results and Analysis

The $\mathrm{NO_x}$ emissions are simulated for one engine with 18 injectors in the annular combustion chamber. For the 2000 km mission profile, the estimated emissions are presented in Table 8.10. For each flight phase, the hydrogen mass and energy fractions, total fuel burnt, and $\mathrm{EI_{NOx}}$ are given.

Table 8.10: Results per flight phase for one engine for a 2000 km mission (one way).

Phase	$\mathrm{H2_{mf}}$ [–]	$\mathrm{H2_{ef}}$ [–]	Fuel burnt [kg]	$\mathrm{EI}_{\mathrm{NO}_x}$ [g/kg]
Taxiing	0.50	0.74	115.9	8.0
Take-off	0.24	0.47	29.7	10.9
Initial climb	0.24	0.47	96.2	10.0
Climb	0.25	0.48	617.5	10.1
Cruise	0.43	0.68	1255.5	11.1
Descent	0.33	0.58	74.6	6.5
App.+Land.	0.31	0.56	98.4	10.8

These emission indices are much lower than those provided by the Cantera model in Table 8.2, as they are currently based on empirical relations. As the Cantera model is limited in $\mathrm{NO_x}$ prediction, these values are expected to provide a better estimation of the actual $\mathrm{NO_x}$ emissions. Driving the emissions down is especially hard in flight phases with a higher hydrogen fraction, as this inherently produces more NO$_{\mathrm{x}}$. These flight phases have thus received extra attention to produce favourable conditions.

The total NO$_{\mathrm{x}}$ emission masses per flight phase are presented in Table 8.11, which accounts for two engines. This includes the total burnt fuel and the NO$_{\mathrm{x}}$ emissions, which are calculated by multiplying the amount of fuel burnt by the emission indices. Additionally, the total emissions per seat per kilometre are computed assuming 180 seats and the nominal range of 2000 km.

Table 8.11: In-flight emission masses for two engines per phase, with totals (2000 km range, 180 passengers).

Phase	Fuel burnt [kg]	NO$_x$ [kg]
Taxiing	231.8	1.85
Take-off	59.4	0.65
Initial climb	192.4	1.92
Climb	1235.0	12.47
Cruise	2511.0	27.87
Descent	149.2	0.97
App.+Land.	196.8	2.13
Total [kg]	4575.6	47.87
Total [g/seat/km]	–	0.13

The NO$_{\mathrm{x}}$ formation is modelled using an empirical relation derived by Lefebvre. Driving factors are the pressure and the size of the CRZ, which increase NO$_{\mathrm{x}}$ production, while an increase in air mass flow causes a reduction, by creating leaner combustion conditions. A better atomisation (smaller SMD) also drives the NO$_{\mathrm{x}}$ emissions down by reducing the hot spots that originate from larger droplets burning up. Thus, as the pressure and air mass flow are dictated by the flight phase (from GasTurb), the injector is optimised to produce a low Sn throughout all flight phases while maintaining the 0.6 blowout limit, and atomise the kerosene fuel in droplets with a small SMD.

8.1.9. Comparison with Reference Data

Similar to the outputs of the Cantera model, these results are also compared against the LEAP-1A29 engine. The emission indices of NO$_{\mathrm{x}}$ are taken from the ICAO Aircraft Emissions Databank (03/2026)[1].

Table 8.12 shows the LTO cycle EI$_{NOx}$ comparison. As the injector is unable to provide a reduction over all phases, it is not possible to easily visualise the NO$_{\mathrm{x}}$ reduction. This is due to two critical phases, the taxiing and the approach and landing, which correspond to the LTO flight phases with the higher hydrogen fractions as specified in Table 8.10. This follows logically from the fact that hydrogen inherently produces more NO$_{\mathrm{x}}$ when combusted.

Table 8.12: EI$_{\mathrm{NOx}}$ comparison per flight phase [g/kg].

Phase	MAVERICK	LEAP-1A29	Reduction [%]
Taxiing	8.0	4.7	+70.2
Take-off	10.9	49.5	78.0
Initial climb	10.0	21.0	52.4
App.+Land.	10.8	9.3	+16.1

To verify compliance with the mission requirement REQ-SUB-PRO-EMI-03 and REQ-SUB-PRO-EMI-07, the NO$_{\mathrm{x}}$ emissions per kN and per passenger-kilometre are calculated by taking the overall nominal mission emissions and dividing these by the range and amount of passengers. The result of this is shown in Table 8.11, which produces an overall NO$_{\mathrm{x}}$ emission that is exactly the value specified in REQ-SUB-PRO-EMI-07. As for the LTO emissions per kN, the results are shown in Table 8.13, where the thrust is taken from Table 5.2.

Table 8.13: NO$_x$ emissions by flight phase.

Phase	Thrust [kN]	NO$_x$ [g]	NO$_x$/kN
Taxiing	16.6	1854	111.7
Take-off	238.2	647	2.7
Initial climb	202.4	1924	9.5
App.+Land.	71.4	2125	29.8

This means REQ-SUB-EMI-07 is not satisfied, as for the low power and high hydrogen phases (taxi and approach), the threshold value is not met. For the take-off and initial climb phases, the requirement is met, and for the approach, the MAVERICK aircraft matches the current emission

---

[1] `https://www.easa.europa.eu/en/domains/environment/icao-aircraft-engine-emissions-databank` (Accessed 14/06/2026)

levels.

8.2. Streamlined Life Cycle Assessment (SLCA)

A Steamlined Life Cycle Assessment (SLCA) is used to quantify the EI over the aircraft life cycle. MAVERICK is expected to have additional EI in non-operational aspects such as maintenance, but a lower EI during operations.

8.2.1. Assumptions

The SLCA relies on the assumptions summarised in Table 8.14. The objective is to preserve consistency with the SLCA method presented by Vivalda [95], while still reflecting the main differences introduced by MAVERICK's hydrogen propulsion architecture.

Table 8.14: Assumptions used in the SLCA methodology.

ID	Assumption	Justification / source
A-LC-01	Similar components between MAVERICK and the A320neo are excluded from the comparison. This includes airframe, nacelle, avionics, furnishing, landing gear, and secondary systems.	Similar components have similar EI, which cancel out.
A-LC-02	MAVERICK's material composition is assumed to be similar to that of the A320neo.	Similar materials have similar EI, cancelling out in comparison.
A-LC-03	The operational environmental impact is not calculated by inserting engine emission outputs into the SLCA. The masses of hydrogen and SAF are converted into environmental impact using Vivalda's inventory.	This keeps the MAVERICK and A320neo assessments consistent.
A-LC-04	The mass of SAF extracted/produced is assumed equal to the mass of SAF used during a mission.	Simplifies the fuel production calculation and is conservative, since it includes contingency fuel that is not consumed on every flight.
A-LC-05	Maintenance is assumed to be spread evenly throughout the lifetime.	Estimating the number of flights per day and creating detailed maintenance schedules is beyond the scope.

8.2.2. Method

The method adopted in this study is based on the work of Vivalda [95], who creates an approach to perform SLCA based on parametric equations. Vivalda's inventory is used for the analysis. The approach is useful because it is constructed for aircraft in the conceptual phase, where only preliminary mass budgets are available, matching the current stage of MAVERICK. Although based on Vivalda's work, the SLCA analysed here focuses on differences with respect to the reference aircraft rather than absolute values. This is achieved by using A320neo values as baseline and applying correction factors to estimate MAVERICK's. Using Equation 8.3, one can estimate each system/process EI:

$$EI_{\mathrm{MAV},i} = W_{\mathrm{MAV},i} \cdot EI_{\mathrm{constant},i} \cdot C_i \tag{8.3}$$

where $W_{\mathrm{MAV},i}$ is the estimated quantity of the system or process, represented by mass, time, or energy; $EI_{\mathrm{constant},i}$ is the EI constant taken from Vivalda's inventory; and C_i is the correction factor applied to account for the difference between MAVERICK and the A320neo, particularly concerning the novel systems. The chosen C_i is based on engineering judgement as explained below:

Insulation: There is additional insulation required for the cryogenic feed system. This adds complex manufacturing and weight [51]. A C_i of +10% is applied.

Thermal management system: There is a need to monitor and control the thermal system more closely, mainly in the propulsion system. Because air conditioning and other thermal management systems remain the same [26, 32], a correction factor of +5% is applied.

Electricity usage: APU is expected to be more advanced in 2040, making the emission footprint of electricity generation smaller, thus a correction factor of -20% is applied.

Daily/Weekly maintenance: Due to novel and complex technologies/systems, day-to-day maintenance is expected to increase [96], due to the cryogenic system. However, it is not expected to increase by much as these checks mainly consist of, for example, oil level and pressures of hydraulics checks [96, 97]. A penalty of +5% is applied.

Ground support: It entails the use of ground service equipment/infrastructure and gate support activities, which are expected to grow for hydrogen-powered aircraft [4, 98]. A correction factor of +10% is applied.

Scheduled maintenance is also expected to increase [97]. This is further analysed in Section 11.2, and the resulting additional maintenance hours are already included in the SLCA, thus no correction factor is required. Similarly, the hydrogen system only affects MAVERICK and is therefore included directly in its assessment, while SAF use is calculated from MAVERICK's mission profile. The novel APU also requires no correction factor, as its increased kg CO_2 -eq is already included in Vivalda's database [95].

The SLCA is split into operational and non-operational phases. Operational impacts are evaluated for one return flight, while non-operational impacts are treated as life cycle burdens. Operational impacts include everything related to every return flight, including, for example, the generation of LH_2 and its use. Non-operational impacts include components that have a one-time impact, including, for example, the hydrogen tank and scheduled maintenance. This keeps mission and life cycle effects separate.

Moreover, the systems and functions are grouped into categories. This makes the analysis more meaningful and avoids assigning small importance to isolated components with small impacts. The systems/functions evaluated in this study are summarised in Table 8.15.

Table 8.15: SLCA components considered in the differential comparison between MAVERICK and the A320neo.

Component	C_i	Phase	Impact group
LH_2 tank production	1.00	Non-operational	Hydrogen system
LH_2 well-to-tank	1.00	Operational	Hydrogen system
LH_2 tank-to-wake	1.00	Operational	Hydrogen system
/kerosene well-to-wake	1.00	Operational	Energy
Novel APU	1.00	Non-operational	Energy
Electricity usage	0.80	Operational	Energy
LH_2 insulation production	1.10	Non-operational	Aircraft system
Thermal management system	1.05	Non-operational	Aircraft system
Organisational maintenance	1.05	Operational	Maintenance
Intermediate maintenance	1.00	Non-operational	Maintenance
Depot maintenance	1.00	Non-operational	Maintenance
Ground support	1.10	Operational	Ground operations

The A320neo baseline EI is estimated using literature values, such as fuel consumption and APU mass, and regulatory sources for operational requirements such as maintenance. Global warming potential, expressed as kg CO_2 -eq, is selected as the impact metric. The calculation sheet can be accessed in the accompanying SLCA spreadsheet [2].

---

[2] SLCA spreadsheet: `https://github.com/mcruz05/MAVERICK-DSE/blob/2126200f834b69f02330374f14c80e993ccd102c/LCA_MAVERICK%20(1).xlsx`

As a summary, the SLCA procedure is implemented as follows. First, the A320neo is defined as the reference aircraft. Second, the systems and processes whose EI is expected to differ are identified. Third, each different system is assigned a quantity, expressed as mass, time, or energy. Fourth, each quantity is multiplied by the corresponding EI constant from Vivalda's database. Finally, a correction factor is applied when the system exists in both aircraft, and its impact is expected to differ from the A320neo baseline.

8.2.3. Results

The A320neo currently runs on kerosene[3], whereas MAVERICK is assumed to combust SAF, as this is the most likely scenario in 2040. To allow for a trustworthy comparison, two scenarios for the A320 are considered: one using kerosene and one using SAF, shown in Figure 8.3. The latter provides a fairer comparison for aircraft entering service in 2040, since by 2050 at least 70% of aviation fuel is mandated to be SAF [3]. Figure 8.16 shows the values for the environmental impact of using kerosene/SAF in the A320neo, and the percentage improvement of MAVERICK for the two scenarios.

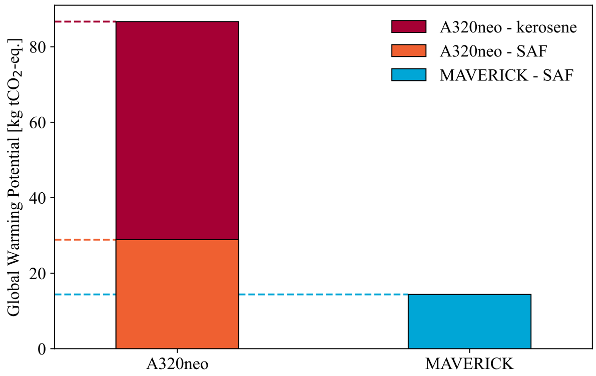

Figure 8.3: Comparison of different fuels used for A320neo vs. MAVERICK operating on SAF. All emissions are transformed into kg CO_2 -eq, for one return flight.

Table 8.16: Fuel EI comparison between MAVERICK operating on SAF and the A320neo operating on either kerosene or SAF.

Comparison case	GWP [kg CO_2-eq.]	Difference
A320neo kerosene	86,676	-83.4%
A320neo SAF	28,892	-50.2%
MAVERICK SAF	14,384	–

As can be seen in Figure 8.16, the optimistic forecast where kerosene is used in current state-of-the-art leads to an 83.4% reduction in emissions. For the conservative estimation where the reference aircraft runs on SAF, MAVERICK still complies with the 50% emission reduction. The fair approach to a SLCA is to compare the two aircraft operating at the same time. Therefore, the remainder of the analysis assumes the A320neo operates on SAF, which is a conservative estimation, as it is not expected that in 2040 aviation will only run on SAF. This is the most conservative approach, as it represents the worst-case scenario for comparison.

The operational EI impact of MAVERICK is 13.96% lower than that of the A320neo, whilst the non-operational impact is 46.5 % higher than the reference aircraft (refer to Table 8.15 for definition of operational and non-operational). The operational impact of MAVERICK is expected to decrease as hydrogen production is still a novel and (environmentally) expensive technology, which is anticipated to decrease in the following years if hydrogen is considered a viable fuel alternative. Note that operational EI is more extensive

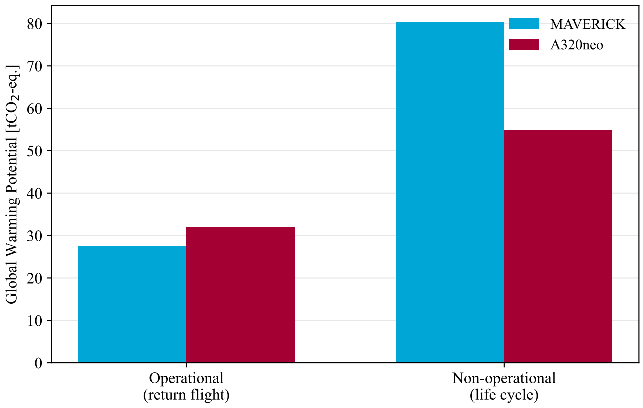

Figure 8.4: Streamlined LCA comparison.

---

[3] `https://www.iata.org/en/programs/sustainability/sustainable-aviation-fuel-saf/` (Accessed: 17/06/2026)

than combustion emissions (see Table 8.15). The results of the SLCA for both operational and non-operational phases are shown in Figure 8.4. Albeit having a larger non-operational life cycle EI due to its increased complexity and novelty, MAVERICK's environmental footprint in the operational phase is reduced compared to current state-of-the-art aircraft.

To avoid directly comparing quantities expressed on different bases, the operational and non-operational results are also normalised to a common functional unit. The operational impacts are already expressed per return flight, and the non-operational impacts are amortised over the assumed aircraft lifetime of 24,000 return flights, which is the design lifetime of the reference aircraft, with whom MAVERICK seeks to be competitive [99]. For MAVERICK, the LH_2 tank impact is counted three times over the lifetime, which is taken as a conservative estimation given the lack of LH2 tank certification documentation [100].

As can be seen in Table 8.17, the operational effects are dominant. The category operational EI are presented in Table 8.18. Only contributions occurring during one return flight are included, such as hydrogen/kerosene generation and usage, operational electricity, daily maintenance checks, and ground support.

Table 8.17: Lifetime-normalised SLCA comparison per return flight.

Phase	**MAVERICK**	**A320neo**	**Difference**
Operational [kgCO_2-eq.]	27,407	31,855	-13.9%
Non-operational [kgCO_2-eq.]	4.79	2.29	+109.6%
Total EI	27,411.79	31,857.29	-13.9%

Table 8.18: Grouped operational SLCA results for MAVERICK and the A320neo per return flight. EI is evaluated in kgCO_2-eq.

Category	**MAVERICK**	**A320neo**	**Difference**
Hydrogen system	10,945.28	0.00	N/A
Energy	16,451.52	31,845.60	-48.34%
Maintenance	6.59	6.28	+5.00%
Ground operations	3.51	3.19	+10.00%
Total operational EI	**27,406.90**	**31,855.07**	**-13.96%**

The results show that MAVERICK introduces additional environmental impact through the hydrogen tank, LH2 production and consumption, cryogenic feed system, modified APU, maintenance, and additional ground support. However, these impacts are fixed penalties, diluting over the aircraft's lifecycle. Operational phases are treated on a return flight basis, whereas non-operational phases are evaluated for the aircraft's lifetime. For a comparison on the same basis, the non-operational phases listed in Table 8.15 are normalised in return flights, and their contribution is summed per category. While the total EI comparison indicates which aircraft has the lower overall impact, this breakdown identifies the sources responsible for the non-operational impact.

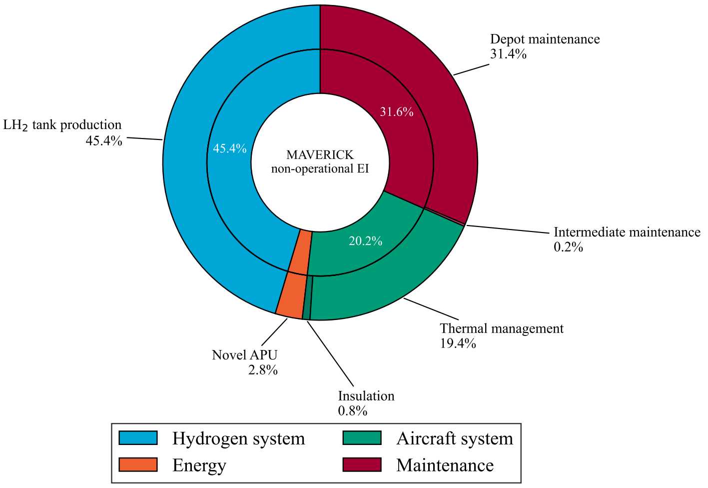

Figure 8.5: MAVERICK's normalised non-operational component EI.

As shown in Figure 8.5, MAVERICK's non-operational environmental impact is mainly driven by the hydrogen system, which accounts for 45.4% of the normalised non-operational EI.

Maintenance is the second-largest contributor, with 31.6% of the total. This is mainly caused by the increased depot maintenance required by the more complex dual-fuel architecture.
Overall, the SLCA indicates that MAVERICK offers environmental benefits during operation, mainly due to the reduction in fuel impact compared with the A320neo. Although the hydrogen architecture introduces additional non-operational environmental costs through the LH2 tank, cryogenic systems, maintenance, and ground support, these impacts become relatively small when distributed over the aircraft's lifetime. Therefore, under the assumptions of this assessment, MAVERICK's operational savings outweigh its added system complexity, making it an environmentally favourable alternative while still highlighting the hydrogen system and maintenance as the main areas for future improvement.

8.3. Noise Emissions

MAVERICK's sustainability objectives extend beyond gaseous and particulate emissions reduction to include noise reduction, since aircraft noise has a significant social impact. With increasingly ambitious European targets aiming to reduce perceived noise by 65% compared to 2000 levels, equivalent to a 15 dB reduction [101], it is important to assess the noise generated by the proposed engine. This is especially relevant since hydrogen combustion studies indicate that noise may increase with higher hydrogen fractions [102]. Typical noise certification is evaluated for three conditions: fly-by, representing climb-out noise; approach, representing approach noise at lower thrust; and sideline, representing lateral noise during maximum thrust take-off.

Similarly to the SLCA, this study compares noise levels between the reference aircraft and MAVERICK. Since MAVERICK's dimensions are mostly comparable to the A320neo, airframe noise is assumed to be comparable. Fan noise is also assumed comparable, as the bypass ratio and blade-tip Mach are similar to the reference engine. The main noise differences are therefore expected from combustion and jet velocity. Following consultation with Prof. Ragni,[4] combustion noise is assumed to be largely shielded by the nacelle, even under multi-fuel combustion. Furthermore, hydrogen/kerosene blended combustion can reduce overall acoustic emissions by approximately 55% [34]. Consequently, MAVERICK's engine noise variation is assumed to be driven by changes in jet exit velocity.

Jet noise is estimated using Lighthill's eighth power law, where subsonic turbulent jet acoustic pressure scales as $p^2 \propto U_j^8$ [103]. Since $SPL = 10\log_{10}(p^2/p_0^2)$, doing a simple mathematical derivation, the noise difference between MAVERICK and the A320neo is given by Equation 8.4:

$$\Delta SPL_{jet} \propto 80\log_{10}\left(\frac{U_{j,MAV}}{U_{j,A320neo}}\right) \tag{8.4}$$

Where ΔSPL_{jet} is the sound level difference between the two aircraft, and $U_{j,MAV}$ and $U_{j,A320neo}$ are the MAVERICK and A320neo exhaust velocities, respectively. Engine noise is certified using Effective Perceived Noise in Decibels (EPNdB), obtained by converting Sound Pressure Level (SPL) to Perceived Noise Level (PNL) and Tone-Corrected Perceived Noise Level (PNLT), then integrating the result over the noise-event duration. This conversion is complex and outside the scope of this analysis. After consulting with Prof. Merino Martinez,[5] changes in SPL are assumed approximately equal to changes in EPNdB, so ΔSPL_{jet} is used as the comparative noise metric. Since this variation depends only on jet exhaust velocity, Table 8.19 presents the ΔSPL_{jet} values for the three certification scenarios and the corresponding velocities. MAVERICK's exhaust velocities are derived from continuity, $U_j \approx (\dot{m}/\rho A)_{exhaust}$, using mass flows from the engine analysis in Section 5.2, while A320neo exhaust velocities are taken from literature.

---

[4] Personal communication with Dr. Daniele Ragni, Associate Professor in Aeroacoustics at Delft University of Technology, on 03/06/2026.

[5] Personal communication with Prof. Merino Martinez, Assistant Professor in Aeroacoustics at Delft University of Technology on 10/06/2026.

Table 8.19: ΔSPL_{jet} for the different certification scenarios [104–106].

Scenario	$U_{j,\text{A320neo}}$ **[m/s]**	$U_{j,\text{MAV}}$ **[m/s]**	ΔSPL_{jet} **[dB]**
Flyby	210	207	-0.49
Approach	120	103	-5.14
Sideline	220	207	-2.09

The negative ΔSPL_{jet} values indicate that MAVERICK is expected to have lower jet noise than the A320neo in all certification scenarios, as it can be seen in Table 8.19. The reduction is small for fly-by, but more significant for approach and sideline due to the lower MAVERICK exhaust velocity in these conditions.

Further noise reductions are possible through technologies such as acoustic liners, which can reduce noise by around 6 dB, and chevron nozzles, which enhance jet mixing and reduce noise by around 5 dB. More advanced concepts, such as active noise control, reduce fan noise by generating anti-phase pressure waves that interfere with the original sound field [101, 103]. Additional operational possibilities can be considered, such as Continuous Descent Approach (CDA), which can reduce approach noise and fuel consumption by avoiding step descent and sudden thrust increases. It is estimated that the CDA approach reduces noise by approximately 4 dB and descent fuel consumption by about 15 to 35

The noise reduction targets set by regulatory bodies are ambitious. Although new technologies make engine noise decrease, the rate of improvement is slowing [103]. Following consultation with Prof. Ragni, these targets are considered unlikely to be achievable even with advanced reduction technologies. Therefore, MAVERICK's predicted noise levels are considered competitive.

8.4. Additional Sustainability Considerations

Adding to the SLCA and noise analysis carried out above, two additional environmental considerations are taken into account. These are studied in smaller depth due to their research immaturity.

Soot: In a kerosene combustion engine, a fraction of fuel is not completely burnt, creating soot particles. Soot particles are hazardous because it pollutes the local air and accelerates global warming [11]. Soot mass is proportional to the amount of burnt kerosene [107], whereas hydrogen does not produce them because it has no carbon. Therefore, the reduction of soot emissions is proportional to the reduction of kerosene combusted. Hence, MAVERICK's reduction in soot emissions is directly proportional to the reduction of kerosene used, or its mass flow. The results of Δsoot are shown in Table 8.20. The amount of kerosene mass flow varies between flight phases. The relative soot reduction with respect to the A320neo can be estimated as:

$$\Delta\text{soot} = \frac{\dot{m}_{ker_{\text{A320}neo}} - \dot{m}_{ker_{MAV}}}{\dot{m}_{ker_{\text{A320}neo}}} \tag{8.5}$$

Table 8.20: Soot emission comparison between the A320neo and MAVERICK in various flight phases. Mass flows are expressed in kg/s [39, 108].

Phase	$\dot{m}_{\text{A320}neo}$	$\dot{m}_{MAV}$	**Δsoot [%]**
Take-off	1.20	0.538	-55.2
Climb	0.79	0.386	-51.2
Cruise	0.312	0.141	-54.7
Approach	0.13	0.283	+54.0

Table 8.20 shows that MAVERICK reduces the kerosene mass flow, and therefore the soot proxy, relative to the A320neo during take-off, climb, and cruise. These phases dominate the fuel burn, so the reduction indicates a lower soot contribution during the main energy-demanding parts of the mission.

The approach phase shows an increase, caused by the higher MAVERICK mass flow of keronese in this condition. Besides their direct environmental effect, soot particle considerations are also relevant because they can contribute to the production of long-lived heat-trapping clouds, known as contrails.

Contrail formation is a very active area of research. Persistent contrail formation is mainly governed by flight location and atmospheric conditions, especially the presence of ice-supersaturated regions, rather than only combustion dynamics [109]. However, combustion outputs still influence contrail formation: water vapour contributes to plume supersaturation, soot and other particles provide nuclei for water condensation and ice-crystal growth. Other contributors include exhaust temperature, volatile particles, sulphur compounds, and lubrication oil droplets. These effects are not treated further due to the scope of this project and the novelty of contrail research [110].

Hydrogen combustion increases the thermodynamic tendency for contrail formation due to higher water vapour emissions, but the reduction of soot (due to the reduction of hydrocarbons burnt) reduces the availability of ice nuclei particles. Therefore, hydrogen aircraft may form contrails under a wider range of conditions while these contrails may contain fewer ice crystals [109, 111]. Further research efforts should be made towards finding the implications of hydrogen combustion on contrails.

9 Verification & Validation

To ensure that the aircraft is designed according to its specifications and can perform as it is designed, a thorough V&V is performed. First, the models used in the design process are verified and validated in Section 9.1. The product verification is performed by means of a compliance matrix in Section 9.2. Lastly, the product validation procedure is described in Section 9.3.

9.1. Model V&V

In-house built software are hereafter called models. Each of these models has been verified and validated using software V&V methods. Longer or more complex models have a more extensive procedure. Commercial software used were also taken into account.

9.1.1. Aerodynamics

The airfoil selection model was tested through a single type of test, as it is a very simple model. The individual functions were tested by computing their outputs by hand and confirming that they match the expected outputs. All functions matched their expected outputs and thus they passed.

The lift and drag model was tested using two types of tests. First, the individual functions were tested to be correct by means of hand calculations. Secondly, the model as a whole was tested by means of sensitivity tests. This was done by varying selected inputs (C_L, e, C_{D_0}, and C_{D_c} of the fuselage) one at a time and checking whether the change of that input gives the expected change in the output. All functions passed the hand calculations test and the varying inputs had the expected effects on the outputs. All tests have thus passed.

The model used to size the HLDs was tested using the same method as for the lift and drag model. The inputs that were varied are $C_{L_{max}}$ in landing configuration, $(c'/c)_{TED}$, and $\frac{S_{wf,LED}}{S_{wf,TED}}$. Again, the functions matched the hand calculations and the input variation matched the expected outputs: all tests passed. The aircraft polar model was also tested using the same method. The inputs that were varied are AR, e, and α_{0L}. All tests passed for this model as well.

9.1.2. Aircraft Sizing

The sizing process of the MAVERICK aircraft utilised methods both newly developed during the project and those that are well established. Both were merged into a single iteration loop, yielding the converged design point. To develop confidence in the model, a series of unit tests was implemented to verify both individual module functionality and the integration logic. For instance, the proper functioning of the matching diagram (Section 3.6, which relates the wing loading to the thrust-to-weight ratio) was verified through unit tests and a hand calculation for specific parameters. The fuel sizing model was cross-validated against the Cantera model (Chapter 8) to confirm the resulting ranges under identical assumptions. At the converged mission fuel mass, the preliminary sizing model estimated a range of 1913 km against the 2000 km design target reproduced by the higher-fidelity Cantera model, a discrepancy of approximately 4.5%. The sizing model is therefore the more conservative of the two, slightly overestimating the fuel mass required to achieve a given range; accordingly, the range diagrams presented in Figure 4.3 are based on the sizing model rather than on the Cantera results. Furthermore, as direct data for the aircraft design point comparison does not exist yet, results were validated against similar single-fuel aircraft, accounting for a multi-fuel penalty. Comparison with A320 gives expected mass increase of around 15% for MTOM, which corresponds to a larger fuselage due to integration with hydrogen tank and additional dual fuel components.

9.1.3. Engine Design

Through the engine design process, several tools were implemented. These include the GasTurb software, a Cantera emissions model, and an injector design model, which are discussed in Chapter 5. These are verified and validated as follows.

The values obtained from the GasTurb software were verified and validated through comparison, using LEAP-1A reference performance values[1] [2].

The code for the Cantera model presented in Section 8.1 was verified and validated using unit tests and comparison to the reference data such as ICAO Aircraft Engine Emission Databank[3] or [92]. Moreover, a comparison of the results was done against the pure-kerosene aircraft case. This resulted in confirmation that the model is consistent throughout the assumptions and presents correct emissions trends for CO, CO_2 and NO_x, even though the values for NO_x emissions may not reflect reality due to the model's assumptions and limitations.

The injector design code was verified and validated using unit tests and comparison to reference data. The model is consistent with the assumptions, although a slight deviation shows up for the SMD, as this is based on an empirical relation derived for much older engines. The trends of Sn, SMD and EI_{NOx} follow patterns that reflect the reference data.

9.1.4. Hydrogen Feed System

The LH_2 piping system model presented in Section 7.2 was verified with unit and integration tests to check if the equations were implemented correctly and the modules interact as they should. The results show physically meaningful outcomes and were validated with the Simulink model. The pipe dimensions and parameters determined and assumed for the initial pipe sizing were implemented in the Simulink model, and the observed pressure drop was consistent across both models. The piping model predicted a pressure drop of 0.08 bar, whereas the Simulink model predicted 0.10 and 0.05 bar for take-off and cruise, respectively. These small absolute differences are considered acceptable, as they are all within 0.2% of the required pressure increase at take-off and 0.5% of that at cruise.

The Simulink model itself was also verified with unit and integration checks to ensure that all the input data and initial conditions were correctly specified and that the parameters and models used for the pumps, pipes, and heat exchangers were selected. The model is classified as a category III model [5], being a complex model with many components and dependencies. It is built using

---

[1] `https://www.kurzke-consulting.de/my-products/engine-models.html?view=article&id=50:cfm56-leap1a&catid=44` (Accessed: 16/06/2026)

[2] Personal communication with Dr. Gangoli Rao, Professor in the Faculty of Aerospace Engineering at Delft University of Technology on 02/06/2026.

[3] `https://www.easa.europa.eu/en/domains/environment/icao-aircraft-engine-emissions-databank` (Accessed: 16/06/2026)

Simulink, which is a commercial software, and uses the Simscape Fluids and CoolProp libraries to model the fluid network and its properties. These are also commercially available and are hence already verified and validated. The Simscape Fluids library uses physical equations and correlations to model fluid properties[4], and the validity of the assumptions made in these models is discussed throughout Section 7.3 and Section 7.4. CoolProp instead determines the thermodynamic properties of fluids by computing partial derivatives of the Helmoltz energy at specified conditions[5]. The models used in both of these libraries are therefore derived directly from physical relations and are assumed to be valid.

Due to the absence of experimental data regarding the feed system that has been developed for MAVERICK, it is difficult to validate the results. Instead, the response of the system when initialised from "cold" initial conditions, as per A-HX-07, is analysed and checked for physically consistent behaviour. The temperatures and pressures recorded throughout the simulation by the sensors shown in Figure 7.2 are plotted in Figure 9.1 for take-off conditions and in Figure 9.2 for cruise conditions. For both conditions, it is observed that the pressures in the system are predominantly constant throughout the simulation, with the expected pressure jumps caused by the pump and compressor at stations 2 and 6. The temperatures are instead observed to rise throughout the transient phase, as energy is added to the hydrogen flowing through the heat exchangers. In the phase where the temperatures plateau at the beginning, at around 30K, the hydrogen is evaporating in the heat exchangers and therefore the temperature recorded at the exits remains constant. When fully gaseous hydrogen leaves the heat exchangers, the temperatures increase until they settle in the steady-state response.

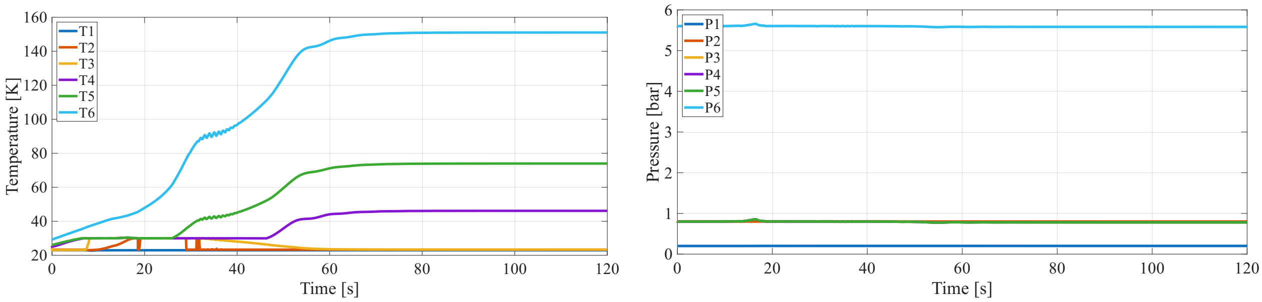

(a) Temperatures measured throughout the feed system during take-off conditions.

(b) Pressures measured throughout the feed system during take-off conditions.

Figure 9.1: Temperatures and pressures throughout the feed system, simulated over 120s at take-off conditions. Each temperature and pressure corresponds to the respective numbered sensor in the system (Figure 7.2).

At take-off conditions, T_2, just upstream of the bleed heat exchanger, is observed to increase while the hydrogen is evaporating. It then lowers again to the expected 23K of the incoming subcooled LH_2. Throughout this transient phase, some temperature spikes in T_2 and T_3 are observed. These are suspected to be numerical errors arising from the interpolation of the hydrogen's properties between certain points in the property tables. In the steady-state, constant temperatures and pressures are achieved in the feed system, indicating a stable, physically valid solution for the conditions in the network. Since the steady-state solution is of interest for the preliminary analysis, these inaccuracies in the transient dynamics are considered acceptable. Due to the high complexity of accurately simulating the transient dynamics for such a complex system and its strong dependence on initial conditions, it is recommended to perform real-world tests on either the full-size system or smaller models to assess the transient dynamics of the system and validate the system response.

---

[4] `https://nl.mathworks.com/help/hydro/index.html` (Accessed: 03/06/2026)

[5] `https://coolprop.org/fluid_properties/PurePseudoPure.html#list-of-fluids` (Accessed: 03/06/2026)

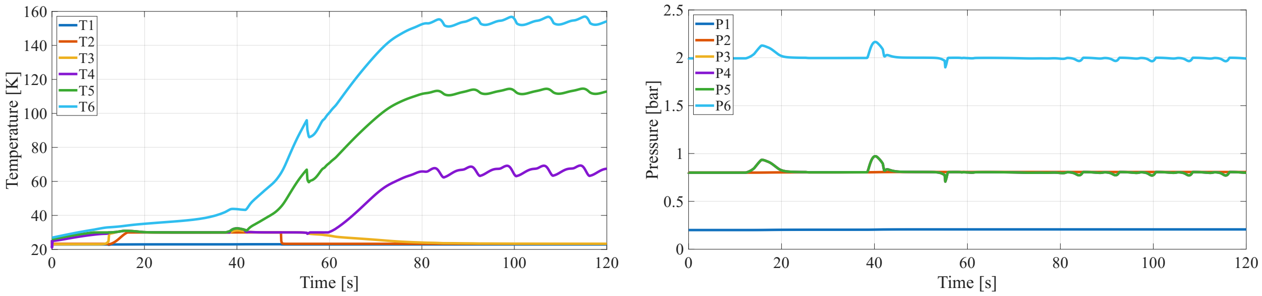

(a) Temperatures measured throughout the feed system during cruise conditions.

(b) Pressures measured throughout the feed system during cruise conditions.

Figure 9.2: Temperatures and pressures throughout the feed system, simulated over 120s at cruise conditions. Each temperature and pressure corresponds to the respective numbered sensor in the system (Figure 7.2).

Similar behaviour is observed for cruise conditions, with the main difference that the steady-state response fails to fully settle into constant temperatures and pressures. Instead, small oscillations are present around the final constant values. This is suspected to be related to the heat transfer coefficient model, as described in A-HX-04. It is possible that in at least one of the heat exchangers, the three zone boundaries fail to fully stabilise, causing the zones to slightly grow or shrink, and make the heat transfer rate fluctuate. The magnitude of the oscillations is observed to vary with the Colburn equation coefficients. It is therefore recommended to perform some tests to empirically determine accurate coefficients for the three zones and compare the response with these more accurate coefficients.

9.1.5. Turbine Cooling

As explained in Section 7.5, the Horlock model is used to quantify the effectiveness of the HPT film cooling [2]. A simple program was constructed based on this model to compute the required cooling air mass flow rate at the take-off condition design point. The code was therefore verified using unit and integration tests based on the Horlock model implementation for this same purpose described by Schneider [81]. These tests successfully verified that the model was correctly implemented.

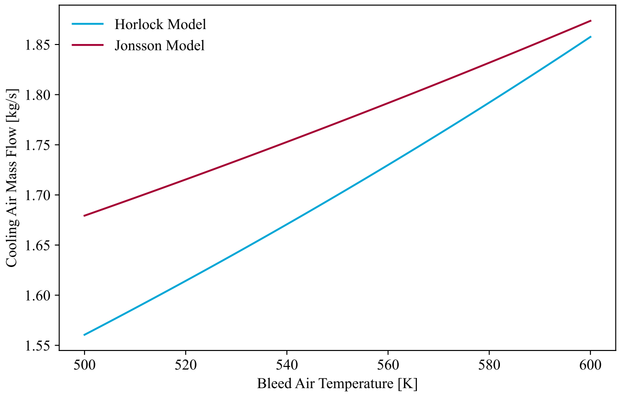

Figure 9.3: Comparison of the predicted cooling mass flow rate at take-off conditions by the Horlock and Jonsson models.

The results were also validated through comparison with the Jonnson model. This model uses slightly different assumptions and formulations, which, like those of the Horlock model, are also based on empirical data. The predicted mass flow rates at the take-off TIT of 1875.38K and hot gas mass flow rate of 45.925kg/s over a range of cooling flow temperatures are presented in Figure 9.3.

Both models show a similar, almost linear relationship between required cooling mass flow rate and required cooling mass flow rate. This shows consistency between the two models and increases confidence in the obtained results. The main difference between the two models is that the Horlock model under-predicts the required cooling mass flow compared to the Jonnson model, with the two models diverging at lower temperatures. At a bleed air temperature of 500K, the Horlock model predicts a required cooling mass flow of around 7.1% less than the Jonnson model. Nevertheless, the Horlock model is expected to be the more accurate of the two as it includes a specific correction for film cooling, while the Jonnson model assumes a more generic convection cooling configuration of the blades [81].

9.1.6. Hydrogen tank design

The vacuum-jacketed LH_2 tank is sized by a chain of closed-form models: thin-wall membrane stress for the inner pressure vessel, external-pressure elastic buckling for the outer jacket (Windenburg–Trilling interframe collapse for the cylinder [61], clamped-sphere buckling for the caps [65]), free-ring buckling for the stiffeners [65], and steady-state Fourier conduction with a latent-heat balance for the insulation and boil-off. Because the model is based on analytical equations, hand calculation is used, and validation reduces to confirming that the predicted thicknesses, heat leak, and boil-off fall within the ranges reported for cryogenic LH_2 tankage.

For verification, the two model families are checked. The membrane laws, Equation 6.1, have a closed-form thickness, so they are verified forward on round numbers: for $r = 2$ m, $p = 2$ bar, $\sigma_y = 400$ MPa and a yield factor SF = 1.5, the hoop rule $t = \mathrm{SF}\, p\, r/\sigma_y$ gives exactly 1.5 mm, which the code reproduces. The buckling laws, Equation 6.2, cannot be inverted for t in closed form, so they are verified in reverse: the solver's thickness is substituted back into the forward collapse formula and must return the design load $\mathrm{SF}_b\, p_{\text{ext}}$. On a round-number jacket ($R = 1$ m, $E = 50$ GPa, $\nu = 0.3$, bay length $L = 1$ m, $p_{\text{ext}} = 1$ bar, buckling factor $\mathrm{SF}_b = 3$) the solver returns 8.24 mm for the cylinder and 2.23 mm for the cap, and back-substitution recovers $p_{\text{cr}} = 3.000$ bar in both cases.

For validation, the tank reaches a gravimetric efficiency of $\eta_{\text{grav}} = m_{\text{LH2}}/(m_{\text{LH2}}+m_{\text{tank}}) = 3435/(3435+1636) \approx 0.68$. This places it at the upper end of the 0.2 to 0.7 range reported for integral LH2 aircraft tanks in the literature[112], which is optimistic but consistent with a slender vacuum-jacketed cylindrical tank operating at low pressure.

9.1.7. Fuel Control System

The fuel control model of Section 6.4 was verified with three tests, each isolating one mechanism, so that every expected output could be computed by hand. The first drives the CG toward an unreachable aft target to check the forward transfer path and the wing-full gate. The second mirrors it toward an unreachable forward target to check the reverse path and the trim-full gate. The third disables transfer to check the per-phase burn schedule in isolation. In every test, the simulated tank levels, CG station, and transfer rate reproduced the hand calculation and the fuel mass was conserved to within solver tolerance, so all three tests passed.

Validation assesses whether the simulated response is physically realistic. The key metric is the precision with which the controller maintains the target centre of gravity: over the simulated mission, the CG was held to within 1.0 mm of the trim set, as seen in Figure 6.5. While such sub-millimetre accuracy is not expected in practice, real systems are subject to sensor noise, actuator delays, and flow measurement uncertainty. This result demonstrates that the fuel transfer logic possesses sufficient authority to actively shift and regulate the CG throughout the flight envelope. The validation therefore supports the modelling approach not as a prediction of achievable precision, but as a confirmation that the control architecture is capable of effective CG management.

9.1.8. Competitiveness Analysis

The differential cost model of Section 11.4 was verified line by line, each line checked in the way it admits. The four cost terms, the year-zero capital outflow, the annual fuel cost, the carbon cost and the flat hydrogen maintenance, are closed-form expressions, so they were verified forward on round-number inputs and each reproduced the hand calculation, with the carbon term correctly collapsing to zero when the carrier mix is set entirely to green LH_2 or SAF.

Validation assesses whether the modelled costs are physically realistic. The fuel cost, the factor that dominates the net present cost, normalises to a per-Available Seat Kilometres (ASK) figure within the range reported for narrow-body operation, and the carbon cost falls by more than half from the kerosene aircraft to MAVERICK, consistent with the LH_2 share of mission energy displacing a matching fraction of the fossil carbon. Because the analysis is purely differential, retaining only the lines that differ and cancelling all revenue and common cost, it cannot be validated as a standalone profitability figure. The validation therefore supports the model not as a prediction of absolute cost, but as a confirmation that the cost ranking and its drivers are sound.

9.1.9. Return on Investment

The return-on-investment model of Section 11.5 was verified by separating its closed-form terms from its two numerically solved roots. The cash-flow terms, the acquisition outflow, the annual revenue and the discounted net present value are closed-form, so they were verified forward on round-number inputs and reproduced the hand calculation, including the annual revenue and first-year free cash flow. The internal rate of return and the break-even revenue are roots of a net present value set to zero and cannot be inverted in closed form, so they were verified in reverse by substitution: setting the unit revenue to the break-even value returned a net present value of zero, matching the zero crossing of the sensitivity sweep, and setting the discount rate to the internal rate of return did likewise. Every check passed.

Validation assesses whether the result is consistent with real airline economics. The unit revenue entering the model, 8.19 c/ASK, is built from the observed Air France-KLM FY2024 yield of 0.0933 e/pax-km and load factor of 0.878 [113], the load factor is close to the IATA 2024 European average[6]. The shortfall the model reports, a 0.39 c/ASK gap to the 8.59 c/ASK break-even, is a fare premium of 4.8% (a yield of 0.0978 e/pax-km) that is within the premium passengers are observed to pay for non budget airlines, and the near-zero internal rate of return of 0.1%, with a lifetime return on investment of +1%, places MAVERICK at the margin of viability, the expected position for a first-generation hydrogen narrow-body carrying a technology premium over a conventional aircraft. The validation therefore supports the model not as a forecast of profit, but as a confirmation that MAVERICK sits within reach of commercial break-even on today's fares.

9.2. Product Verification

To verify that the final MAVERICK design conforms to the requirements, a requirements compliance matrix is presented in Appendix A. Most of the requirements are met, while some requirements can only be verified in a later design stage. One important mission requirement (REQ-MIS-SUS-01) is only partially met, and will require additional analysis before the detailed design is finalised.

9.3. Product Validation

Before the final design can take flight, it needs to be validated that it performs as it is designed to do. This will be done by testing the main subsystems (engine, aerodynamics, structures, fuel system) and the complete aircraft. The whole procedure will take at least five years, but might take longer due to the novel systems [7]. The specific procedures for each testing phase are presented in this section.

The designed engine will be tested at the Turnkey test cell facility in Brussels, operated by Safran Test Cells, which provides test engineers and an aero-acoustic testing option [8]. Because MAVERICK uses both hydrogen and kerosene, all standard engine tests will be carried out across the full range of hydrogen-to-kerosene ratios, to confirm performance and safety at every operating condition. These tests include thrust level tests (take-off, climb, and cruise), fuel consumption tests at cruise, efficiency tests, thrust ramp-up tests, and noise level tests, plus safety tests covering extreme temperatures, endurance, reliability, object ingestion, structural integrity, and fire. Flashback testing requires extra attention, since the higher adiabatic flame speed of hydrogen makes this engine more susceptible to flashback than conventional engines [34]. Aerodynamic performance will be validated by wind tunnel testing at the European Transonic Windtunnel (ETW) in Cologne, a facility used for new aircraft development that simulates subsonic and transonic flow at the correct Reynolds number

---

[6] `https://www.iata.org/en/pressroom/2025-releases/2025-01-30-01/` (Accessed 16/06/2026)

[7] `https://www.easa.europa.eu/en/domains/aircraft-products/aircraft-certification#group-easa-related-content` (Accessed 22/06/2026)

[8] `https://www.safran-group.com/products-services/turnkey-test-cells-and-upgrades` (Accessed: 19/05/2026)

using low-temperature nitrogen flow on a sub-scale model, with full engineering support included [9]. These tests will validate lift, drag, pitching moment, and lateral stability across the full flight envelope, along with control surface and HLD performance, shockwave formation, and aeroelastic effects.

The structural integrity of the aircraft will be validated in collaboration with Applus+ IMA. The company has a testing site in Dresden and is experienced with aircraft testing at all scales, from component testing to full product testing [114]. The main structural tests that will be performed are on the landing gear, wings, fuselage, and the full aircraft. The landing gear will be tested for energy absorption and structural performance in landing simulation tests. The wings will be tested to comply with bending limits. The fuselage will be tested to sustain the cabin pressurisation by repeated pressurisation cycles. Additionally, it will be tested in overpressurised conditions to ensure it will not burst, even in abnormal conditions. Finally, the full aircraft will be tested to limit load without permanent deformation and to ultimate load without failure. Additionally, it is validated to sustain the cyclic loading of flights.

The novel fuel system requires additional testing. In addition to the standard testing that will be done on the kerosene fuel system, the hydrogen tank, pipes, valves, pumps, and heat exchangers need to be tested. The tank will be tested for pressurisation and thermal cycles, leaking and permeation, frost formation, and high impact stresses. The pipes and valves will be tested for leaking and frost formation. These tests can be carried out with Applus+ IMA [114]. The pumps and heat exchangers will be tested for performance over the full engine map and will be subjected to reliability tests. Additionally, the hydrogen leak detection and venting system must be thoroughly tested to ensure proper functioning of these systems in both operating and emergency conditions.

Lastly, the aircraft will be validated during a flight testing campaign. This campaign will be performed after all the ground tests have been carried out to confirm that the aircraft also functions as intended in real-world scenarios. The campaign covers, among other things, performance tests (in take-off, climb, cruise, descent, and landing conditions), stability and control tests, One-Engine Inoperative (OEI) tests, subsystem tests, emissions tests, noise tests, and emergency situation tests. This testing phase will be carried out at Rotterdam The Hague airport. This airport is chosen because it is part of GOLIAT[10], a development project for hydrogen infrastructure at airports. It already has LH_2 refuelling facilities for R&D and has performed tests with a hydrogen-powered aircraft before[11].

These activities are all part of the certification plan, shown in Figure 9.4. This provides an overview to certify MAVERICK in accordance with CS-25 regulations [115].

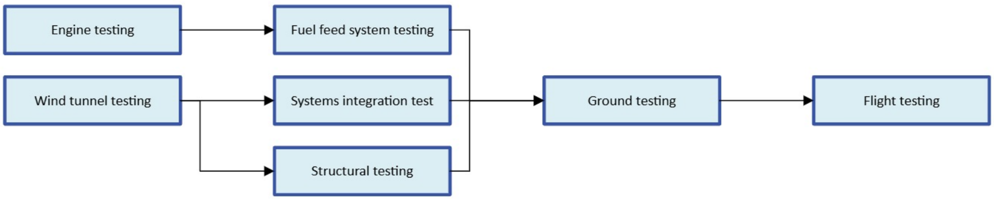

Figure 9.4: Post production certification plan for the MAVERICK aircraft including product validation. This provides a high-level overview of the procedures that are necessary for certification.

Additional tests or procedures may be required depending on changing regulations or stricter standards. In case of failed tests, this may require alterations of the design and retesting of other steps. Certification activities parallel to the production include leak and pressure tests, and are highlighted using blue blocks in Section 11.1.

---

[9] `https://www.etw.de/` (Accessed: 20/05/2026)

[10] `https://www.research.airbus.com/en/products-systems/goliat` (Accessed: 16/06/2026)

[11] `https://www.europesays.com/netherlands/17797` (Accessed: 16/06/2026)

9.4. Sensitivity Analysis

A sensitivity analysis is performed to assess how variations in design inputs affect the final configuration. Since the aircraft is still in the conceptual design phase, several input parameters are uncertain, and their influence on the main results must be studied. This allows the most critical design drivers to be identified and indicates which assumptions require further analysis in future design phases.

9.4.1. Assumptions

The sensitivity model has two major implicit assumptions, listed in Table 9.1.

Table 9.1: Assumptions used in the sensitivity model.

ID	Assumption	Justification / source
A-SA-01	The one-at-a-time sensitivity assumes variables are independent.	Used due to computational expense. Neglects the coupling between inputs.
A-SA-02	Spearman correlation assumes monotonic relationships.	Good for non-linear trends, but if a variable has a non-monotonic effect on MTOM, it may under-represent its importance.

9.4.2. Method

The design process is a multi-script model, with various inputs and outputs. The chosen output for the sensitivity study was the MTOM, as this is a major result from design. This sensitivity analysis was separated into two analyses: one-at-a-time sensitivity and simulation sensitivity using Latin Hypercube Sampling (LHS).

One-at-a-time sensitivity analysis was used to identify the input variables with the largest influence on the MTOM calculation. The iteration converged design values were first used as the baseline input set. Each variable was varied by ±10%, one at a time, keeping the remaining values constant. The resulting MTOM values for the negative and positive perturbations, $MTOM_-$ and $MTOM_+$, were then compared with the baseline value, $MTOM_0$. A normalised central sensitivity coefficient was calculated for each input variable using Equation 9.1:

$$S_i = \frac{1}{2\Delta x}\frac{MTOM_+ - MTOM_-}{MTOM_0} \tag{9.1}$$

where $\Delta x = 0.10$ is the perturbation applied to the input variable. The variables were ranked according to the absolute value of S_i, so that the largest values indicate the strongest influence on MTOM. A ±10% variation was selected because it is representative of intrinsic uncertainty during design but is not large enough to introduce non-physical behaviour in the model. The most influential variables were then used as inputs for the simulation.

The LHS method was used to perform the simulation, as the conventional Monte Carlo simulation would be computationally expensive because a large number of full MTOM model iterations would be required to properly sample the input space. The LHS method reduces this cost by forcing the samples to be more evenly distributed in the input range, allowing the same design space trends to be acquired with fewer model simulations. The simulation using the LHS algorithm used in this analysis is as follows:

1. Each selected variable from the one-at-a-time sensitivity analysis was assigned a uniform distribution centred on its converged baseline value, μ_i, with bounds of ±10%: $X_i \sim \mathcal{U}(0.9\mu_i, 1.1\mu_i)$. The uniform distribution was selected instead of a normal distribution because the uncertainty of the design inputs is not yet known at this stage, so all values in the defined range are assumed equally likely.

2. Each uniform distribution was divided into 50 equal intervals, corresponding to the 50 Latin Hypercube samples.
3. For each variable, one value was randomly sampled from each interval. The sampled values were then randomly combined across the different variables to create 50 input sets.
4. The Class II sizing model was run once for each sampled input set.
5. The resulting MTOM values were used to estimate the uncertainty range and to calculate Spearman correlations between the sampled input variables and MTOM.

9.4.3. Results

A tornado plot was created using the one-at-a-time sensitivity results. This plot is presented in Figure 9.5 and shows the behaviour of the MTOM for when a certain parameter is varied by ±10%, while maintaining all the other parameters constant. Only inputs that vary the MTOM by more than 1% in at least one of the two scenarios are shown.

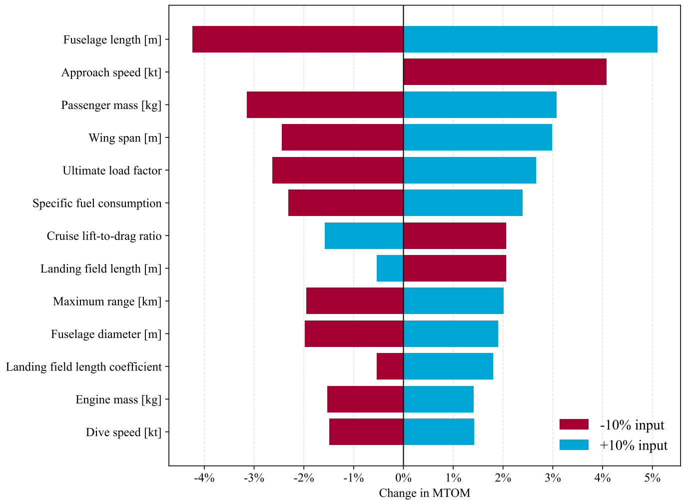

Figure 9.5: One-at-a-time sensitivity tornado plot.

The model is said to be linear with a certain input if $|\Delta MTOM_{-}| \approx |\Delta MTOM_{+}|$ (using the second-order central difference formula). As can be seen in Figure 9.5, most input variables show approximate linear behaviour. Nevertheless, some variables show clear non-linear behaviour, namely the approach velocity, landing field length, and landing field length coefficient. An interesting result is that the approach speed response is not symmetric. This seems to be due to the approach speed requirement being close to a landing limit. The requirement behaves as expected for a stricter requirement. When the approach speed is increased, the requirement becomes relaxed, but the aircraft does not become lighter because another sizing requirement probably becomes dominant.

Hence, the Pearson correlation coefficient is not sufficient to analyse the interdependence of a given input and the output MTOM, as it only captures linear correlation. Therefore, Spearman correlation is used to study the non-linear correlation between a certain input and the MTOM. The results of the study are summarised in Table 9.2, together with an assessment of the physical meaningfulness of each correlation. This provides an additional layer of model validation.

Table 9.2: Spearman rank correlation between sampled input variables and MTOM.

Variable	Spearman ρ	Interpretation
Fuselage length	0.62	Longer fuselage increases MTOM
Passenger mass	0.48	Higher payload increases MTOM
Ultimate load factor	0.43	Higher structural loads increase MTOM
Approach speed	-0.41	Higher v_{app} relaxes landing constraint
Maximum range	0.34	Higher range increases fuel mass and MTOM
TSFC	0.33	Higher fuel consumption increases MTOM
Dive speed	0.33	Higher design speed increases structural mass
Wing span	0.27	Larger span increases structural mass thus increasing MTOM

As can be seen in Table 9.2, the correlation between the most relevant inputs has the expected physical meaning. Input variables with a Spearman coefficient below 0.2 were omitted, as their impact on MTOM is weak. Table 9.3 summarises the MTOM statistics obtained from the LHS analysis. Further analysis could be conducted with greater computational resources to obtain more robust and reliable sensitivity results.

Table 9.3: Latin Hypercube sampling statistics for MTOM.

Statistic	Value	Unit
Number of simulations	50	-
Mean MTOM	96942.21	kg
Standard deviation	5813.23	kg
Coefficient of variation	6.00	%
Minimum MTOM	86005.37	kg
5th percentile MTOM	88410.28	kg
Median MTOM	97171.89	kg
95th percentile MTOM	106242.38	kg
Maximum MTOM	107276.59	kg

10

Operating the Aircraft

Now that the preliminary design of the aircraft is finalised and validated. It can now be described how it will be operated and which logistics have to be put into place for it to fly seamlessly. The different mission phases and their respective operations and logistics are described in Section 10.1. Section 10.2 dives deeper into the airborne phase and explores how the pilot interacts with the management of the dual fuel mixture. Section 10.3 describes the APU. Finally, Section 10.4 describes how the different subsystems of the MAVERICK aircraft relate to each other.

10.1. Operations and Logistics Concept

Due to the novelty of the MAVERICK aircraft, it will not be operated as current state-of-the-art aeroplanes. It will need infrastructure related to hydrogen. This section is divided into the different parts of flight, namely: pre-flight (Subsection 10.1.1), airborne (Subsection 10.1.2), post-flight (Subsection 10.1.3), and unusual events (Subsection 10.1.4). The maintenance is discussed later in Section 11.2. The Figure 10.1 shows an overview of the flow of operations explained in this section.

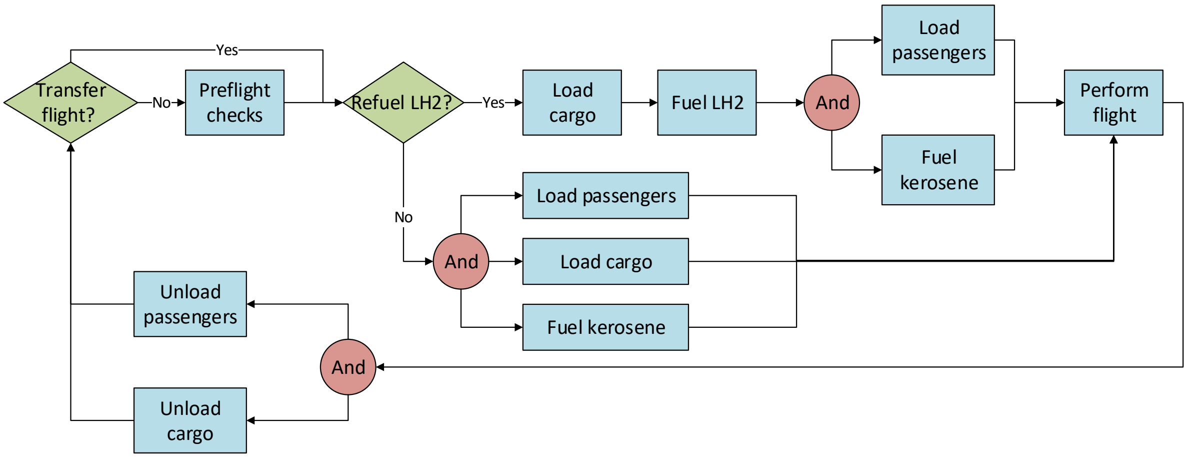

Figure 10.1: Flow of operations discussed in this section

10.1.1. Pre-Flight

Before the aircraft gets to fly, multiple checks are done, the aircraft is refuelled, and the payload is boarded.

Pre-Flight Checks

Safety exterior inspection: The first check to be done before flying is to assess the safety around the aircraft, see that the wheel chocks are put in place, that the ground crew is present and that the environment is deemed safe [116]. Additionally, if it is the first flight after the aircraft has been on the ground for a prolonged period of time, e.g. overnight, or more than 10 hours, it should be checked that the tube needed to vent boiled off hydrogen is removed [116]. The logistics surrounding this mechanism are further explained in Subsection 10.1.3.

Preliminary cockpit preparation: After confirmation that the exterior around the aircraft is checked, there is a preliminary cockpit preparation that aims to check the aircraft setup and that it is safe before the APU is turned on [116]. For example, the batteries are checked, the hydraulic conditions are evaluated, Electronic Centralised Aircraft Monitoring (ECAM) pages are checked, and it is ensured that the parking brakes are put on [116]. It is also verified that the emergency equipment is present in the cockpit [116]. For this aircraft, the pressure in the hydrogen tank will also be evaluated if it is in a nominal state.

Pre-flight inspection or walk around: During the preflight inspection, which is done before every non-transfer flight, the captain walks around the aircraft in a clockwise direction, and checks its external conditions for any unusual elements such as oil, fuel leaks, impacts[1]. They also check the external sensors such as the pitot tubes, the static ports, and the angle of attack sensors[1]. They verify that all doors and latches are closed, that intakes and exhausts are clear, that safety pins are removed and that the landing gears are nominal[1]. The additional checks specific to the MAVERICK aircraft are: checking for icing that could indicate a leak in the tank or the piping systems when external temperatures are not freezing, and checking that the panels on the rear fuselage are well attached.

Cockpit preparation: After the preflight inspection, the pilots prepare the cockpit for flight. It is not expected that this step will be very different from the reference aircraft. The only additional measure is to check that the interface of the hydrogen system is nominal, which is explained in detail in Section 10.2, as well as the trim tank status.

---

[1] `https://studylib.net/doc/27798949/a320-walkaround?p=7` (Accessed: 09/06/2026)

Refuelling
The refuelling of the aircraft must be done sequentially. First, the hydrogen will be loaded in the rear tank before kerosene. The hydrogen refuelling should take around 30 minutes [4]. Because of the novelty of this operation, it is advised to have a safety perimeter of 20 m [117], meaning that the boarding and loading of the cargo cannot be done simultaneously.

The LH_2 can be brought with two methods, the first method is having a bowser come next to the aircraft at the gate, and the second option is to have the fuel being brought with pipes [4]. The bowser option has smaller upfront costs and is easier to implement. It can also act as a transitional phase towards the more invasive underground piping system, whose implementation will occur later in the aircraft's lifetime. Furthermore, smaller airports that have less demand for fuel could prefer this option [98].

The second option, which would be implemented later in the aircraft's lifetime when other hydrogen-powered aircraft will enter the market, is to have an underground piping system that brings the hydrogen all the way from the storage zone to the gate. The implementation of this concept brings noticeably high upfront costs and reduced airport operations during the period of the works, but it can reduce turnaround time considerably over time. Having such a system in airports that will have high demands for hydrogen will also declutter the ground traffic and thus increase safety on the ground. When this option is implemented, LH_2 bowsers should still be present on airport grounds to deliver fuel to remote parking locations and for emergency refuelling [98]. LH_2 piping systems might not be compatible with the already existing Jet A-1, as building this infrastructure would require the whole distribution system to be rebuilt [98]. This is not preferable to do when the MAVERICK aircraft still uses kerosene.

Independent of the LH_2 delivery to the gate option used, there should be LH_2 storage facilities in or around the airport. According to [4], there should be enough backup storage capacity for 3 days of the LH_2 demand of the peak day in a year, and the amount of LH_2 stored should not fall under 90% to account for problems in the supply route. As GH_2 cannot be prevented from forming, and increasing tank pressure, it will need to be vented off. Additionally, boiled-off GH_2 leaks from the tank due to its atom size, but those daily losses are small (0.1% for small storage to 0.035% for large storage) and are cheaper than additional cooling systems [4].

The delivery system that connects the fuel truck to the aircraft tank will be composed of a tube at the end of which there will be a self-sealing quick disconnect system with a minimum gauge pressure of 0.2 bar [98]. This system has the advantage of sealing the pipe with very limited spillage and does not need to be purged as the gauge pressure prevents penetration [98].

Regarding the safety of the refuelling operation, Mangold et al. [98] argue that three measures need to be followed to be protected against explosions: avoiding explosive atmosphere, avoiding ignition sources when explosive atmosphere can occur, and limiting the effects of the explosion to harmless levels. If all hydrogen systems are completely sealed and all equipment, such as the bowser, the aircraft, and all surrounding vehicles, are grounded, then there should be no necessity to have a safety perimeter, which would allow the parallel boarding of passengers and cargo. It is then decided to keep the safety perimeter at the aircraft's beginning of life, and assess its necessity later, when there are fewer unknowns surrounding the liquid hydrogen refuelling.

The remaining steps before take-off are similar to those of conventional aircraft, namely: loading the payload, which includes loading passengers, cargo, and other products; taxiing, where the hydrogen mass flow fraction will be 50 % as shown in Table 5.4 and Table 5.5.

10.1.2. Airborne

The steps of the airborne phase are: take-off, climb, cruise, descend, approach, and land. During flight, the biggest novelty of the MAVERICK aircraft is the management of the dual-fuel system, which will be done automatically. The pilot will, however, be able to override this decision in case an event does not happen as planned. This management is explained in greater detail in Section 10.2, which describes what the pilot sees with relations to the hydrogen systems. Additionally, the automatic management of the fuel system is explained more in depth in Section 10.4. The fuel mixtures of the different steps of the airborne phase are shown in Table 5.4 and Table 5.5.

10.1.3. Post-Flight

After landing, the aircraft taxis back to the apron. This process is identical to its pre-flight equivalent. Similarly, the needed unloading of the payload is done the same way as for conventional airliners.

One consideration is the fact that hydrogen needs to stay in the tanks even if the aircraft stays on the ground overnight or for longer periods of time. This is done to avoid repeated thermal loads on the tank that could lead to its premature failure. Leaving the hydrogen in the tanks for prolonged periods of time also leads to Boil-Off Gas (BOG) that needs to be vented, which must be done in a safe manner.

An option of venting is having a valve on the tank that is connected to a venting stack reaching the top of the vertical tail. To ensure safety, the venting must be done 60 m away from any occupied building [117]. Since the fuselage is 50 m long, as stated in Table 3.11, it can be decided that the aircraft is parked 10 m away from the terminal with the nose pointing towards it to respect the safety perimeter. However, venting the BOG into the atmosphere is not favourable for fuel efficiency, and a system that could recuperate the GH_2 has to be implemented. The venting in the atmosphere option is thus not preferred, but the venting valve is still kept for redundancy and is relegated to a second role, as an extra safety measure.

The other option, which is preferred in terms of safety and fuel efficiency, is to recuperate the GH_2 to keep the system sealed, which removes the need for the 60 m safety perimeter. This is done through a tube that is connected to a compressed GH_2 tank, which is placed on a trailer next to the aircraft. The collected GH_2 is used to pressurise the bowsers for refuelling. When hydrogen fuelled aviation is well implemented, this BOG can be reliquefied.

10.1.4. Unusual events

Multiple possible incidents or accidents are identified in this section. Each of them is followed by a contingency plan as advice on what to do in case these events occur. This section is linked to Section 2.4.

Problem with the dual fuel mass flows

In case there is a problem with the management of both mass flows, and if one type of fuel runs out faster than it should, there should be a mass flow sensor to ensure that no fuel is being consumed faster than it should. If the fuel goes over that threshold, an alarm should ring to notify the pilots of the issue if they have not noticed it by then. After this, they should decide whether to override the automatic decision of the flight computer or to divert the aircraft. The fuel mixtures should be adjusted according to a fuel schedule prepared for each mission, which will be controlled by FADEC.

Emergency landing

Due to hydrogen's wide flammability range and low ignition energy, dedicated venting strategies are required for both emergency in-flight scenarios and ground operations. In an emergency landing scenario, the aircraft should use an emergency venting system that releases hydrogen from the tank ullage through an aft vent outlet. The system should vent gaseous hydrogen into the free stream, away from engines, hot surfaces, electrical systems, and cabin, so that the plume is rapidly diluted below the flammability limit before interacting with the aircraft or ground environment.

In case the aircraft must land with fully empty kerosene tanks and a full hydrogen tank, it will need assistance on the ground as 2% of the MTOM will be on the nose wheel, making the aircraft difficult to manoeuvre on the ground.

Pressure in hydrogen tank is too high

For this event, multiple systems exist for different levels of criticality. In case the pressure increase is manageable, there are two resealable valves on the tank that are connected to the venting stack in the vertical tail. They release the built-up GH_2 and are activated at different pressures. If the pressure rises too quickly and it becomes critical for the tank's structural integrity, a burst disk expels all the excess pressure.

Hydrogen leak

In case a hydrogen leak is detected, the valves in the hydrogen piping are closed, and the hydrogen system from the tank is vented, using the same system as for emergency landings. The fuel mode is automatically switched to the fully kerosene mode using the FADEC. The aircraft is then diverted to the closest airport, and a maintenance team is brought to purge the hydrogen systems and to identify the leaking source to repair it.

Sensors giving a false alarm

To mitigate this risk, there will be multiple sensors for redundancy. There should be at least 3 of each kind such that the flight computer can decide to ignore the measurement of the one that gives a different reading than the other two. Doing so avoids the effects of sensor misreadings.

10.1.5. Implications for Aircraft Operators

The new systems brought into the MAVERICK aircraft leads to novel operations surrounding it. For example, the pilots will need to be trained to deal with the fuel feed system even though they will not manage it directly. This will be done through learning the theory behind it and learning how it works, then having practical exercises in simulators. After that, they will go on the real aircraft to get certified to fly it. Emphasis is to be placed on the handling of emergencies arising from the failure of various components of the feed system, and the actions to take, as discussed in Subsection 10.2.2. The nominal operation of the aircraft will be very similar to other aircraft in its class, like the A320 and Boeing 737 families, in order to reduce the additional total training that will be required to certify pilots. Ground crew will also need to be trained for the hydrogen refuelling system. And aircraft mechanics will also be certified to perform maintenance on the MAVERICK aircraft in accordance with the maintenance plan.

10.2. Data Handling & Communication Flow: Pilot Interface

In sight of the novel hydrogen technology that is implemented in MAVERICK, it is very important to consider the role of the pilots in operating these systems. This section addresses the interface of the pilots with the hydrogen feed and trim tank systems, and the level of automation that will be used to monitor and control the aircraft systems. As a result, this section represents both the Data Handling and Communication Flow of the aircraft. As mentioned above, to ensure the competitiveness of MAVERICK with other aircraft in its class, such as the Airbus A320 and Boeing 737 families, as little additional pilot training and workload as possible should be required to operate the aircraft. Therefore, the data handling and communication flow must be as similar as possible. This is a driving consideration for the pilot interface philosophy.

10.2.1. Data Available to the Pilots

As described in Section 7.7, the monitoring of the fuel feed system will be carried out by many sensors, measuring temperatures, pressures, and hydrogen mass flow rates at various locations in the system. This data is of great importance to ensure that the system is operating correctly and safely, but it is not necessary for the pilots to always see all this data. If the pilots had to constantly monitor that the conditions in all these locations were in nominal ranges, it would greatly increase the pilot workload. Therefore, during normal operation, the pilots will not be expected to monitor all the conditions in the feed system. Instead, they will be monitored and controlled by the Hydrogen Feed Control Computer (HFCC), which will only alert the pilots if a reading reaches a dangerous range. For example, if the measured temperature of the hydrogen in the pipes rises to abnormally high values, or if there is a discrepancy in mass flow out of the tank and that at the injector, indicating a potential leak. In such a situation, the pilots are prompted to intervene and decide the best course of action, as will be discussed in Subsection 10.2.2.

The most relevant information for the pilots is instead the status of pumps and valves throughout the system, and the amount of hydrogen that is in the tank. The hydrogen fuel system would therefore be monitored similarly to how the kerosene fuel system is monitored, and shall be presented to the pilots on the same screen. The reference aircraft, the Airbus A320 (and other modern Airbus aircraft), present this kind of information to the pilots on one of the cockpit screens by means of the ECAM system[2], displayed in Figure 10.2a. The ECAM presents the pilots with important data on multiple aircraft systems. A similarly structured page may be used, displaying additional information on the status of the tank shut-off and hydrogen cross-feed valves, pumps, and hydrogen quantity and temperature. Moreover, the fuel flows of both kerosene and hydrogen are displayed, as well as the hydrogen-kerosene mixture ratio. These are all important parameters for the pilots to be aware of, to gauge how much fuel is on board and how much is being consumed.

In addition, the pilots should be aware of the status of the front trim tank. Information on the quantity of fuel in the trim tank and whether the valve and transfer pump are active to allow fuel to be transferred to and from the trim tank will also be displayed. As described in Section 6.4, this transfer of fuel will be done automatically, as it is a process that affects the stability of the aircraft. The rate at which fuel is transferred shall hence not be interfered with by the pilots during nominal operation. Nevertheless, the pilots will monitor this process and will be able to override the system to manually fill or empty the trim tank, as will be discussed in Subsection 10.2.2. To present this information, a modified version of the A320's ECAM fuel page has been developed to combine the existing data regarding the kerosene fuel system with the hydrogen system and trim tank. The modified page is presented in Figure 10.2b.

(a) ECAM fuel page of the Airbus A320[3]

(b) Proposed modified ECAM page to display additional data of hydrogen fuel system

Figure 10.2: Comparison of the original and modified ECAM fuel pages.

The proposed display also makes use of colour coding to ease the distinction of information. Kerosene-related values, such as fuel on board and flow rate, are displayed in white, while those related to hydrogen are shown in blue. This helps to easily distinguish the two. Furthermore, pumps, fuel lines, and valves are shown in green when operating nominally, and are represented by squares, lines, and circles, respectively, like in the A320. The orientation of the line bisecting the pumps and valves signifies whether they are on or off; if it connects the fuel line that passes through it, it is on, and otherwise it is off. This helps the pilots to easily monitor the flow of fuel.

---

[2] `https://skybrary.aero/articles/electronic-centralized-aircraft-monitor-ecam` (Accessed: 12/06/2026)

[3] `https://safetyfirst.airbus.com/fuel-monitoring-on-a320-family-aircraft/` (Accessed: 12/06/2026)

To further ease this, elements are shown in orange in a situation when they are on but are instead recommended to be off, and vice versa. This is illustrated in Figure 10.2b, where the trim tank pump is off, but the aircraft senses that it should instead be turned on during that specific flight phase. This also helps the pilots to immediately notice if a system is not being operated nominally.

10.2.2. Level of Automation and Pilot Inputs

To further ensure that abnormal operating conditions are immediately noticed by the pilots, warning messages will be displayed in the cockpit with an audible sound. Aside from those related to the operation of the kerosene fuel system and other normal aircraft systems, there will be warning messages related to the hydrogen system. In these alerts, distinctions are made between leaks being *suspected* and *detected*, where the latter is confirmed through agreement of multiple independent sensors and undergoes automatic protective action. Pilots are alerted of the following through the ECAM system, which also indicates the source sensor type and location. The most important alerts have been identified as the following:

Table 10.1: Hydrogen System Warnings and Cautions

Red Warnings (repetitive chimes) for dangerous situations needing immediate pilot action	
LH_2 Tank Leak	In case of a suspected leakage of hydrogen from the tank. This warning arises from a combination of the mass flow rate, capacitive tank level, and ullage/bottom pressure sensor readings. Besides, data on structural health is obtained from the optical fibres within the tank, with additional hydrogen concentration sensors surrounding the tank. If a leak were to happen, and data from multiple sensors point to the same conclusion, the pilots must divert to the nearest suitable airport and have the aircraft inspected on the ground.
H_2 Fuel Feed Leak	In case of a suspected leakage within the hydrogen feed system. Data is gathered from temperature and pressure readings within pipes, within annuli, and from hydrogen concentration sensors. The first action in case of leak detection and confirmation involves closing shut-off valves and transitioning to kerosene-only operation. If this eliminates the required redundancy, procedures are aligned with those in case of an LH_2 tank leak.
LH_2 Tank Rupture Disk Active	In case the rupture disk gets activated due to over-pressure in the LH_2 tank. The relevant shut-off valves are activated, and operation is switched to the kerosene-only mode.
H_2 Fuel System Isolation	In case the automatic isolation of part of the hydrogen fuel feed system is active. Pilots must divert to the nearest suitable airport and have the aircraft inspected on the ground.
Amber Cautions (single chime), requires attention but not immediately hazardous	
LH_2 Tank Temperature High	In case the temperature gradient in the tank rises excessively. This indicates that boil-off may be high and indicates possible problems regarding the tank system.
LH_2 Tank Pressure High	In case the pressure in the tank is sensed to be above 2.2 bar. The pilots then has the option to switch to kerosene-only operation.
LH_2 Tank Pressure Low	In case the pressure in the tank is sensed to be below 1.7 bar. This would only appear if the system regulating the tank pressure through a heat exchanger provided an insufficient pressure rise in the ullage. The pilots then have the option to (temporarily) switch to operation on only kerosene, allowing the heat exchange of liquid to warm gaseous hydrogen to reach the required levels.
LH_2 Feed Temperature High	In case the temperature in the LH_2 part of the fuel feed system rises dangerously near its saturation conditions. This can lead to exceeded limits on LH_2 pipes. Once confirmed, the bleed air input to the heat exchanger decreases. The pilot has the option to switch to kerosene-only operation.

GH_2 Feed Temperature Low	In case the temperature past the heat exchangers is below the lowest sufficient for the injector, 150K (as aforementioned in Chapter 5). The pilot has the option to switch to the recirculation loop, as used during engine initiation for initial LH_2 heating, or increase bleed air input to the heat exchanger.
H_2 Feed Pressure Low	In case the pressure in hydrogen feed systems drops below that required, which cannot be compensated by the control system adjusting the pump and compressor power. This may indicate pump or compressor failure, automatically activating shut-off valves on the feed system. The pilot has the option to transition to kerosene-only operation, or manually activate additional shut-off valve closure.
H_2 Valve Mismatch	In case the indicated valve position does not match the one measured within a specified time interval.
H_2 System Unavailable	In case H_2 use is impossible and operation is kerosene-only.
Cautions presenting no hazard	
H_2 Venting Active	In case a pressure relief valve gets activated to discharge GH_2. Pilots must be aware of ongoing venting, especially during ground operations and maintenance.
H_2 Sensor Fault	In case sensors in the fuel feed system (temperature, pressure, structural health, hydrogen concentration) provide invalid, conflicting or no data.

The data flow described in this section is summarised in the diagram below (Figure 10.3).

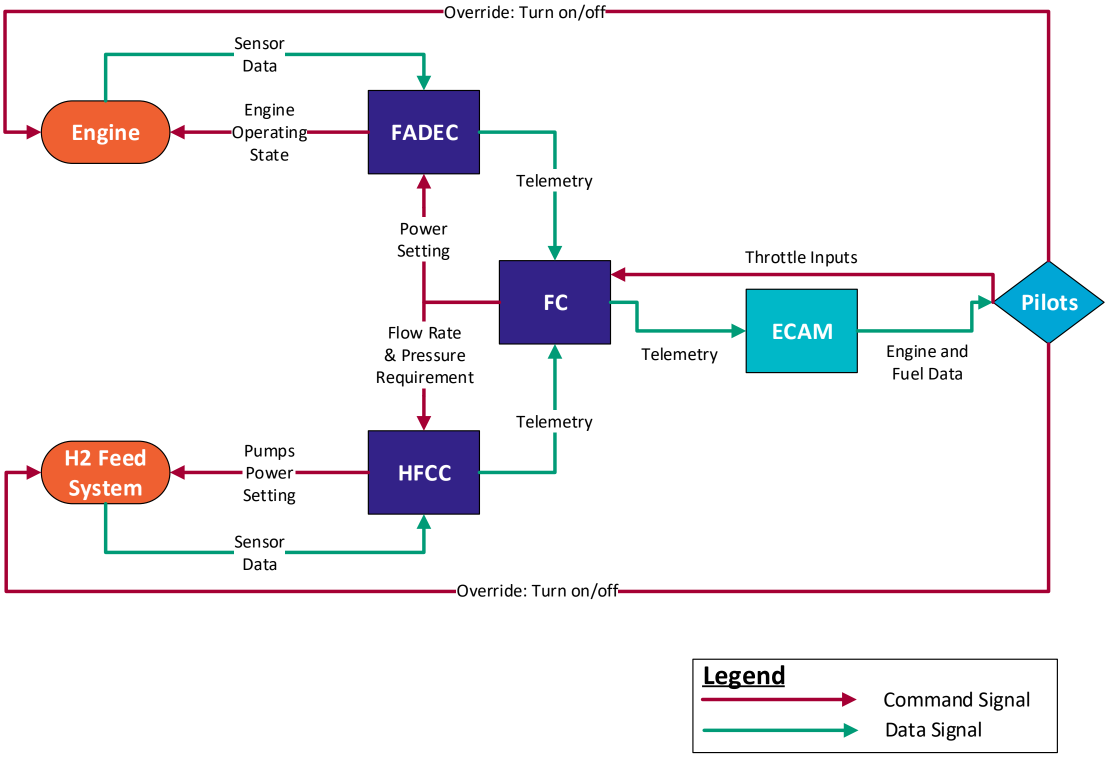

Figure 10.3: Data handling block diagram, showing the data and command flows between the propulsion system pilots, via the Flight Computer (FC), FADEC, and HFCC.

10.3. Auxiliary Power Unit (APU)

On conventional aircraft, the main function of the APU is to start the main engines. It also provides power to the pneumatic (including air conditioning) and hydraulic systems, as well as electrical power during ground operations. During flights, in case of engine failure, the APU provides electrical and pneumatic power[4]. The APU is not strictly a necessary system; however, it helps achieve a competitive value proposition (stakeholder requirement REQ-STK-COST-01) as alternatives for the provision of power on the ground are expensive. The weight savings of not including an APU are only economical for long-range operations [118]. It is hence opted for its inclusion. Furthermore, the APU is powered with kerosene, as the hydrogen feed system startup requires high electrical power and APU provides a significant part of that power. Additionally, the APU must be capable of turning on even in case the hydrogen system is deactivated, hence powering the system on hydrogen is excluded.

In the MAVERICK aircraft, the APU cannot be situated in its conventional location at the tip of the tail cone. This is because the cryogenic LH_2 tank is located in the aft fuselage and tail-cone of the aircraft. A new location for the APU must be found due to thermal management and safety considerations. Since the APU produces large amounts of heat while the tank must keep the LH_2 cryogenic, keeping the low temperatures in the tank would require thicker walls, which add weight to the aircraft. More crucially, the APU is a considerable fire hazard. EASA Certification Specification (CS) regulations dictate specific guidelines to ensure any possible fires arising due to APU operations are prevented [119].

Due to the limited capacity of kerosene carried on the MAVERICK aircraft, the centre fuel tank (located in the wing box through the fuselage) is not used for fuel storage. This presents a suitable location for APU relocation, as it is far from the LH_2 tank. It can be made easily accessible through a hatch and the exhaust can be safely routed to the side of the fuselage, aft of the wing. As fire safety is paramount, titanium firewalls surround the APU in its position centrally in the fuel tank. The internal components layout with the APU included is visualised in Figure 10.4.

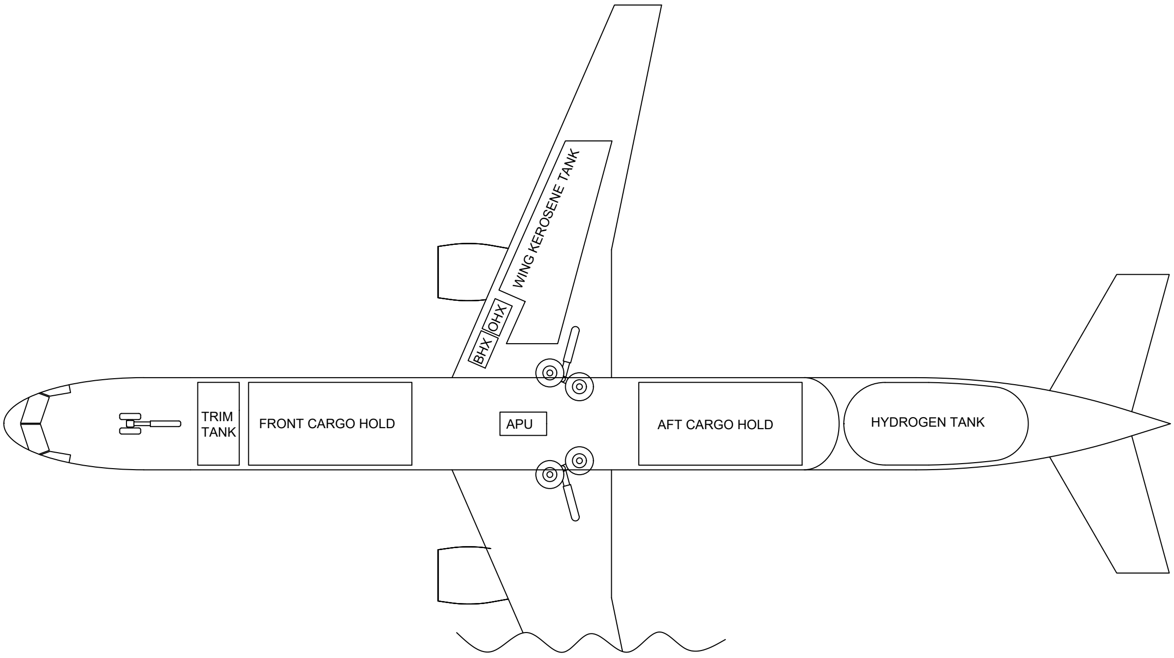

Figure 10.4: Internal components layout, showing the tanks, cargo holds, retracted landing gear, APU, and heat exchangers. Both the bleed air heat exchanger (BHX) and the oil heat exchanger (OHX) are shown.

10.4. Electrical System

MAVERICK will require an electrical system to handle the electrical power needs of the aircraft. All the conventional electrical and electronic systems will need to be supplied with power in all

---

[4] `https://prod-edam.honeywellaerospace.com/content/dam/honeywell-edam/aero/en-us/products/power-and-propulsion/auxiliary-power-units/common/documents/hon-aero-n61-1544-000-0001-honeywell-aerospace-apu-overview-brochure-v1-en.pdf?download=false` (Accessed: 15/06/2026)

flight phases. On top of this, MAVERICK's principal additional power requirement comes from the hydrogen feed system. The cryogenic turbopumps and the gas compressor will require a significant amount of power to operate, especially during take-off, where demand is highest.

The A320NEO's two engine-powered electrical generators produce around 90kV A of three-phase Alternating Current (AC) power each[5]. Assuming an average power factor of 0.90 lagging for the aircraft's AC systems [120], this results in an actual available power of $2 \times 90 \times 0.90 = 162$kW. A single engine generator can supply power to the entire aircraft, except for some secondary Direct Current (DC) systems[5], so it is estimated that the aircraft's conventional systems' average power requirement is around half of this; around 81kW.

These power supplies are not enough to provide power to all aircraft systems, as well as to the hydrogen feed system during take-off, due to the gas compressors' very high power demand. The power demand during cruise and take-off is summarised in Table 10.2. To achieve this power demand, larger generators are required compared to those of the A320NEO, outputting approximately 45.1% more power. MAVERICK's engines will produce approximately 22.1% more power than the A320NEO's LEAP-1A engines [104]. Therefore, the required generator power extraction would not scale linearly to MAVERICK's engines, so larger and or more efficient generators would have to be used to achieve this. Detailed generator design is beyond the scope of this early design phase, but it is recommended as an important future analysis to prove the feasibility of such a generator, and potentially update the required engine power output and size. A more detailed electrical analysis of all onboard systems should also be performed to determine ways in which the aircraft's other systems' power consumption can be decreased.

Table 10.2: Electrical power supply and demand at and cruise take-off

Item	**Power at Cruise** [kW]	**Power at Take-off** [kW]	**Note**
Supply			
Engine generators	235	235	+45.1% w.r.t. A320NEO
APU generator	0	117.5	Scaled with engine generators
Battery packs (×2)	0	230	19.2 kW h total
Total supply	**235**	**583**	
Demand			
Conventional aircraft systems	81	81	Same as A320NEO
Gas compressors	149.4	498	As per Table 7.4
Boost pumps	4.4	4.4	As per Table 7.4
Total demand	**235**	**583**	

At take-off, the required power cannot be achieved even by the larger 117.5kW generators. The APU can also generate electricity, with the A320NEO's being able to match the power output of the engine generators at 90kV A[5], or another 81kW of actual power. It could therefore be used during take-off only to provide additional electrical power. If a larger and or more efficient APU generator is used, scaled up by the same amount as the engine generators, it could also generate 117.5kW of power, for a total of 352.5kW. The final 230kW of power would need to be supplied by two additional high-voltage battery packs.

For a preliminary weight estimate, the batteries would need to provide the 148.5kW for a period of up to 5 minutes during take-off, yielding a total energy requirement of $230.0 \times 5/60 = 19.2$kW h.

---

[5] `https://pilot.sinej.com/airbus-a320-electrical-source-priority-emergency-power/` (Accessed: 13/06/2026)

Lithium-ion batteries are selected as they are the most promising architecture for future high-performance aerospace and automotive applications [121]. Lithium-ion cells can achieve specific energy densities of up to 300W h kg^{-1} [121]. To account for casings, wirings, and thermal and battery management hardware, the specific energy density of a battery pack will be lower; for electric cars, this can be around 77% [122]. In addition, due to the short discharge time (C-rate of 10C to 20C), to preserve battery life, the depth of discharge should be limited to around 30% [123]. This would result in a total battery mass of $19200/(0.30 \times 0.77 \times 300) = 279.6$kg. Although this value is just a preliminary estimate, it is a relatively small mass increase, and the batteries would be able to provide the required power during take-off. It is recommended to study the possibility of such batteries in later design stages, as they would be able to provide a significant amount of power and could hence be even larger to reduce the power requirement by the APU. The batteries can also be charged in flight by the engine generators when power demand is lower, to provide power to the compressors even in cruise. With some careful mission strategy planning the generators could therefore not need to be increased in size by so much. The battery sizing is summarised in Table 10.3.

Table 10.3: Battery pack preliminary sizing parameters

Parameter	**Value**	**Note**
Power shortfall to cover	230 kW	After engine generators and APU
Discharge duration	5 min	Take-off phase
Energy required	19.2 kWh	$230 \times 5/60$
Cell specific energy	300 Wh/kg	Li-ion [121]
Pack efficiency factor	77%	Casing, wiring, BMS, thermal hardware [122]
Depth of discharge	30%	High C-rate (10–20C) operation [123]
Estimated battery mass	**~280 kg**	$19200 / (0.30 \times 0.77 \times 300)$

The required high-voltage battery packs (HV BAT 1 & 2) required for the gas compressors are integrated into the electrical system developed for MAVERICK. Due to the similarity of MAVERICK's other systems to the A320's, the layout of the electrical system will be similar[7], illustrated in Figure 10.5. AC power is generated by the engine generators (GEN 1 & 2), the APU generator (APU GEN), or the external/ground power source (EXT PWR). The AC power is distributed by two buses to flight controls, flight computers, avionics, and hydraulic pumps[7]. The AC buses can also directly provide power to the hydrogen feed system, via the H2 SYS BUS 1 & 2. Some AC power is converted to DC transformer rectifiers (TR 1 & 2), to be stored in 28V batteries (BAT 1 & 2) and distributed to various smaller electronic components in the aircraft. DC power can also be converted back to AC power if needed with inverters (INV 1 & 2). Both a DC and an AC essential (ESS) bus are present, to distribute power from the batteries and emergency generator (EMER GEN) to essential components in an emergency.

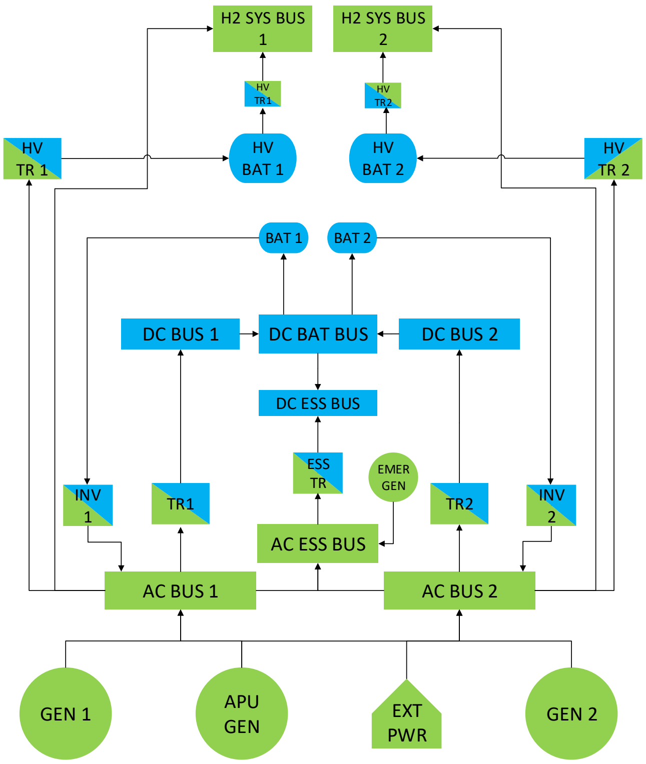

Figure 10.5: Electrical block diagram of MAVERICK's electrical system. Green components are AC powered, blue ones are DC.

11

Market Entry

At this stage, the aircraft's entry into market is considered. The Project Design and Development Logic (PD&D), shown in Section 11.6, is concerned with the activities of the MAVERICK aircraft after the DSE phase is over. This starts directly at the end of the project and continues until the large-scale operation of the aircraft. Multiple phases from the PD&D are further expanded in this chapter. The diagram starts with the *Presentation of work*, labelled with the number 6, to maintain consistency with the Project Plan [124].

The production is described in Section 11.1, and Section 11.2 explains the maintenance considerations and plan. A cost estimation is outlined in Section 11.3, then the competitiveness and the return on investments and operational profits are studied in Section 11.4 and Section 11.5, respectively. Finally, all of these processes are shown in a timeline found in Section 11.6.

11.1. Production Plan

The aim of the production plan is to minimise production risk and ensure compliance with CS-25 manufacturing certification standards [115]. Thus, the overarching assembly sequence for MAVERICK mirrors the industry standard assembly line philosophy used for standard narrow-body commercial aircraft, such as the Airbus A320neo.

11.1.1. High Level Overview of Production Process

The production process of the MAVERICK aircraft is divided into multiple high-level modules. It starts with material supply, which includes material preparation before manufacturing. The next step includes the manufacturing process of all aircraft components. Once the elements are produced,

---

[7] https://pilot.sinej.com/airbus-a320-electrical-source-priority-emergency-power/ (Accessed: 13/06/2026)

the sub-assembly process takes place, when groups of components are mounted together, such as the wing group or fuselage group. Subsequently, all systems and subsystems are integrated and the assembly process is finalised. The next step is the testing of the final product, where it is verified and validated. Finally, the certification is conducted, and once the product is accepted and signed off by airworthiness authorities, it is delivered to a customer. The whole process is shown in a block diagram in Figure 11.1.

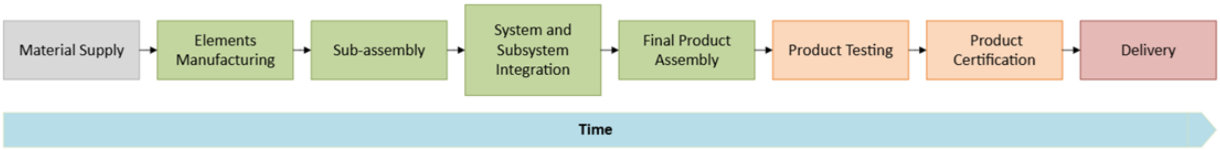

Figure 11.1: High-level production flow diagram.

11.1.2. Final Assembly Line (FAL)

The FAL represents the final stages of the production process, in which all sub-assemblies and systems are integrated. A flow diagram of this process is shown in Figure 11.2, with the critical path highlighted in red. The critical path presents the sequence of tasks that requires the most time to complete. Larger time margins were assigned to activities involving novel technologies, reflecting their higher development and introduction uncertainty.

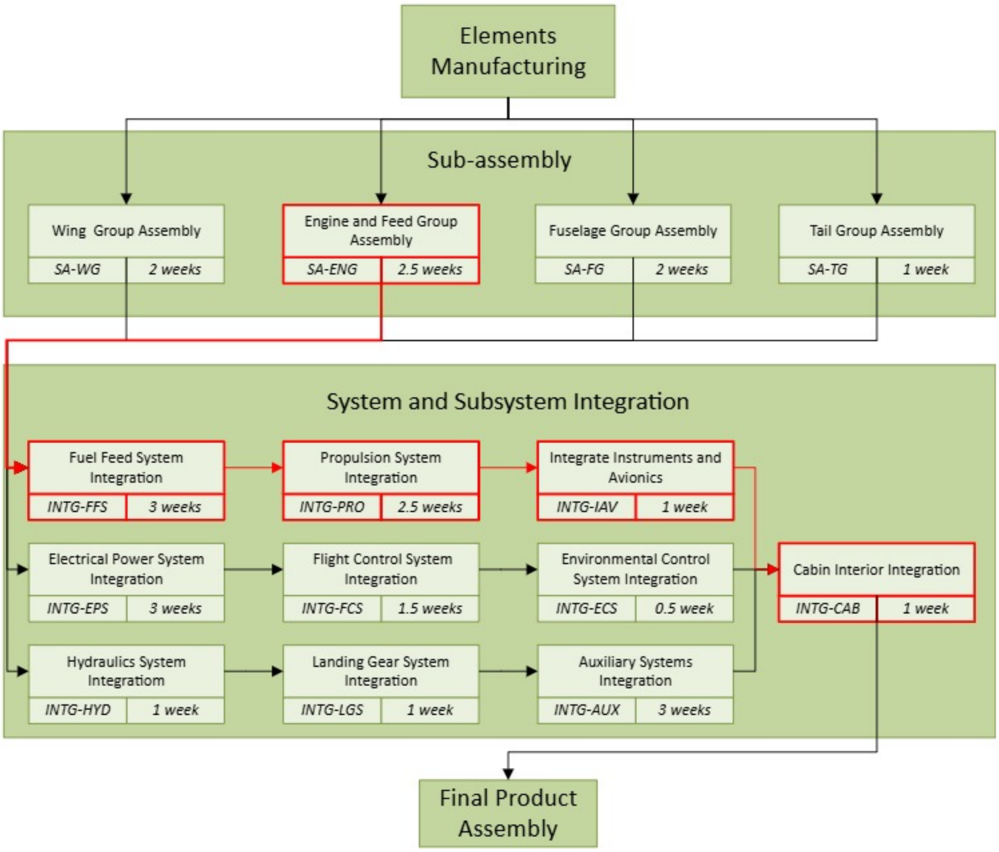

Figure 11.2: The FAL flow diagram with critical path shown in red. Time duration is based on engineering judgement, taking into account the size, mass, and complexity of systems.

11.1.3. Detailed Sub-System Manufacturing and Integration

Since the major changes of the MAVERICK aircraft are related to the propulsion, feed systems, and storage, the production plan focuses more attention on the distinctive and novel components of the aircraft. Each activity in the manufacturing process has its block, containing an identifier and a duration, which creates a clear overview of the activities for the production of the aircraft. The different horizontal lanes represent decoupled production pathways, indicating that these activities can be performed simultaneously. Traversing these lanes represents the chronological order of events, from manufacturing to assembly and integration.

Hydrogen Tank Assembly

The process shown in Figure 11.3 represents the assembly of the hydrogen fuel tank. Unlike standard kerosene fuel tanks, the LH_2 requires a large volume, vacuum-insulated containment, which changes the manufacturing of this specific fuel tank and its integration in the airframe. The LH_2 fuel tank is discussed in Chapter 6, consisting of an inner aluminium shell and an outer Carbon Fibre Reinforced Plastic (CFRP) shell and stiffeners. The tank is assembled using a Modular Mounting System on Linear Axes (MML) concept, which allows for parallel production of the inner and outer shells while maintaining low development costs [125]. The aluminium shell is fabricated using techniques such as rolling, spinning, and welding, followed by heat treatment and surface preparation. Special care is taken regarding the weld seams and their failure points, which leads to higher production times and this is thus included in the critical path [126]. The outer shell is fabricated using Automated Fibre Placement (AFP) over a collapsible mandrel, after which the composite stiffeners are bonded to the skin to provide buckling resistance against atmospheric pressure [127]. The entire assembly is nested with MLI, and the annular space is evacuated to a vacuum.

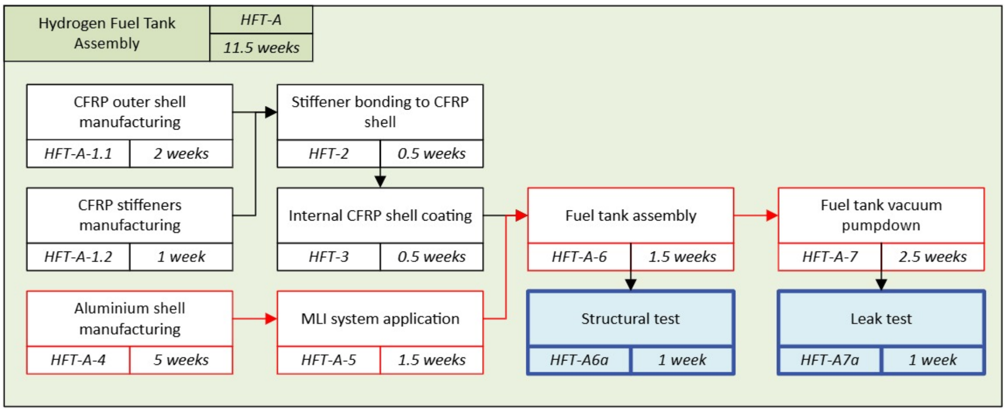

Figure 11.3: Hydrogen fuel tank assembly with critical path shown in red.

Cryogenic Fuel Feed Lines Assembly

The cryogenic fuel feed lines are detailed in Figure 11.4. The manufacturing and integration of the cryogenic feed lines relies on Vacuum-Jacketed Piping (VJP) architecture to prevent liquid hydrogen boil-off during transport to the engines. The process begins in parallel tracks with the fabrication of the inner carrier pipe and the outer vacuum jacket. Similar to the LH_2 fuel tank, this is followed by the MLI system, but it takes less time for the pipes as they have a simpler and uniform shape. Due to the routing complexities of the airframe, the piping is split into segments, after which the entire annular gap within the piping is evacuated to vacuum to eliminate convective heat leaks. Again, Figure 11.4 shows the critical path in red.

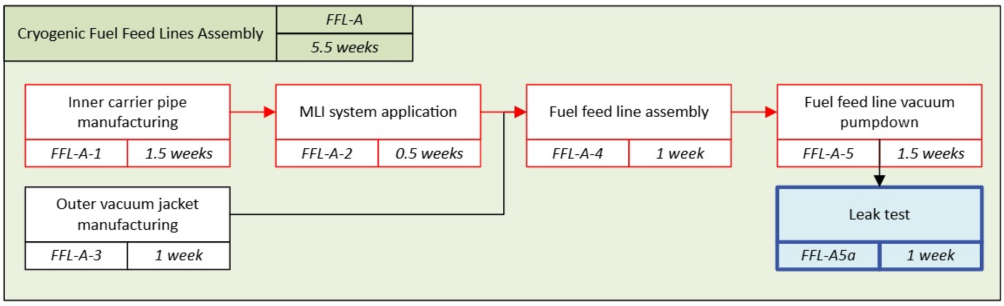

Figure 11.4: Cryogenic fuel feed lines assembly with critical path shown in red.

Engine Assembly

The engine production process is adjusted to account for combustion of hydrogen and kerosene, and is shown in Figure 11.5.

The injector must facilitate highly intense Jet in Cross-Flow (JICF) mixing to prevent thermal NO_x formation while managing severe flashback risks. To achieve the required geometry, the entire injection head is manufactured as a single component using Laser Powder Bed Fusion (LBPF) additive manufacturing. This process allows the complex, parallel internal routing channels for both fuel types to be created into a single unit, eliminating the leak risks and geometric constraints associated with conventionally joined components [128].

The extreme flame temperatures and fast reaction kinetics of hydrogen combustion severely increase the thermal load on the combustor walls. The liner and casing thus require extra coating and cooling. The additively manufactured injection head is mechanically mated to the coated liner and outer casing. The completed dual-fuel combustion module undergoes rigorous high-pressure leak verification before it is delivered to the main assembly line for integration with the high-pressure compressor and turbine modules to form the engine core.

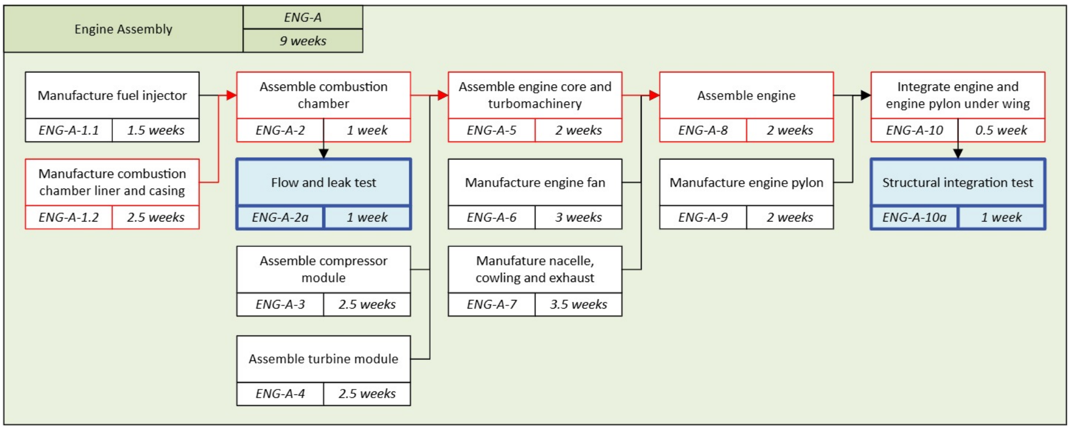

Figure 11.5: Engine assembly process with main focus on the combustion chamber and critical path shown in red.

Complete Hydrogen Fuel Feed System Assembly

The integration of the LH_2 feed system is a more complex process, outlined in Figure 11.6. This assembly covers multiple structures, shown as circles. The wing and fuselage integration can be performed simultaneously.

The heat exchangers are integrated in the wing structure, close to the engine. The fuel feed lines are connected to the heat exchanger and the engine, completing this loop with the addition of the final gas pump. For the fuselage, a cryogenic pump is integrated close to the tank, after which the fuel feed lines are connected and integrated all the way to the connection point in the wing. Shut-off and pressure relief valves are also manufactured and integrated, which are tested using pressure tests. Once these tests are passed and the full feed system is integrated, flow and leak tests are performed.

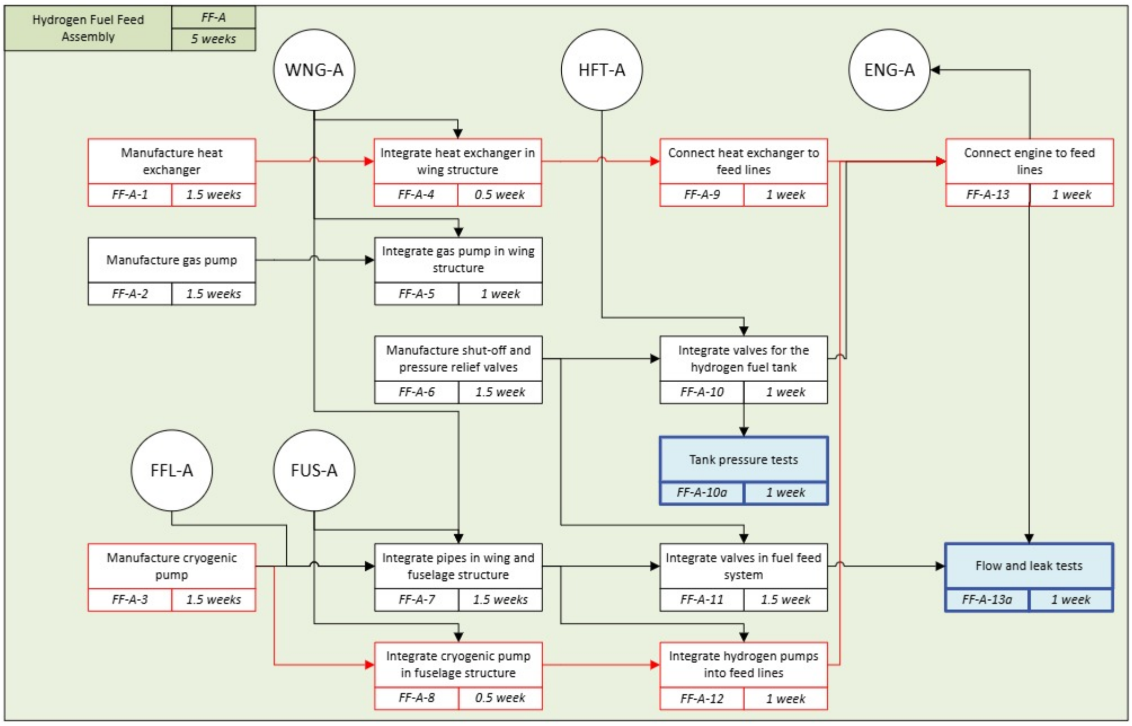

Figure 11.6: Hydrogen fuel feed system integration with critical path shown in red. The circles represent completed assemblies or structures.

11.2. Maintenance

This section focuses on the maintenance considerations that need to be taken into account specifically for the MAVERICK aircraft. It elaborates on what adaptations need to be made from a conventional aircraft. The aspects discussed in this section are the fuel system maintenance (encompassing the hydrogen tank, the pipes, the pressure regulators, the heat exchangers and the sensors) and the engine. Maintenance intervals and total man-hours are also considered here. It is expected that the hydrogen storage and distribution system will increase maintenance effort by around 22% to 32% compared to the reference aircraft [97]. Since information on the maintenance of aircraft with hydrogen combustion is lacking, the increase in maintenance effort for the MAVERICK aircraft is estimated to be even higher due to the different engine.

Type of Check	Interval
Daily	1 day
Weekly	7 days
Line	40 Flight Hour (FH)
A-checks	400 FH
C-checks	1.5 years
5-years	5 years or 5000 Flight Cycle (FC)
D-chechs	10 years

Table 11.1: Types of scheduled maintenance checks of the MAVERICK aircraft and intervals

Checks that can eventually be followed by maintenance are scheduled based on FH, FC or calendar days. Table 11.1 shows the different types of checks and their intervals. Daily checks are done every day before the aircraft starts flying, and the increase in maintenance effort is estimated to be 5% for this aircraft as already mentioned in Subsection 8.2.2. As the duration of a daily check is 2 hours [96], the additional time will be 6 minutes. Additionally, a walk-around is performed before every flight to check for any leakage or exterior impact damage, as explained in Subsection 10.1.1. Then, line maintenance is done every 40 FH. This usually takes from 6 to 24 hours and can be done at the gate at night to not constrain daily operations. Weekly checks are also done. When this check is done, there is no need for an additional daily check. The weekly check lasts 3 hours [96]. Accounting for an increase of 5%, the additional time required for this maintenance event is 9 minutes. Next, A-checks should be done after 400 FH. These are usually performed in an airport hangar. The C-checks are done every year and a half and would take around 1 to 2 weeks of work. During this check, major structural elements are inspected. Finally, the D-checks are the heaviest maintenance events and are performed every 10 years. During this check, the hydrogen tanks are emptied and purged with nitrogen, and the aircraft's condition is brought back to as good as new. In addition to these common checks, the aircraft will also have a specific category of checks caused by its special systems, which will be performed every 5 years or 5000 FC. An overview of the additional maintenance in terms of years for the MAVERICK aircraft is seen in Figure 11.7. The values for the check intervals are on the lower bound to stay on the safe side, as the aircraft is operating novel technology, even though this has a more pricey outcome.

It is important to note that the values of intervals – and eventually man-hours – presented here are an advice to the maintenance organisms. As this maintenance advice brings additional tasks which increase the aircraft's downtime, it could be decided that instead of having fixed and scheduled maintenance tasks, they could be more flexible. They would then be performed when the sensors observe that the system's performance has deteriorated, and thus reduce the amount of downtime. In all cases, however, the task intervals and Maintenance Man Hours (MMH) required will be revised based on how the aircraft behaves during its life.

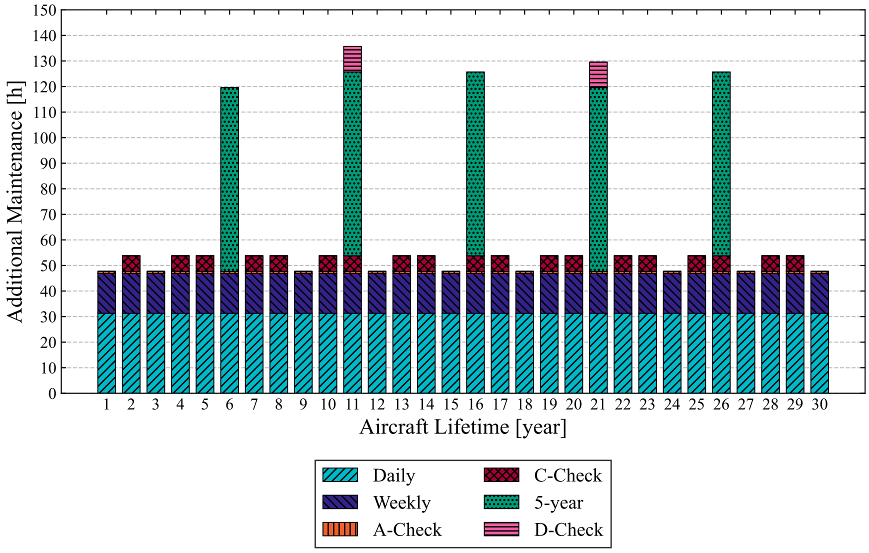

Figure 11.7: Additional maintenance overview in terms of years.

11.2.1. Fuel System Maintenance

As the hydrogen systems are not yet widely implemented in the aeronautical industry, a lot of precautions have to be taken around them to ensure maximum safety while the technologies reach more maturity. This subsection is based on the work of Meissner et al. [97].

For the cryogenic hydrogen tanks, an internal inspection has to be performed at least every 10 years, or at least every 10 000 FC. For this, the tank will need to be completely purged, then disconnected from a resealable valve to let a borescope in. This inspection will be done during D-checks. However, it is preferable to visually inspect the external tank more often, during A-checks and C-checks, as this type of check can be performed during a line maintenance layover by opening a door. During D-checks, it is also advised to perform a special detailed inspection of the tank fixtures, similar to the engine connection to the wing. If, after internal and/or external inspections, it is observed that a structural repair needs to be done on the tank, it has to be disconnected and removed from the aircraft through the top panels of the fuselage. After the repairs are completed, the tank will need to undergo further testing similar to the one after manufacturing, which typically includes pressure tests, radiography of welds, and a visual inspection.

The valves' function is to provide a reliable sealing capability. Since they work in such adverse conditions, they need to be checked during a five-year check. It is, however, advised to remove them from the aircraft every 15 000 FC to thoroughly inspect them and eventually replace them. Their removal is scheduled for D-checks. The pumps' scheduled maintenance will be similar to the valves' one.

The pipes have sensors to detect any leakage in a timely manner, as explained in Subsection 7.7.2. In addition to that, their exterior will be visually inspected every five years, and a borescope inspection will be performed during D-checks. If a non-routine structural repair has to be done on a pipe joint, a hydrostatic leakage test will be done.

In case of a drastic pressure rise in the tank, the aircraft is equipped with the explosion-prevention system explained in Section 10.1. It acts similarly to a non-resealable burst disk. It cannot be internally inspected as it is strongly advised not to interfere with its closing system. It is thus decided to change the system during the 5-year maintenance event.

The boil-off relieving valve will be resealable so it can be checked thoroughly without depleting during C-checks. The heat exchangers will be checked and maintained during C-checks.

11.2.2. Engine Maintenance

The engine shop maintenance of a conventional engine is scheduled after 9000 FH [96]. During this process, the engine is removed from the aircraft and transported via an air suspension system to an engine workshop. It is then visually inspected for damage, also internally through a borescope. If necessary, a test run is also done to determine the scope of the maintenance that will be conducted. The engine is then disassembled sequentially into its subsystems. The different parts are cleaned and inspected, where necessary repairs and maintenance are performed. Some parts with a limited life get replaced, and non-destructive testing is done on the different modules to check for possible cracks. After this, the engine is reassembled and then tested for compliance with the engine manual. It is then mounted back on the aircraft, and a test flight might be performed as additional checks. [129]

Extra attention should be given during maintenance to the elements exposed to higher temperatures and humidity due to the combustion of hydrogen. The combustion chamber will have to be inspected more frequently for heat damage; this is why the engine will be checked every 5000 FC. As hydrogen combustion produces more water vapour as well, a maintenance task will have to be dedicated to check its effects because it increases the high temperature oxidation of the material in the exhaust [130].

11.2.3. Overview of Scheduled Tasks for different Checks

A summary of the additional maintenance tasks with their intervals and estimated time in MMH is found in Table 11.2.

Table 11.2: Overview of additional maintenance due to the specific systems of the MAVERICK aircraft with advised MMH[97].

Element to be maintained	Type of check	Interval	Time required (MMH)
Internal tank	D-check	10 years	1
External tank	A-check	400 FH	0.2
	C-check	1.5 years	0.6
Valves	5 years	5 years/5000 FC	0.4
	D-check	10 years	3
Pumps	5 years	5 years/5000 FC	0.8
	D-check	10 years	6
Pipes	5 years	5 years/5000 FC	2
	D-check	10 years	1.5
Emergency Vent Outlet	5 years	5 years/5000 FC	1.5
Boil-off Relieving Valve	C-check	1.5 years	2.5
Heat-Exchangers	C-check	1.5 years	3

11.3. Cost Estimation

The purpose of the cost estimation is to estimate Research, Development, Test, and Evaluation (RDTE) and prototyping costs for MAVERICK. The method provided by Roskam is used [131]. The main inputs are the maximum take-off mass, maximum equivalent airspeed, number of RDTE aircraft, number of production aircraft, engine cost, labour rates, and Roskam correction factors [131]. Hydrogen systems are taken into account using correction factors for novel technologies provided by Roskam. Certification costs are included under *Production flight-test operations*. A baseline production volume of 300 aircraft is assumed, consistent with the expected market share used in the market analysis. The resulting cost breakdown is shown in Table 11.3.

Table 11.3: Grouped cost estimation results for the production of 300 aircraft.

Cost item	Programme cost [M EUR]	Unit cost [M EUR]	Share [%]
Research, development, testing and evaluation			
Engineering, support and development testing	394.9	1.32	19.6
Flight-test aircraft and operations	1,017.7	3.39	50.4
Test facilities, RDTE profit and financing	605.4	2.02	30.0
Total RDTE cost	**2017.9**	**6.73**	**100.0**
Manufacturing and acquisition			
Additional airframe engineering and design	279.5	0.93	1.3
Aircraft production programme	17,882.3	59.61	80.2
Production flight-test operations	82.8	0.28	0.4
Manufacturing finance and profit	4,054.4	13.51	18.2
Total manufacturing acquisition cost	**22,299.0**	**74.33**	**100.0**
Total cost	**24,316.9**	**81.06**	**100.0**

As shown in Table 11.3, the estimated unit acquisition cost including amortised RDTE is €81.1 M for the baseline production volume of 300 aircraft. This corresponds to approximately 54.0% of the assumed sale price of €150 M. The manufacturing acquisition cost is the dominant contributor, while the amortised RDTE cost contributes €6.7M per aircraft. This shows that the cost model does not capture the programme risk, supplier margins and airline discounts. A more in-depth cost analysis should be performed during the detailed design phase to better estimate the total program costs.

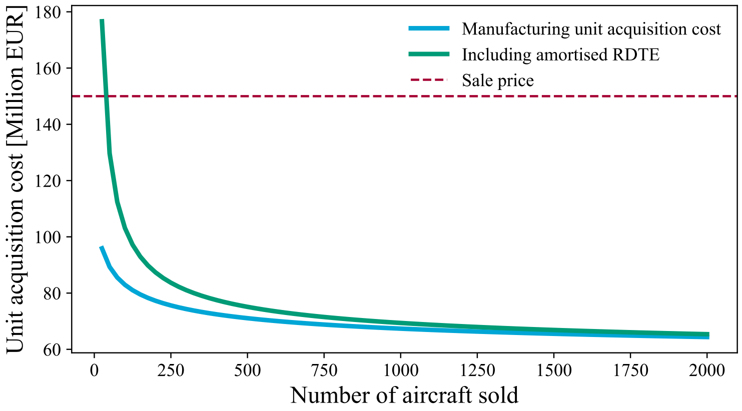

Figure 11.8: Roskam-based unit acquisition cost as a function of total production quantity.

Figure 11.8 shows that the unit acquisition cost is sensitive to the number of aircraft produced. At small production volumes, the cost including amortised RDTE is high because the whole development cost is distributed among a small number of aircraft. When production increases, the RDTE contribution per aircraft decreases and the non-linear production cost reduces the unit cost. For the baseline case, the unit cost remains well below the assumed sale price, showing that the programme can be financially viable if the expected production volume is achieved.

11.4. Competitiveness Analysis

MAVERICK's competitiveness is assessed against the two propulsion categories most likely to compete in the narrow-body market: aircraft flying solely on LH_2 and conventional aircraft flying on the required SAF blend. The comparison is conducted on a differential cost basis under the assumptions listed in Table 11.4.

Table 11.4: Assumptions used in the differential cost comparison.

ID	Assumption	Justification / source
A-CS-01	The three candidate aircraft are of similar size and technology level, sharing a common airframe, payload, speed and seat utilisation rate.	They compete in the same narrow-body class and are comparable in technology, so only the energy pathway differs.
A-CS-02	The three aircraft share a similar platform. The comparison is conducted on a differential basis that retains only the cost components that differ. All revenue and common operating costs are excluded.	Identical passengers, seat utilisation rate and network give identical revenue and common costs, which cancel out.
A-CS-03	Future cash flows are discounted to present value at a discount rate of 2%.	The discount rate captures the opportunity cost of the capital investment.
A-CS-04	The aircraft is bought outright in year 0 and no salvage value is recovered at end of life.	The salvage value is highly uncertain, excluding it reduced uncertainty and is a conservative assumption.
A-CS-05	Energy demand is set on a typical mission, full-seat basis (MJ per ASK).	Simplification for easy calculation
A-CS-06	The EU ETS carbon price applies only to the fossil Jet A-1 share. HEFA, eSAF and green LH_2 are excluded.	ReFuelEU and the EU ETS treat sustainable aviation fuels and green hydrogen as zero-rated[132].

ID	Assumption	Justification / source
A-CS-07	The kerosene pathway is a blend of Jet A-1, HEFA and eSAF set by the ReFuelEU mandate trajectory.	ReFuelEU SAF and synthetic sub-mandate shares[3].
A-CS-08	Year-indexed prices are interpolated linearly between years with available data, and extrapolated linearly beyond 2050.	Lack of data.
A-CS-09	The Jet A-1 and HEFA prices are held constant across the horizon.	Jet A-1 is held constant for simplification. The HEFA price is held constant on the basis of the IATA report[133].
A-CS-10	MAVERICK is assumed to be priced at 150M€	Specified by mission requirement REQ-MIS-COST-01

11.4.1. Annual energy and carbon cost

The annual fuel cost $C_{\text{fuel}}(y)$ and annual carbon cost $C_{\text{carbon}}(y)$ in operating year y are

$$C_{\text{fuel}}(y) = e \cdot A \sum_i x_i(y) \frac{p_i(y)}{LHV_i}, \qquad C_{\text{carbon}}(y) = \frac{e\,A}{1000} P_{\text{CO}_2}(y) \sum_{i \notin \text{ETS-free}} x_i(y) \frac{\kappa_i}{LHV_i}. \tag{11.1}$$

Where A is the annual ASK flown by one aircraft and e its energy intensity (energy per ASK), so the annual fuel energy is $e \cdot A$. Each pathway burns a year-dependent blend of energy carriers with shares $x_i(y)$ (summing to one), per mass price $p_i(y)$ and lower heating value LHV_i. Under the EU ETS, sustainable aviation fuels (HEFA, eSAF) and green LH_2 are zero-rated, so the carbon price falls only on the fossil Jet A-1 share, with per-mass carbon factor $\kappa_i = 3.16$ and carbon price $P_{\text{CO}_2}(y)$.

11.4.2. Cash flow and net present cost

Let P be the acquisition price, capital enters in year 0 as the aircraft is assumed to be paid upfront. The invested capital, $I_0 = P$. The differential operating cost in ownership year k collects energy, carbon and hydrogen-specific scheduled maintenance M_k, $O_k = C_{\text{fuel}}(y) + C_{\text{carbon}}(y) + M_k$. The differential cash flow is then $CF_0 = -I_0$ and $CF_k = -O_k$ for $k = 1, \dots, N$, where r is the discount rate, taken at 2%. Discounting at r and reversing the sign gives the net present cost, NPC

$$\text{NPC} = -\sum_{t=0}^{N} \frac{CF_t}{(1+r)^t}. \tag{11.2}$$

The decision metric is the NPC itself. Because the excluded costs are common to all three aircraft, their differential NPCs are directly comparable, and the aircraft with the lowest NPC is the cheapest and therefore preferred. Table 11.5 shows all the fixed inputs used for the NPC.

Table 11.5: Scalar input parameters of the differential cost model.

Parameter	Symbol	Unit	Value	Source
Operations and utilisation				
Annual flight hours per aircraft	–	hr	2 800	[134] [1]
Annual available seat-kilometres per aircraft	A	ASK/yr	423×10^6	[1]
Economics and finance				
Entry into service	y_{EIS}	–	2040	–
Ownership life	N	yr	20	–
Discount rate	r	%	2	Table 11.4
Aircraft (energy intensity and capital)				
Kerosene energy intensity	e_{kero}	MJ/ASK	0.78	[135]
MAVERICK energy intensity	e_{mav}	MJ/ASK	0.90	Section 5.2
Full-H_2 energy intensity	e_{H_2}	MJ/ASK	1.06	[135]
MAVERICK LH_2 energy share	x_{LH_2}	%	61.7	Section 5.2
Kerosene acquisition price	P_{kero}	M€	110	[7]
MAVERICK acquisition price	P_{mav}	M€	150	–
Full-H_2 acquisition price	P_{H_2}	M€	144.1	[7, 136]
Hydrogen-system scheduled maintenance				
Annual LH_2 check cost	–	M€	1.84	[134, 136]

Seen in Table 11.5, McKinsey[136] suggest that a LH_2 aircraft will have 31% more capital expenditure than a similar aircraft entering service in 2035, using the current list price of the A320neo, a price of 144.1 M€is obtained for the LH_2 aircraft. This is lower than MAVERICK, which is unexpected as there are more systems to certify. The LH_2 aircraft does have a higher energy intensity, as expected, since a full hydrogen system will lead to a heavier aircraft compared to MAVERICK.

Variable prices are shown in Table 11.6 and interpolated piecewise linearly between them, with linear extrapolation along the slope of the final two data points beyond the last data point. The SAF mandate and its synthetic sub-mandate are instead held piecewise constant, stepping to the next required percentage at the years where the mandate increases.

Table 11.6: Year-indexed input trajectories, given at anchor years and interpolated/extrapolated linearly. The underlined values are taken from the source listed, while the non-underlined values are interpolated.

Quantity	Unit	2030	2035	2040	2045	2050	Source
Jet A-1 price	€/kg	$\underline{0.73}$	$\underline{0.73}$	$\underline{0.73}$	$\underline{0.73}$	$\underline{0.73}$	[137]
HEFA price	€/kg	$\underline{2.10}$	$\underline{2.10}$	$\underline{2.10}$	$\underline{2.10}$	$\underline{2.10}$	[137]
eSAF price	€/kg	$\underline{6.50}$	5.81	5.13	4.44	$\underline{3.75}$	[138]
LH_2 price	€/kg	4.05	$\underline{3.90}$	3.75	3.60	$\underline{3.45}$	[9]
EU ETS carbon price	€/t_{CO_2}	$\underline{145}$	$\underline{197}$	265	332	$\underline{400}$	[2]
SAF mandate (total)	%	$\underline{6}$	$\underline{20}$	$\underline{34}$	$\underline{42}$	$\underline{70}$	[3]
SAF sub-mandate (synthetic)	%	$\underline{1.2}$	$\underline{5}$	$\underline{10}$	$\underline{15}$	$\underline{35}$	[3]

11.4.3. Results

The differential net present cost at the 2% baseline rate is given in Table 11.7. The full-hydrogen aircraft is cheapest at 387.1 M€, the kerosene aircraft follows at 396.1 M€, and MAVERICK is the most expensive at 418.1 M€.

---

[1] Derived from `https://web.mit.edu/airlinedata/www/Aircraft&Related.html` and `https://www.lufthansagroup.com/en/company/fleet/brussels-airlines/airbus-a320.html` (accessed 2026-06-12).

[2] `https://assets.ctfassets.net/1u811bvgvthc/6A6aMSYbA3aCQZT7n0muQi/021511e2aecc15d6efa7169647389fe5/EU-ETS_scenarios.pdf`, `https://about.bnef.com/insights/commodities/eu-ets-market-outlook-1h-2024-prices-valley-before-rally/`, `https://www.enerdata.net/publications/executive-briefing/carbon-price-projections-eu-ets.html` (Accessed:12-06-2026)

Table 11.7: Differential cost results at the 2% baseline discount rate. All entries are present values in M€.

Cost item	Kerosene	MAVERICK	LH_2
Capital	110.0	150.0	144.1
Fuel	218.2	208.0	212.9
Carbon	67.9	30.0	0.0
H_2 mtce	0.0	30.1	30.1
NPC	396.1	418.1	387.1

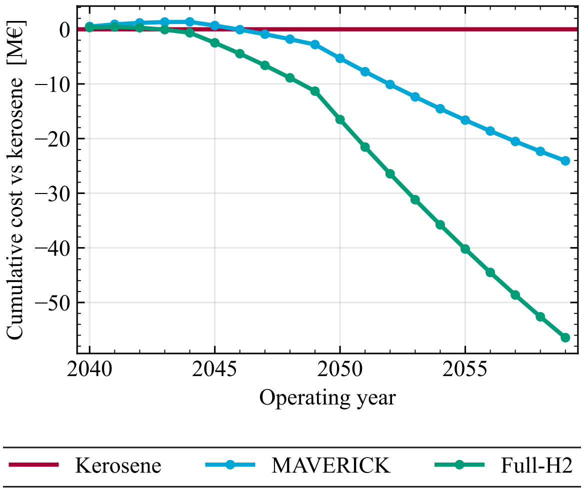

Figure 11.9: Cumulative difference in operating cost by year compared to kerosene aircraft.

MAVERICK has the lowest fuel cost of the three at 208.0 M€, a smaller carbon cost than the kerosene aircraft, 30.0 M€compared to 67.9 M€, and the same hydrogen-specific maintenance charge as the full-hydrogen aircraft. It is nonetheless the most expensive overall, because these advantages do not offset its acquisition price of 150 M€, the highest of the three, and the carbon it still pays, where the full-hydrogen aircraft pays none. MAVERICK is only the most expensive choice when priced at 150 M€, this is due to assumption A-CS-10, later in Subsection 11.4.4, it can be seen that MAVERICK has the ability of being the most affordable option. The full-hydrogen aircraft offsets the hydrogen-specific maintenance charge by paying no carbon, while the kerosene aircraft offsets its carbon bill by having a low acquisition price. Figure 11.9 shows the difference in annual operating cost for each aircraft with respect to the kerosene baseline.

11.4.4. Sensitivity Analysis

To assess MAVERICK's financial feasibility, a sensitivity analysis is performed to identify the scenarios in which MAVERICK can outperform them in terms of cost.

Cost-parity thresholds

MAVERICK can decrease its NPC in two ways: a more efficient propulsion and aerodynamic configuration reduces energy intensity, while cheaper manufacturing can lower cost. As a result, both are targets MAVERICK can engineer toward. Kerosene, carbon, and hydrogen prices, by contrast, are set by markets and policies that the project cannot steer, so they are held fixed here as scenario inputs rather than treated as design variables. Holding the other two aircraft fixed at 396.1 M€(kerosene) and 387.1 M€(full-hydrogen), Table 11.8 reports how far each controllable parameter must fall for MAVERICK to overtake each rival. Both costs scale linearly, so each sweep is a straight line.

Table 11.8: MAVERICK break-even thresholds at the 2% baseline discount rate.

Swept input	Current	Cheaper than kerosene	Cheapest of all
Energy intensity e_{mav} [MJ/ASK]	0.90	< 0.82	< 0.78
Acquisition price P_{mav} [M€]	150	< 128	< 119

To undercut the kerosene aircraft, MAVERICK must reach an energy intensity of 0.82 MJ/ASK or an acquisition price of 128 M€, to become the cheapest of the three. These tighten to 0.78 MJ/ASK or 119 M€. The efficiency target is plausible as the LH_2 system matures, for instance through fully composite LH_2 tanks[3]. The cheapest threshold of 0.78 MJ/ASK is more demanding, as it would require a hydrogen-carrying aircraft to match the energy intensity of a purely kerosene one, which the mass and volume penalty of the LH_2 system makes difficult to achieve. The price targets are more probable given the estimated production cost is only 81.1 M€ including RDTE, which means the unit cost of 150 M€ can be lowered to make it competitive. An alternative approach is the 30.1 M€ maintenance charge, which alone exceeds MAVERICK's 22 M€ gap to the kerosene aircraft. Reducing it through digital-twin monitoring and component-failure prognostics is a possible route to undercut the kerosene aircraft without any gain in efficiency or price. The sweep can be seen in Figure 11.10

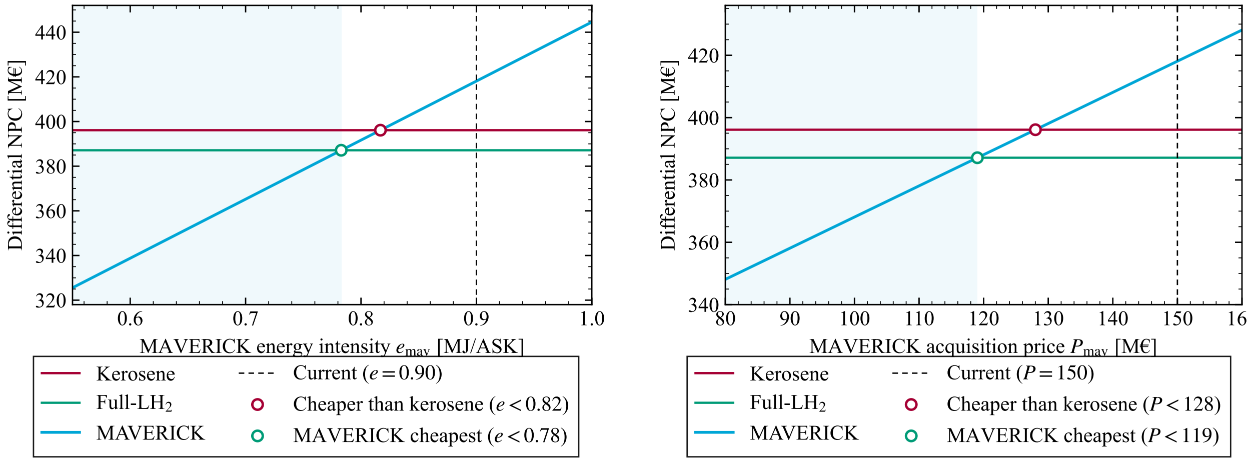

(a) Energy intensity swept.

(b) Acquisition price swept.

Figure 11.10: MAVERICK's NPC at different energy intensity (a), and acquisition price (b). Using Equation 11.2

Price-scenario sensitivity

The previous sweeps varied MAVERICK's own inputs. The scenarios below instead vary the external input, the market price of EU ETS carbon emission, the green LH_2 and the kerosene-pathway price, the last containing the blended Jet A-1, HEFA and eSAF fuels, each scaled across its full trajectory from half to twice the baseline price in Table 11.6. Unlike the internal variables, a change in a commodity's price affects more than one aircraft at once. A higher carbon or kerosene-pathway price raises the kerosene aircraft's cost the most, and MAVERICK's partly through its kerosene fraction, while leaving the carbon-free full-hydrogen aircraft unaffected. A higher LH_2 price, conversely, raises the full-hydrogen cost most, and MAVERICK's partly, while leaving the kerosene aircraft unaffected. The resulting crossings are collected in Table 11.9 and shown in Figure 11.11.

Table 11.9: Effect of the three external prices on MAVERICK's ranking.

Exogenous price	MAVERICK beats kerosene	MAVERICK beats full-hydrogen
EU ETS carbon price	≥ 158%	never
Green LH_2 price	≤ 80%	≥ 131%
Kerosene-pathway price	≥ 118%	≤ 68%

At the central estimate, MAVERICK is the most expensive of the three, as seen in Table 11.7. In every sweep, its weakest position is the central band, and a large move in any of the three prices pulls it up by overtaking one rival. The single-pathway aircraft behaves the opposite way, each cheap at the centre but each with a direction that makes it the most expensive.

The kerosene aircraft under a high carbon price or a costly fuel blend, the full-hydrogen aircraft under a high LH_2 price. MAVERICK overtakes the kerosene aircraft once the carbon price rises to

---

[3] `https://www.nlr.org/newsroom/case/liquid-hydrogen-composite-tanks-for-civil-aviation/` (Accessed 15-06-2026)

about 58% above its central path throughout the programme life. This could be possible under an aggressive climate policy. MAVERICK also overtakes the kerosene aircraft if the blended kerosene fuel rises about 18%, which a fuel price shock can deliver, seen from the Iran conflict in 2026 when fuel prices jumped 55%[4].

The LH_2 sweep adds the symmetric result, MAVERICK is cheaper than kerosene whenever hydrogen is at least 20% below its baseline price and cheaper than the full-hydrogen aircraft whenever hydrogen is at least 31% above it. No single external price makes MAVERICK the outright cheapest. Only the internal factors of Table 11.8 can do that. The external sweeps confirm that its standing is robust to the market and policy conditions it does not control, and improves under a rising carbon price.

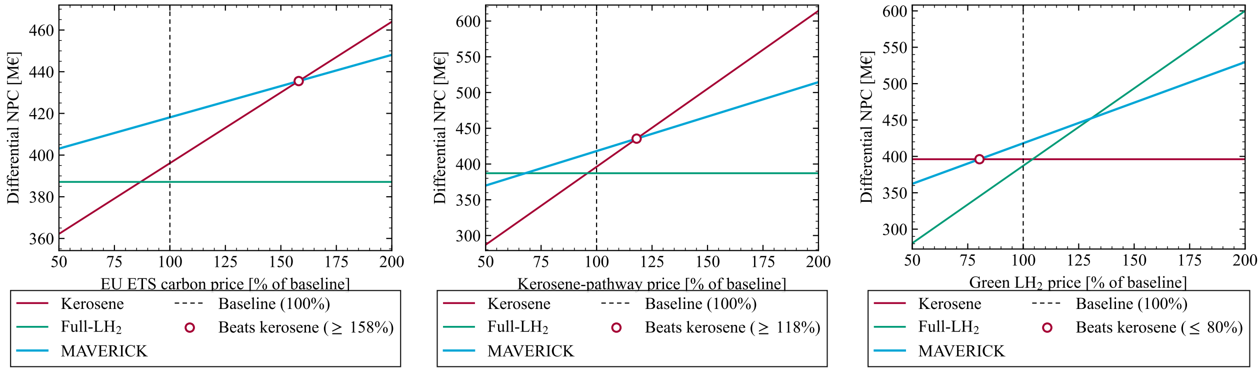

(a) Carbon price swept. **(b)** Kerosene-pathway price swept. **(c)** LH_2 price swept.

Figure 11.11: Differential net present cost of the three aircraft as each price is scaled from 50% to 200% of its baseline trajectory.

11.4.5. Stakeholder Value Proposition

The NPC ranking places MAVERICK last, but that outcome is driven by acquisition price, a one-time cost incurred at purchase. The full-hydrogen acquisition price of 144.1 M€ adopted here is itself a low estimate, because a new hydrogen aircraft carries larger cryogenic tankage and an entirely new powertrain and would plausibly cost more than MAVERICK rather than less. Using the lower figure is therefore conservative, since it understates MAVERICK's capital position relative to the full-hydrogen aircraft and biases the ranking against MAVERICK. On the two measures that determine competitiveness during service, MAVERICK is superior to each rival on one measure. Relative to the kerosene aircraft, MAVERICK has a lower operating cost. Its lifetime operating cost in present value, comprising fuel, carbon, and hydrogen maintenance, is 268.1 M€ against 286.1 M€ for the kerosene aircraft. This is an operating-cost advantage of 18.0 M€. While there are additional maintenance costs for MAVERICK, this advantage arises because, under this model's central price assumptions, hydrogen has been cheaper than the SAF blend combined with its carbon permit on a per-megajoule (€/MJ) basis since 2035, which makes hydrogen the lower-cost energy carrier in this scenario. By supplying half of MAVERICK's energy as hydrogen, the design reduces its operating cost relative to the kerosene aircraft. However, the reduced fuel cost and the carbon saving do not appear in the overall ranking because they are offset by capital expenditure, which is incurred once rather than recurring each year in service.

Relative to the full-hydrogen aircraft, the advantage is operability, and it increases once risk is considered. MAVERICK retains a conventional kerosene dispatch capability, so it can operate from any airport in the existing network regardless of whether that airport supplies hydrogen, and it can adopt hydrogen incrementally as supply becomes available at individual airports. The full-hydrogen aircraft has no such alternative, it can only be based and dispatched at airports with LH_2 infrastructure. Its lower cost depends on an infrastructure rollout that remains years away and may not extend to every route. This limitation is most significant in the case of a diversion. Adverse

---

[4] `https://www.cnbc.com/2026/04/21/oil-price-iran-war-middle-east.html` (Accessed 15-06-2026)

weather, traffic congestion, or a technical fault can require any aircraft to land at an unplanned airport, and a full-hydrogen aircraft diverted to an airport without hydrogen cannot refuel. The aircraft and its passengers are then grounded until hydrogen is transported to the airport. A costly and high-risk outcome that MAVERICK avoids because it can always refuel on kerosene and continue the flight. MAVERICK also carries lower entry-into-service risk, as a new hydrogen powertrain is likely to experience more early-life reliability problems in the opening years of hydrogen operation, whereas MAVERICK combines its hydrogen system with an established conventional system that improves the aircraft's reliability while the new technology matures. The full-hydrogen aircraft has no such alternative, it can only be based and dispatched at airports with LH_2 infrastructure, so its lower cost depends on an infrastructure rollout that remains years away and may not reach every route.

These two advantages are assessed differently by each stakeholder. For an airline, MAVERICK reduces the operating cost compared to a kerosene aircraft and removes the dispatch and diversion risk of a hydrogen aircraft and the early-life reliability risk associated with the new powertrain. Additionally, the fleet can decarbonise at the rate at which airports start to support LH_2 rather than requiring the entire network to convert first. MAVERICK also spreads fuel-price risk across two energy carriers, because each mission uses both LH_2 and kerosene-SAF, a price shock in either fuel raises only the partial cost attributable to that carrier, whereas a single-fuel type is fully exposed to the shock. For a financier or lessor, the kerosene fallback keeps the asset operable and transferable at every airport and protects it from being stranded during a diversion. This preserves both its utilisation and its residual value and widens the resale market relative to a full-hydrogen aircraft. Since a full-hydrogen aircraft's value depends on infrastructure that may not be delivered. For a regulator or an investor, MAVERICK is a decarbonisation measure that can be deployed at entry into service, reducing carbon emissions by more than half immediately, rather than conditionally on the prior development of a hydrogen ecosystem. The acquisition premium that determines MAVERICK's position in the ranking is the cost of this position, and it decreases as the LH_2 system matures and as its 30.1 M€ maintenance charge and its energy-intensity gap diminish.

11.5. Return on Investments and Operational Profits

A return on investment analyses whether MAVERICK recovers its purchase over its service life, which the differential study of Section 11.4 cannot show because it cancels all revenue and every common cost.

The aircraft is bought outright in year zero at a cost of P. In each ownership year k, it earns a flat revenue of R per ASK, on the annual ASK A, and pays the full operating cost O_k. That cost collects the energy and carbon terms of Section 11.4, the maintenance rate c_{maint} annualised through the flight hours H, and the miscellaneous operation items o_j sourced per ASK, $O_k = C_{\text{fuel}}(y) + C_{\text{carbon}}(y) + c_{\text{maint}} \cdot H + A \sum_j o_j$. The discount rate r, the ownership life N and the outright purchase are taken unchanged from Section 11.4. The cash flow and its net present value are

$$CF_0 = -P, \qquad CF_k = R \cdot A - O_k, \qquad \text{NPV} = \sum_{t=0}^{N} \frac{CF_t}{(1+r)^t}. \tag{11.3}$$

The unit revenue that sets the net present value to zero is the break-even revenue L, equal to the levelised cost per ASK, $L = \left(P + \sum_k O_k(1+r)^{-k}\right) / \sum_k A(1+r)^{-k}$. A unit revenue R above L returns a profit and one below it a loss.

11.5.1. Inputs

The unit revenue is $R = Y\,LF$, with Y the passenger yield and LF the load factor. The energy intensity, fuel mix, carbon treatment, acquisition price, discount rate, ownership life and annual ASK are inherited from Table 11.5; the added inputs are listed in Table 11.10. Miscellaneous operation items o_j are in euro-cents per ASK from the EUROCONTROL standard inputs[5]. The load factor and yield

---

[5] `https://ansperformance.eu/economics/cba/standard-inputs/latest/chapters/aircraft_operating_costs.html` (Accessed 16-06-2026)

are the Air France-KLM FY2024 group passenger figures [113], which blend the low-cost subsidiary Transavia and give a conservative revenue base. The maintenance cost of 2058e/hr is from [134, 136], values inherited from Table 11.5 are marked with a dagger.

Table 11.10: Inputs to the analysis (2026 euros).

Finance, utilisation, maintenance, revenue		*Operating lines o_j [c/ASK]*	
Acquisition P [M€]†	150	Flight-deck crew	0.402
Discount rate r [%]†	2	Administration	0.338
Ownership N [yr]	25	Ground	0.278
Annual ASK A [10^6]†	423	Marketing	0.244
Annual flight hours H [hr/yr]	2800	Cabin crew	0.226
Maintenance c_{maint} [€/hr]	2058	Navigation charges	0.169
Load factor LF	0.878	Airport charges	0.162
Passenger yield Y [€/pax-km]	0.0933	Passenger service	0.158
		Information technology	0.026
		Flight-equipment insurance	0.004

11.5.2. Result

At the Air France-KLM revenue of 8.19 c/ASK, MAVERICK earns 34.7 M€ a year and a first-year free cash flow of 6.2 M€. The investment metrics are collected in Table 11.11. The programme is close to break-even but does not clear it: the net present value is −32.5 M€, the internal rate of return is 0.1% and the lifetime return on investment is +1%. The undiscounted cash flow recovers the acquisition only at the very end of the life, a simple payback of 25 years. On a discounted basis, there is no payback. The break-even revenue is 8.59 c/ASK, which the earned 8.19 c/ASK falls short of by 0.39 c/ASK. Because the cost base is fixed, the net present value is linear in the unit revenue, so the verdict turns on the yield, as Table 11.12 shows.

Table 11.11: MAVERICK investment metrics at the 2% discount rate and the Air France-KLM revenue, with the levelised cost build that sets the break-even revenue.

Investment metrics		*Levelised cost [c/ASK]*	
NPV @ 2% [M€]	−32.5	Fuel (LH$_2$+kerosene)	2.97
IRR [%]	0.1	Capital (acquisition)	1.82
Lifetime ROI [%]	+1	Maintenance (airframe+eng+H$_2$)	1.36
Payback, simple [yr]	25	Carbon (EU ETS)	0.43
Annual revenue [M€]	34.7	Operating lines o_j (ten)	2.01
Revenue earned [c/ASK]	8.19	**Break-even revenue** L	**8.59**

Table 11.12: Sensitivity of the net present value to the revenue per ASK, with the cost base held fixed. The central case is 8.19 c/ASK and the break-even is 8.59 c/ASK.

Revenue [c/ASK]	7.00	8.00	8.19	8.59	9.00	10.00
NPV [M€]	−131	−48	−33	0	+34	+117
Discounted payback [yr]	none	none	none	25	20	13

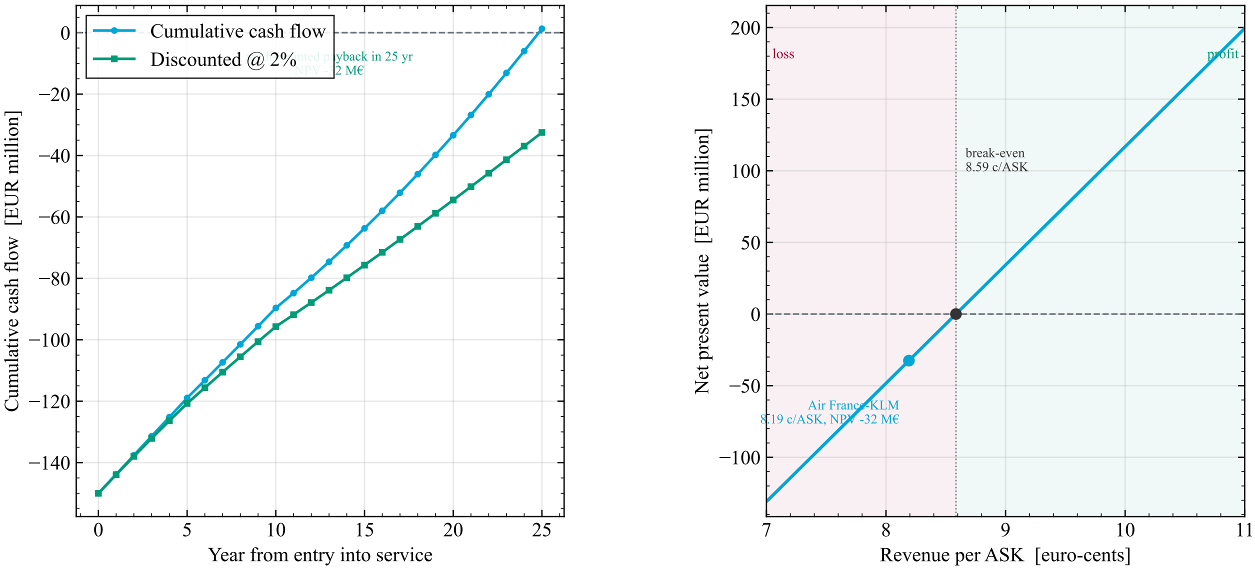

(a) Cumulative cash flow and payback.

(b) Net present value against revenue per ASK.

Figure 11.12: MAVERICK return on investment at the 2% discount rate and the Air France-KLM revenue.

11.5.3. Results

MAVERICK comes close to but does not clear break-even at the blended revenue a full-service group earns today. The shortfall is the cost of the hydrogen technology, since fuel, capital and maintenance, the three largest lines, are three-quarters of the cost and each carries a premium over a conventional narrow-body. Closing the gap on the revenue side requires the unit revenue to rise from 8.19 to the 8.59 c/ASK break-even, an increase of 0.39 c/ASK, or 4.8% on the fare, equal to a yield of 0.0978 e/pax-km. The earned 8.19 c/ASK is the FY2024 group passenger figure, which blends the low-cost subsidiary Transavia [113]. A full-service operation earns more, 8.43 c/ASK in the fourth quarter of 2024 [113] and between 8.39 c/ASK over the first half of 2025 and 8.79 c/ASK in the second quarter [139]. The break-even of 8.59 c/ASK sits in the upper part of that range, above the Q4 2024, H1 2025, but below the Q2 2025 peak, so MAVERICK clears its costs only if it holds full-service yields at their stronger end, not low-cost ones. The sensitivity in Table 11.12 shows the programme turning profitable once the revenue clears the break-even, reaching a thirteen-year payback at 10 c/ASK.

11.6. Post-DSE Timeline

Section 11.1 explores the production phase in more detail, as these are crucial product phases for the success of a novel technology. This section treats the Post-DSE process in a holistic manner. The revised development approach is based on the knowledge gained during the DSE and includes an initial roadmap for detailed engineering, prototype manufacturing, validation testing, certification activities, and entry into the market.

The post-DSE phase is assumed to be conducted by a team of 10 engineers, working on full-time roles (8-hour work days), on-site (5 days a week). The major phases and key milestones include:

1. **Detailed Subsystem Design (2026–2029):** The post-DSE phase starts with maturing the preliminary aircraft, propulsion, tank, and fuel-feed designs into detailed subsystem definitions.
2. **Prototype Production (2029–2031):** Scaled prototypes and representative test articles are manufactured to support early integration and validation activities.
3. **Verification, Validation, and Documentation (2031–2033):** The main design assumptions, subsystem performance, and integration choices are verified and validated through analysis, testing, and documentation.
4. **Flight Testing and Certification (2033–2037):** Full-scale ground and flight tests are developed

to demonstrate compliance with certification requirements and validate operational safety.

5. **Production Scale-Up (2037–2039):** The production system is prepared and gradually scaled towards full-rate manufacturing.
6. **Market Entry (2039–2040):** Initial deliveries, customer support, and entry-into-service activities are completed.
7. **Maintenance (2040 onwards):** Maintenance procedures, spare-part supply, and operator support are continued during service life.
8. **End-of-Life Planning (2040 onwards):** End-of-life and circularity planning are refined as operational data becomes available.
9. **Next-Generation Design (2040 onwards):** Lessons learned from MAVERICK are used to identify improvements for future aircraft generations.

The overview above summarises the main post-DSE development phases. To clarify how these phases are translated into concrete activities, a Work Flow Diagram is provided in Appendix A. This diagram expands the roadmap by showing the key task groups, their sequencing, and the main dependencies between design, testing, certification, production, and entry into service.

12

Conclusion

This report presented the preliminary design of MAVERICK, a 180-passenger single-aisle aircraft entering service in 2040 that burns hydrogen and kerosene/SAF simultaneously in the same engine. It will be a transitional step between conventional kerosene aviation and a fully hydrogen-powered fleet, showing the potential of hydrogen while having the operational and regulatory advantages of kerosene. Its central objective is to halve lifecycle CO_2 and NO_x emissions relative to the A320neo while keeping the operational flexibility of a conventional narrow-body. The market analysis confirmed the rationale, tightening emissions regulation, rising SAF mandates, and carbon pricing increasingly penalise kerosene-only operators, and MAVERICK's dual-fuel architecture lets airlines fly from hydrogen-ready hubs while still serving destinations without LH_2 infrastructure, an option unavailable to hydrogen-only concepts such as Airbus ZEROe. The aircraft is therefore positioned as a flexible decarbonisation tool for European flag carriers on core 1000–2000 km routes, optimised for a 2000 km nominal mission with a 3000 km maximum range. The kerosene tank is sized for the full 3000 km, so the mission can be completed even with an empty hydrogen tank. On the other hand, the hydrogen tank is sized to deliver the 50% CO_2 reduction over the nominal mission, assuming no LH_2 refuelling at the destination. This latter case drove the fuel mass, weight, centre of gravity, and stability budgets.

The engine is the core innovation. Rather than designing a new engine, the proven CFM LEAP-1A core was retained and modelled in GasTurb, with only the two emissions-critical components, the injector and combustion chamber, redesigned for dual-fuel operation. A phase-dependent strategy raises hydrogen fractions during long, low-thrust phases (taxi, cruise) and lowers them at high thrust (take-off, climb), managed in flight by the FADEC. For the nominal mission the fuel mixture is bounded by the kerosene allowance with exactly 50% CO_2 reduction, with 838 kg of hydrogen and 1450 kg of kerosene per engine. An annular TAPS combustor was selected for its mature low-NO_x performance, paired with a bespoke staged injector with separate gaseous-hydrogen and liquid-kerosene paths, partial premixing through small orifices, twin air swirlers, and a central axial air stream to suppress flashback, the chief hazard from hydrogen's high flame speed. It holds a stable swirl number of 0.678 at cruise while respecting an auto-ignition residence-time limit of order 0.02 ms. The liquid hydrogen is stored at 2 bar in a double-walled aft tank and delivered to the injector by a split system, containing a cryogenic boost turbopump, two heat exchangers, and a gas compressor. This system injects 0.1968 kg/s of hydrogen at 55.94 bar and a minimum of 150 K at take-off. The heat exchangers exploit hydrogen as a heat sink, cooling engine bleed air (reused for cabin conditioning and HPT cooling) and oil; the full network was modelled in Simulink/Simscape with CoolProp properties and duplicated as two independent branches.

The sustainability analysis confirmed the environmental case while exposing its main caveat. Carbon-bearing emissions fall sharply wherever hydrogen displaces kerosene, with CO down up to 99.7% in taxi and soot roughly 55% lower at high power, and the streamlined LCA shows operational impact 13.96% below the A320neo on SAF. The 50% target is met on a fuel/CO_2 basis, and jet noise is marginally lower in all certification conditions. The principal limitation is that modelled NO_x remains high, reflecting hydrogen's higher flame temperature and acknowledged model shortcomings, and is the foremost area for follow-up research. Verification and validation defined a campaign repeating all engine tests across the full hydrogen-to-kerosene range with particular attention to flashback, plus cryogenic tank, leak-detection, and flight testing at the hydrogen-equipped Rotterdam The Hague airport, while the operations concept covered LH_2 ground handling, dual-fuel pilot interfaces, and an emergency kerosene-only fallback. The financial analysis presents the principal constraint: When priced at 150 M€ MAVERICK carries the highest net present cost of the three architectures considered (418.1 M€) and falls marginally short of break-even, with an NPV of -32.5 M€ and a break-even revenue of 8.59 c/ASK against the 8.19 c/ASK earned today, the shortfall being attributable to the hydrogen technology premium. In summary, MAVERICK demonstrates that simultaneous hydrogen-kerosene combustion in a minimally modified, proven engine core is a credible route to halving narrow-body emissions by 2040 while retaining infrastructure flexibility. The quantification of NO_x emissions, the cost premium, and the maturity of hydrogen infrastructure and certification define the priorities for the next phase of development.

13 Bibliography

[1] Pollock, T., and Tin, S., "Nickel-Based Superalloys for Advanced Turbine Engines: Chemistry, Microstructure and Properties," *Journal of Propulsion and Power*, Vol. 22, 2006, pp. 361–374. https://doi.org/10.2514/1.18239.

[2] Horlock, J. H., *Advanced Gas Turbine Cycles*, Pergamon, 2003.

[3] European Parliament and Council of the European Union, "Regulation (EU) 2023/2405 of the European Parliament and of the Council of 18 October 2023 on Ensuring a Level Playing Field for Sustainable Air Transport (ReFuelEU Aviation)," Official Journal of the European Union, L 2023/2405, 2023.

[4] Hoelzen, J., Flohr, M., Silberhorn, D., Mangold, J., Bensmann, A., and Hanke-Rauschenbach, R., "H2-powered aviation at airports - Design and economics of LH2 refueling systems," *Energy Conversion and Management: X*, Vol. 14, 2022. https://doi.org/10.1016/j.ecmx.2022.100206.

[5] Arena Lázaro, A., Cienkowski, D., de Gouvêa Pinto e Cruz, M., Koncevičius, S., Nootenboom, T., Nowacki, M., Orzu, M., Rinalducci, L., Valkering, L., and Wang, Y., "Midterm Report: Multi-fuel Aircraft for Viable Emission-Reduction with Integrated Combustion of Hydrogen and Kerosene (MAVERICK)," Design Synthesis Exercise Report, Delft University of Technology, Delft, NL, May 2026.

[6] Clean Aviation Joint Undertaking, "Clean Sky 2 Technology Evaluator: Second Global Assessment 2024 – Final Report," Tech. rep., Clean Aviation Joint Undertaking, Nov. 2024. URL https://www.clean-aviation.eu/sites/default/files/2024-11/CS2_TE_25.11.2024_FINAL.pdf.

[7] Airbus, "2018 Average List Prices for Airbus Aircraft," , jan 2018. URL https://www.airbus.com/sites/g/files/jlcbta136/files/2021-07/new-airbus-list-prices-2018.pdf, accessed: 29-04-2026.

[8] European Union Aviation Safety Agency, "ReFuelEU Aviation: First Annual Technical Report," Tech. rep., European Union Aviation Safety Agency, October 2025. URL https://www.easa.europa.eu/en/newsroom-and-events/press-releases/easa-publishes-report-sustainable-aviation-fuel-scale-progress, accessed: 04-05-2026.

[9] Steer, "Analysing the Costs of Hydrogen Aircraft," Final report, Steer, Apr. 2023. URL https://uploads.transportenvironment.org/production/files/Study-Analysing-the-costs-of-hydrogen-aircraft_2024-04-29-153800_ufib.pdf, prepared for Transport & Environment, supported by the European Climate Foundation.

[10] European Union Aviation Safety Agency, *Easy Access Rules for Air Operations (Regulation (EU) No 965/2012)*, EASA, 2026. Consolidated version of Regulation (EU) No 965/2012 with AMC and GM. Accessed: 2026-05-12.

[11] ICAO Secretariat, "Local Air Quality – Overview," *ICAO Environmental Report 2016*, International Civil Aviation Organization, 2016, Chap. 3, pp. 73–74. URL https://www.icao.int/sites/default/files/sp-files/environmental-protection/Documents/EnvironmentalReports/2016/ENVReport2016_pg73-74.pdf.

[12] Vos, R., *Introduction to Airplane Design*, Delft University of Technology, 2023.

[13] Cecere, D., Giacomazzi, E., and Ingenito, A., "A review on hydrogen industrial aerospace applications," *International Journal of Hydrogen Energy*, Vol. 39, No. 20, 2014, pp. 10731–10747. https://doi.org/10.1016/j.ijhydene.2014.04.126.

[14] Roskam, J., *Airplane Design, Part V: Component Weight Estimation*, Design, Analysis and Research Corporation, Ottawa, KS, 1985.

[15] Oliviero, F., "Aircraft Balance," Lecture slides, AE3211-I Systems Engineering and Aerospace Design, 2026.

[16] Oliviero, F., "Requirement Analysis and Design Principles for Aircraft Stability and Control, Parts 1 and 2," Lecture slides, AE3211-I Systems Engineering and Aerospace Design, 2026.

[17] Scholz, D., "Aircraft Design: Empennage Sizing," , 2015. URL https://www.fzt.haw-hamburg.de/pers/Scholtz/HOOU/AircraftDesign_11_EmpennageSizing.pdf.

[18] Dahl, B. A., and Sakurai, S., "Semi-Levered Shrink Landing Gear," U.S. Patent 10,800,516 B2, Oct. 2020. Issued October 13, 2020; assigned to The Boeing Company; U.S. Application No. 15/611,844.

[19] Mellor, M. L., Long, M. A., and Odell, R. B., "Semi-Levered Landing Gear and Associated Method," U.S. Patent 8,448,900 B2, May 2013. Filed March 24, 2010, Application No. 12/730,598.

[20] Oliviero, F., "Aircraft aerodynamic analysis: estimation of lift & drag," , 2024.

[21] Oliviero, F., "Aircraft aerodynamic analysis: mobile surfaces of the wing," , 2024.

[22] Harris, C. D., "NASA supercritical airfoils: A matrix of family-related airfoils," Tech. rep., Langley Research Center, 3 1990.

[23] Offringa, A., "Manufacturing systems for thermoplastic composites," , 3 2026.

[24] Prasad, N. E., Gokhale, A. A., and Wanhill, R. J. H., *Aluminum-Lithium Alloys : Processing, Properties, and Applications*, Elsevier Science, 2014.

[25] Toray Carbon Fibers America, Inc., "T800H Technical Data Sheet, No. CFA-007," , 2018. URL https://www.fibermax.eu/image/catalog/MDS/Yarn%20MDS/CarbonT800MDS.pdf, accessed: 2026-06-17.

[26] Mattingly, J. D., *Aircraft Engine Design*, Aiaa, 2002.

[27] Air Quality Expert Group (AQEG), "Air Pollution Arising from Hydrogen Combustion," Tech. rep., Department for Environment, Food and Rural Affairs (DEFRA), Nov. 2024. URL https://uk-air.defra.gov.uk/assets/documents/reports/cat05/2411071337_H2_combustion_note_proof.pdf, published 7 November 2024, accessed 10 June 2026.

[28] Liu, Y., Sun, X., Sethi, V., Nalianda, D., Li, Y. G., and Wang, L., "Review of modern low emissions combustion technologies for aero gas turbine engines," *Progress in Aerospace Sciences*, Vol. 94, 2017, pp. 12–45. https://doi.org/10.1016/j.paerosci.2017.08.001.

[29] Purohit, A. L., Nalbandyan, A., Malte, P. C., and Novosselov, I. V., "NNH mechanism in low-NOx hydrogen combustion: Experimental and numerical analysis of formation pathways," *Fuel*, Vol. 292, 2021, p. 120186. https://doi.org/https://doi.org/10.1016/j.fuel.2021.120186, URL https://www.sciencedirect.com/science/article/pii/S0016236121000624.

[30] Singh, S., Amerighi, M., Scopolini, N., Andreini, A., Harth, S. R., and Trimis, D., "Effect of H2 and Jet-A1 fuel split on flame stability and pollutant emissions from low-swirl burner," *Proceedings of the Combustion Institute*, Vol. 41, 2025, p. 105858. https://doi.org/10.1016/j.proci.2025.105858.

[31] Brand, J., Sampath, S., Shum, F., Bayt, R., and Cohen, J., "Potential use of hydrogen in air propulsion," *AIAA international air and space symposium and exposition: the next 100 years*, 2003, p. 2879.

[32] Palies, P., "2 - Premixed combustion for combustors," *Stabilization and Dynamic of Premixed Swirling Flames*, Academic Press, 2020, pp. 57–103. https://doi.org/10.1016/B978-0-12-819996-1.00010-X.

[33] Boyce, M. P., *Gas Turbine Engineering Handbook*, 2nd ed., Gulf Professional Publishing, Boston, MA, 2002.

[34] Dave, K., Link, S., De Domenico, F., Schrijer, F., Scarano, F., and Gangoli Rao, A., "Kerosene-H2 blending effects on flame properties in a multi-fuel combustor," *Fuel Communications*, Vol. 23, 2025, p. 100139. https://doi.org/10.1016/j.jfueco.2025.100139.

[35] Choe, J., and Mastorakos, E., *Experimental Investigation of Non-premixed Hydrogen Flames in a Lab-Scale Rich-Quench-Lean Combustor*, 2025. https://doi.org/10.2514/6.2025-1329.

[36] Stickles, R., and Barrett, J., "TAPS II Technology: Final Report – Technology Assessment," Final Report DTFAWA-10-C-00046, Federal Aviation Administration, Washington, DC, USA, Jun. 2013.

[37] European Commission, "Technology Readiness Levels (TRL)," Tech. rep., 2014. URL https://ec.europa.eu/research/participants/data/ref/h2020/wp/2014_2015/annexes/h2020-wp1415-annex-g-trl_en.pdf.

[38] Marek, C., Smith, T., and Kundu, K., "Low emission hydrogen combustors for gas turbines using lean direct injection," *41st AIAA/ASME/SAE/ASEE joint propulsion conference & exhibit*, 2005, p. 3776.

[39] Ang, A. W. X., Gangoli Rao, A., Kanakis, T., and Lammen, W., "Performance analysis of an electrically assisted propulsion system for a short-range civil aircraft," *Proceedings of the Institution of Mechanical Engineers, Part G: Journal of Aerospace Engineering*, Vol. 233, No. 4, 2019, pp. 1490–1502. https://doi.org/10.1177/0954410017754146.

[40] Ishak, M. S. A., and Mohd Jaafar, M. N., "The Effect of Swirl Number on Reducing Emissions from Liquid Fuel Burner System," *Jurnal Mekanikal*, , No. 19, 2005, pp. 48–56.

[41] Lefebvre, A. H., and Ballal, D. R., *Gas Turbine Combustion: Alternative Fuels and Emissions*, 3rd ed., CRC Press, Boca Raton, FL, 2010.

[42] San Benito Pastor, D. G., and Parmentier, N., "Impact of Fuel Conditioning and Combustor Injection Temperature on a Hydrogen Turboprop," *Journal of Engineering for Gas Turbines and Power*, Vol. 148, No. 6, 2026, p. 061012.

https://doi.org/10.1115/1.4069844.

[43] Ebrahimi, A., Rolt, A., and Sanders, D., "A Comparative Assessment of Alternative Liquid Hydrogen Heat Exchanger Architectures for Fuel Preconditioning in Turboshaft Engines," *Hydrogen*, Vol. 7, No. 2, 2026, p. 74. https://doi.org/10.3390/hydrogen7020074.

[44] Link, S., Dave, K., de Domenico, F., Gangoli Rao, A., and Eitelberg, G., "Experimental analysis of dual-fuel (CH4/H2) capability in a partially-premixed swirl stabilized combustor," *International Journal of Hydrogen Energy*, Vol. 101, 2025, pp. 427–437. https://doi.org/10.1016/j.ijhydene.2024.12.286.

[45] Hura, H. S., Sabla, P. E., Cooper, J. N., Duncan, B. S., Mongia, H. C., and Lohmueller, S. J., "Fuel Nozzle Assembly for Reduced Exhaust Emissions," , 5 2002. US Patent 6,389,815 B1, assigned to General Electric Company, filed Sep. 8, 2000.

[46] McMasters, M. A., Benjamin, M. A., Mancini, A., and Lohmueller, S. J., "Fuel Nozzle," , 8 2014. US Patent 8,806,871 B2, assigned to General Electric Company, filed Mar. 27, 2009.

[47] Su, J., "Unsteady Aerodynamic Response Characteristics of Gas Turbine Fuel Injectors," Ph.D. thesis, Loughborough University, 2017.

[48] Rolls-Royce plc, *The Jet Engine*, 5th ed., Rolls-Royce plc, 1996.

[49] Shchepakina, E. A., Zubrilin, I. A., Kuznetsov, A. Y., Tsapenkov, K. D., Antonov, D. V., Strizhak, P. A., Yakushkin, D. V., Ulitichev, A. G., Dolinskiy, V. A., and Hernandez Morales, M., "Physical and Chemical Features of Hydrogen Combustion and Their Influence on the Characteristics of Gas Turbine Combustion Chambers," *Applied Sciences*, Vol. 13, No. 6, 2023, p. 3754. https://doi.org/10.3390/app13063754.

[50] Brewer, G. D., Morris, R. E., Lange, R. H., and Moore, J. W., "Study of the Application of Hydrogen Fuel to Long-Range Subsonic Transport Aircraft, Volume I: Summary Report," NASA Contractor Report NASA CR-132558, Lockheed-California Company and Lockheed-Georgia Company, Hampton, VA, Jan. 1975.

[51] Boddorff, A. K., "Choosing the Right Stuff: Material Selection for Liquid Hydrogen Aircraft Cryotanks," Tech. Rep. NASA/TM-20250007133, National Aeronautics and Space Administration, Langley Research Center, Hampton, VA, Jul. 2025.

[52] Mital, S. K., Gyekenyesi, J. Z., Arnold, S. M., Sullivan, R. M., Manderscheid, J. M., and Murthy, P. L. N., "Review of Current State of the Art and Key Design Issues With Potential Solutions for Liquid Hydrogen Cryogenic Storage Tank Structures for Aircraft Applications," Tech. Rep. NASA/TM-2006-214346, National Aeronautics and Space Administration, Glenn Research Center, Cleveland, OH, Oct. 2006.

[53] Johnson, W. L., "Thermal Analysis of Low Layer Density Multilayer Insulation Test Results," Tech. Rep. NASA/TM-2011-216639, NASA Kennedy Space Center, 2011.

[54] Wang, Z., Wang, Y., Afshan, S., and Hjalmarsson, J., "A review of metallic tanks for H2 storage with a view to application in future green shipping," *International Journal of Hydrogen Energy*, Vol. 46, No. 9, 2021, pp. 6151–6179. https://doi.org/10.1016/j.ijhydene.2020.11.168.

[55] National Aeronautics and Space Administration, "Space Shuttle: Super Lightweight External Tank," Tech. Rep. FS-2005-04-025-MSFC, Marshall Space Flight Center, Apr. 2005. URL https://www.nasa.gov/sites/default/files/113020main_shuttle_lightweight.pdf, accessed 09-06-2026.

[56] Simon, N. J., Drexler, E. S., and Reed, R. P., "Review of Cryogenic Mechanical and Thermal Properties of Al-Li Alloys and Alloy 2219," Tech. Rep. NISTIR 3971, National Institute of Standards and Technology, Boulder, Colorado, Dec. 1991. Prepared for: Astronautics Laboratory (AFSC), Air Force Space Technology Center, Edwards AFB, California.

[57] Agilan, M., Phanikumar, G., and Sivakumar, D., "Weld Solidification Cracking Behaviour of AA2195 Al–Cu–Li Alloy," *Transactions of the Indian Institute of Metals*, Vol. 71, 2018, pp. 2667–2670. https://doi.org/10.1007/s12666-018-1425-6.

[58] Loftus, Z., Arbegast, W. J., and Hartley, P. J., "Friction Stir Weld Tooling Development for Application on the 2195 Al-Cu-Li Space Transportation System External Tank," *Trends in Welding Research: Proceedings of the 5th International Conference*, ASM International, Pine Mountain, GA, USA, 1998.

[59] *Fabrication and Testing of Electron Beam Welded Alloy AA2219 Aluminum Pressure Vessels for High-Pressure Hydrogen Service*, Pressure Vessels and Piping Conference, Vol. Volume 6B: Materials and Fabrication, 2014. https://doi.org/10.1115/PVP2014-28858.

[60] ASM International, "2219 and Alclad 2219: High-Temperature Alloy," *Properties and Selection of Aluminum Alloys*, ASM Handbook, ASM International, Materials Park, OH, USA, 2019.

[61] Windenburg, D. F., and Trilling, C., "Collapse by Instability of Thin Cylindrical Shells under External Pressure," Tech. Rep. 385, David W. Taylor Model Basin (DTMB), Washington, DC, USA, 1934. URL https://dome.mit.edu/handle/1721.3/48059, also published in Trans. ASME **56** (1934) 819–825.

[62] Noordman, B., Wit, A. d., Creemers, R., Nijenhuis, A. t., Ubels, R., Ramaswamy, K., Tripathi, A. K., Liddel, P., Cullinan, J., and Lecce, L., "Design, Analysis and Optimisation of a Vacuum-Insulated Composite Conformal LH2 Tank," *Engineering Proceedings*, Vol. 133, No. 1, 2026. https://doi.org/10.3390/engproc2026133165.

[63] *Boiler and Pressure Vessel Code, Section VIII, Division 1: Rules for Construction of Pressure Vessels*, American Society of Mechanical Engineers (ASME), New York, NY, USA, 2023rd ed., 2023. Paragraphs UG-27, UG-28, UG-29 and UG-32.

[64] Hutchinson, J. W., "Buckling of spherical shells revisited," *Proceedings of the Royal Society A: Mathematical, Physical and Engineering Sciences*, Vol. 472, No. 2195, 2016, p. 20160577. https://doi.org/10.1098/rspa.2016.0577.

[65] Timoshenko, S. P., and Gere, J. M., *Theory of Elastic Stability*, 2nd ed., McGraw-Hill, New York, NY, USA, 1961.

[66] Sosounov, V., and Orlov, V., *Experimental turbofan using liquid hydrogen and liquid natural gas as fuel*, 1990. https://doi.org/10.2514/6.1990-2421.

[67] Brewer, G. D., Morris, R. E., Davis, G. W., Versaw, E. F., Cunnington, J., G. R., Riple, J. C., Baerst, C. F., and Garmong, G., "Study of Fuel Systems for LH2-Fueled Subsonic Transport Aircraft, Volume 1," NASA Contractor Report NASA-CR-145369-VOL-1, NASA, Jul. 1978.

[68] Crane Co., "Flow of Fluids Through Valves, Fittings, and Pipe," Tech. Rep. Technical Paper No. 410, Crane Co., 2009. See Chapter 2, "Flow Through Valves and Fittings", and Appendix A K-factor tables for valves and fittings, including 90-degree elbows/bends.

[69] CryoWorks, "Specification for Vacuum Insulated Piping: General Fabrication, Testing and Purchasing," , 2019. Section 3.2 states that vacuum-jacket wall thickness shall conform to ASME BPVC Section VIII, Division 1, UG-28.

[70] "ASTM B241/B241M: Standard Specification for Aluminum and Aluminum-Alloy Seamless Pipe and Seamless Extruded Tube," , 2022. Covers aluminium and aluminium-alloy seamless pipe and extruded tube for pressure applications, including standard pipe sizes from ANSI H35.2/H35.2M.

[71] Sarr, A., Jézégou, J., and de Saqui-Sannes, P., "Sizing of Fuel Distribution and Thermopropulsion Systems for Liquid-Hydrogen-Powered Aircraft Using an MBSE Approach," *Aerospace*, Vol. 12, No. 6, 2025. https://doi.org/10.3390/aerospace12060554.

[72] CSM Cryogenic Specialty Manufacturing, "Cryopreservation in Life Sciences: Vacuum Jacketed Technology and Heat Leak Performance," , 2023. URL https://www.csm-cryogenic.com/images/uploads/editor/files/MKT%20Cryopreservation%20Catalog%20R00.pdf, see pp. 13–14, heat leak/performance comparison table and Case #1. Accessed: 2026-06-17.

[73] Fesmire, J. E., and Johnson, W. L., "Cylindrical cryogenic calorimeter testing of six types of multilayer insulation systems," *Cryogenics*, Vol. 89, 2018, pp. 58–75. https://doi.org/10.1016/j.cryogenics.2017.11.004.

[74] Rame, E., Hartwig, J. W., and McQuillen, J. B., "Flow Visualization of Liquid Hydrogen Line Chilldown Tests," *50th AIAA/ASME/SAE/ASEE Joint Propulsion Conference*, 2014.

[75] Csomor, A., and Sutton, R., "Small, High-Pressure Liquid Hydrogen Turbopump," NASA Contractor Report NASA CR-135188, Rockwell International, Rocketdyne Division, Canoga Park, California, 1977. Prepared for NASA Lewis Research Center under Contract NAS3-17794.

[76] Sun, J., Shi, T., Wang, R., Chen, X., and Peng, X., "Thermodynamic performance investigation and multi-objective optimization of the subcooled liquid hydrogen centrifugal pump for hydrogen refueling stations," *International Journal of Hydrogen Energy*, Vol. 244, 2026, p. 155709. https://doi.org/10.1016/j.ijhydene.2026.155709.

[77] Harsito, C., Yun, J.-E., Shin, J.-Y., and Kim, J.-M., "Optimal Design of a Liquid Hydrogen Centrifugal Pump Impeller," *Energies*, Vol. 17, No. 24, 2024. https://doi.org/10.3390/en17246299.

[78] Toscano, W. M., and Hoagland, L. C., "The Thermodynamic Performance of Oil-Flooded Helium Screw Compressors," *Journal of Engineering for Industry*, Vol. 99, No. 3, 1977, pp. 749–753. https://doi.org/10.1115/1.3439308.

[79] Middlebrook, J., Graham, G., and Anderson, R., "Centrifugal Compressor," , Apr. 2021.

[80] Ting, D., "Chapter 18 - Heat exchangers," *Thermofluids*, Academic Press, 2022, pp. 373–395. https://doi.org/10.1016/B978-0-323-90626-5.00009-4.

[81] Schneider, B., "Turbine cooling air estimation in thermodynamic simulations," *CEAS Aeronautical Journal*, 2024. https://doi.org/10.1007/s13272-024-00776-0.

[82] *Hydrogen Use in Internal Combustion Engines*, College of the Desert, revision 0 ed., Dec. 2001.

[83] Yin, B., Qiu, H., Dong, F., Wang, Z., Jia, H., and Xie, X., "Study on the pressurization liquid hydrogen supply characteristics in hydrogen fuel cell vehicles," *Energy*, Vol. 338, 2025, p. 138897. https://doi.org/https://doi.org/10.1016/j.energy.2025.138897.

[84] Brewer, G. D., and Morris, R. E., "Tank and Fuel Systems Considerations for Hydrogen Fueled Aircraft," *SAE Aerospace Engineering and Manufacturing Meeting*, SAE International, Warrendale, PA, 1975, pp. 1–16. https://doi.org/10.4271/751093.

[85] Ciminello, M., Carandente Tartaglia, C., and Caramuta, P., "Optical Sensing Technologies for Cryo-Tank Composite Structural Element Analysis and Maintenance," *Applied Sciences*, Vol. 15, No. 15, 2025. https://doi.org/10.3390/app15158748.

[86] Yang, D., Oh, J., Lee, G., Lee, S., and Choi, S., "Detection of hydrogen gas leak using distributed temperature sensor in green hydrogen system," *International Journal of Hydrogen Energy*, Vol. 82, 2024, pp. 910–922. https://doi.org/10.1016/j.ijhydene.2024.07.450.

[87] Qanbar, M. W., and Hong, Z., "A Review of Hydrogen Leak Detection Regulations and Technologies," *Energies*, Vol. 17, No. 16, 2024. https://doi.org/10.3390/en17164059.

[88] Pijolat, C., Tournier, G., Breuil, P., Matarin, D., and Nivet, P., "Hydrogen detection on a cryogenic motor with a SnO2 sensors network," *Sensors and Actuators B: Chemical*, Vol. 82, No. 2, 2002, pp. 166–175. https://doi.org/10.1016/S0925-4005(01)01002-4.

[89] Menon, S. K., Kumar, A., and Mondal, S., "Advancements in hydrogen gas leakage detection sensor technologies and safety measures," *Clean Energy*, Vol. 9, No. 1, 2025, pp. 263–277.

[90] Benet, G., Blanes, F., SimÃş, J., and PÃľrez, P., "Using infrared sensors for distance measurement in mobile robots," *Robotics and Autonomous Systems*, Vol. 40, No. 4, 2002, pp. 255–266. https://doi.org/10.1016/S0921-8890(02)00271-3.

[91] Fausing Olesen, J., and Shaker, H. R., "Predictive Maintenance for Pump Systems and Thermal Power Plants: State-of-the-Art Review, Trends and Challenges," *Sensors*, Vol. 20, No. 8, 2020, p. 2425. https://doi.org/10.3390/s20082425.

[92] Bernardo, V., and Fageda, X., "The impact of new aircraft on carbon emissions," *Transportation Research Part D: Transport and Environment*, Vol. 147, 2025, p. 104949. https://doi.org/10.1016/j.trd.2025.104949.

[93] Mösl, K. G., "On the Formation of Nitrogen Oxides During the Combustion of Partially Pre-Vaporized Droplets," Dissertation, Technische Universität München, München, Germany, 2012. URL https://www.epc.ed.tum.de/fileadmin/w00cgc/td/Forschung/Dissertationen/moesl12.pdf.

[94] Acosta, W. A., "Experimental Study of the Spray Characteristics of a Research Airblast Atomizer," Tech. Rep. NASA TM-86911, USAAVSCOM-TR-84-C-18, E-2404, National Aeronautics and Space Administration, Lewis Research Center and U.S. Army Research and Technology Laboratories (AVSCOM), Cleveland, Ohio, mar 1985. Prepared for the Thirtieth International Gas Turbine Conference and Exhibit, Houston, Texas, March 17-21, 1985.

[95] Vivalda, P., and Fioriti, M., "Stream Life Cycle Assessment Model for Aircraft Preliminary Design," *Aerospace*, Vol. 11, No. 2, 2024, p. 113. https://doi.org/10.3390/aerospace11020113.

[96] Rahn, A., Schuch, M., Wicke, K., Sprecher, B., Dransfeld, C., and Wende, G., "Beyond flight operations: Assessing the environmental impact of aircraft maintenance through life cycle assessment," *Journal of Cleaner Production*, Vol. 453, 2024. https://doi.org/10.1016/j.jclepro.2024.142195.

[97] Meissner, R., Sieb, P., Wollenaupt, E., Haberkorn, S., and Wende, G., "Towards climate-neutral aviation: Assessment of maintenance requirements for airborne hydrogen storage and distribution systems," *International Journal of Hydrogen Energy*, Vol. 48, 2023, pp. 29367–29290. https://doi.org/10.1016/j.ijhydene.2023.04.058.

[98] Mangold, J., Silberhorn, D., Moebs, N., Dzikus, N., Hoelzen, J., Zill, T., and Strohmayer, A., "Refueling of LH2 Aircraft–Assesment of Turnaround Procedures and Aircraft Design Implication," *Energies*, Vol. 15, 2022. https://doi.org/10.3390/en15072475.

[99] Pfingstl, S., Steinweg, D., Zimmermann, M., and Hornung, M., "On the Potential of Extending Aircraft Service Time Using Load Monitoring," *arXiv preprint arXiv:2008.03138*, Vol. v4, 2021.

[100] Aerospace Technology Institute, "Cryogenic Hydrogen Fuel System and Storage: Roadmap Report," Roadmap Report FZO-PPN-MAP-0027, Aerospace Technology Institute, FlyZero, Mar. 2022.

[101] Liu, X., Zhao, D., Guan, D., Becker, S., Sun, D., and Sun, X., "Development and progress in aeroacoustic noise reduction on turbofan aeroengines," *Progress in Aerospace Sciences*, Vol. 130, 2022, p. 100796. https://doi.org/10.1016/j.paerosci.2021.100796.

[102] Zhou, H., and Irons, R., "Hydrogen-enriched combustion in domestic burners: Stability, emissions, and acoustics," *International Journal of Hydrogen Energy*, Vol. 175, 2025, p. 151449. https://doi.org/10.1016/j.ijhydene.2025.151449.

[103] "Aeroacoustics of Flight Vehicles: Theory and Practice, Volume 1: Noise Sources," NASA Reference Publication 1258, Vol. 1, National Aeronautics and Space Administration, Washington, DC, Aug. 1991.

[104] European Union Aviation Safety Agency, "Type-Certificate Data Sheet No. EASA.E.110: LEAP-1A and LEAP-1C Series Engines," Tech. Rep. EASA.E.110, European Union Aviation Safety Agency, May 2026. URL https://www.easa.europa.eu/en/downloads/20086/en, issue 14, 11 May 2026.

[105] EUROCONTROL, "EUROCONTROL Method for Estimating Aviation Fuel Burnt and Emissions," Tech. rep., EUROCONTROL, Jun. 2016. URL https://www.eurocontrol.int/sites/default/files/2019-03/emep-eea-air-pollution-emission-inventory-method-v1.0.pdf, edition 1.0.

[106] Federal Aviation Administration, "AC 36-4D: Noise Standards: Aircraft Type and Airworthiness Certification," Tech. Rep. Advisory Circular 36-4D, Federal Aviation Administration, Oct. 2017. URL https://www.faa.gov/documentLibrary/media/Advisory_Circular/AC_36-4D.pdf, issued 12 October 2017.

[107] DiNenno, P. J., Drysdale, D., Beyler, C. L., Walton, W. D., Custer, R. L. P., Hall, J., John R., and Watts, J., John M. (eds.), *SFPE Handbook of Fire Protection Engineering*, 3rd ed., National Fire Protection Association, Quincy, MA, 2002. Society of Fire Protection Engineers.

[108] Tsikrika, I., "A320neo Engines Modeling," Diploma thesis, National Technical University of Athens, 2020. https://doi.org/10.26240/heal.ntua.20426.

[109] Megill, L., and Grewe, V., "Investigating the limiting aircraft-design-dependent and environmental factors of persistent contrail formation," *Atmospheric Chemistry and Physics*, Vol. 25, 2025, pp. 4131–4149. https://doi.org/10.5194/acp-25-4131-2025.

[110] National Academies of Sciences, Engineering, and Medicine, *Developing a Research Agenda on Contrails and Their Climate Impacts*, The National Academies Press, Washington, DC, 2025. https://doi.org/10.17226/29073.

[111] Pettersson, S. M., Azar, C., and Johansson, D. J. A., "Climate impact of contrail cirrus from hydrogen combustion aircraft," *EGUsphere*, 2025. https://doi.org/10.5194/egusphere-2025-3535, preprint.

[112] Huete, J., and Pilidis, P., "Parametric study on tank integration for hydrogen civil aviation propulsion," *International Journal of Hydrogen Energy*, Vol. 46, No. 74, 2021, pp. 37049–37062. https://doi.org/10.1016/j.ijhydene.2021.08.194.

[113] Air France-KLM, "Full Year 2024 Results," Press release, Mar. 2025. URL https://www.airfranceklm.com/sites/default/files/2025-03/20250305-fy-2024-afklm-press-release-english.pdf.

[114] IMA, A., "Test and Development Center for the Aerospace Industry," , May 2018.

[115] European Aviation Safety Agency, *Certification Specifications for Large Aeroplanes (CS-25): Amendment 3*, EASA, Cologne, Germany, Sep. 2007. URL https://www.easa.europa.eu, consolidated version, Annex to ED Decision 2007/010/R.

[116] *Flight Crew Operating Manual*, Airbus, 2019. pp. 5890-5901.

[117] Jaffary, Z., and Zhang, Y., "Hydrogen as an aviation fuel: Safety concerns and mitigation strategies," *Transport Economics and Management*, Vol. 3, 2025, pp. 432–440. https://doi.org/10.1016/j.team.2025.11.001.

[118] Scholz, D., "An Optional APU for Passenger Aircraft," *CEAS Air & Space Conference 2015*, Council of European Aerospace Societies (CEAS), 2015. URL https://www.fzt.haw-hamburg.de/pers/Scholz/Airport2030/Airport2030_PUB_CEAS_15-09-07_Scholz.pdf.

[119] *Easy Access Rules for Auxiliary Power Units (CS-APU): Initial Issue*, European Union Aviation Safety Agency (EASA), Feb. 2018. URL https://www.easa.europa.eu/en/downloads/45463/en, publication date: 22 February 2018.

[120] "Aircraft Electric Power Characteristics," Military Standard MIL-STD-704F, United States Department of Defense, Mar. 2004. URL https://ieee.li/pdf/standards-handbooks/MIL-STD-704F.pdf.

[121] Sciatti, F., Tamburrano, P., Distaso, E., Amirante, R., Radogna, A. V., Morciano, A., and Grassi, G., "A comprehensive overview of lithium-ion batteries for electric vehicles: Materials, performance, safety, recycling, and emerging technologies," *Journal of Energy Storage*, Vol. 144, 2026, p. 119694. https://doi.org/10.1016/j.est.2025.119694.

[122] Koloch, J., Heienbrok, M., Kasperek, M., and Lienkamp, M., "From Cell to Pack: Empirical Analysis of the Correlations Between Cell Properties and Battery Pack Characteristics of Electric Vehicles," *World Electric Vehicle Journal*, Vol. 16, No. 9, 2025. https://doi.org/10.3390/wevj16090484.

[123] Yang, M.-H., Lin, B.-M., Yeh, S.-F., and Tsai, J.-S., "The New High Power Design of 8Ah Li-ion Battery for HEV Application," *World Electric Vehicle Journal*, Vol. 2, No. 2, 2008, pp. 107–112. https://doi.org/10.3390/wevj2020107.

[124] DSE Group 21, "Project Plan: Multi-fuel Aircraft for Viable Emission-Reduction with Integrated Combustion of Hydrogen and Kerosene (MAVERICK)," Project plan, Delft University of Technology, Faculty of Aerospace Engineering, 2026. Design Synthesis Exercise.

[125] "A Modular Assembly Concept for Large-Volume CFRP Hydrogen Tanks for Passenger Aircraft," *MDPI*, Vol. 133, No. 1, 2026, p. 179. URL https://www.mdpi.com/2673-4591/133/1/179.

[126] Alves, M. L., Santana, P., Fernandes, N., and Martins, P. A. F., "Fabrication of metallic liners for composite overwrapped pressure vessels," *The International Journal of Advanced Manufacturing Technology*, Vol. 67, 2013, pp. 2671–2680. https://doi.org/10.1007/s00170-012-4682-2.

[127] Graf, N. A., Schieleit, G. F., and Biggs, R., "Adhesive Bonding Characterization of Composite Joints for Cryogenic Usage," Tech. rep., Lockheed Martin Space Systems Company - Michoud Operations, 2000. Document ID: 20010020380, NASA Technical Reports Server.

[128] Buchholz, M., Gruber, S., Selbmann, A., Marquardt, A., Meier, L., Müller, M., Seifert, L., Leyens, C., Tajmar, M., and Bach, C., "Flow rate improvements in additively manufactured flow channels suitable for rocket engine application," *CEAS Space Journal*, Vol. 15, 2023, pp. 715–728. https://doi.org/10.1007/s12567-022-00476-7.

[129] Hinsch, M., *Industrial Aviation Management: A Primer in European Design, Production and Maintenance Organisations*, Springer, Berlin, Heidelberg, 2019.

[130] Pint, B. A., Pillai, R., Romedenne, M., and Dryepondt, S., "The Effect of Higher Water Vapor Content in H2-Fired Turbines on High Temperature Durability," *Proceedings of ASME Turbo Expo 2023 Turbomachinery Technical Conference and Exposition*, Boston, Massachusetts, 2023.

[131] Roskam, J., *Airplane Design, Part VIII: Airplane Cost Estimation: Design, Development, Manufacturing and Operating*, Design, Analysis and Research Corporation, Ottawa, KS, 2006.

[132] European Commission, "Commission Implementing Regulation (EU) 2018/2066 of 19 December 2018 on the monitoring and reporting of greenhouse gas emissions pursuant to Directive 2003/87/EC of the European Parliament and of the Council, and amending Commission Regulation (EU) No 601/2012," Official Journal of the European Union, L 334, 31.12.2018, pp. 1–93. Consolidated version 02018R2066, in force 27 May 2025, 2018.

[133] International Air Transport Association, "Global Feedstock Assessment for SAF Production: Outlook to 2050," Technical report, International Air Transport Association (IATA), 2025. URL https://www.iata.org/globalassets/iata/publications/sustainability/global-feedstock-assessment-for-saf-production-outlook-to-2050.pdf.

[134] Aircraft Commerce, "A320 Family Maintenance Analysis & Budget," *Aircraft Commerce: Aircraft Owner's & Operator's Guide*, 2006, pp. 18–31. URL https://www.aircraft-commerce.com/wp-content/uploads/aircraft-commerce-docs/Aircraft%20guides/A320%20FAMILY/ISSUE%2044-A320%20MTCE.pdf, accessed: 2026-04-24.

[135] Mukhopadhaya, J., and Rutherford, D., "Performance Analysis of Evolutionary Hydrogen-Powered Aircraft," White paper, International Council on Clean Transportation, Jan. 2022. URL https://theicct.org/wp-content/uploads/2022/01/LH2-aircraft-white-paper-A4-v4.pdf.

[136] McKinsey & Company, "Hydrogen-Powered Aviation: A Fact-Based Study of Hydrogen Technology, Economics, and Climate Impact by 2050," Report, Clean Sky 2 Joint Undertaking and Fuel Cells and Hydrogen 2 Joint Undertaking, Luxembourg, 5 2020. https://doi.org/10.2843/471510.

[137] European Union Aviation Safety Agency, "2024 Aviation Fuels Reference Prices for ReFuelEU Aviation," Briefing note, EASA, Apr. 2025. URL https://www.easa.europa.eu/en/document-library/general-publications/2024-aviation-fuels-reference-prices-refueleu-aviation, accessed 15 June 2026.

[138] Project SkyPower, "Accelerating the Take-Off for e-SAF in Europe: Project SkyPower Insights Report," Tech. rep., Project SkyPower, 10 2024. URL https://project-skypower.org/sites/default/files/2024-10/Project%20SkyPower%20Insights%20Report%20Oct%202024_final.pdf.

[139] Air France-KLM Group, "Second Quarter 2025 Results Press Release," Air France-KLM Group press release, Jul. 2025. URL https://www.airfranceklm.com/sites/default/files/2025-07/2025-q2-afklm-press-release_pr.pdf, passenger unit revenue per ASK 8.46 euro cents, Q2 2025.

A

Requirements Compliance Matrix

Table A.1: Requirements Compliance Matrix (O = Open (to be fulfilled in a later design stage), NA = Not Applicable).

Req. ID	Requirement	✓?	Explanation
Mission Requirements			
REQ-MIS-PERF-01	The aircraft shall have a maximum range at full passenger payload of at least 3000 km.	✓	Section 4.3
REQ-MIS-PERF-02	The aircraft shall have a maximum endurance at nominal cruise with reduced payload (including fuel reserve) of at least 6 h.	✓	The endurance at the maximum ferry range is 6.76 h.
REQ-MIS-PERF-03	The aircraft shall achieve a cruise speed of at least 700 km/h.	✓	Section 4.1
REQ-MIS-PERF-04	The aircraft shall maintain a cruise altitude of at least 29,000 ft.	✓	Section 4.1
REQ-MIS-PERF-05	The take-off distance shall not exceed 2100 m.	✓	The take-off field length is 1900 m.
REQ-MIS-PERF-06	The landing distance shall not exceed 1500 m.	✓	The landing field length is 1500 m.
REQ-MIS-PERF-07	The wing span shall be less than 36 m.	✓	Section 4.1
REQ-MIS-SAFE-01	The aircraft shall comply with all applicable regulations of CS-25.	O	
REQ-MIS-SAFE-02	The aircraft shall achieve a reliability level equivalent to the reference aircraft.	O	
REQ-MIS-SAFE-03	The aircraft maintenance cost shall be approximately equal to that of the reference aircraft.	✗	LH$_2$ system has additional maintenance and cost[136].
REQ-MIS-SAFE-04	The aircraft maintenance labour shall be approximately equal to that of the reference aircraft.	✗	The maintenance labour is expected to increase by around 25-35 %, see Section 11.2.
REQ-MIS-SUS-01	The NO$_x$ emissions per passenger-kilometre shall be reduced by 50% compared to reference aircraft.	✗	Requirement partially met, see Section 8.1.
REQ-MIS-SUS-02	The CO$_2$ emissions per passenger-kilometre shall be reduced by at least 50% compared to reference aircraft.	✓	Reduction of 55.4% on the nominal mission.
REQ-MIS-SUS-03	The aircraft shall be carbon neutral when operated with a combination of SAF and hydrogen.	✓	The fuels are carbon neutral and the aircraft does not have other emissions than from the engines.
REQ-MIS-SUS-04	The aircraft parts shall be no less recyclable or re-processable than those of the reference aircraft.	✓	Section 4.2.
REQ-MIS-SUS-05	The aircraft shall meet the noise requirements specified in ICAO Chapter 14.	✓	Section 8.3.
REQ-MIS-OPER-01	The aircraft shall support single-airport hydrogen refuelling for out-and-back missions.	✓	Aircraft was designed and converged for this requirement.
REQ-MIS-OPER-02	The maximum turnaround time shall be 60 minutes with hydrogen refuelling and 45 minutes with kerosene refuelling.	✗	Hydrogen refuelling takes 30 minutes; no other loading can be done simultaneously.
REQ-MIS-OPER-03	The aircraft shall provide a nominal passenger capacity of 180 passengers.	✓	The aircraft can accommodate 180 passengers.
REQ-MIS-OPER-04	The aircraft shall provide passenger comfort levels comparable to the reference baseline aircraft.	✓	Cabin is designed with 75 cm seat pitch that is comparable to reference aircraft.
REQ-MIS-COST-01	The target unit cost per aircraft shall be €150 million.	✓	Section 11.3.
Propulsion Requirements			
REQ-SYS-PRO-01	Components that will be in direct contact with hydrogen shall not be made from materials that are susceptible to hydrogen embrittlement.	✓	Materials chosen are not susceptible to hydrogen embrittlement.
REQ-SYS-PRO-02	The propulsion system shall provide 60 kN of thrust to at an altitude of 29,000 ft at a true airspeed of 700 km/hr.	✓	Each engine is able to provide a thrust at said altitude and speed of 44.41 kN and 42.72 kN at full hydrogen and full kerosene, respectively.
REQ-SYS-PRO-03	The propulsion system shall provide 286 kN of thrust at take-off conditions.	✓	Each engine able to provide a thrust of 159 kN.
REQ-SYS-PRO-04	The propulsion system shall have a Specific Fuel Consumption of at most 6.5 g/kN/s in cruise conditions.	✓	The specific fuel consumption of 5.947 g/kN/s in cruise conditions for nominal mission.
REQ-SYS-PRO-05	The propulsion system shall provide sufficient thrust to achieve a climb gradient of 2.4% at a velocity of (1.13/1.15)*stall speed (in take-off configuration) with one engine inoperative in take-off configuration.	✓	Section 3.3.
REQ-SYS-PRO-06	The propulsion system shall be able to continuously operate and provide sufficient thrust to sustain a 1.6G manoeuvre up to an altitude of 29,000 [ft].	O	
REQ-SYS-PRO-07	The propulsion system shall be able to accelerate from 15% to 95% take-off thrust within 5 seconds.	O	

Req. ID	Requirement	✓?	Explanation
REQ-SYS-PRO-08	The dry weight of the propulsion system shall be no more than (TBD) [kg].	O	Necessary a full CC design.
REQ-SYS-PRO-09	If used with SAF and hydrogen, assuming the input is completely carbon neutral, the aircraft shall generate no additional carbon emissions.	✓	LH_2 does not add CO_2 emissions.
REQ-SYS-PRO-10	In case of multiple engines, these engines shall be isolated from each other such that failure in one engine does not affect the operation of the other.	✓	Engines are separated by the fuselage and have separated fuel supply systems.
REQ-SYS-PRO-11	The propulsion system shall not cause the aircraft to exceed the certified noise limits (ICAO Annex 16 Volume I Chapter 14) in any fuel mode: kerosene, SAF, or liquid hydrogen.	✓	Section 8.3.
REQ-SYS-PRO-12	The propulsion system shall not require additional maintenance compared to the reference aircraft, relative to the amount of parts or subsystems.	✓	Engine follows the same design as the LEAP-1A, apart from the injector, which has an additional hydrogen feed line requiring no additional maintenance.
REQ-SYS-PRO-13	The propulsion system shall provide sufficient thrust to achieve a climb gradient of > 0% at lift-off velocity with one engine inoperative in take-off configuration and gear down.	O	
REQ-SYS-PRO-14	The propulsion system shall provide sufficient thrust to achieve a climb gradient of > 1.2% at a velocity of 1.18*stall speed with one engine inoperative in cruise conditions.	✓	Section 3.3.
REQ-SYS-PRO-15	The propulsion system shall provide sufficient thrust to achieve a climb gradient of > 2.1% at a velocity of (1.2/1.4)*stall speed (in landing configuration) with one engine inoperative in landing configuration.	✓	Section 3.3.
Propulsion Subsystem Requirements			
REQ-SUB-PRO-FEED-01	The fuel feed system shall be laid out independently per engine, such that a failure results in a maximum of one engine loss.	✓	Each engine has independent feed lines.
REQ-SUB-PRO-STOR-01	The kerosene fuel tank shall have a sufficient volume to store 13.8 m^3 of kerosene fuel.	✓	Kerosene trim and wing tanks are sized accordingly to fuel sizing Section 3.2.
REQ-SUB-PRO-STOR-02	The hydrogen fuel tank shall have a sufficient volume to store 51.94 m^3 of hydrogen fuel.	✓	Hydrogen tank is sized accordingly to Chapter 6, and space in rear of fuselage is accommodated.
REQ-SUB-PRO-STOR-03	The kerosene fuel tank shall have an expansion space of at least 2% of the tank capacity.	✓	Volume calculated with with kerosene density and fuel mass is multiplited with 2% safety factor.
REQ-SUB-PRO-STOR-04	In case of liquid hydrogen storage, the hydrogen fuel tank shall be able to function nominally from a temperature of 19 degrees Kelvin up to room temperature.	✓	Material property is verified at both temperature extremes in addtion to structural analysis.
REQ-SUB-PRO-STOR-05	In case of gaseous hydrogen storage, the hydrogen fuel tank shall be able to withstand a pressure of (TBD)*nominal working pressure.	NA	H2 is stored in liquid form.
REQ-SUB-PRO-STOR-06	The hydrogen fuel tank shall have a Thermal Pressure Relief Device (TPRD), with a vent port in accordance to UN-134 (7.1.1).	NA	TPRD not needed for a liquid hydrogen tank, replaced with pressure relief valve.
REQ-SUB-PRO-ENG-01	The combustion chamber shall sustain temperatures up to (TBD) [K] due to fuel combustion.	O	Necessary in detailed CC design.
REQ-SUB-PRO-ENG-02	The engine maximum cross-sectional diameter shall not be larger than 2.55 m.	✓	Preliminary engine sizing.
REQ-SUB-PRO-ENG-03	The exhaust temperature should not exceed (TBD) K at cruise conditions.	O	
REQ-SUB-PRO-EMI-01	The aircraft shall reduce CO2 emissions per passenger-kilometre by at least 50% compared to the A320neo for the nominal design mission.	✓	Reduction of 55.4% on the nominal mission.
REQ-SUB-PRO-EMI-02	The aircraft shall calculate CO2 emissions using separate fuel burn contributions from kerosene/SAF and hydrogen.	O	Outside the scope of the project.
REQ-SUB-PRO-EMI-03	The aircraft shall not exceed, in any fuel mode, an LTO-cycle NOx characteristic emission level of 13.0 g/kN, representing a 50% reduction relative to the reference engine (PW1127G-JM).	✗	LTO-cycle emission level at low power is higher than 13.0 g/kN, but satisfied For take-off and climb.
REQ-SUB-PRO-EMI-04	The aircraft shall not exceed, in any fuel mode, an LTO-cycle CO characteristic emission level of 14.79 g/kN, representing a 50% reduction relative to the reference engine (PW1127G-JM).	✓	Reduction achieved for fully-kerosene mode.
REQ-SUB-PRO-EMI-05	The propulsion system, when operating in a SAF/kerosene mode, shall emit CO, nvPM mass, and nvPM number concentrations below the TBD thresholds of the selected emissions measurement method.	O	
REQ-SUB-PRO-EMI-06	In climb and cruise, the aircraft shall emit no more than 28 gCO_2/pax-km tank-to-wake on the nominal mission.	✓	Cumulative emission level of 24.98 g/pax-km.
REQ-SUB-PRO-EMI-07	In climb and cruise, the aircraft shall emit no more than 0.13 gNOx/pax-km on the nominal mission.	✓	Cumulative emission level of 0.13 g/pax-km.
REQ-SUB-PRO-EMI-08	In liquid H2 cruise, H_2O emissions shall be be less than TBD kg H_2O/kg H2.	O	The project quantifies only CO, CO_2 and NO_x.
SUB-PRO-NOISE-01	The aircraft shall not exceed 95.7 EPNdB lateral under certification noise conditions.	✓	Noise levels in accordance with reference aircraft,

Req. ID	Requirement	✓?	Explanation
SUB-PRO-NOISE-02	The aircraft shall not exceed 0.4 EPNdB flyover under certification noise conditions.	✓	Noise levels in accordance with reference aircraft,
SUB-PRO-NOISE-03	The aircraft shall not exceed 99.5 EPNdB approach under certification noise conditions.	✓	Noise levels in accordance with reference aircraft,
Aerodynamic Surfaces Requirements			
REQ-SYS-AER-01	The aerodynamic design shall enable a maximum range of at least 3000 km at full passenger payload.	✓	Section 4.3.
REQ-SYS-AER-02	The aerodynamic design shall enable cruise at ≥29,000 ft.	✓	Section 4.1.
REQ-SYS-AER-03	The aerodynamic design shall enable cruise at ≥ 700 km/h.	✓	Section 4.1.
REQ-SYS-AER-04	The aerodynamic design shall support take-off within ≤2100 m at the relevant take-off mass.	✓	Take-off field length considered during design.
REQ-SYS-AER-05	The aerodynamic design shall support landing within ≤1500 m at the relevant landing mass	✓	Landing field length considered during design.
REQ-SYS-AER-06	The aerodynamic configuration shall provide sufficient lift in all mission phases: take-off, climb, cruise, descent, approach, landing, and go-around.	✓	Section 4.1.
REQ-SYS-AER-07	The aircraft shall maintain acceptable aerodynamic performance over the expected centre-of-gravity range caused by dual-fuel operation and LH_2 fuel consumption	✓	Section 3.5.
REQ-SYS-AER-08	The aerodynamic configuration shall enable an endurance of E≥6 h at nominal cruise conditions with reduced payload, including reserves.	✓	The endurance at the ferry range is 6.76 h.
REQ-SYS-AER-09	The aircraft shall define take-off safety speed such that $V_2 \geq 1.13V_{SR}$ at maximum take-off mass.	✓	Section 3.6.
REQ-SYS-AER-10	With landing gear retracted, take-off flaps set, and one engine inoperative, the aircraft shall achieve second-segment climb gradient γ ≥2.4%	✓	Section 3.6.
REQ-SYS-AER-11	The aerodynamic design shall contribute to compliance with ICAO Chapter 14 noise requirements	✓	Airframe similar with reference aircraft, which complies with ICAO 14.
REQ-SYS-AER-12	The wing loading W/S shall be selected such that take-off, landing, stall-speed, and climb-gradient constraints are simultaneously satisfied.	✓	Conditions satisfied in matching diagram (Section 3.6)
REQ-SYS-AER-13	TOFL shall be measured from brake release to 35 ft screen height.	✓	Definition used in Section 3.6.
REQ-SYS-AER-14	Landing distance shall be measured from 50 ft screen height to full stop.	✓	Definition used in Section 3.6.
REQ-SYS-AER-15	The reference stall speed, VSR, shall not be less than 3,7 km/h (2 kt) or 2%, whichever is greater, above the speed at which the device operates.	✓	Section 3.6.
REQ-SYS-AER-16	In approach configuration, with one engine inoperative, the aircraft shall achieve approach climb gradient γ ≥2.1%.	✓	Section 3.6.
REQ-SYS-AER-17	In clean final takeoff climb configuration, with one engine inoperative, the aircraft shall achieve climb gradient γ ≥1.2%.	✓	Section 3.6.
REQ- SYS-AER-18	In landing configuration, with all engines operating, the aircraft shall achieve landing climb gradient γ ≥3.2%.	✓	Section 3.6.
REQ-SYS-AER-19	The aircraft shall achieve a climb gradient of γ ≥0% at lift-off velocity with one engine inoperative in take-off configuration and gear down.	✓	Section 3.6.
REQ-SYS-AER-20	The approach speed of the aircraft in landing configuration shall be no less than 1.23 times the stall speed.	✓	Stall speed in landing configuration is 110 kts.
REQ-SYS-AER-21	The approach speed of the aircraft must be 224 km/h (121 kt) or more but less than 261 km/h (141 kt) IAS.	✓	Approach speed is 140 kts.
Aerodynamic Surfaces Subsystems Requirements			
REQ-SUB-AER-W-01	The wing shall achieve a cruise lift-to-drag sufficient to meet 3000 km range.	✓	Section 4.3.
REQ-SUB-AER-W-02	The wing shall be sized so that wing loading allows compliance with ≤2100 m take-off distance.	✓	The take-off field length is 1900 m.
REQ-SUB-AER-W-03	The wing shall be sized so that wing loading allows compliance with ≤1500 m landing distance.	✓	The landing field length is 1500 m.
REQ-SUB-AER-W-04	The wing planform shall account for structural integration, fuel-system integration, and possible LH_2 tank layout constraints.	✓	Section 4.2.
REQ-SUB-AER-W-05	The airfoil shall provide a cruise lift coefficient to meet ≥700 km/h with low profile drag.	✓	Section 4.1.
REQ-SUB-AER-W-06	The wing span shall be smaller than 36 m.	✓	Section 4.1.
REQ-SUB-AER-HLD-01	The take-off high-lift system shall provide sufficient $C_{L,\,max,\,TO}$ to satisfy OEI second-segment climb γ ≥2.4%.	✓	The high-lift system provides a $C_{L,\,max,\,TO}$ of 2.2
REQ-SUB-AER-HLD-02	The high-lift system shall provide enough $C_{L,\,max,\,LD}$ for landing within 1500 m.	✓	Section 4.1.
REQ-SUB-AER-HLD-03	The high-lift system shall not impose additional maintenance compared with the reference aircraft	✗	More complex type of flaps requiring more maintenance. However, no additional maintenance compared to the A321neo.
REQ-SUB-AER-F-01	Any fuselage enlargement or fairing caused by LH_2 storage shall maintain the aerodynamic capability of the aircraft.	✓	Section 4.1.

Req. ID	Requirement	✓?	Explanation
REQ-SUB-AER-F-02	The configuration shall preserve passenger comfort comparable to the reference aircraft while meeting aerodynamic efficiency needs.	✓	Section 4.1.
REQ-SUB-AER-T-01	The horizontal tail shall provide sufficient trim authority without excessive cruise trim drag.	✓	Section 3.5.
Structures Requirements			
REQ-SYS-STR-01	The aircraft structure shall withstand a limit load factor of [TBD] g at any speed up to the Design Diving Speed without permanent deformation.	O	
REQ-SYS-STR-02	The aircraft structure shall withstand a limit load factor of [1.5* TBD] g at any speed up to the Design Diving Speed without failure.	O	
REQ-SYS-STR-03	The aircraft structure shall withstand a limit load factor of -1 at any speed up to the Design Diving Speed without permanent deformation.	O	
REQ-SYS-STR-04	The aircraft structure shall withstand a limit load factor of $-1 \cdot 1.5$ at any speed up to the Design Diving Speed without failure.	O	
REQ-SYS-STR-05	The aircraft cabin must be pressurised to provide a pressure altitude of at most 2438 m.	O	
REQ-SYS-STR-06	The airframe structure shall withstand limit ground loads resulting from ground contact at 3.05 m/s sink velocity with maximum landing weight TBD.	O	
REQ-SYS-STR-07	The structure of the aircraft shall not be less be recyclable than that of the reference aircraft.	✓	Section 4.2.
REQ-SYS-STR-08	The aircraft shall achieve a lower total lifecycle environmental impact than the reference aircraft.	✓	Section 8.2.
Structures Subsystems Requirements			
REQ-SUB-STR-LG-01	The landing gear shall not be placed within the wing box or within the location of the HLDs.	✗	Landing gear retracts into the wing box.
REQ-SUB-STR-FUS-01	The fuselage structure shall withstand the combined loads of maximum internal pressure of [TBD] and aerodynamic flight loads up to Vd, without permanent deformation.	O	
REQ-SUB-STR-FUS-02	The fuselage structure shall withstand an ultimate internal pressure of [1.5*TBD] without structural failure.	O	
REQ-SUB-STR-KET-01	The kerosene fuel tank structure shall withstand an ultimate hydrostatic pressure of [TBD] kPa.	O	
REQ-SUB-STR-HYT-01	The hydrogen storage structure shall withstand an ultimate hydrostatic pressure of 200 kPa.	✓	Chapter 6.
Control and Stability Requirements			
REQ-SYS-CS-01	The aircraft shall be safely controllable and manoeuvrable during take-off, climb, level flight, descent, approach, go-around, approach, and landing.	✓	Section 3.5.
REQ-SYS-CS-02	The aircraft shall remain controllable following sudden failure of the critical engine.	O	
REQ-SYS-CS-03	The airplane shall be in static equilibrium during the following phases: fuelling, loading, boarding.	✓	Section 3.8.
REQ-SYS-CS-04	The aircraft shall be controllable and manoeuvrable during go-around with all engines operating, including flight crew workload.	O	
REQ-SYS-CS-05	The aircraft shall maintain stability and controllability over the full operational CG range caused by passenger loading, SAF/kerosene consumption, LH_2 consumption, and cryogenic tank placement.	✓	Section 3.5.
REQ-SYS-CS-06	The aircraft shall remain stable and controllable during take-off within 2100 m.	✓	Section 3.5.
REQ-SYS-CS-07	The aircraft shall remain stable and controllable during landing within 1500 m.	✓	Section 3.5.
REQ-SYS-CS-08	The aircraft shall be longitudinally, directionally, and laterally stable in all flight conditions.	O	
REQ-SYS-CS-09	The aircraft shall define a certified flight envelope including allowable weight, CG, speed, altitude, flap setting, gear configuration, and thrust condition combinations.	O	
REQ-SYS-CS-10	The aircraft shall remain longitudinally controllable in power-off glide conditions at speeds up to $1.3V_{SR1}$.	O	
Control and Stability Subsystems Requirements			
REQ-SUB-CS-HT-01	The horizontal tail shall provide sufficient pitch control to trim and manoeuvre the aircraft over the complete CG envelope.	✓	Tail is sized according to controllability limits.
REQ-SUB-CS-VT-01	The vertical tail and rudder shall provide sufficient directional control after critical engine failure.	O	
REQ-SUB-CS-VT-02	The vertical tail shall account for asymmetric thrust from the dual-fuel propulsion architecture and engine-out cases.	O	
REQ-SUB-CS-FC-01	The flight control system shall provide safe pitch, roll, and yaw control.	O	
REQ-SUB-CS-LG-01	The tip over angle of the landing gear shall be > 10°.	✓	Section 3.8.
REQ-SUB-CS-LG-02	The turnover angle of the landing gear shall be smaller than 55°.	O	Vertical dimension of CG was not yet determined.
REQ-SUB-CS-LG-03	The load on the nose landing gear shall be at least 8% of the aircraft weight	✓	Nose landing gear carry 10% of the MTOM.
REQ-SUB-CS-LG-04	The load on the nose landing gear shall be at most 15% of the aircraft weight.	✓	Nose landing gear carry 10% of the MTOM.

Req. ID	Requirement	✓?	Explanation
REQ-SUB-CS-LG-05	The lateral ground clearance angle shall be larger than 8 for the inner engine.	✓	10° achieved at lowered gear.
REQ-SUB-CS-LG-06	The lateral ground clearance angle shall be larger than 5 for the outer engine.	✓	Outer engine was not installed.
REQ-SUB-CS-W-01	The dihedral shall be larger than 3° and smaller than 7°.	✓	Dihedral of 6°.
Ground Operation Subsystems Requirements			
REQ-SYS-GOP-01	The aircraft shall complete a turnaround for kerosene-only refuelling, within 45 minutes.	✓	
REQ-SYS-GOP-02	The aircraft shall complete a turnaround for kerosene and hydrogen refuelling, within 60 minutes.	✗	Section 10.1.
REQ-SYS-GOP-03	The aircraft shall require no more than one hydrogen refuelling to complete an outbound-and-return nominal mission.	✓	Section 2.3.
REQ-SYS-GOP-04	The aircraft shall be compatible with kerosene/SAF refuelling using conventional airport refuelling procedures.	✓	Section 10.1.
REQ-SYS-GOP-05-2	The aircraft shall enable the safe release of excess hydrogen.	✓	Ground and in-flight venting is considered.

Functional Flow Diagram

Functional Breakdown Structure

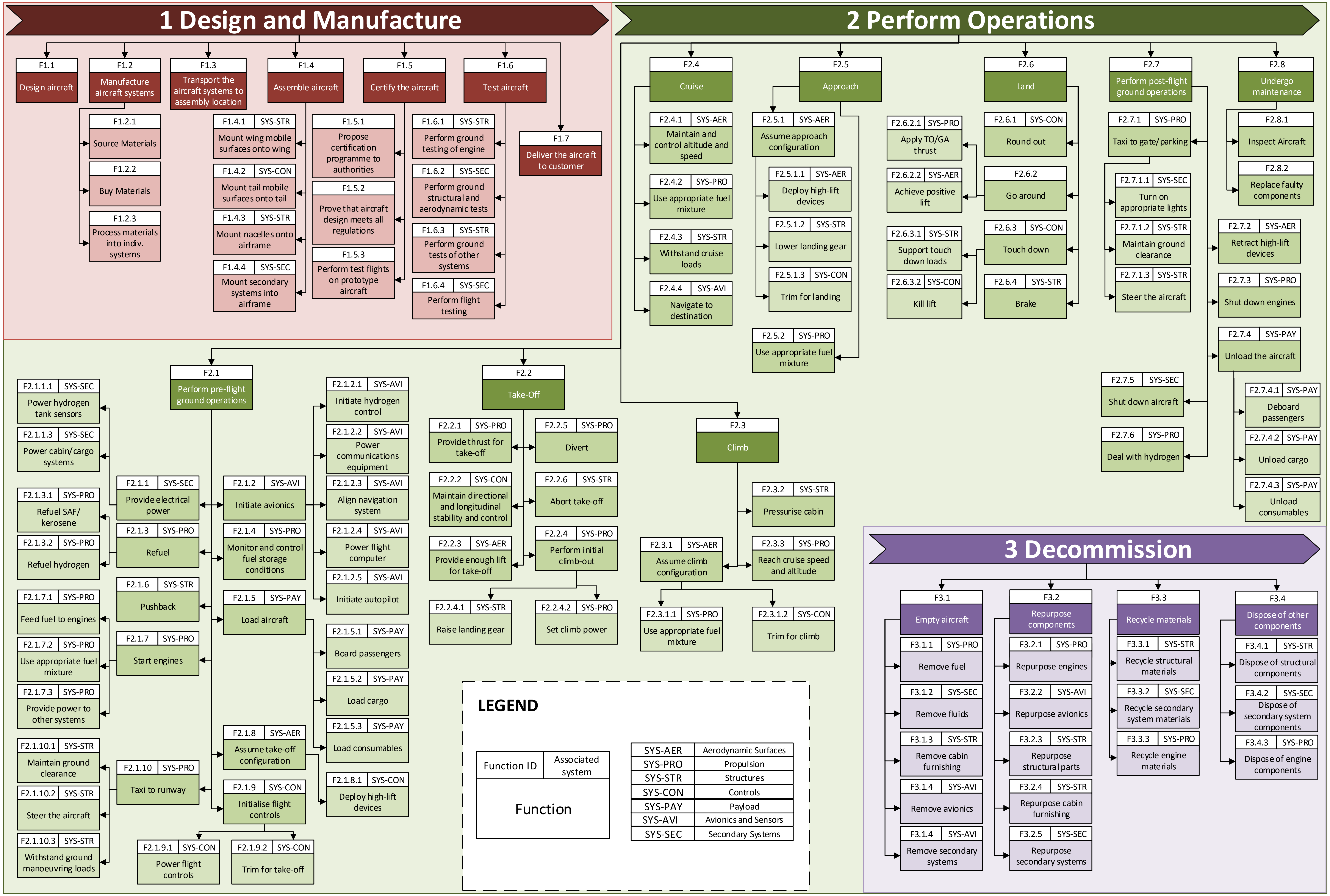

1 Design and Manufacture

- F1.1 Design aircraft
- F1.2 Manufacture aircraft systems
  - F1.2.1 Source Materials
  - F1.2.2 Buy Materials
  - F1.2.3 Process materials into indiv. systems
- F1.3 Transport the aircraft systems to assembly location
- F1.4 Assemble aircraft
  - F1.4.1 SYS-STR Mount wing mobile surfaces onto wing
  - F1.4.2 SYS-CON Mount tail mobile surfaces onto tail
  - F1.4.3 SYS-STR Mount nacelles onto airframe
  - F1.4.4 SYS-SEC Mount secondary systems into airframe
- F1.5 Certify the aircraft
  - F1.5.1 Propose certification programme to authorities
  - F1.5.2 Prove that aircraft design meets all regulations
  - F1.5.3 Perform test flights on prototype aircraft
- F1.6 Test aircraft
  - F1.6.1 SYS-STR Perform ground testing of engine
  - F1.6.2 SYS-SEC Perform ground structural and aerodynamic tests
  - F1.6.3 SYS-STR Perform ground tests of other systems
  - F1.6.4 SYS-SEC Perform flight testing
- F1.7 Deliver the aircraft to customer

2 Perform Operations

- F2.1 Perform pre-flight ground operations
  - F2.1.1 SYS-SEC Provide electrical power
    - F2.1.1.1 SYS-SEC Power hydrogen tank sensors
    - F2.1.1.3 SYS-SEC Power cabin/cargo systems
  - F2.1.2 SYS-AVI Initiate avionics
    - F2.1.2.1 SYS-AVI Initiate hydrogen control
    - F2.1.2.2 SYS-AVI Power communications equipment
    - F2.1.2.3 SYS-AVI Align navigation system
    - F2.1.2.4 SYS-AVI Power flight computer
    - F2.1.2.5 SYS-AVI Initiate autopilot
  - F2.1.3 SYS-PRO Refuel
    - F2.1.3.1 SYS-PRO Refuel SAF/ kerosene
    - F2.1.3.2 SYS-PRO Refuel hydrogen
  - F2.1.4 SYS-PRO Monitor and control fuel storage conditions
  - F2.1.5 SYS-PAY Load aircraft
    - F2.1.5.1 SYS-PAY Board passengers
    - F2.1.5.2 SYS-PAY Load cargo
    - F2.1.5.3 SYS-PAY Load consumables
  - F2.1.6 SYS-STR Pushback
  - F2.1.7 SYS-PRO Start engines
    - F2.1.7.1 SYS-PRO Feed fuel to engines
    - F2.1.7.2 SYS-PRO Use appropriate fuel mixture
    - F2.1.7.3 SYS-PRO Provide power to other systems
  - F2.1.8 SYS-AER Assume take-off configuration
    - F2.1.8.1 SYS-CON Deploy high-lift devices
  - F2.1.9 SYS-CON Initialise flight controls
    - F2.1.9.1 SYS-CON Power flight controls
    - F2.1.9.2 SYS-CON Trim for take-off
  - F2.1.10 SYS-PRO Taxi to runway
    - F2.1.10.1 SYS-STR Maintain ground clearance
    - F2.1.10.2 SYS-STR Steer the aircraft
    - F2.1.10.3 SYS-STR Withstand ground manoeuvring loads
- F2.2 Take-Off
  - F2.2.1 SYS-PRO Provide thrust for take-off
  - F2.2.2 SYS-CON Maintain directional and longitudinal stability and control
  - F2.2.3 SYS-AER Provide enough lift for take-off
  - F2.2.4 SYS-PRO Perform initial climb-out
    - F2.2.4.1 SYS-STR Raise landing gear
    - F2.2.4.2 SYS-PRO Set climb power
  - F2.2.5 SYS-PRO Divert
  - F2.2.6 SYS-STR Abort take-off
- F2.3 Climb
  - F2.3.1 SYS-AER Assume climb configuration
    - F2.3.1.1 SYS-PRO Use appropriate fuel mixture
    - F2.3.1.2 SYS-CON Trim for climb
  - F2.3.2 SYS-STR Pressurise cabin
  - F2.3.3 SYS-PRO Reach cruise speed and altitude
- F2.4 Cruise
  - F2.4.1 SYS-AER Maintain and control altitude and speed
  - F2.4.2 SYS-PRO Use appropriate fuel mixture
  - F2.4.3 SYS-STR Withstand cruise loads
  - F2.4.4 SYS-AVI Navigate to destination
- F2.5 Approach
  - F2.5.1 SYS-AER Assume approach configuration
    - F2.5.1.1 SYS-AER Deploy high-lift devices
    - F2.5.1.2 SYS-STR Lower landing gear
    - F2.5.1.3 SYS-CON Trim for landing
  - F2.5.2 SYS-PRO Use appropriate fuel mixture
- F2.6 Land
  - F2.6.1 SYS-CON Round out
  - F2.6.2 Go around
    - F2.6.2.1 SYS-PRO Apply TO/GA thrust
    - F2.6.2.2 SYS-AER Achieve positive lift
  - F2.6.3 SYS-CON Touch down
    - F2.6.3.1 SYS-STR Support touch down loads
    - F2.6.3.2 SYS-CON Kill lift
  - F2.6.4 SYS-STR Brake
- F2.7 Perform post-flight ground operations
  - F2.7.1 SYS-PRO Taxi to gate/parking
    - F2.7.1.1 SYS-SEC Turn on appropriate lights
    - F2.7.1.2 SYS-STR Maintain ground clearance
    - F2.7.1.3 SYS-STR Steer the aircraft
  - F2.7.2 SYS-AER Retract high-lift devices
  - F2.7.3 SYS-PRO Shut down engines
  - F2.7.4 SYS-PAY Unload the aircraft
    - F2.7.4.1 SYS-PAY Deboard passengers
    - F2.7.4.2 SYS-PAY Unload cargo
    - F2.7.4.3 SYS-PAY Unload consumables
  - F2.7.5 SYS-SEC Shut down aircraft
  - F2.7.6 SYS-PRO Deal with hydrogen
- F2.8 Undergo maintenance
  - F2.8.1 Inspect Aircraft
  - F2.8.2 Replace faulty components

3 Decommission

- F3.1 Empty aircraft
  - F3.1.1 SYS-PRO Remove fuel
  - F3.1.2 SYS-SEC Remove fluids
  - F3.1.3 SYS-STR Remove cabin furnishing
  - F3.1.4 SYS-AVI Remove avionics
  - F3.1.4 SYS-AVI Remove secondary systems
- F3.2 Repurpose components
  - F3.2.1 SYS-PRO Repurpose engines
  - F3.2.2 SYS-AVI Repurpose avionics
  - F3.2.3 SYS-STR Repurpose structural parts
  - F3.2.4 SYS-STR Repurpose cabin furnishing
  - F3.2.5 SYS-SEC Repurpose secondary systems
- F3.3 Recycle materials
  - F3.3.1 SYS-STR Recycle structural materials
  - F3.3.2 SYS-SEC Recycle secondary system materials
  - F3.3.3 SYS-PRO Recycle engine materials
- F3.4 Dispose of other components
  - F3.4.1 SYS-STR Dispose of structural components
  - F3.4.2 SYS-SEC Dispose of secondary system components
  - F3.4.3 SYS-PRO Dispose of engine components

LEGEND

Function ID	Associated system
Function	

SYS-AER	Aerodynamic Surfaces
SYS-PRO	Propulsion
SYS-STR	Structures
SYS-CON	Controls
SYS-PAY	Payload
SYS-AVI	Avionics and Sensors
SYS-SEC	Secondary Systems

Project Design & Development Logic

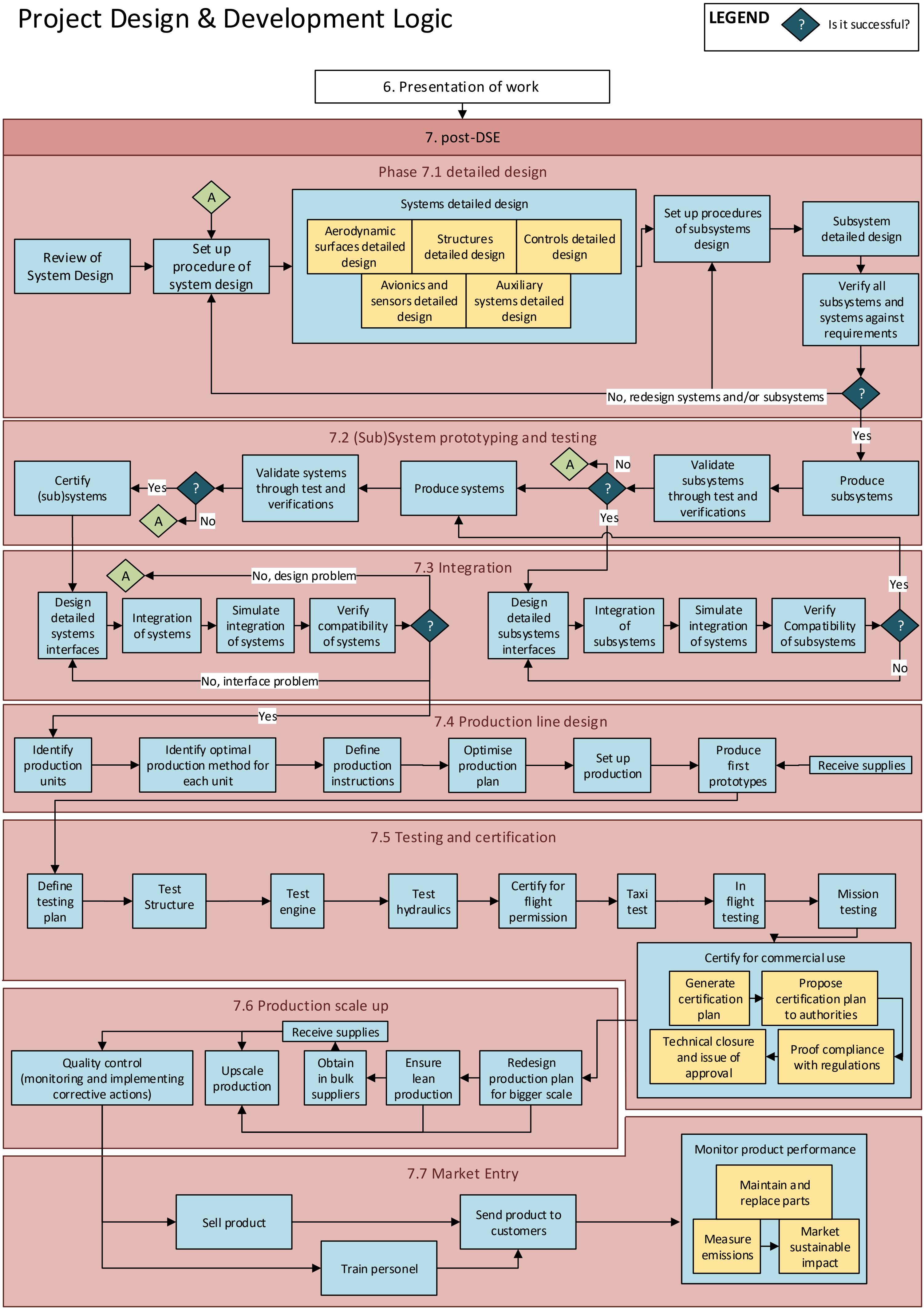

Post-DSE Work Flow Diagram